Université catholique de Louvain
Louvain School of Engineering
Institute of Mechanics, Materials
and Civil Engineering

Turbulent heat transfer in T-junctions

Doctoral dissertation presented by

Michail Georgiou

Supervisor:
Prof. Miltiadis Papalexandris (UCL)

Thesis Committee:
Dr. Vincent Deledicque (Bel V)
Prof. Eric Deleersnijder (UCL)
Dr. Holger Grosshans (PTB)
Prof. Thomas Pardoen (President) (UCL)
Prof. Sandra Soares-Frazao (UCL)

In partial fulfilment of the requirements for the degree of Doctor in Engineering Sciences

This doctoral research has been funded by Bel V

Louvain-la-Neuve, December 2017

To my mother and my sister

Acknowledgements

I would first like to express my sincere gratitude to Bel V, a subsidiary of the Belgian Federal Agency of Nuclear Control. Without their financial support I would have never had the opportunity to work on such an interesting project. I particularly want to thank Dr. Vincent Deledicque of Bel V for following closely my doctoral research.

I would also like to thank deeply my supervisor, Prof. Miltiadis Papalexandris, for his continuous and limitless support through the whole project. He was always available to discuss, not just issues related to my research, but also issues related to my personal and professional growth. For this reason I will always be indebted to him.

Many thanks are also addressed to the members of the committee of the thesis. The external member, Dr. Holger Grosshans, for accepting to be in the committee and for sharing his views on research and his passion for science. Prof. Sandra Soares-Frazao for her insightful observations over the duration of the project that have helped me to become a better scientist, and for her constructive criticism during the private defence of the thesis. Prof. Eric Deleersnijder for his valuable remarks and helpful comment that substantially improved the quality of this text. Finally, I am grateful to Prof. Thomas Pardoen for accepting to chair the doctoral committee and for his insightful comments and suggestions.

I would like to thank Dr. Valerie Gelbgras of Ansys Inc. for many fruitful discussions and suggestions. I also want to thank my colleague, Davide Monsorno, for sharing the same office with me over the last four years and for the many intuitive discussions that we had through this time. It was an honour to be in the same space with such a brilliant scientist and personality. Many thanks are also dedicated to Dr. Christos Varsakelis, Dr. Panagiotis Antoniadis, and Dr. Lucio De Fusco for the fruitful discussions I had with over these years.

I would also like to express my gratitude to my housemates in Brussels, Axel, Nelles, Inés, Joana, Hanna and Catalina. Sharing a house with them has provided the best substitute of a family that someone can have while living abroad. I want to also thanks the many and good friends that I have made in Brussels and Louvain-la-Neuve.

Living abroad can be difficult and for this reason I would like to thank all my friends in Cyprus for the support they provided. Despite being quite far, they were all the time there for me and they will eternally be my “Agapoules”.

Finally, I want extend my heartfelt gratitude to my family for supporting me emotionally and financially all these years. My late father, and my mother that has been always there for me listening to my problems. I also want to thank my sister Constantina and her husband Andreas for their help over these years.

Michail Georgiou
Louvain-la-Neuve, December 2017.

Abstract

This PhD dissertation consists of a detailed study of the mixing between a turbulent crossflow and an incoming jet in a T-junction. Our study is focused on the complex flow structures that emerge in such flows. Special attention is also paid to the flow field in the near-wall regions.

In the first part of the thesis we describe the governing system of equations, which is derived from the low-Mach-number asymptotic expansion of the Navier-Stokes-Fourier equations. This asymptotic expansion has the advantage that the resulting energy equation is essentially decoupled from the momentum equation, which leads to significant computational savings. We also present the algorithm that we have implemented for the numerical treatment of the governing equations. This algorithm is a generalisation of the popular projection method for constant-density flows to variable density ones.

In the second part we report on wall-resolved and experimentally validated Large-Eddy Simulations (LES) of constant-density flows. The bulk Reynolds number of the crossflow is $15,000$. Further, we consider cases with two different momentum ratios, namely, $M_R = 2$ and $M_R = 0.5$. In the presentation of the results we elaborate on the main features of the flow, namely, the shear layers that emanate from the corners of the entry of the jet, the large recirculation bubble downstream the incoming jet, and the mixing process beyond the reattachment point. For validation purposes, we compare our simulations with existing experimental data. This comparison shows good agreement between our numerical predictions and the measurements. First and second-order statistics of the flow are also presented and analysed in detail. Our simulations reveal two features of the flow that have not been reported before in studies of T-junctions. The first one is a secondary small-scale recirculation region between the entry of the jet and the large recirculation bubble. The second one is the negative turbulent kinetic energy production that occurs in the recirculation bubble and close to the reattachment of the flow. The analysis of our results further reveals that just across the entry of the jet, the boundary layer at the wall opposite to the jet experiences a favourable pressure gradient due to a Venturi effect induced by the incoming jet. In turn, this favourable pressure gradient contributes to the local relaminarization of the flow. On the other hand, the boundary layer downstream the recirculation bubble experiences an adverse pressure gradient. In both cases, a significant deviation from the law of the wall is confirmed. These findings provide an explanation for the poor performance of wall functions in LES modelling for flows in T-junctions.

In the third part of this dissertation we examine turbulent heat transfer in gas-gas flows via LES. The bulk Reynolds number is again set at $15,000$. Emphasis is placed on the role of the temperature as an active scalar and on the effects of thermal stratification to the emerging structures in the flow field. Herein we discuss in detail the main features of the flow, such as the shear layer between the two streams, the regions of flow acceleration due to the Venturi effect, the recirculation regions, and the thermal mixing downstream the reattachment point of the flow. We also elaborate on the first and second-order statistics of flow quantities, including the turbulent heat fluxes, and on the near-wall behaviour of the streamwise velocity component. Our numerical predictions compare favourably with existing experimental measurements, as regards both the temperature field and the turbulent heat fluxes. Our study also includes a spectral analysis of the temperature signal at selected locations near the solid boundaries, which is helpful for assessing the risk of thermal fatigue at the walls of the T-junction. According to this analysis, for the flow conditions considered herein, the walls of the T-junction are indeed susceptible to thermal fatigue.

In the fourth part we perform a Direct Numerical Simulations (DNS) of turbulent heat transfer in liquid-liquid flows. The bulk Reynolds number is set $6,000$. Herein particular emphasis is placed on the analysis of the instantaneous features of the flow field. According to it, mixing is initialised via mushroom-like structures of streamwise vorticity formed at the interface of the crossflow and the incoming jet. It is significantly enhanced, however, when this shear layer merges with the one formed between the incoming jet and the recirculation bubble. We also compute the budget of the Turbulent-Kinetic-Energy (TKE) which provides additional information about the turbulence generation mechanisms in the flow of interest. TKE is mostly produced at the cores of the shear layers and it is transported toward the walls of the horizontal channel where it is eventually dissipated. Further, we have conducted a wall-resolved LES in order to assess the capacity of this approach for accurately simulating flows in T-junctions. Our comparisons show good overall agreement between the predictions of DNS and LES, which is particularly encouraging given that the LES grid is 22 times coarse than that of the DNS.

Contents

List of Figures

List of Tables

Nomenclature

List of symbols

c	speed of sound
c_p	specific heat of the fluid under constant pressure
c_v	specific heat of the fluid under constant volume
C_f	skin friction coefficient
C_k	convection of turbulent kinetic energy
C_p	pressure coefficient
D_k	viscous diffusion of turbulent kinetic energy
f	auxiliary flux
$\mathbf{g}$	gravity vector
k	turbulent kinetic energy
k_r	residual kinetic energy
l	length
L_x	dimension of the domain in the streamwise x-direction
L_y	dimension of the domain in the vertical y-direction
L_z	dimension of the domain in the spanwise z-direction
M_R	ratio between the momentum flux of the crossflow and the incoming jet
$\hat{n}$	unit outward normal vector
N_x	number of computational nodes in the streamwise x-direction
N_y	number of computational nodes in the vertical y-direction
N_z	number of computational nodes in the spanwise z-direction

p	pressure
p^0	*thermodynamic* pressure
p^1	*static* pressure
p_{m}	modified pressure
P_k	production of turbulent kinetic energy
Q	Q-criterion
ρ	density
$\mathcal{R}$	universal gas constant
S	power spectral density
$\boldsymbol{S}$	rate-of-strain tensor
t	time
τ_{w}	wall stress
T	temperature
$\mathcal{T}$	shear rate of strain
T_k	transport of turbulent kinetic energy
T_R	ratio between the temperature of the hot and the cold stream
$\mathbf{u} = (u, v, w)$	velocity vector
$\tilde{\boldsymbol{u}} = (\tilde{u}, \tilde{v}, \tilde{w})$	*provisional*, or *intermediate* velocity vector at the predictor step
$\breve{\boldsymbol{u}} = (\breve{u}, \breve{v}, \breve{w})$	*provisional*, or *intermediate* velocity vector at the corrector step
x	streamwise spatial coordinate
y	vertical spatial coordinate
$\hat{\boldsymbol{y}}$	unit vector along the vertical direction
z	spanwise spatial coordinate
γ	specific heat ratio
δ	half-height of the channel
Δt	time step
Δx	streamwise grid length
Δy	vertical grid length

Δz	spanwise grid length
ϵ_k	viscous dissipation of turbulent kinetic energy
η	Kolmogorov length-scale
η_θ	temperature microscale
θ	normalised temperature
κ	thermal conductivity coefficient
κ_t	eddy conductivity coefficient
μ	dynamic viscosity coefficient
μ_t	eddy dynamic viscosity coefficient
ν	kinematic viscosity coefficient
ν_t	eddy kinematic viscosity coefficient
Π_k	pressure correlation with the dilatation of fluctuation
$\boldsymbol{\tau}$	deviatoric part of viscous stress tensor
τ_η	Kolmogorov time-scale
ϕ_k	work of fluctuating pressure through fluctuating motions
Φ_k	work of mean pressure through fluctuating motions
$\boldsymbol{\Omega}$	vorticity tensor

Subscripts

b.w.	bottom wall
f.n.	first node
i	order of appearance of the cell along the x-axis
$i+1$	value at the center of the neighbouring cell along the x-direction
$i+\frac{1}{2}$	value at the cell-interface along the x-direction
j	order of appearance of the cell along the y-axis
k	order of appearance of the cell along the z-axis
ref	reference value
rms	root mean square
t.w.	top wall

VD	Van Driest transformation

Superscripts

0	term of order 0
1	term of order 1
n	value at the time-level n
$*$	predicted value
$+$	wall-normalised
$'$	fluctuating component of Reynolds decomposition
$''$	fluctuating component of density weighted Favre decomposition

Abbreviations

BI-CGSTAB	**BIC**onjugate **G**radient **S**tabilized **M**ethod
DNS	**D**irect **N**umerical **S**imulations
ECC	**E**mergency **C**ore **C**ooling
FFT	**F**ast **F**ourier **T**ransform
HVAC	**H**eating **V**entilation **A**ir-**C**onditioning
ILUT	**I**ncomplete **L**ower **U**pper **T**hreshold
LES	**L**arge **E**ddy **S**imulations
LWR	**L**ight **W**ater **R**eactor
LOCA	**L**oss **O**ff **C**oolant **A**ccident
MILES	**M**onotonically **I**ntegrated **L**arge **E**ddy **S**imulations
RANS	**R**eynolds **A**veraged **N**avier **S**tokes
RMS	**R**oot **M**ean **S**quare
PTS	**P**ressurised **T**hermal **S**hock
TKE	**T**urbulent **K**inetic **E**nergy

Non-dimensional numbers

$Pr = (c_p \mu)/\kappa$	Prandtl number. Measure of the ratio of the momentum and thermal diffusivities.
$Re = (\rho\, l\, u)/\mu$	Reynolds number. Measure of the ratio of inertia and viscous forces.
$Ri = \lvert \boldsymbol{g} \rvert\, l \,/\, u^2$	Richardson number. Measure of the ratio of gravity to the flow inertia.
$St = f\, l \,/\, u$	Strouhal number. Dimensionless number describing oscillating flow mechanisms.

Chapter 1

Introduction

1.1 Turbulent flows in T-junctions and applications

This thesis consists of an in-depth study of the interaction and mixing between a turbulent crossflow and an incoming jet in a T-junction. Due to their high efficiency in mixing, T-junctions are found in several industrial applications. We first outline some instructive examples.

T-junctions are used in a wide range of applications related to heating, ventilation and air conditioning (HVAC). For example, they are encountered in many components of heating and sanitary systems of buildings. They are also found in the piping and plumbing systems of ships and aeroplanes as well as in AC units of automobiles. In figure 1.1 we show an illustration of the AC unit of an automobile. According to this figure, air that is cooled from the evaporator is mixed with hot air that enters the AC from the heater core in a T-junction. By understanding the emerging flow patterns one can adjust the flow rates so as to enhance the thermal mixing between the two streams. This, in turn, may result in the downsizing of the AC unit which is beneficial for the automotive industry.

Furthermore, T-junctions are encountered in the cooling circuits of nuclear reactors which employ liquid water as a cooling medium. In figure 1.2 we provide an example of how T-junctions are used in these circuits. In particular, a cold liquid jet enters the horizontal channel so as to decrease the temperature of the hot liquid crossflow. However, the incomplete thermal mixing between the two fluids results in the development of large temperature gradients in the vicinity of the entry of the jet. These, in turn, render T-junctions susceptible to thermal fatigue. More specifically, the high-amplitude temperature fluctuations that develop close to the

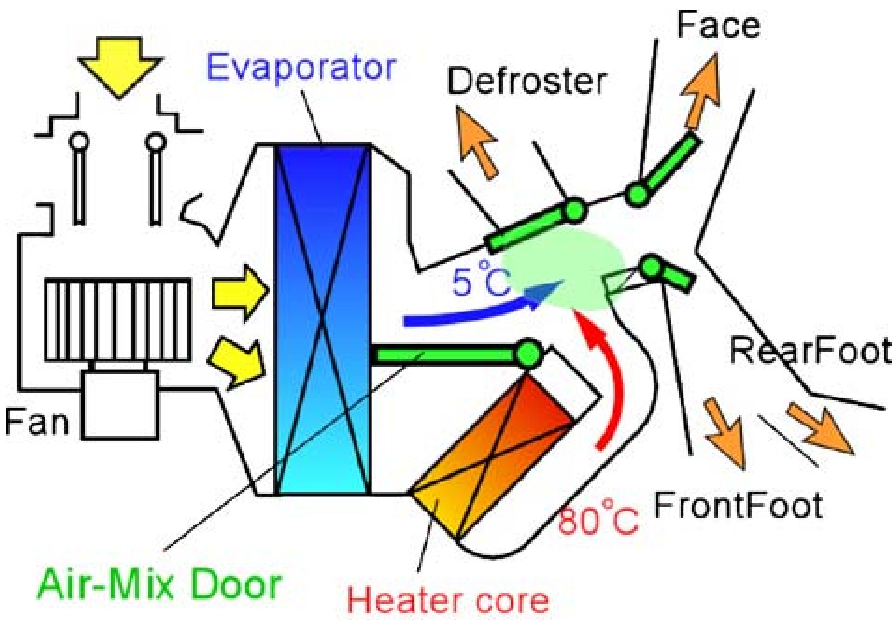

Figure 1.1: Illustration of a HVAC unit in automobiles. This image is reprinted from [1], with permission from Springer Science & Business Media.

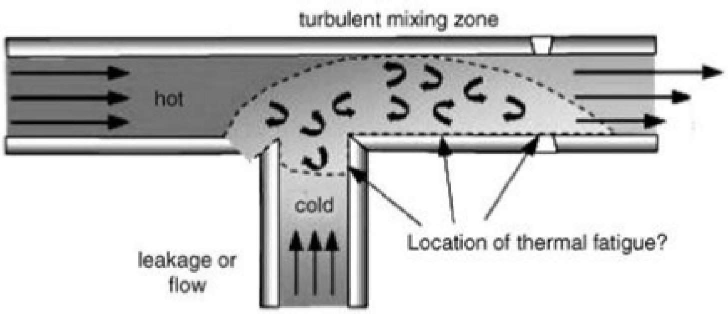

Figure 1.2: Example of T-junctions in cooling systems of nuclear reactors. This image is reprinted from [5], with permission from Elsevier.

walls of the piping system result in thermal stresses which may cause cracking due to thermal fatigue [2]. This phenomenon is also known as "thermal stripping" and is of particular concern in the design and maintenance of cooling circuits of nuclear reactors. In fact, it may lead to important incidents; see, for example, those described in [3] and [4].

In addition, in nuclear reactors, T-junctions play an important role in emergency cooling circuits. For example, they are used as a counter measure for Loss of Coolant Accidents (LOCA). In figure 1.3 we show an illustration of the flow

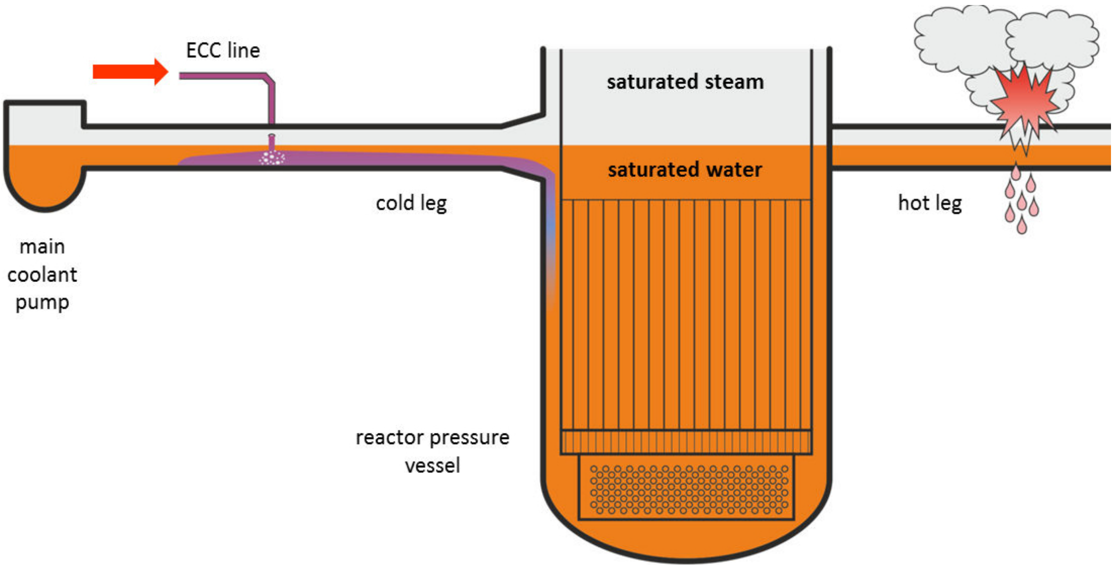

Figure 1.3: Illustration of the flow in the T-junctions during LOCA in Pressurised Water Reactors (PWR). Source: Helmholtz-Zentrum Dresden-Rossendorf, `https://www.hzdr.de/db/Cms?pOid=25292&pNid=3017`.

during these situations. Accordingly, the water in the pipe that provides the core of the reactor vessel with coolant, also known as "cold leg", begins to evaporate and turns into a steam-liquid mixture. This, in turn, decreases the cooling capacity of the circuit and may cause the melting of the core of the reactor. For this to be avoided, the Emergency Core Cooling (ECC) mechanism is activated. This results in the injection of high pressure cold water from the ECC line.

The interaction of the liquid jet with the two-phase mixture in the cold leg gives rise to complex phenomena, such as entrainment of bubbles to the bulk of the crossflow. In addition, in many regions of the T-junction stratification effects become important. Further, the sudden change of direction that the two streams experience when they reach the core of the reactor affects significantly the flow field. Despite the efficiency of this cooling mechanism, the injection of pressurised cold water leads to the development of large thermal stresses. These render the walls of the reactor susceptible to the Pressurised Thermal Shock (PTS), *i.e.* the development of large thermal stresses at the pipe system of nuclear reactors under highly pressurised conditions. This is one of the most important issues regarding nuclear reactor safety [6].

1.2 Recent advancements in the study of turbulent flows in T-junctions

Due to their numerous industrial applications, flows in T-junctions have attracted considerable interest and many research efforts have been dedicated to their study. In this section we outline experimental and computational studies that have focused on turbulent mixing in this geometry.

As concerns experimental studies, Kamide et al. [7] examined flows in T-junctions with circular cross-sections at various momentum ratios M_R. The momentum ratio is defined as the ratio of the momentum flux of the crossflow to that of the incoming jet. In these experiments, the Reynolds number was ranging from $30,000$ to $100,000$. According to these authors, at low momentum ratios (lower than 0.35), a wake region is formed downstream the entry of the jet. On the other hand, at higher momentum ratios, a large recirculation bubble is developed instead. In their study with the same geometry and similar Reynolds numbers, Walker et al. [8] observed the formation of two counter-rotating vortices in the recirculation bubble and showed that the highest root mean square (rms) velocities are located in the mixing zone between this bubble and the jet.

De Tilly and Sousa [9] examined the mixing process in T-junctions with rectangular cross-sections at high momentum ratios and confirmed that mixing was intensified when the crossflow was turbulent. They attributed the mixing enhancement to the formation of large-scale structures at the shear layer that was formed between the jet and the crossflow. According to the same study, when the crossflow was laminar these large-scale structures did not develop and the mixing between the jet and the crossflow was significantly smaller. In addition, Hirota et al. [10, 11] examined turbulent flows in rectangular cross-sections for Reynolds numbers of $15,000$ and $25,000$. They observed a vertical oscillation of the incoming jet as well as the formation of longitudinal eddies at the shear layer that is formed between the incoming jet and the recirculation bubble. Further, it is worth mentioning that various authors have studied this flow, in connection with the thermal stripping phenomenon; see, for example, the efforts the Vattenfall R&D research group [12, 13], Naik-Nimbalkar et al. [14], Lin et al. [15] and references therein.

Beside experimental studies, several computational efforts focused on turbulent flows in T-junctions as well. The most appropriate method of investigating this flow is Direct Numerical Simulations (DNS). In DNS, the computational mesh is sufficiently fine to resolve all the scales of the flow. However, this increases significantly the computational cost of this method. In fact, the cost of DNS becomes prohibitively high as the Reynolds number increases. Therefore, currently, this methodology is limited to low and moderate turbulent Reynolds numbers, *i.e.* Reynolds numbers smaller than $100,000$.

One may also study numerically these flows via Reynolds-Averaged-Navier-Stokes (RANS). In this method, the Reynolds decomposition is applied to the governing equations so as to obtain their averaged version. RANS provides information about the average values of the flow quantities. On the other hand, it yields no information about the dynamic features of turbulent flows.

Alternatively, one can investigate numerically these flows by means of Large Eddy Simulations (LES). This method amounts to applying a spatial filter to the governing equations of the problem. The structures larger than the width of the spatial filter are directly resolved while those that are smaller, are modelled. This methodology yields information about the unsteady motion of the large structures of the flow while its computational cost is significantly reduced, in comparison to DNS. For these reasons, it is often applied to flows in T-junctions.

Hu and Kazimi [16] performed one of the first LES of turbulent heat transfer in T-junctions. According to this study, LES can predict fairly well the regions in which the maximum temperature fluctuations are developed. Lee et al. [17] also studied flows in T-junctions that are related to the thermal stripping phenomenon with the Reynolds number ranging from $20,000$ to $200,000$. These authors examined how a crack in the solid boundary of the T-junction grows due to thermally induced wall stresses and showed that in flows with large temperature gradients the crack grows significantly faster. Subsequently, many authors have examined flows in this geometry via LES; see, for example, [18–20] and references therein. However, most of these LES of flows in T-junctions were underresolved, with respect to the complexity of the flow.

More recently, the appreciation of the complexity of the flow, backed-up by the ever increasing computational resources, has prompted researchers to perform LES at much finer grids that revealed more details about the dynamic features of the flow. For example, Sakowitz et al. [21, 22] performed LES of flows in both circular and rectangular T-junctions for Reynolds numbers of the order $10,000$ and studied the vorticity field of such flows. They reported that, in both geometries, the shear layer that is formed between the jet and the crossflow oscillates with a Strouhal number of order one. Also, based on the findings of their LES study, Howard and

Serre [23, 24] concluded that mixing is enhanced by the horseshoe and counter-rotating vortices that are formed near the entry of the incoming jet. In addition, Tunstall et al. [25] studied turbulent flows in T-junctions with an upstream elbow for a Reynolds number of $100,000$. They showed that the curvature upstream the jet entry leads to the formation of Dean vortices[1] [26, 27] that play an important role in the mixing process between the two streams. Finally, over the last years, Direct Numerical Simulations (DNS) were performed in turbulent mixing in T-junctions. Wu et al. [28, 29] have performed one of the first DNS on flows with high momentum ratios for a Reynolds number of $3,333$. However, they did not resolve the geometry of the jet and an artificial inflow was imposed instead.

1.3 Main challenges in the simulation of flows in T-junctions

Even though the flow configuration in T-junctions is conceptually simple, one has to tackle several challenges in order to simulate sufficiently well the resulting flow field.

First of all, in applications related to thermal mixing, there are large temperature gradients. These, in turn, affect significantly the physics of the flow. Therefore, one has to employ an algorithm that is able to treat such flows.

In addition, one needs to provide accurate turbulent velocity inflow data for the crossflow and the incoming jet. As Ndombo and Howard [30] have shown, the inflow condition plays an important role in the successful modelling of flows in T-junctions. These authors showed that the use of reliable turbulent inflow data is necessary for the accurate predictions of the flow field near the walls of the T-junction. Moreover, one has to impose a turbulent outflow condition. This condition has to ensure that the turbulent structures are exiting smoothly the computational domain, without affecting the flow field in this vicinity.

Furthermore, one has to be very careful in the selection of the dimensions of the computational domain. The distance of the inflow planes from the region in which the mixing process takes place must be sufficiently long in order for the flow field to not be distorted. The same applies for the outflow plane. However, the choice of these distances is not simple and preliminary simulations may be necessary in order for these to be defined.

[1] A secondary flow in curved pipes and channels that appears in the form of counter-rotating cells.

Further, the grid configuration for the simulation of flows in T-junctions is challenging. The interaction of the two streams results in the formation of several structures, such as shear layers and recirculation bubbles whose extent is not known a priori. Therefore, one has to perform preliminary simulations for the assessment of the extent of those. Further, the size of these structures may differ considerably. For example, those that are formed in the near-wall region can be significantly smaller than those formed at the bulk of the T-junction. The designed grid must be able to resolve all these structures. This, in turn, necessitates the use of a very fine grid into many regions of the flow under study. Moreover, the grid has to be configured appropriately so as to eliminate grid-induced oscillations in the numerical results. For example, a small stretching factor needs to be used in regions with non-uniform grid spacing. In addition, the grid cells must have low aspect ratios.

Furthermore, turbulence has to be modelled appropriately. Other than turbulence generated close to the walls of the T-junction, the interaction of the two streams enhances the levels of turbulence throughout the computational domain. On the other hand, in some regions, a temperature-induced increase of the viscosity of the fluid may result in the relaminarization of the flow. Therefore, if LES is conducted, one has to ensure that the unresolved scales are modelled in accordance with the phenomena that take place in each region of the flow.

1.4 Objectives and outline of the thesis

Despite the progress achieved thus far in the understanding of flows in T-junctions, several questions regarding their properties remain open. More specifically, the interaction of the crossflow with the incoming jet gives rise to several complex phenomena which are not yet sufficiently understood. The present work aims to fill this gap. Accordingly, we set the following objectives.

- Developing a computational framework (software) that will allow us to accurately predict the dynamic features of the flow of interest and the interplay between the important forces, such as buoyancy, and physical mechanisms, like shear-induced turbulence etc.

- Studying at a high level of detail the mixing process in isothermal and non-isothermal flows in T-junctions.

- Investigating in depth the role of the temperature as an active scalar, in both gas-gas and liquid-liquid flows.
- Performing, to the best of our knowledge, the first ever DNS of thermal mixing in T-junctions at the Reynolds number of $6,000$.
- Examining in detail the flow structures in the near-wall regions of the T-junction.
- Assessing the risk of thermal fatigue in the walls of T-junction.

To this end, we have employed a robust and computationally efficient algorithm for flows with large temperature gradients. In our simulations we take into account inertia effects that are induced by temperature gradients. In other words, we do not employ the Boussinesq approximation. Further, we perform wall-resolved simulations via parallel computing. In particular, close to the walls of the T-junction, we use a sufficiently fine grid in LES, and evidently in DNS, so as to resolve directly the flow structures in these regions. In addition, we examine the high-order statistics of the flow and implement visualisation techniques that allow us to study the flow structures in the flow of interest. Moreover, we conduct an analysis of the properties of the time-signals of the flow variables.

This thesis is structured as follows. In the second chapter we describe the governing equations. In addition, we elaborate on the numerical algorithm that we implement in a computational software for the numerical treatment of these equations. In this chapter we also provide a detailed description of the implementation of the boundary conditions and turbulence modelling. Further, we describe the parallelization techniques that we use in the software that we develop.

In the third chapter we present the results of LES of turbulent isothermal flows in T-junctions. In this part we perform simulations for flows with low and high momentum ratios so as to examine the impact of this parameter on the mixing processes. We also describe the main features of the flow and compare the obtained results of our simulations with existing experimental data. In addition, we perform an analysis of the first- and second-order statistics of the flow.

In the fourth chapter we show the results of LES of turbulent heat transfer in gas-gas flows in T-junctions. In this part we present the results of our numerical simulations of flows with low and high temperature ratios. In particular, we explain the main features of the flow and elaborate on the statistics of the temperature, velocity components and turbulent heat fluxes. This chapter also includes a comparisons with experiments. In addition, we perform a time-series analysis of the temperature signal at selected locations of the flow field in order to assess the risk of thermal fatigue.

Finally, in the fifth chapter we present the results of DNS and LES of turbulent heat transfer in liquid-liquid flows in T-junctions. This chapter includes a detailed analysis of the instantaneous structures that are formed in the flow under study. In addition, we present the budget of the turbulent kinetic energy which provide additional insight on the turbulent production mechanisms that take place in flows in T-junctions. Further, we assess the capabilities of LES on modelling turbulent heat transfer in T-junctions. This is done by performing a comparison between the predictions of LES with those of DNS.

In this thesis, we investigate turbulent flows at moderate Reynolds numbers, *i.e.* it varies from $6,000$ to $15,000$. The range of Reynolds numbers that is examined in this thesis is close to those of AC applications in automobiles. However, our investigations are not relevant to nuclear applications. This is because the Reynolds number in these flows is characteristically high. In particular, due to the very low viscosity of pressurised liquid water [31], it may reach the value of several millions. Such Reynolds numbers are many orders of magnitude larger than those studied in this thesis.

The results that are presented in the rest of the thesis are based on the following articles

- **M. Georgiou** and M.V. Papalexandris. Numerical study of turbulent flow in a rectangular T-junction. *Phys. Fluids*, **29**(6):065106, 2017 [32]

- **M. Georgiou** and M.V. Papalexandris. Turbulent mixing in T-junctions: the role of the temperature as an active scalar. *Int. J. Heat Mass Transfer*, **115**(B):793-809, 2017 [33]

- **M. Georgiou** and M.V. Papalexandris. Turbulent heat transfer in liquid-liquid flow in a T-junction. *Under review* [34]

Chapter 2

Governing equations and numerical algorithm

2.1 Introduction

In the flows of interest, density may vary significantly due to temperature gradients but the flow is incompressible because the Mach number is characteristically low [35]. Variable-density, low-Mach-number flows are very common in physical and industrial applications. For this reason they have attracted considerable interest over the past years.

For the numerical study of low-Mach-number flows in T-junctions, one can employ the compressible Navier-Stokes-Fourier (NSF) equations. However, the time-step would be excessively small because of the fast-propagating acoustic waves and the corresponding Courant-Friedrichs-Lewy (CFL) condition for numerical stability. This difficulty can be circumvented by employing the low-Mach-number approximation of the NSF equations. This is obtained by expanding the equations in pertubation series with respect to the Mach number. In the resulting system, the momentum and energy are essentially decoupled, in the sense that the work of surface forces (including the pressure) is negligible and does not enter the energy equation. In addition, since compressibility effects are not important, the restriction in the time-step imposed by the CFL condition does not apply anymore. Therefore, significantly larger time-steps can be used in the numerical simulation of flows of interest.

To integrate numerically the low-Mach-number equations, one can extend the methods that are used in the constant-density "incompressible" Navier-Stokes equations. Probably one of the most robust approaches is the projection method

[36]. In the "standard" incompressible Navier-Stokes equations this procedure is straightforward, because continuity implies that the velocity field is divergence free. However, in variable-density flows this procedure is more complicated because it involves the time-derivative of the density. In flows with large temperature and density gradients, such as those studied in this thesis, this time-derivative can be very stiff, thereby leading to numerical instabilities. For this reason many studies have been dedicated to the implementation of projection-based algorithms in low-Mach-number flows.

For example, Cook and Riley [37] examined turbulent reactive plumes and proposed the computation of this time-derivative via second-order explicit schemes. They also used a third-order Adams–Bashforth method for the momentum equation and showed that this algorithm is stable in such flows for temperature ratios up to 3. In a similar manner, de Charentenay et al. [38] investigated turbulent flames. These authors used third order schemes for this term and solved numerically flows with even larger temperature ratios. Pierce and Moin [39] implemented spatial filters on this time-derivative which increased considerably the stability of the algorithm in combustion applications.

However, Nicoud [40] mentioned that, in channel flows these algorithms become unstable for wall-temperature ratios larger than 4. In addition, he proposed an alternative algorithm for solving the low-Mach-number equations. This algorithm is based on a mixed Runge-Kutta/Crank-Nicolson time-integration scheme and a variable-coefficient Poisson equation for the pressure. Finally, a review and study on available different algorithms for the treatment of unsteady low-Mach-number flows can be found in [41].

In our numerical simulations, we use the algorithm proposed by Lessani and Papalexandris [42] which is based on a predictor-corrector time-integration scheme. This algorithm employs a projection method for the momentum equation that results in a constant-coefficient Poisson equation. This is a significant advantage over other algorithms that rely on variable-coefficient Poisson equation, such as the one proposed in [40], because it increases considerably the computational efficiency of the simulations. Further, it employs a collocated grid that offers computational simplicity and can be straightforwardly extended to curvilinear coordinate systems. To avoid the well known odd-even decoupling problem of collocated grids, the algorithm includes an extension of the flux interpolation technique of Rhie and Chow [43] to variable density flows. This algorithm is quite robust and has been shown to be stable enough for channel flows with wall-temperature ratios up to 9.

This chapter is structured as follows. In section 2.2 we describe the NSF equations. Then, in section 2.2 we present the low Mach number expansion of the aforementioned equations. Next, in section 2.3 we elaborate on the numerical algorithm that we have implemented for the numerical treatment of those. In sections 2.5-2.8 we provide information about turbulence modelling, implementation of boundary conditions, the decomposition of the computational domain and algorithm parallelization. Finally, section 2.9 summarises.

2.2 Governing equations

Since our study deals with single phase non-reacting flows, the governing system of equations underlying the flows we examine are the Navier-Stokes-Fourier equations. In this context, let $\hat{x}$, $\hat{y}$, $\hat{z}$ denote the spatial coordinates. Let, $\hat{\rho}$, $\hat{\boldsymbol{u}} = (\hat{u}, \hat{v}, \hat{w})$, $\hat{p}$, $\hat{T}$ denote the density, velocity vector, pressure and the temperature of the fluid, with the superscript $\hat{}$ denoting dimensional quantities. On the other hand, symbols without superscript are reserved for non-dimensional quantities. In dimensional form, the conservation laws for the mass, momentum and energy read, respectively,

$$\frac{\partial \hat{\rho}}{\partial \hat{t}} + \nabla \cdot (\hat{\rho}\hat{\mathbf{u}}) \; = \; 0\,, \tag{2.1}$$

$$\frac{\partial \hat{\rho}\hat{u}}{\partial \hat{t}} + \nabla \cdot (\hat{\rho}\hat{\boldsymbol{u}}\hat{\boldsymbol{u}}) \; = \; -\nabla \hat{p} + \nabla \cdot \hat{\boldsymbol{\tau}} + \hat{\rho}\hat{\boldsymbol{g}}\,, \tag{2.2}$$

$$\hat{\rho}\hat{c}_p \frac{\partial \hat{T}}{\partial \hat{t}} + \hat{\rho}\hat{c}_p \hat{\boldsymbol{u}} \cdot \nabla \hat{T} - \left(\frac{\partial \hat{p}}{\partial \hat{t}} + \hat{\boldsymbol{u}} \cdot \nabla \hat{p} \right) \; = \; (\hat{\boldsymbol{\tau}} : \nabla \hat{\boldsymbol{u}}) + \nabla \cdot \left(\hat{\kappa} \nabla \hat{T} \right) . \tag{2.3}$$

In the momentum equation (2.2), $\hat{\boldsymbol{g}} = (0, -\hat{g}, 0)$ stands for the vector of the gravitational acceleration. Further, $\hat{\boldsymbol{\tau}}$ denotes the deviatoric part of the viscous stress tensor,

$$\hat{\boldsymbol{\tau}} \; = \; \hat{\mu} \left(\nabla \hat{\boldsymbol{u}} + (\nabla \hat{\boldsymbol{u}})^T - \frac{2}{3} (\nabla \cdot \hat{\boldsymbol{u}}) \boldsymbol{I} \right), \tag{2.4}$$

with $\hat{\mu}$ and $\boldsymbol{I}$ being the dynamic viscosity and identity matrix respectively. In the energy equation (2.3), $\hat{c}_p$ is the specific heat of the fluid, $\hat{\kappa}$ is the fluid's thermal conductivity while " : " denotes the double inner product (in this case, since $\hat{\tau}$ is symmetric, the double inner product and the double dot product coincide). If, for example, the fluid is an ideal gas, the equation of state reads

$$\hat{p} \;=\; \hat{\mathcal{R}}\hat{\rho}\hat{T}\,, \tag{2.5}$$

with $\hat{\mathcal{R}}$ being the gas constant.

The governing equations are non-dimensionalized with respect to a set of reference variables, $\hat{L}_{\mathrm{ref}}$, $\hat{u}_{\mathrm{ref}}$, $\hat{\rho}_{\mathrm{ref}}$, $\hat{p}_{\mathrm{ref}}$, $\hat{T}_{\mathrm{ref}}$. Also, $\hat{c}_{p\mathrm{ref}} = \hat{c}_p(\hat{T}_{\mathrm{ref}})$, $\hat{\mu}_{\mathrm{ref}} = \hat{\mu}(\hat{T}_{\mathrm{ref}})$, $\hat{\kappa}_{\mathrm{ref}} = \hat{\kappa}(\hat{T}_{\mathrm{ref}})$. In non-dimensional form they read

$$\frac{\partial \rho}{\partial t} + \nabla\cdot(\rho\mathbf{u}) \;=\; 0\,, \tag{2.6}$$

$$\frac{\partial \rho\mathbf{u}}{\partial t} + \nabla\cdot(\rho\mathbf{u}\mathbf{u}) \;=\; -\frac{\hat{p}_{\mathrm{ref}}}{\hat{\rho}_{\mathrm{ref}}\,\hat{u}_{\mathrm{ref}}^2}\nabla p + \frac{1}{Re}\nabla\cdot\boldsymbol{\tau} + \rho\,\boldsymbol{Ri}\,, \tag{2.7}$$

$$\begin{aligned}\rho c_p\frac{\partial T}{\partial t} + \rho c_p\boldsymbol{u}\cdot\nabla T - \frac{\gamma-1}{\gamma}\left(\frac{\partial p}{\partial t} + \boldsymbol{u}\cdot\nabla p\right) \;&=\; \frac{\gamma-1}{Re}M^2\,(\hat{\boldsymbol{\tau}} : \nabla\hat{u})\\ + \frac{1}{Re\,Pr}\nabla\cdot(\kappa\nabla\,T)\,.\end{aligned} \tag{2.8}$$

In this equation, Re is the Reynolds number, $\boldsymbol{Ri} = (0, -Ri, 0)$ with Ri being the Richardson number, M is the Mach number and Pr is the Prandtl number. These are defined by

$$Re \;=\; \frac{\hat{\rho}_{\mathrm{ref}}\,\hat{u}_{\mathrm{ref}}\,\hat{L}_{\mathrm{ref}}}{\hat{\mu}_{\mathrm{ref}}}\,,\quad Ri \;=\; \frac{\hat{g}\hat{L}_{\mathrm{ref}}}{\hat{u}_{\mathrm{ref}}^2}\,,\quad M \;=\; \frac{\hat{u}_{\mathrm{ref}}}{\hat{c}_{\mathrm{ref}}}\,,\quad Pr \;=\; \frac{\hat{\mu}_{\mathrm{ref}}\,\hat{c}_{p\mathrm{ref}}}{\hat{\kappa}_{\mathrm{ref}}}\,.$$

In these expressions $\hat{c}_{\mathrm{ref}} = \sqrt{\gamma\,\hat{p}_{\mathrm{ref}}/\hat{\rho}_{\mathrm{ref}}}$ is the reference speed of sound and γ is the ratio of the specific heats of the fluid $\gamma = \hat{c}_p/\hat{c}_v$.

The equation of state in non-dimensional form reads

$$p \;=\; \rho T\,. \tag{2.9}$$

Low-Mach-number expansion

We proceed to derive the low-Mach-number expansion of the governing equations. To this end, the square of the Mach number scaled with γ is introduced as a pertubation parameter, $\varepsilon = \gamma M^2$. Since the procedure is standard, we describe only the basic steps of the derivation. For a more detailed description on the derivation of the low-Mach number approximation for the compressible NSF equations the reader is referred to [42, 44].

We first expand all the variables in a perturbation series of powers of ε. For instance,

$$p \;=\; p^0 + \varepsilon\, p^1 + O(\varepsilon^2)\,, \quad \boldsymbol{u} \;=\; \boldsymbol{u}^0 + \varepsilon\, \boldsymbol{u}^1 + O(\varepsilon^2)\,, \quad \text{etc.} \tag{2.10}$$

Next, we insert these expansions in equations (2.6)-(2.8) and collect terms of the same order. At order $O(1/\epsilon)$, the momentum equation (2.7) yields

$$\nabla p^0 \;=\; 0\,. \tag{2.11}$$

According to this relation, p^0 does not vary in space, *i.e.* it is a function of time only. p^0 is usually referred to as the thermodynamic pressure.

Collecting the terms of $O(1)$ in equations (2.6)-(2.8) yields

$$\frac{\partial \rho^0}{\partial t} + \nabla \cdot (\rho^0 \mathbf{u}^0) \;=\; 0\,, \tag{2.12}$$

$$\frac{\partial \rho^0 \mathbf{u}^0}{\partial t} + \nabla \cdot (\rho^0 \mathbf{u}^0 \mathbf{u}^0) \;=\; -\nabla p^1 + \frac{1}{Re} \nabla \cdot \boldsymbol{\tau}^0 + \rho^0 \boldsymbol{Ri}\,, \tag{2.13}$$

$$\rho^0 c_p \frac{\partial T^0}{\partial t} + \rho^0 c_p \mathbf{u}^0 \cdot \nabla T^0 \;=\; \frac{1}{Re\,Pr} \nabla \cdot (\kappa^0 \nabla T^0) + \frac{\gamma - 1}{\gamma} \frac{dp^0}{dt}\,. \tag{2.14}$$

The second-order term of the expansion of the pressure, p^1, is interpreted as the static pressure. The system of equations (2.12)-(2.14) is the sought-after low-Mach-number approximation of the NSF equations. In these relations the surface stresses, p^1, $\boldsymbol{\tau}^0$, do not enter the energy equation (2.14). Therefore, the momentum equation (2.13) and the energy equation (2.14) are essentially decoupled.

Finally, by inserting the expansions for ρ and T into the state equation (2.9) we obtain

$$p^0 \;=\; \rho^0 T^0\,. \tag{2.15}$$

In flows in T-junctions that are studied in the context of this thesis, the domain is assumed to be open with constant ambient pressure. Therefore, for the flows under study the last term in the right-hand side of (2.14) is identically zero.

2.3 Numerical method

In this section we describe the algorithm that we have implemented in the context of this thesis. This algorithm is implemented in the C++ programming language. It is based on a predictor-corrector method to march in time, from $t^{n+1} = t^n + \Delta t$ and the time-step, Δt, is computed from the condition

$$\Delta t \leq \min\left(\frac{\Delta x}{|u|}, \frac{\Delta y}{|v|}, \frac{\Delta z}{|w|}\right) C\,, \tag{2.16}$$

with C being the Courant number that is always smaller than unity. It should be noted that this is a necessary but not sufficient condition for stability: see, for example the discussion in [45]. Further, the superscripts $n-1$, n and $n+1$ denote the quantities at the corresponding time level. In addition, the superscript $*$ stands for values at the predictor stage.

Predictor-corrector projection scheme

Predictor

At the beginning of each time-step we first compute the prediction temperature T^* from relation (2.14) based on the values of the previous time-step t^n. As concerns the time-integration of the energy equation (2.14), the term $\rho c_p \mathbf{u} \cdot \nabla T$ is computed explicitly. The diffusive term in the spanwise z-direction $\frac{1}{Re\,Pr}\frac{\partial}{\partial z}(\kappa \frac{\partial}{\partial z} T)$ is computed explicitly as well. On the other hand, the diffusion terms in the streamwise x-direction and normal y-direction are computed implicitly via a Crank-Nicolson scheme. This is due to the existence of wall boundaries in these two directions. In particular, in order to resolve the flow field in the near-wall regions we need to use grid cells of very small size. Therefore, the explicit computation of the diffusion terms in these directions would require a very small time-step. This conundrum is avoided with the choice of the Crank-Nicolson scheme. However, this implicit time-integration gives rise to linear systems for the computation of the temperature. This, in turn, increases considerably the computational cost of the algorithm. Nevertheless, the gain from the larger time-steps is bigger than the additional cost of solving linear systems. For this reason we opted for the aforementioned time-integration strategy. The predicted temperature T^* is computed by solving the linear systems resulting from

$$c_p^n \rho^n \frac{T^* - T^n}{\Delta t} = \mathrm{Res}_T(\rho^n, \mathbf{u}^n, T^n)$$
$$+ \frac{1}{2\,Re\,Pr}\left(\frac{\partial}{\partial x}\left(\kappa^n\left(\frac{\partial T^*}{\partial x} + \frac{\partial T^n}{\partial x}\right)\right) + \frac{\partial}{\partial y}\left(\kappa^n\left(\frac{\partial T^*}{\partial y} + \frac{\partial T^n}{\partial y}\right)\right)\right). \quad (2.17)$$

In this equation Res_T groups the terms that are computed explicitly and it is given by

$$\mathrm{Res}_T = -\rho c_p \mathbf{u} \cdot \nabla T + \frac{1}{Re\,Pr}\frac{\partial}{\partial z}\left(\kappa \frac{\partial T}{\partial z}\right). \quad (2.18)$$

After the computation of T^*, the density ρ^* is evaluated from the equation of state (2.15)

$$\rho^* = \frac{p^0}{T^*}. \quad (2.19)$$

Next, we compute the prediction of the velocity vector field $\mathbf{u}$ and the static pressure p^1. In flows with large density gradients, such as the ones studied in the context of this thesis, the numerical treatment of the gravitational force can be very cumbersome and cause stability issues on the numerical integration of the governing system of equations. One way to increase the robustness of the numerical algorithm is to express the pressure field in the form of the modified pressure, $p_\mathrm{m} = p^1 + \rho\,Ri\,y$; see for example, Hong and Walker [46]. Therefore, we substitute

$$\rho Ri = \frac{\partial(\rho Ri\,y)}{\partial y} - y\,\frac{\partial(\rho Ri)}{\partial y} \quad (2.20)$$

in equation (2.13) so as to obtain

$$\frac{\partial(\rho \boldsymbol{u})}{\partial t} + \nabla \cdot (\rho \boldsymbol{u}\boldsymbol{u}) + \nabla p_\mathrm{m} = \frac{1}{Re}\nabla \cdot \boldsymbol{\tau} + Ri\,y \nabla \rho\,. \quad (2.21)$$

In order to compute the velocity vector field $\mathbf{u}$ and the modified pressure p_m, we first calculate $\tilde{\boldsymbol{u}}$ (also referred to as *auxiliary* velocity) which is given by

$$\frac{\rho \tilde{\mathbf{u}}}{\Delta t} \equiv \frac{\rho \mathbf{u}}{\Delta t} - \nabla \cdot (\rho \boldsymbol{u}\boldsymbol{u}) + \frac{1}{Re}\nabla \cdot \boldsymbol{\tau}. \quad (2.22)$$

For the time-integration of equation (2.22) we use the Crank-Nicolson scheme for the viscous terms in the wall-normal directions and the Adams-Moulton method for the convective and the viscous term in the spanwise direction. The terms which are integrated explicitly are grouped into the residuals for the velocities

$\mathrm{Res}_{\mathbf{u}} = (\mathrm{Res}_u\,, \mathrm{Res}_v\,, \mathrm{Res}_w)^T$ that are given by

$$
\begin{aligned}
\mathrm{Res}_u \;=\; & -\nabla\cdot(\rho\boldsymbol{u}u) + \frac{1}{Re}\left[-\frac{2}{3}\frac{\partial}{\partial x}\left(\mu\left(\frac{\partial v}{\partial y}+\frac{\partial w}{\partial z}\right)\right)\right.\\
& \left. + \frac{\partial}{\partial y}\left(\mu\frac{\partial v}{\partial x}\right) + \frac{\partial}{\partial z}\left(\mu\left(\frac{\partial u}{\partial z}+\frac{\partial w}{\partial x}\right)\right)\right], \qquad (2.23a)
\end{aligned}
$$

$$
\begin{aligned}
\mathrm{Res}_v \;=\; & -\nabla\cdot(\rho\boldsymbol{u}v) + \frac{1}{Re}\left[\frac{\partial}{\partial x}\left(\mu\frac{\partial u}{\partial y}\right)\right.\\
& \left. -\frac{2}{3}\frac{\partial}{\partial y}\left(\mu\left(\frac{\partial u}{\partial x}+\frac{\partial w}{\partial z}\right)\right) + \frac{\partial}{\partial z}\left(\mu\left(\frac{\partial v}{\partial z}+\frac{\partial w}{\partial y}\right)\right)\right], \qquad (2.23b)
\end{aligned}
$$

$$
\begin{aligned}
\mathrm{Res}_w \;=\; & -\nabla\cdot(\rho\boldsymbol{u}w) + \frac{1}{Re}\left[\frac{\partial}{\partial x}\left(\mu\frac{\partial u}{\partial z}\right) + \frac{\partial}{\partial y}\left(\mu\frac{\partial v}{\partial z}\right)\right.\\
& \left. + \frac{\partial}{\partial z}\left(\frac{4}{3}\mu\frac{\partial w}{\partial z} - \frac{2}{3}\mu\left(\frac{\partial u}{\partial x}+\frac{\partial v}{\partial y}\right)\right)\right]. \qquad (2.23c)
\end{aligned}
$$

Further, to facilitate the presentation of the discretized momentum equation (2.22) we group together the coefficients of the stress-tensor terms that are treated implicitly. For this purpose we introduce two auxiliary diagonal tensors $\mathcal{C}$ and $\mathcal{D}$ defined by $\mathcal{C} = \mathrm{diag}(\frac{4}{3}, 1, 1)$ and $\mathcal{D} = \mathrm{diag}(1, \frac{4}{3}, 1)$. Then, the discretized form of (2.22) reads

$$
\begin{aligned}
\frac{\rho^*\tilde{\boldsymbol{u}} - \rho^n\boldsymbol{u}^n}{\Delta t} \;=\; & \frac{3}{2}\mathrm{Res}_{\boldsymbol{u}}(\rho^n, \boldsymbol{u}^n) - \frac{1}{2}\mathrm{Res}_{\boldsymbol{u}}(\rho^{n-1}, \boldsymbol{u}^{n-1})\\
+\,\mathcal{C}\,\frac{1}{2\,Re}\frac{\partial}{\partial x}\left(\mu^n\left(\frac{\partial\tilde{\boldsymbol{u}}}{\partial x}+\frac{\partial\boldsymbol{u}^n}{\partial x}\right)\right) & + \mathcal{D}\,\frac{1}{2\,Re}\frac{\partial}{\partial y}\left(\mu^n\left(\frac{\partial\tilde{\boldsymbol{u}}}{\partial y}+\frac{\partial\boldsymbol{u}^n}{\partial y}\right)\right). \qquad (2.24)
\end{aligned}
$$

Having calculated $\tilde{\boldsymbol{u}}$, we proceed with the discretization of equation (2.21). This is done in an analogous manner with the discretization of (2.22) using the predicted values identified by “$*$”. The resulting equation reads

$$
\frac{\rho^*\boldsymbol{u}^*}{\Delta t} \;=\; \frac{\rho^*\tilde{\boldsymbol{u}}}{\Delta t} - \nabla p^*_{\mathrm{m}} + Ri\,\nabla\rho^* y. \qquad (2.25)
$$

Next, we perform the projection step. In particular, we take the divergence of equation (2.25) and we substitute the term $\nabla\cdot(\rho^*\boldsymbol{u}^*)$ by the time derivative of the density, $\frac{\partial\rho}{\partial t}$, based on the continuity equation (2.6). In turn, this time-derivative is approximated by a second-order backward difference scheme. According to [42] this choice increases considerably the stability of the proposed algorithm. In this manner we arrive at an elliptic equation in which p_{m} is the only unknown:

$$\nabla^2 p_{\mathrm{m}}^* = \frac{1}{\Delta t}\nabla \cdot (\rho^* \tilde{\boldsymbol{u}}) + \frac{3\rho^* - 4\rho^n + \rho^{n-1}}{2\Delta t^2} + Ri\, \nabla \cdot (y \nabla \rho^*). \tag{2.26}$$

Once the above linear system of equations is solved we go back to equation (2.25) and compute the predicted values of $\boldsymbol{u}^*$.

Corrector

In the corrector stage the state variables are updated to time $t^{n+1} = t^n + \Delta t$, following the same sequence of steps as in the predictor stage.

For the computation of T^{n+1} we solve the energy equation which reads

$$\begin{aligned} c_p^n\, \rho^* \frac{T^{n+1} - T^n}{\Delta t} &= \mathrm{Res}_T(\rho^*, \mathbf{u}^*, T_{\mathrm{av}}) \\ &+ \frac{1}{2\, Re\, Pr}\left(\frac{\partial}{\partial x}\left(\kappa^n\left(\frac{\partial T^*}{\partial x} + \frac{\partial T^n}{\partial x}\right)\right) + \frac{\partial}{\partial y}\left(\kappa^n\left(\frac{\partial T^*}{\partial y} + \frac{\partial T^n}{\partial y}\right)\right)\right), \end{aligned} \tag{2.27}$$

with $T_{\mathrm{av}} = 0.5(T^n + T^*)$.

Next, we compute ρ^{n+1} by using the state equation (2.19)

$$\rho^{n+1} = \frac{p^0}{T^{n+1}}. \tag{2.28}$$

To compute the auxiliary velocity of the corrector step, $\breve{\boldsymbol{u}}$, we solve the following equation with $\mathrm{Res}_{\boldsymbol{u}} = (\mathrm{Res}_u\, , \mathrm{Res}_v\, , \mathrm{Res}_w)^T$ given by equation (2.23):

$$\begin{aligned} \frac{\rho^* \breve{\boldsymbol{u}} - \rho^n \boldsymbol{u}^n}{\Delta t} &= \frac{1}{2}\left(\mathrm{Res}_{\boldsymbol{u}}(\rho^*, \boldsymbol{u}^*) + \mathrm{Res}_{\boldsymbol{u}}(\rho^n, \boldsymbol{u}^n)\right) \\ &+ \mathcal{C}\, \frac{1}{2\, Re}\frac{\partial}{\partial x}\left(\mu^n\left(\frac{\partial \breve{\boldsymbol{u}}}{\partial x} + \frac{\partial \boldsymbol{u}^n}{\partial x}\right)\right) + \mathcal{D}\, \frac{1}{2\, Re}\frac{\partial}{\partial y}\left(\mu^n\left(\frac{\partial \breve{\boldsymbol{u}}}{\partial y} + \frac{\partial \boldsymbol{u}^n}{\partial y}\right)\right). \end{aligned} \tag{2.29}$$

In order to compute the velocities $\boldsymbol{u}^{n+1}$ we take the divergence of

$$\frac{\rho^{n+1}\boldsymbol{u}^{n+1}}{\Delta t} = \frac{\rho^{n+1}\breve{\boldsymbol{u}}}{\Delta t} - \nabla p_{\mathrm{m}}^{n+1} + Ri\, \nabla \rho^{n+1} y\, . \tag{2.30}$$

This results in a Poisson equation for the modified pressure p_{m}^{n+1} given by

$$\nabla^2 p_{\mathrm{m}}^{n+1} = \frac{1}{\Delta t}\nabla \cdot (\rho^{n+1} \breve{\boldsymbol{u}}) + \frac{3\rho^{n+1} - 4\rho^n + \rho^{n-1}}{2\Delta t^2} + Ri\, \nabla \cdot (y \nabla \rho^{n+1}). \tag{2.31}$$

Once p_{m}^{n+1} is computed, it is substituted in equation (2.30) to obtain $\boldsymbol{u}^{n+1}$.

It should be noted that in their article, Lessani and Papalexandris [42] proposed an additional reintegration of the energy from t^n to t^{n+1} with the same two-stage method but with using the final values of both density and velocity. According to these authors, this additional reintegration increases the robustness and stability of the algorithm. In our numerical studies, we have also implemented this step without observing any considerable differences in the numerical results. Therefore, for the purposes of computational efficiency, this step is omitted in the algorithm. Further, it should be mentioned that in order to validate the code, we reproduced the results of turbulent heat transfer in channels presented in [42, 47].

As already mentioned, this algorithm is adopted from [42]. However, in our studies we use a different time-integration strategy. In particular, we integrate implicitly the viscous and diffusion terms of equations (2.13) and (2.14) in the streamwise x- and vertical y-directions. Finally, in figure 2.1 we present a simplified flow chart that summarises the steps for both predictor and corrector stages of the computational algorithm that we use in our studies.

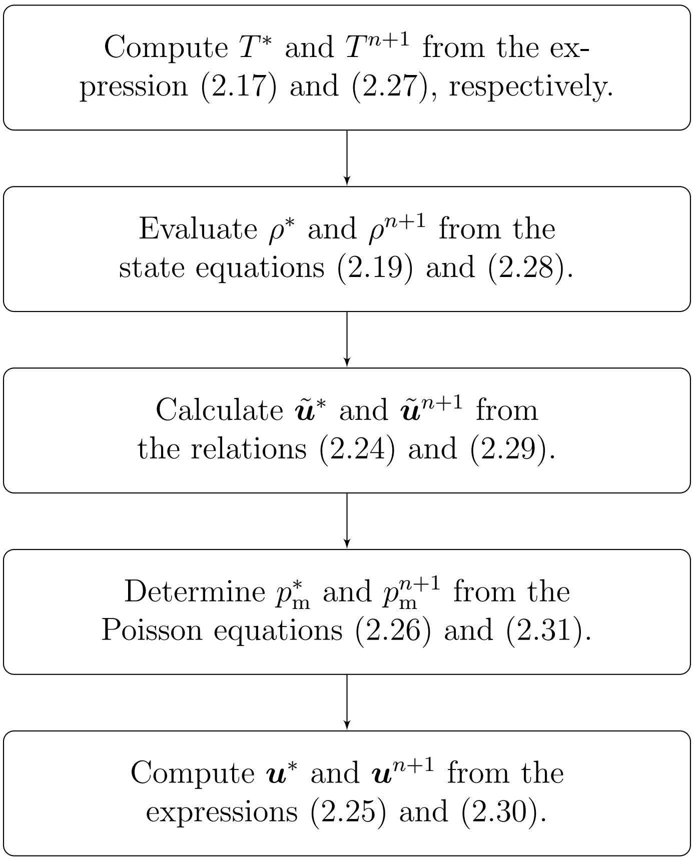

Figure 2.1: Simplified flow chart of the steps of the numerical algorithm.

2.4 Spatial discretization

For the spatial discretization of the governing equations we employ a collocated grid, *i.e.* all the variables are evaluated in the cell centre. In the description that follows, the grid cells are uniquely identified by the indices $\{i, j, k\}$, corresponding to the order of appearance of the cell along the x, y and z-axis respectively. The dimensions of each cell are $\Delta x_i, \Delta y_j$ and Δz_k. Further, subscripts with integer coefficients (for example, i, $i+1$ etc) stand for quantities at the centres of the computational cells. Also, half-integer coefficients (*e.g.*, $i-1/2$, $i+1/2$), stand for quantities that are evaluated at the cell-interfaces along the direction that the index represents. In addition, for the manipulation of the discrete operators we assume a *rectilinear* grid, *i.e.* a grid in which the size of the cells in each of the three directions varies only along the respective direction, $\Delta x_i = \Delta x_i(i)$, $\Delta y_j = \Delta y_j(j)$ and $\Delta z_k = \Delta z_k(k)$.

In order to facilitate the description of the discretization schemes that are used in our thesis we introduce two elementary operations. The weighted interpolation operation of a quantity $\phi_{i,j,k}$ in the streamwise, normal, and spanwise directions is given by,

$$\overline{\phi}^{x}_{i,j,k} = \frac{\Delta x_{i-\frac{1}{2}}\, \phi_{i+\frac{1}{2},j,k} + \Delta x_{i+\frac{1}{2}}\, \phi_{i-\frac{1}{2},j,k}}{\Delta x_{i+\frac{1}{2}} + \Delta x_{i-\frac{1}{2}}}\,, \tag{2.32a}$$

$$\overline{\phi}^{y}_{i,j,k} = \frac{\Delta y_{j-\frac{1}{2}}\, \phi_{i,j+\frac{1}{2},k} + \Delta y_{j+\frac{1}{2}}\, \phi_{i,j-\frac{1}{2},k}}{\Delta y_{j+\frac{1}{2}} + \Delta y_{j-\frac{1}{2}}}\,, \tag{2.32b}$$

$$\overline{\phi}^{z}_{i,j,k} = \frac{\Delta z_{k-\frac{1}{2}}\, \phi_{i,j,k+\frac{1}{2}} + \Delta z_{k+\frac{1}{2}}\, \phi_{i,j,k-\frac{1}{2}}}{\Delta z_{k+\frac{1}{2}} + \Delta z_{k-\frac{1}{2}}}\,, \tag{2.32c}$$

respectively.

In addition, we introduce a finite-difference operation which is annotated by $\frac{\delta}{\delta x}$, $\frac{\delta}{\delta y}$ and $\frac{\delta}{\delta z}$ along the three directions. It is defined by

$$\frac{\delta \phi_{i,j,k}}{\delta x} = \frac{\phi_{i+\frac{1}{2},j,k} - \phi_{i-\frac{1}{2},j,k}}{x_{i+\frac{1}{2}} - x_{i-\frac{1}{2}}}\,, \tag{2.33a}$$

$$\frac{\delta \phi_{i,j,k}}{\delta y} = \frac{\phi_{i,j+\frac{1}{2},k} - \phi_{i,j-\frac{1}{2},k}}{y_{j+\frac{1}{2}} - y_{j-\frac{1}{2}}}\,, \tag{2.33b}$$

$$\frac{\delta\phi_{i,j,k}}{\delta z} = \frac{\phi_{i,j,k+\frac{1}{2}} - \phi_{i,j,k-\frac{1}{2}}}{z_{k+\frac{1}{2}} - z_{k-\frac{1}{2}}}. \tag{2.33c}$$

It is well known that collocated grids are susceptible to the odd-even decoupling problem that produces spurious oscillations in the pressure field. In order to avoid this problem we employ a generalised version of the flux interpolation method proposed in [42]. According to this method, the velocities are interpolated on the interfaces of the cells to yield the values that are used in the calculations of the convective terms, instead of the cell centred values. To this end, let us introduce the auxiliary fluxes f_u, f_v and f_w, given by

$$f_u|_{i+\frac{1}{2},j,k} = \overline{(\rho\tilde{u})_{i+\frac{1}{2},j,k}}^{x} - \frac{\delta p_{\mathrm{mo}\,i+\frac{1}{2},j,k}}{\delta x}\Delta t + Ri\,\frac{\delta\rho_{i+\frac{1}{2},j,k}}{\delta x}y\,\Delta t\,, \tag{2.34a}$$

$$f_v|_{i,j+\frac{1}{2},k} = \overline{(\rho\tilde{v})_{i,j+\frac{1}{2},k}}^{y} - \frac{\delta p_{\mathrm{mo}\,i,j+\frac{1}{2},k}}{\delta y}\Delta t + Ri\,\frac{\delta\rho_{i,j+\frac{1}{2},k}}{\delta y}\overline{y_{j+\frac{1}{2}}}^{y}\,\Delta t\,, \tag{2.34b}$$

$$f_w|_{i,j,k+\frac{1}{2}} = \overline{(\rho\tilde{w})_{i,j,k+\frac{1}{2}}}^{z} - \frac{\delta p_{\mathrm{m}\,i,j,k+\frac{1}{2}}}{\delta z}\Delta t + Ri\,\frac{\delta\rho_{i,j,k+\frac{1}{2}}}{\delta z}y\,\Delta t\,. \tag{2.34c}$$

These expressions are valid for the predictor stage. For the corrector stage we follow the same procedure but we replace $(\tilde{u}, \tilde{v}, \tilde{w})$ by $(\breve{u}, \breve{v}, \breve{w})$, according to equation (2.30). It should be noted that for the initialisation of the algorithm at $t = 0$, the auxiliary fluxes used in the calculation of $\mathrm{Res}_{\boldsymbol{u}}$ and Res_T are given only as a function of the velocity and density at the initial condition.

Having defined the interpolation and differential operations we present in more detail the spatial discretization of terms of particular interest. We first describe the discretization of the advection term $\rho c_p \boldsymbol{u}\cdot\nabla T$, of equation (2.18). This term is of particular importance because it is the only non-linear term in the energy equation. The corresponding term in the momentum equation, *i.e.* the convective term, is meditated by the pressure gradient and the continuity equation which have a “smoothening” effect [48]. However, no such mechanism is available in the energy equation. For this reason, this term can yield sharp temperature gradients that might result to overshoots of the temperature. To avoid such situations, particular attention has to be paid on its discretization. In this thesis it is computed by employing the following scheme,

$$\boldsymbol{u}\cdot\nabla T \approx \overline{\overline{u}^{x}_{i,j,k}\frac{\delta T_{i,j,k}}{\delta x}}^{x} + \overline{\overline{v_{i,j,k}}^{y}\frac{\delta T_{i,j,k}}{\delta y}}^{y} + \overline{\overline{w_{i,j,k}}^{z}\frac{\delta T_{i,j,k}}{\delta z}}^{z}\,. \tag{2.35}$$

In the context of our research, we tested different discretization schemes as well. For example, we examined a scheme that employs the auxiliary fluxes defined in equations (2.34a)-(2.34c). Nevertheless the discretization given in equation (2.35) is proven to be more stable for the flows that this thesis investigates. We have also examined the appropriateness of upwind-biased schemes, such as the first-order scheme for the advection equation and the extension of the third-order QUICK scheme for non-uniform grids [49]. However, these schemes were proven to be excessively diffusive and for this reason they are not used in our numerical simulations. Several authors have proposed alternative schemes for the computation of this term, such as the Total Variation Diminishing (TVD) schemes with limiters [50], which, although, they have not been tested in our studies. The discretization of the diffusive term in equation (2.18) reads

$$\begin{aligned}\nabla \cdot (\kappa \nabla T) \approx \frac{\delta}{\delta x}\left(\overline{\kappa_{i,j,k}}^{x}\frac{\delta T_{i,j,k}}{\delta x}\right) + \frac{\delta}{\delta y}\left(\overline{\kappa_{i,j,k}}^{y}\frac{\delta T_{i,j,k}}{\delta y}\right) \\ + \frac{\delta}{\delta z}\left(\overline{\kappa_{i,j,k}}^{z}\frac{\delta T_{i,j,k}}{\delta z}\right) .\end{aligned} \tag{2.36}$$

With regard to the convective terms in the residuals of the momentum equation, given by relation (2.23), we introduce the auxiliary fluxes f_u, f_v and f_w. In their discretized form they read

$$\nabla \cdot (\rho \boldsymbol{u}\boldsymbol{u}) = \left.\frac{\delta f_u\, \overline{\boldsymbol{u}}^{x}}{\delta x}\right|_{i+\frac{1}{2},j,k} + \left.\frac{\delta f_v\, \overline{\boldsymbol{u}}^{y}}{\delta y}\right|_{i,j+\frac{1}{2},k} + \left.\frac{\delta f_w\, \overline{\boldsymbol{u}}^{z}}{\delta z}\right|_{i,j,k+\frac{1}{2}} . \tag{2.37}$$

The viscous terms that are treated explicitly are computed in a manner similar to the heat diffusion terms for the expression (2.36). Special attention should be paid to the terms containing cross-derivatives. An example is the diffusion term, $\frac{\partial}{\partial x}\left(\mu\frac{\partial u}{\partial y}\right)$, which is discretized according to

$$\frac{\partial}{\partial x}\left(\mu\frac{\partial u}{\partial y}\right) = \frac{\delta}{\delta x}\left(\overline{\mu_{i,j,k}}^{x}\frac{\delta \overline{u_{i,j,k}}^{xy}}{\delta y}\right) . \tag{2.38}$$

Similarly for all terms containing cross-derivatives, the interpolation operation should be applied in the corresponding two dimensions.

2.5 Turbulence modelling

As concerns numerical studies of turbulent flows, there are three approaches, Reynolds-Averaged-Navier-Stokes (RANS), Direct Numerical Simulations (DNS) and Large Eddy simulations (LES).

The fist approach, RANS, amounts on solving the equations for the mean velocity field, thus it does not provide information about the dynamic features of the flow. For this reason it is not used in this thesis. In DNS, the computational mesh is sufficiently fine that it resolves all turbulent scales of the flow which, in turn, increases prohibitively its computational cost. On the other hand, in LES only the large turbulent structures of the flow are resolved while the smaller structures are modelled. The rationale behind this approach is that the large structures are highly dependent on the flow conditions, hence it is difficult to model their behaviour. On the contrary, the smaller structures behave in a more universal manner thus rendering their modelling easier. The advantage of LES is that it is computationally cheaper than DNS while it still provides information about the unsteady motion of the large structures of the flow. For this reason, it is has often been applied in numerical simulations of turbulent flows in T-junctions.

In figure 2.2 we present a comparison of the predictions of RANS and LES in flows in T-junctions that is performed by Sakowitz et al. [22]. In particular, we show a streamline emerging from the top entry of the vertical channel as extracted from the mean velocity field. According to this figure, LES predicts that this streamline turns steeply and becomes parallel to the walls of the horizontal channel. However, further downstream, it turns towards the top wall. In contrast, the streamline extracted from the predictions of RANS stays parallel to the walls of the horizontal channel and does not turn towards the top wall. Further, according to the same authors, RANS provides erroneous predictions regarding the vortical structures that are developed in flows in T-junctions. Thus, they concluded that scale-resolving methods, such as DNS and LES, are more appropriate for simulating flows in T-junctions. For these reasons, in our studies we perform LES and DNS.

According to the LES approach, first the governing equations (2.12)-(2.14) are spatially filtered. The filtering operation reads

$$\overline{\phi(\boldsymbol{x})} = \int F(\boldsymbol{x} - \boldsymbol{x}')\, \phi(\boldsymbol{x}')\, d\boldsymbol{x}' \,, \tag{2.39}$$

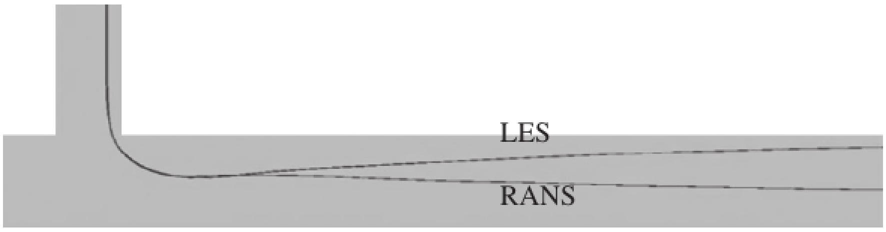

Figure 2.2: Comparison of the predictions of LES and RANS in flows in T-junctions. In this figure we show the trajectory of a streamline that emerges from the vertical channel which is extracted from the averaged velocity field. This image is reprinted from [22], with permission from Elsevier.

with F being the filtering operator. Herein, F, is a box filter that is represented by the computational grid. This approach is also referred to as *implicit filtering*. Upon filtering, ϕ is decomposed into $\phi = \overline{\phi} + \phi''$. Even though this operation is similar to the Reynolds decomposition, which decomposes a quantity ϕ to its steady component, $<\phi>$, and its fluctuation, ϕ', there are important differences between the two operations. More specifically, the filtered quantity $\overline{\phi}$ is also a random field while the mean of the unfiltered quantity, ϕ'', is not necessarily zero, $<\phi''> \neq 0$. In addition, to eliminate density fluctuation correlations, we use a density-weighted filtering operation $\tilde{\phi} = \frac{\overline{\rho\phi}}{\overline{\rho}}$ that was introduced by Favre [51]. The filtered version of the governing equations reads

$$\frac{\partial\overline{\rho}}{\partial t} + \nabla\cdot(\overline{\rho}\tilde{\mathbf{u}}) = 0\,, \tag{2.40}$$

$$\frac{\partial\overline{\rho}\tilde{\mathbf{u}}}{\partial t} + \nabla\cdot(\overline{\rho}\tilde{\mathbf{u}}\tilde{\mathbf{u}}) = -\nabla\,\overline{p} + \frac{1}{Re}\nabla\cdot\bar{\boldsymbol{\tau}} - \overline{\rho}\mathrm{Ri}\,\widehat{\boldsymbol{y}}, -\nabla\cdot\left(\overline{\rho}\widetilde{\boldsymbol{u''}\boldsymbol{u''}}\right), \tag{2.41}$$

$$\overline{\rho}c_p\frac{\partial\tilde{T}}{\partial t} + \overline{\rho}c_p\tilde{\mathbf{u}}\cdot\nabla\tilde{T} = \frac{1}{Re\,Pr}\nabla\cdot(\kappa\nabla\tilde{T}) - \overline{\rho}\widetilde{\boldsymbol{u''}\cdot\nabla T''}\,. \tag{2.42}$$

In order to close the above system of equations, we need to introduce appropriate models for the non-linear residual terms, $\nabla\cdot\left(\overline{\rho}\widetilde{\boldsymbol{u''}\boldsymbol{u''}}\right)$ and $\overline{\rho}\widetilde{\boldsymbol{u''}\cdot\nabla T''}$. The momentum equation (2.41) is closed by employing the eddy-viscosity hypothesis, first introduced by Boussinesq [52]. According to the "energy cascade" scenario, the larger scales of the flow provide with energy the smaller scales. Based on this, the aforementioned hypothesis takes into account the effect of the unresolved scales via an additional (eddy) viscosity whose action is to subtract energy from the resolved scales of the flow. This hypothesis reads

$$-\bar{\rho}\widetilde{\boldsymbol{u}''\boldsymbol{u}''} - \frac{1}{3}k_{\mathrm{r}} \;=\; \mu_t \left(\nabla\tilde{\boldsymbol{u}} + (\nabla\tilde{\boldsymbol{u}})^T - \frac{2}{3}(\nabla\cdot\tilde{\boldsymbol{u}})\boldsymbol{I} \right) , \tag{2.43}$$

with k_{r} being the residual kinetic energy $k_{\mathrm{r}} = (\widetilde{\boldsymbol{u}\boldsymbol{u}})\,\boldsymbol{I}$ that is included in the modified filtered pressure. Smagorinsky [53] first introduced this approximation and he proposed the following expression for the computation of the eddy viscosity

$$\mu_t = C_{\mathrm{S}}\,\overline{\rho}\,\Delta^2\overline{\mathcal{T}} . \tag{2.44}$$

In the equation above, C_{S} stands for Smagorinsky constant, Δ for the filter's width which is estimated as $\Delta = (\Delta x\,\Delta y\,\Delta z)^{1/3}$ and $\overline{\mathcal{T}}$ is the characteristic filtered rate of strain that is defined by

$$\overline{\mathcal{T}} = \frac{1}{2}\left(\left(\nabla\tilde{\boldsymbol{u}} + (\nabla\tilde{\boldsymbol{u}})^T \right) : \left(\nabla\tilde{\boldsymbol{u}} + (\nabla\tilde{\boldsymbol{u}})^T \right) \right)^{\frac{1}{2}} . \tag{2.45}$$

Expression (2.44) is the basis for many models that estimate the subgrid-scales of the flow, also referred to as *subgrid models* [54]. There are two approaches regarding the computation of the contribution of the subgrid-scales. In the first, the contribution is computed explicitly by using a subgrid model. Alternatively, Boris et al. [55] suggested that one could rely on the dissipation introduced by the the numerical schemes used for the discretization of the governing equations. This approach, also known as *implicit modelling*, has minimal computational cost. However, it depends strongly on the fineness of the computational grid and provides no control over the contribution of the subgrid stresses.

Herein, we explicitly compute the contribution of the subgrid scales and, more specifically, we employ the dynamic model presented by Moin et al. [56] for the computation of μ_t. This model is an extension to variable-density flows of the popular dynamic procedure proposed by Germano et al. [57], combined with the least-squares technique proposed by Lilly [58]. We opted for this model because, beside being straightforward to implement, its contribution is eliminated in the near-wall regions as well as in regions where flow relaminarizes.

The dynamic procedure outlined above, occasionally gives rise to negative values of the eddy-viscosity μ_t. This theoretically means that energy is transferred from the subgrid to the resolved scales of the flow. However, negative values of μ_t can render the simulations unstable. For this reason, several approaches have been proposed to eliminate them. In our study, we average in the homogeneous direction and the remaining negative values are clipped to zero which is a common practice in LES simulations of turbulent flows in T-junctions [25]. Further, it should be mentioned that in the context of our research we have tested alternative approaches for the elimination of these negative values, such as local averaging or localised subgrid models such as the one proposed by Piomelli and Liu [59]. However, the differences in the results obtained with these alternative approaches turned out to be minimal.

In order to model the non-linear term $\overline{\rho}\widetilde{\boldsymbol{u''} \cdot \nabla T''}$ in the energy equation (2.42) we employ the gradient assumption first introduced by Eidson [60]. This is similar to the eddy viscosity hypothesis and reads

$$-\,\overline{\rho}\widetilde{\boldsymbol{u''} \cdot \nabla T''} \;=\; \kappa_t \nabla \tilde{T}\,. \tag{2.46}$$

The eddy conductivity κ_t is related to the eddy viscosity μ_t by the following expression

$$\kappa_t = \frac{\mu_t c_p}{Pr_t}\,, \tag{2.47}$$

with Pr_t being the turbulent Prandtl number. This is the only unknown in the equation above.

Herein, Pr_t is assumed constant and equal to 0.9. It should be mentioned that we have also implemented the dynamic procedure proposed by Moin et al. [56] without observing any differences in the numerical results. This remark is in accord with the findings of Zainali and Lessani [61]. These authors showed that κ_t is essentially non-affected by the choice of a constant or dynamically computed Pr_t. In fact, to the best of our knowledge, all previous LES for T-junctions were based on a constant turbulent Prandtl number whose value is either equal or close to unity. For example, in the simulations presented in [19, 20, 62] the turbulent Prandtl number was set equal to 0.85, whereas in [23, 24] it was set equal to unity.

Treatment of the wall regions

A critical issue in wall-bounded flows is the treatment of the wall region because the flow in this region provides the principal mechanism for turbulent generation. Therefore, this region should be sufficiently resolved. However, this requires very fine grids which, in turn, increase substantially the computational cost of the simulations. An alternative approach is to employ a wall model; see, for example the discussion in [54]. Wall models reduce considerably the computational cost of simulations of wall-bounded flows without affecting the statistical properties of turbulence, at least for certain types of flows. However, as Jayaraju et al. [62] remarked, wall models perform poorly in flows in T-junctions. This is attributed to the complexity of the flow under study in comparison with simple channel flows. In particular, the interaction of the two streams results in several separation and reattachment zones that render the application of existing wall models quite challenging and cumbersome. For this reason, we have opted for wall-resolved numerical simulations. Thus, the no-slip condition is applied to all three velocity components. As for the size of the grid in the near-wall regions, more details are provided later on.

2.6 Boundary conditions

Inflow and outflow conditions

In the simulations of flows in T-junctions we have to impose turbulent velocity inflow conditions. As shown by Ndombo and Howard [30], the accuracy of the numerical results is strongly dependent on the quality of this condition. For this reason special attention is paid on its implementation.

In order to assign turbulent inflow condition, we can either employ data obtained by auxiliary simulations or generate velocity profiles of synthetic turbulence. The first approach consists of auxiliary simulations to produce reliable turbulent inflow data and comes in two variants. According to the first variant, the computation of the auxiliary simulation is performed simultaneously with the main simulation. In the second one, the auxiliary simulation is carried out in advance and the inflow data are stored to a numerical database.

In the second approach, the turbulent inflow data can be generated by a stochastic reconstruction of the velocity field by adding fluctuations with specific spectral properties to the mean velocity profile. There are several methods for the generation of synthetic turbulence, see for example [63–65] as well as the relevant discussion in the monograph of Sagaut [54].

Herein, we opted for the use of auxiliary simulations that are performed simultaneously with the simulation of the flow in the T-junction. Even though this choice is computationally more expensive, it is also the most accurate. Further, despite the small computational cost of the second approach, *i.e* stochastic reconstruction, this choice requires the prolongation of the computational domain so as to provide enough space for the turbulent structures to develop. Therefore, it increases considerably the computational cost of this option.

To avoid spatial interpolation errors, the grid resolution for each auxiliary simulation is the same as in the corresponding inlet of the computational domain of the T-junction. Additionally, for the elimination of time-interpolation errors, the time-step used in the auxiliary simulations is the same with the one in the principal simulation. When the inflow data are stored to a numerical database time-interpolation errors cannot be avoided and for this reason we did not follow this approach.

As concerns the outflow boundary condition, we have implemented the convective boundary condition that is widely used in simulations of turbulent flows. This condition allows the vortical structures to exit the computational domain with minimal distortion and when applied to a scalar field ϕ to an outflow plane normal to the x-direction, it reads

$$\frac{\partial \phi}{\partial t} + U_{\mathrm{conv}} \frac{\partial \phi}{\partial x} \; = \; 0\,. \tag{2.48}$$

In this equation U_{conv} is the convective velocity and it is set equal to the maximum value of the streamwise velocity at the outflow plane and at the previous time-step. Further, the computation of the advective term in equation (2.48) is performed via the standard second-order accurate upwind scheme for the advection equation. Finally, it should be stressed that, when necessary, we add a corrective constant to the velocity field normal to the outflow plane [66]. This constant is introduced in order to ensure that mass is conserved and that the outflow condition is able to balance changes in the inflow mass flow rate as well as density variations in the interior of the domain. In addition, the constant is always three orders of magnitude smaller than the velocity field normal to the outflow plane and its effect on the resulting flow field is minor.

As for the temperature field, at the inflows we impose uniform temperature profiles while the convective boundary condition, shown in equation (2.48), is used for the outflow. On the other hand, a zero Neumann condition is imposed at the walls. Further, a zero Neumann condition is given for the pressure in all the boundaries of the computational domain. Finally, the boundary condition for the auxiliary velocities $\tilde{\boldsymbol{u}}$ and $\breve{\boldsymbol{u}}$ is set so as to satisfy equations (2.22) and (2.29) respectively and for the predictor step reads

$$\tilde{\boldsymbol{u}}_{\mathrm{wall}} \; = \; \boldsymbol{u}^{n}_{\mathrm{wall}} + \frac{\Delta t}{\rho^{*}_{\mathrm{wall}}} \left(\nabla p^{n}_{\mathrm{wall}} - Ri\, \nabla \rho^{*}_{\mathrm{wall}}\, y \right). \tag{2.49}$$

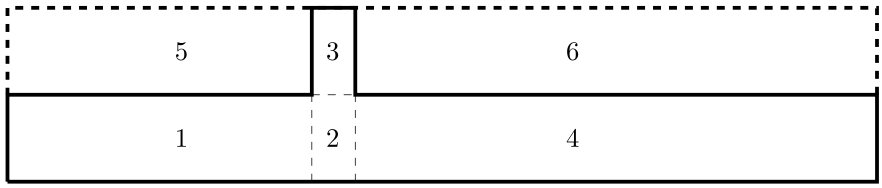

Figure 2.3: Illustration of the domain decomposition that is performed in our numerical simulations. The thick dashed lines show the original rectangular domain and the black solid lines show the resulting computational domain after the domain decomposition. The thin dashed lines show the interior boundaries between sub-domains.

2.7 Decomposition of the computational domain

As already mentioned above, in our studies we have used a rectilinear grid. This results in a computational domain that has the shape of a rectangular parallelepiped. Therefore, in order to simulate flows in T-junctions, the computational domain should be decomposed appropriately. In figure 2.3 we show a simplified two-dimensional illustration of our computational domain. The initial shape of the computational domain is shown with thick dashed lines while the resulting shape of the domain after its decomposition is shown with solid black lines. Finally, with thin dashed lines we show the interior boundaries of the sub-domains.

As this figure shows, the domain is decomposed into six sub-domains. The sub-domains 1, 2 and 4, cover the horizontal channel while the one named as 3 covers the smaller vertical channel. As for the regions of the rectangle named as 5 and 6, with an exception of a row of cells that is used as ghost-cells, they are kept inactive throughout the entire duration of our numerical simulations.

The implementation of this domain decomposition is straightforward and is performed by adding an additional iteration loop that iterates only over subdomains 1-4. On the other hand, the population of matrices during the solution of linear systems is slightly more complex. In order to fill the matrices efficiently, we are introducing an index map which modifies the coordinates of the rectangular prism into the ones for the geometry of the T-junction. Finally, special attention is paid on the corners of the decomposed computational domain. More specifically, the third sub-domain has one common ghost-cell with the first and the fourth subdomains. Therefore, in order to not have conflicting boundary conditions in these locations, we update the value of the ghost-cell accordingly to the sub-domain where the operations are performed.

2.8 Algorithm paralellization

To increase the computational efficiency and reduce the computing time, the algorithm described above is parallelized using the OpenMP application programming interface [67]. OpenMP consists of a number of compiler directives and library routines and it is designed for shared memory multiprocessing programming. For the numerical simulations performed in the context of this thesis we have used a server containing four Intel Xeon E7-4820 v3 processors totalling 40 cores and 128 Gb of RAM. By using the directives provided by OpenMP, the parallelization of the terms that are computed explicitly is straightforward.

Nevertheless, for the numerical solution of linear systems via parallel algorithms, we need to perform particular rearrangements in the solution procedure in order for it to be parallelized efficiently. For example, for the computation of the auxiliary velocities $\tilde{\boldsymbol{u}}$ and $\breve{\boldsymbol{u}}$ we take advantage of the fact that they are computed explicitly in the spanwise direction. Therefore, instead of solving a linear system with a left-hand side of size $N_x \times N_y \times N_z$ we solve N_z systems of size $N_x \times N_y$. The matrix population of the N_z systems and the computation of the right hand side of equations (2.24) and (2.29) is performed in parallel by all acting cores. On the other hand, each core is assigned to solve one of the N_z linear systems. In order to solve the afore-mentioned linear systems we use the stabilised biconjugate gradient iterative method (Bi-CGSTAB) proposed by der Vorst [68]. More specifically, we employ the implementation of the algorithm provided by EIGEN [69] which is a template library for linear algebra.

For the solution of the two Poisson equations for the pressure (2.26) and (2.31) we follow a different strategy. The iterative procedure described above performs a larger number of simulations before converging to a solution for these equations. This, in turn, results in a significant increase of the algorithm's computational cost. For this to be avoided, we use a direct solver. In order to use a direct solver, the left-hand side of equations (2.26) and (2.31) must be factorised accordingly. This is an operation that is computationally time consuming. However, since the left-hand side in these equation is constant, the factorisation procedure is done once at the initialization stage of the algorithm.

The direct solver that is employed for the linear systems for the pressure is PARDISO [70], a high-performance parallel solver of large sparse linear systems provided by Intel® MKL programming language library. This choice reduces considerably the computing time for the computation of equations (2.26) and (2.31) while providing a very accurate solution. However, the excessively large size of the square matrices in the left-hand side of these equations, renders the use of direct solvers cumbersome. To reduce the size of the matrices, we assume a solution in the form of finite Fourier series in the spanwise homogeneous direction

$$\phi^k = \sum_{m=0}^{N_z-1} \check{\phi}^m \, e^{-i2\pi km/N} \; = \sum_{m=0}^{N-1} \check{\phi}^m \, \left(\cos(2\pi km/N) + i\,\sin(2\pi km/N)\right) . \tag{2.50}$$

In this equation $\check{\phi}^m$ stands for the Fourier coefficient corresponding to wavenumber m. This, in turn, enables us to use the Fast Fourier Transform (FFT). In this manner, instead of solving one system with the square matrices having dimension $N_x \times N_y \times N_z$, we solve N_z systems where the matrices have dimensions $N_x \times N_y$. In what follows, we briefly describe the procedure applied on the solution of equations (2.26) and (2.31). In particular, we describe the solution for equation (2.26) which in discretized form reads

$$P^*_{xy_k} + c_1 {P^*}_{k-1} + c_2 {P^*}_k + c_3 {P^*}_{k+1} \; = \; \mathrm{RHS}_{xy_k} . \tag{2.51}$$

In P^*_{xy} we group the discretized terms for $\frac{\partial^2 p_{\mathrm{m}}}{\partial x^2} + \frac{\partial^2 p_{\mathrm{m}}}{\partial y^2}$. Also, c_1, c_2 and c_3 are the coefficients that result from the discretization of the term $\frac{\partial^2 p}{\partial z^2}$ for $k-1$, k and $k+1$ respectively. Additionally, in RHS^*_{xy} we group all the terms on the right-hand side of equations (2.26) which are computed in parallel by all acting cores. We then perform the discrete Fourier transform of the relation (2.51) so as to get

$$\sum_{m=0}^{N_z-1} \check{P}{*}^m_{xy} \, e^{-i2\pi km/N} + \sum_{m=0}^{N_z-1} \check{P}{*}^m \, \left(c_1 e^{-i2\pi k(m-1)/N} + c_2 e^{-i2\pi km/N} + c_3 e^{-i2\pi k(m+1)/N}\right)$$
$$= \sum_{m=0}^{N-1} \mathrm{R\check{H}S}^m_{xy} . \tag{2.52}$$

By employing trigonometric identities and setting equal the coefficients of $e^{-i2\pi km/N}$ in equation (2.52) we obtain

$$\check{P}{*}^m_{xy} + \check{P}{*}^{m-1} + \left(2\cos\left(\frac{2\pi m}{N}\right) - 2\right) \check{P}{*}^m + \check{P}{*}^{m+1} \; = \; \mathrm{R\check{H}S}^m_{xy} . \tag{2.53}$$

This is the linear system of equations that we solve with PARDISO. Once the solution for $\check{P}{*}$ is obtained, we perform the inverse Fourier transform in order to obtain the values of ${p_{\mathrm{m}}}^*$. Finally, it is worth mentioning that for the computation of the Fourier and the inverse Fourier transforms we use FFTW [71], a parallel programming library routine for computing discrete Fourier transforms.

2.9 Summary

In this chapter we presented the governing equations of the flow under study and their low-Mach-number approximation. We also described the numerical algorithm that is employed for the numerical treatment of these low-Mach number equations. This algorithm is based on a predictor-corrector time-advancement scheme and a projection method that yields a constant-coefficient Poisson equation for the calculation of the pressure.

Further, we briefly described the subgrid models that are used in our LES simulations. In addition, we elaborated on the implementation of the turbulent inflow condition, which plays an important role on the accuracy of simulations of turbulent flows in T-junctions. Finally, we outlined the procedure for the parallelization of the numerical algorithm that is implemented especially for the present work, with emphasis on the Poisson solver for the pressure.

Chapter 3

Isothermal turbulent flows in T-junctions

3.1 Introduction

In this chapter we report on numerical studies of isothermal turbulent flows in T-junctions. An important issue regarding Large Eddy Simulations of flows in T-junctions is the resolution of the near-wall regions of the flow. To the best of our knowledge, the majority of previous studies were based on LES that did not resolve the near-wall regions because of the increased computational cost. Instead, they relied on wall models, also referred to as "wall functions". However, as shown by Jayaraju et al. [62] and more recently by Tunstall et al. [72], the use of wall-functions for simulating flows in T-junctions results in erroneous estimation of the near-wall temperature and velocity fluctuations.

Despite the progress achieved thus far in the understanding of flows in T-junctions, there are several questions regarding their properties in the near-wall regions. More specifically, due to flow separation and reattachment, the complexity of the flow field close to the walls of the T-junction increases substantially. The main objectives of this study are to advance our understanding of the flows of interest and to examine more closely the underlying physics in these region. An additional objective of this work is to create a database of numerical results for this complex flow that can be used for validation purposes. To this end, we

The results of this chapter have been published in: M. Georgiou and M.V. Papalexandris. 2017 Numerical study of turbulent flow in a rectangular T-junction. *Phys. Fluids* **29(6)**,065106. [32]

perform wall-resolved LES of the interaction between two turbulent streams in a rectangular T-junction with periodic boundary conditions in the spanwise direction. Further, we consider two different cases, one with a high and one with a low momentum ratio ($M_R = 2$ and $M_R = 0.5$, respectively) and assess their differences and similarities.

To the best of our knowledge, this is one of the first wall-resolved LES for flows in T-junctions. The fine resolution used near the solid boundaries has allowed us to identify two new features that have not been reported before for T-junctions, thereby affirming the complexity of the flow field near the walls and downstream the incoming jet. The first new feature is a small-scale recirculation zone situated between the entry of the jet and the large recirculation bubble. The second one is a region where the production term of turbulent kinetic energy is negative. This region is located inside the large recirculation bubble and close to the point of reattachment of the flow. In this chapter we also present a detailed analysis of the statistics of the flow, thus providing additional insight and physical information, particularly as regards the mixing process between the crossflow and the incoming jet and the near-wall behaviour of the flow. A noteworthy contribution of this analysis is the identification of boundary layers that are characterised by favourable or adverse pressure gradients and the examination of their role to the flow dynamics.

This chapter is structured as follows. In section 3.2 we outline the numerical algorithm and describe the numerical setup of our simulations, including the implementation of turbulent inflow conditions. In section 3.3 we present the numerical results. This consists of the description of the main features of the flow, the comparisons with experiments and the analysis of the statistics of the flow. Finally, section 3.4 concludes.

3.2 Numerical setup and computational aspects

In this section we outline the numerical method employed in our simulations and elaborate on the flow geometry and the computational grid. In general terms, the numerical setup and domain configuration are defined so as to simulate the experimental study of Hirota et al. [11]. In those experiments, the authors investigated the interaction between a crossflow and a jet, having different temperatures, in a T-junction with rectangular cross-sections. Nonetheless, Hirota et al. [11] reported that the velocity measurements were performed under isothermal conditions. In these experiments the bulk Reynolds number was $Re_{\mathrm{b}} = 15,000$ and the momentum ratio was $M_R = 2$. Using standard convention, M_R is defined as the ratio between the momentum fluxes, $\rho U^2 A$, of the crossflow and the incoming jet, with U and A being the bulk velocity and cross-section area, respectively. In our study we have kept the same values of Re_{b} and M_R as in the experiments mentioned above. Further, we have performed additional simulations with the same Re_{b} but with $M_R = 0.5$ in order to examine the effect of varying the momentum flux of the jet.

3.2.1 Outline of the numerical method

Since our study concerns LES we solve numerically the incompressible, spatially-filtered Navier Stokes equations. For non-dimensionalisation purposes, the bulk velocity of the crossflow U_{c} is chosen as the reference velocity, whereas the half-width of the main channel δ is chosen as the reference length. In non-dimensional form, the governing equations read

$$\nabla \cdot \mathbf{u} \;=\; 0\,, \tag{3.1}$$

$$\frac{\partial \mathbf{u}}{\partial t} + \mathbf{u} \cdot \nabla \mathbf{u} \;=\; -\frac{1}{\rho}\nabla p + \frac{1}{Re}\nabla \cdot ((\nu + \nu_t)\nabla \mathbf{u})\;. \tag{3.2}$$

In equation (3.2), Re is the Reynolds number defined as

$$Re \;=\; \frac{U_{\mathrm{c}}\,\delta}{\nu}\,, \tag{3.3}$$

with U_{c} being the bulk velocity of the crossflow. As such, Re is half the bulk Reynolds numbers Re_{b}, so that in our case $Re = 7,500$. Also, ν_t denotes the eddy viscosity that is computed by the procedure outlined in section 2.5 and represents the transport and dissipation of kinetic energy to the subgrid (unresolved) turbulent structures of the flow. Further, the components of the spatially-filtered velocity vector $\mathbf{u}$ will be denoted as $\mathbf{u} = (u,\, v,\, w)$.

The numerical treatment of the above equations is based on a variation of the time-accurate algorithm of Lessani and Papalexandris [42] described in chapter 2 with the time-step being determined by the CFL condition with a Courant number being smaller than unity.

3.2.2 Flow geometry and grid resolution

An illustration of the flow geometry is provided in figure 3.1. According to the convention adopted herein, the x-axis is aligned with the streamwise direction, *i.e.* the direction of the crossflow along the main channel. The y-axis is aligned with the wall-normal direction and the z-axis points with the spanwise direction. The distance between the walls of the main channel is 2δ, whereas the distance between the walls of the jet is δ. In our simulations, the crossflow enters the computational domain from the left inflow boundary of the main channel, while the jet enters from the bottom inflow boundary of the smaller transverse channel, as shown in figure 3.1. The two streams mix downstream the entry of the jet and the combined stream exits the domain from the right outflow boundary of the main channel.

In their numerical study of a jet in an unconfined crossflow, Muppidi and Mahesh [73] concluded that the extent of the computational domain of the transverse channel must be at least equal to the jet diameter, δ, in order for the velocity statistics of the jet to be independent of the crossflow. Accordingly, in our simulations we satisfy this requirement by setting the length of the transverse channel equal to 2δ. For the same reason, the extent of the crossflow in the main channel (*i.e.* the distance between the upstream inflow and the entry of the jet) is set equal to 5δ. Finally, the distance between the jet entry and the outflow at the right is set equal to 13δ so as to capture as much as possible the mixing process between the incoming jet and the crossflow.

Periodic boundary conditions are applied in the spanwise direction. This choice offers significant computational savings when compared with wall boundary conditions that would require high grid resolution near the boundary. Nonetheless, periodic conditions still allow for meaningful comparisons with experiments. In fact, in their numerical study of impinging jets, Jones and Wille [74] reported that their predictions at the symmetry plane were independent of the type of spanwise boundary conditions. This, in turn, implies that it is feasible to compare our predictions with the measurements of Hirota et al. [11] at the symmetry plane by applying periodic conditions in the spanwise direction. Finally, the length of the computational domain in the spanwise direction is set equal to $\frac{4}{3}\pi\delta$. This length is deemed sufficient for the development of the pertinent turbulent structures of the flow.

Next, we describe the discretization of the computational domain. The presence of the incoming jet is expected to result in significant flow inhomogeneities

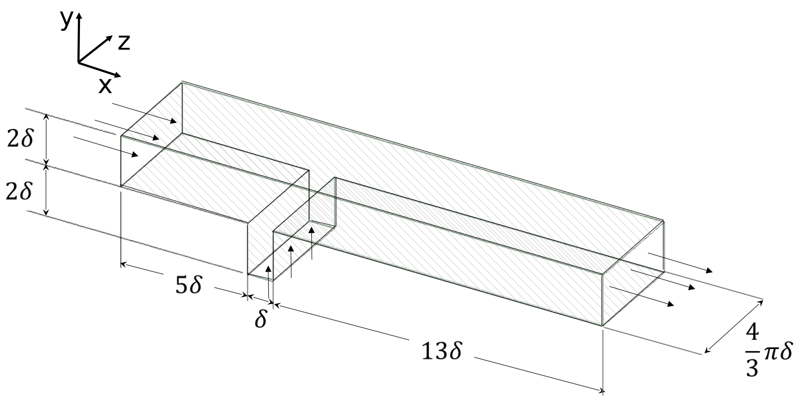

Figure 3.1: Illustration of the computational domain for our simulations of turbulent flow in a T-junction.

along the streamwise direction. In other words, the emerging flow field is characterised by the development of structures of different sizes that evolve along the streamwise direction and interact with each other. For this reason, we are required to use a computational grid that is non-uniform both in the streamwise and in the wall-normal directions. On the other hand, a uniformly spaced grid is employed in the homogeneous spanwise direction. Henceforth, all lengths will be given in non-dimensional values, that is, scaled with δ.

An illustration of the computational grid is provided in figure 3.2. In order to determine the required grid resolution, we proceed as follows. First, we place the origin of the axes at the downstream corner of the entry of the jet. Then, the computational domain is divided in three sections. The first one consists of the main channel upstream the jet, defined by $-5 < x \leq -1$ and $0 < y < 2$. The second section covers the transverse channel and is defined by $-1 < x \leq 0$ and $-2 \leq y < 0$. Finally, the third section covers the remaining part of the main channel and is defined by $-1 < x < 13$ and $0 < y < 2$. The average velocity in these sections is different and so is the "local" Reynolds number Re_l, that is, the Reynolds number based on the average velocity and the half-width in each section. This implies that different resolution requirements have to be fulfilled in the three sections.

In our study we have followed the guidelines of Zang [75] for grid spacing in the wall-normal directions, according to which one should put at least one node between $0 < y^+ < 1$ and at least three nodes between $0 < y^+ < 10$. In these relations, following standard notation, y^+ stands for the normalised wall coordinate, defined by $y^+ = \frac{y u_\tau}{\nu}$ with $u_\tau = \sqrt{\frac{\tau_\mathrm{w}}{\rho}}$ being the local friction velocity and τ_w the wall shear stress in the particular section that it is estimated based on the "local" Reynolds number, Re_l. According to the same guidelines, the grid spacing in the streamwise and spanwise directions should fulfil $\Delta x^+ < 80$ and $\Delta z^+ < 30$, respectively, where $x^+ = \frac{x u_\tau}{\nu}$ and $z^+ = \frac{z u_\tau}{\nu}$. Also, we refined progressively the grid along the streamwise direction in the section where the crossflow and the incoming jet meet. The rationale for this refinement is to resolve as accurately as possible the two shear layers that are formed at the corners of the entry of the incoming jet, at $x = -1$ and $x = 0$, respectively. In addition, further downstream from the entry of the incoming jet we keep the grid spacing in the x-direction sufficiently small so as to capture the merging of the two streams.

The first section is the one with the relatively coarser grid in the x-direction. This choice is motivated by the fact that no mixing occurs therein. The local Reynolds number is estimated to be $Re_l = 7,500$. The grid spacing in the streamwise direction varies between $0.15 < \Delta x^+ < 28$, with the spacing becoming progressively smaller as we approach the entry of the jet. The stretching factor in this region is kept small, reaching a maximum of 1.15 at $x = -1$. In the (wall-normal) y-direction, where the viscous sublayer is directly resolved, the first node off the wall is situated at $y^+_{\mathrm{f.n}} \approx 0.3$, which corresponds to $y/\delta \approx 8.7 \times 10^{-4}$. Further, 11 nodes are placed in the region between $0 < y^+ < 10$. The grid spacing in the y-direction follows a hyperbolic tangent distribution and increases up to $\Delta y^+ \approx 8$ at the centerline. Also, the maximum stretching factor is 1.08 and occurs next to the walls. On the other hand, in the spanwise direction, Δz is constant with $\Delta z^+ \approx 12$. It should be clarified that the values of Δx^+, Δy^+ and Δz^+ mentioned herein are approximate because τ_w varies slightly during the simulations. The grid in this section consists of $60 \times 96 \times 64$ cells.

In the second section, the transverse channel, the local Reynolds number is estimated at $Re_l \approx 7,500$ for the case where the momentum ratio M_R is equal to 0.5. The first node normal to the wall is situated at $x^+_{\mathrm{f.n}} \approx 0.2$. Further, 10 nodes are situated between $0 < x^+ < 10$. The grid spacing in this direction also follows a hyperbolic tangent distribution and increases up to $\Delta x^+ \approx 6$ at the centerline of the transverse channel. The stretching factor is also kept small, with a peak value of 1.12 close to the walls. In the y-direction and for $2.5 < y < 4$, Δy is kept

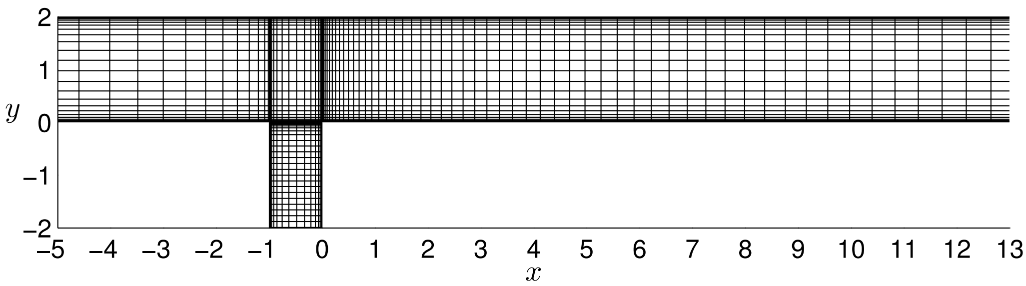

Figure 3.2: Illustration of the computational grid. For visualisation purposes only a fraction of the computational cells is shown.

constant with $\Delta y^+ \approx 4$. Then, as we approach the entry of the jet, the grid is refined up to a value of $\Delta y^+ \approx 0.2$ with a maximum stretching factor equal to 1.1 at $y = 0$. Finally, in the spanwise direction Δz and corresponds to $\Delta z^+ \approx 12$. The grid in this section consists of $64 \times 96 \times 64$ cells.

The third section is the most intensive one from the computational point of view because it covers the interaction of the jet with the crossflow and the formation of shear layers that emanate from the corners of the entry of the jet. For momentum ratio $M_R = 0.5$, the local Reynolds number is estimated at $Re_l \approx 15,000$. At the y-direction, the first node away from the wall is at $y^+_{\mathrm{f.n}} = 0.65$ and 7 nodes are placed between $0 < y^+ < 10$. The coarser spacing in the y-direction is at the centerline of the channel with $\Delta y^+ \approx 19$. Along the x-direction, Δx^+ is stretched smoothly from 0.3 at the downstream corner of the entry of the jet to 40 at the outflow boundary. The maximum stretching factor is 1.15 and it is at $x = 0$. Finally, in the spanwise direction Δz is constant with $\Delta z^+ \approx 24.5$. Overall, the grid in this section consists of $216 \times 96 \times 64$ cells. An overview of the discretization of the computational domain is provided in table 3.1.

Section	1	2	3
Extent	$-5 < x < -1$ $0 < y < 2$	$-1 < x < 0$ $-2 < y < 0$	$-1 < x < 13$ $0 < y < 2$
Estimated Re_l	$7,500$	$7,500$	$15,000$
Resolution x-dir.	$0.15 < \Delta x^+ < 28$	$0.2 < \Delta x^+ < 6$	$0.5 < \Delta x^+ < 40$
Resolution y-dir.	$0.3 < \Delta y^+ < 8$	$0.3 < \Delta y^+ < 4$	$0.65 < \Delta y^+ < 19$
Number of cells	$60 \times 96 \times 64$	$64 \times 96 \times 64$	$216 \times 96 \times 64$

Table 3.1: Overview of the discretization of the computational domain.

Finally, we note that, by design, an LES can resolve only the large flow scales, and that the number of resolved scales increases as the mesh is refined. For this reason, and in contrast to steady-state RANS simulations, the concept of grid refinement study is ill-posed [76]. In LES of complex flows: numerical grid convergence can be determined only via comparisons with DNS in which all turbulent scales are resolved. But this contradicts the purpose of performing LES in the first place; the main reason for performing LES is to avoid the computationally expensive DNS.

3.2.3 Implementation of inflow and outflow conditions

In our simulations, we have to provide two turbulent inlet conditions: one for the crossflow and one for the incoming jet. As described in chapter 2, the accurate implementation of turbulent inlets has long been recognised to play a critical role in the simulation flows in T-junctions [30]. In this study we run two auxiliary turbulent channel-flow simulations for the two inflow conditions. In these auxiliary simulations, the streamwise dimension of the computational domain is $4\pi\delta$, while the wall-normal and spanwise dimensions are set equal to the ones of the inlets of the T-junction. To avoid spatial interpolation errors, the grid resolution is the same as in the corresponding inlets of the T-junction. Finally, for the outflow boundary, we implemented the convective boundary condition given in (2.48).

3.3 Discussion of the numerical results

In this section we elaborate on the main features of the flow for both momentum ratios, namely, $M_R = 2$ and $M_R = 0.5$. In the discussion that follows, the mean (average) of a scalar quantity ϕ is denoted by $< \phi >$ and refers to averaging both in time and in the homogeneous spanwise direction. The fluctuating component of ϕ is denoted by ϕ'. Finally, ϕ_{rms} denotes the root mean square (rms) value of ϕ', *i.e.* $\phi_{\text{rms}} =< \phi'\phi' >^{1/2}$.

The simulations are initialised by injecting fluid from the vertical channel to the crossflow. Accumulation of statistical data of the flow field is initialised after the flow has becomes statistically stationary. The stationarity of the flow is estimated by a combination of the procedures used in [77] and [73]. More specifically, we first let the simulation run for 10 "flow-through" times. In this case a flow-through time is approximated by the ratio between the length of the domain after the incoming jet and the bulk velocity of the flow just downstream the recirculation bubble, *i.e.* for $M_R = 2.0$ it is approximately equal to 13/1.5=8.67 time units. After 10 flow-through times we start to collect statistics. Flow stationarity is verified by comparing statistics with increasing number of samples (and hence increasing flow time over which statistics are computed). Then, flow quantities are averaged over 20 non-dimensional time units, which is deemed to be a sufficiently long period for statistical analysis. In fact, in the context of our study, we performed averaging over longer periods without observing any difference in the results.

Some of the important features of the flow are depicted in figure 3.3 which shows streamlines extracted from the mean velocity field for both momentum ratios considered in our study. Henceforth, these will be referred to as *average streamlines*. From this figure it can be inferred that close to the turbulent inlet of the main channel, the crossflow remains unaffected by the incoming jet. However, as we approach the entry of the jet, and because of the high momentum flux of the jet, the crossflow streamlines start to bend and tilt upwards. In other words, since the crossflow cannot penetrate the jet, it behaves as if the jet was an obstacle and moves around it. A similar observation has been reported by Muppidi and Mahesh [78] on their study of a jet in an unconfined crossflow.

By analogy, the average streamlines of the jet start to bend before the jet entry and inside the transverse channel. They continue to bend after they enter the main channel until they align with its walls and become parallel to the average streamlines of the crossflow. In turn, this change of direction results in the formation of a large recirculation bubble downstream the location of the entry of the jet. This separation zone is one of the most characteristic features of the flow and, furthermore, its interaction with the incoming jet plays a crucial role on the dynamics of the flow downstream.

Also, the average streamlines shown in figure 3.3 aid in locating the interfaces between the crossflow, the jet and the recirculation bubble. In turn, these interfaces serve to identify the zones where fluid mixing occurs. More specifically, we can infer that a shear layer is formed between the crossflow and the jet. Its origin is located at a very short distance from the upstream corner of the entry of the jet. In its early stages, this shear layer is fairly thin. Then it starts to spread so that most of the mixing occurs in the region where the average streamlines of the crossflow and of the incoming jet are aligned with the walls of the main channel. The second shear layer is formed between the jet and the recirculation bubble and originates from the downstream corner of the entry of the jet. It is characterised by much stronger shear and higher spread angle, which implies much higher levels of mixing.

Additional information about the main features of the flow can be found in figure 3.4 which shows the amplitude of the in-plane mean velocity field, given by

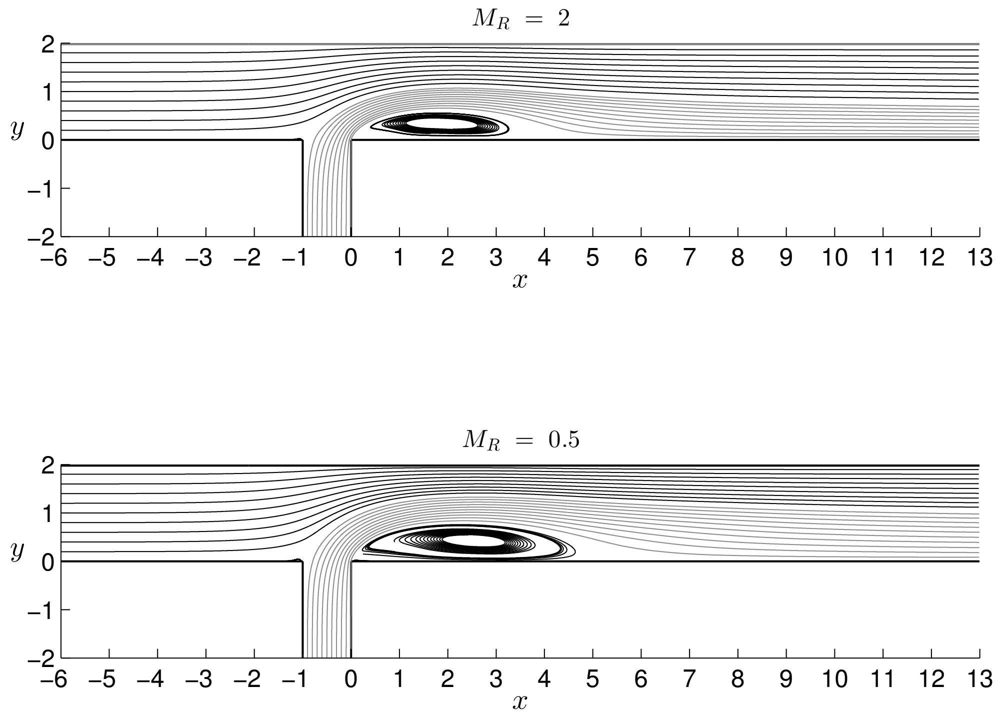

Figure 3.3: Average streamlines, extracted by the mean velocity field, for the two momentum ratios, M_R, considered herein. In this figure we show 9 streamlines emerging from the left entry of the horizontal channel. The distance between those is 0.2. In a similar manner, we show 9 streamlines emerging from the bottom entry of the vertical channel with the distance between those being 0.1. Further, we depict two streamlines downstream the entry of the jet in order to visualise the large recirculation bubble in this region. Top image: $M_R = 2$. Bottom image: $M_R = 0.5$.

$u_a = (< u >^2 + < v >^2)^{1/2}$ for the two momentum ratios considered in our study. In particular, this figure depicts an additional flow structure centred around the upstream corner of the entry of the jet. It consists mainly of another recirculation zone. In the y-direction it extends from a point below the jet entry (inside the transverse channel) up to the origin of the first shear layer that was mentioned above. This structure is typical of jets in unconfined crossflows [78, 79] and of flows in T-junctions [80].

From figure 3.4 we can identify two additional features of the flow under study. The first one is the progressive increase of the velocity amplitude downstream the location of the entry of the jet. In other words, the fluid particles of the crossflow accelerate as they circumvent the incoming jet. This is due to the presence of the jet which essentially reduces the cross-section area of the crossflow. Because of this area reduction, the crossflow accelerates. In other words, this is a Venturi

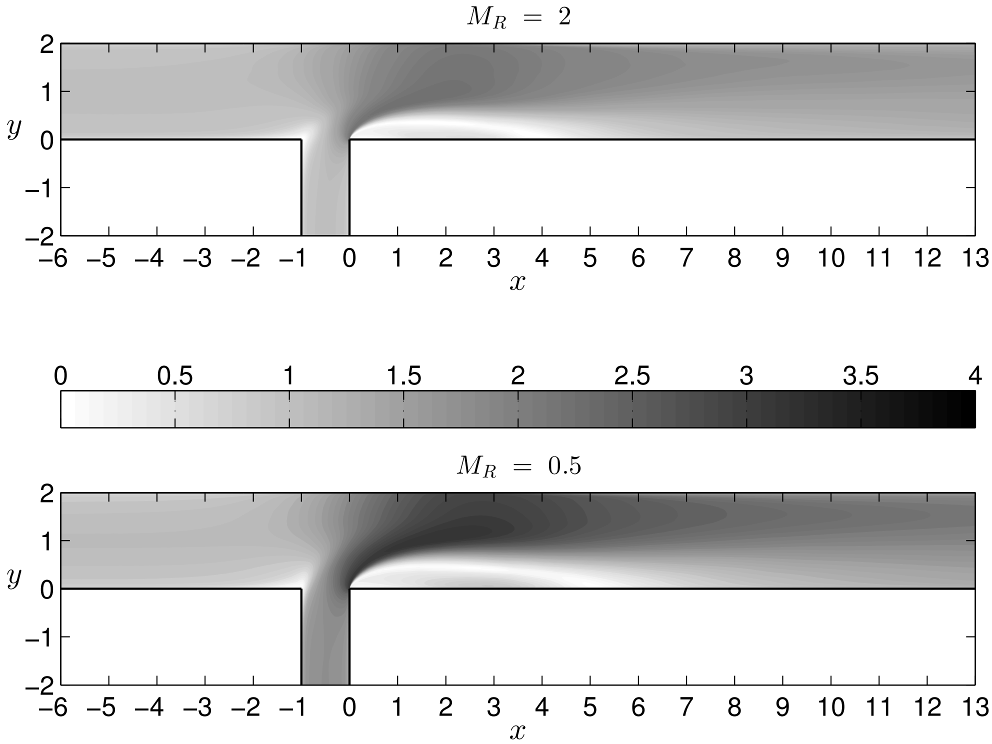

Figure 3.4: Contour plots of the amplitude of the in-plane mean velocity, $u_a = (< u >^2 + < v >^2)^{1/2}$. The lightly coloured area around the upstream corner of the entry of the jet represents an additional recirculation zone. Top image: $M_R = 2$. Bottom image: $M_R = 0.5$.

effect and, evidently, it is more pronounced at higher incoming jet velocities. This feature does not appear in jets in unconfined crossflows because in those cases the cross-section area is infinite due to the absence of an upper solid boundary. Actually, another difference is that in T-junctions, the presence of the top wall of the channel forces the jet to bend earlier. As a result, the jet aligns with the walls of the main channel considerably faster than in unconfined flows.

The second additional feature is the strong acceleration of the jet in the vicinity of the downstream corner of its entry. This acceleration is a manifestation of the Venturi effect produced jointly by the crossflow and the large recirculation bubble. This feature has been reported by Howard and Serre [23] who conducted simulations of cylindrical T-junctions and is also observable in the numerical results of Schaupp et al. [81].

Interestingly, our simulations also reveal the formation of two additional small recirculation zones adjacent to the corners of the entry of the jet, as can be shown in figure 3.5. The one adjacent to the upstream corner, shown in figure 3.5.a, is

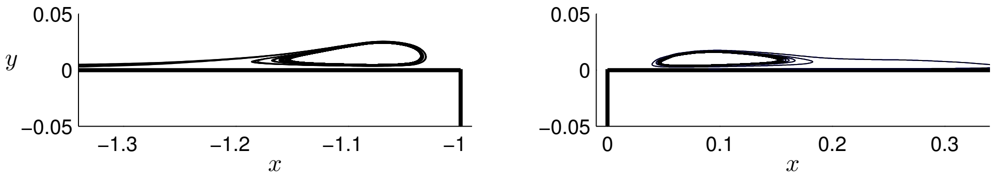

Figure 3.5: Average streamlines in the vicinity of the entry of the jet depicting two secondary recirculation zones. Momentum ratio, $M_R = 2$. Left image: upstream corner of the entry of the jet. Right image: downstream corner of the entry of the jet.

equivalent to the well-known horse-shoe vortex that is observed in jets in unconfined crossflows; see, for example, the experimental observations of Andreopoulos and Rodi [82], and Kelso et al. [79], as well as the simulations of Muppidi and Mahesh [78] and Howard and Serre [23] and references therein. It should be noted that in the flow considered herein, a horse-shoe vortex cannot be formed because the incoming jet spans the entire z-direction. On the other hand, the small recirculation zone in the downstream corner, shown in figure 3.5.b has not been reported before. This small structure is fairly localised and it is not yet clear if it affects the flow dynamics downstream.

Next, we turn our attention to the vorticity distribution in the flow domain. In figure 3.6 we show a representation of the instantaneous vorticity field based on the Q-criterion introduced by Hunt et al. [83]. The quantity Q measures the difference between the amplitudes of the skew-symmetric and symmetric parts of the velocity-gradient tensor and is defined by

$$Q = 2\left(|\boldsymbol{\Omega}|^2 - |\boldsymbol{S}|^2\right) , \tag{3.4}$$

where $\boldsymbol{\Omega} = [\nabla \boldsymbol{u} - (\nabla \boldsymbol{u})^T]$ is the vorticity tensor and $\boldsymbol{S} = [\nabla \boldsymbol{u} + (\nabla \boldsymbol{u})^T]$ the rate-of-strain tensor. As such, positive values of Q correspond to non-zero vorticity amplitude. Furthermore, the higher the value of Q, the higher the amplitude of the vorticity is. The most distinct feature in this figure is the shedding of strong spanwise vortical structures (rollers) by the shear layer emanating from the downstream corner of the entry of the jet. As the shear layer spreads out, these rollers are convected downstream. Moreover, some of them start to interact with the large recirculation bubble and eventually get entrapped therein.

As regards the shear layer of the upstream corner of the entry of the jet, the plots in figure 3.6 provide further evidence that it originates from a point slightly above the corner. Also, according to these plots, it is considerably weaker

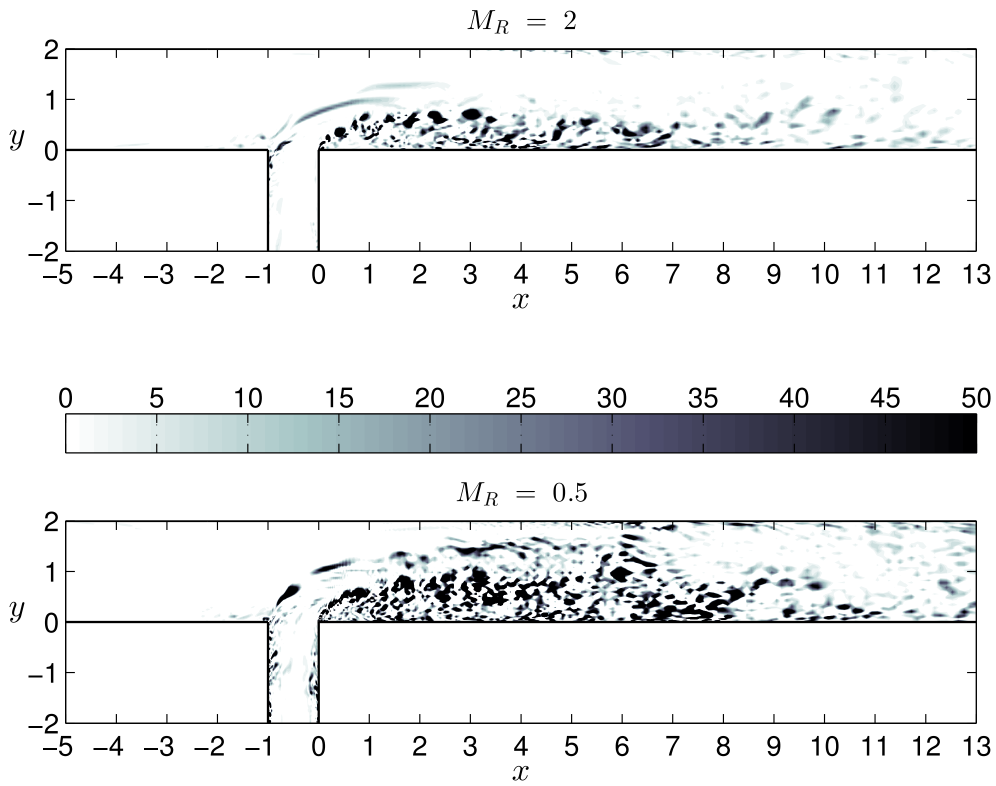

Figure 3.6: Visualisation of the vorticity field based on the Q-criterion. The images show contour plots of the quantity Q at the spanwise location $z = 1.4$. Top image: $M_R = 2$, bottom image: $M_R = 0.5$.

and generates much less vorticity than the shear layer of the downstream corner. When $M_R = 2$, this shear layer spreads rapidly, thereby reducing its strength even further. On the other hand, in the case of $M_R = 0.5$, this shear layer persists at longer distances and eventually merges with the shear layer of the downstream corner.

Additionally, figure 3.6 reveals a thin zone of increased amounts of vorticity close to the top wall of the main channel and at $x \approx 5$. The appearance of this zone is explained as follows. As the crossflow passes over the hump of the recirculation bubble, it starts to expand, which implies the formation of an adverse pressure gradient. This is not strong enough to cause flow separation, nonetheless it causes the decrease of the streamwise velocity u near the top wall. Eventually u reaches a minimum value, which coincides with the location where the vortical structures appear. We therefore infer that these structures are formed due to the expansion of the crossflow. The extent of this zone is significant in both cases. As expected, the vortical structures are considerably intensified when $M_R = 0.5$ because the

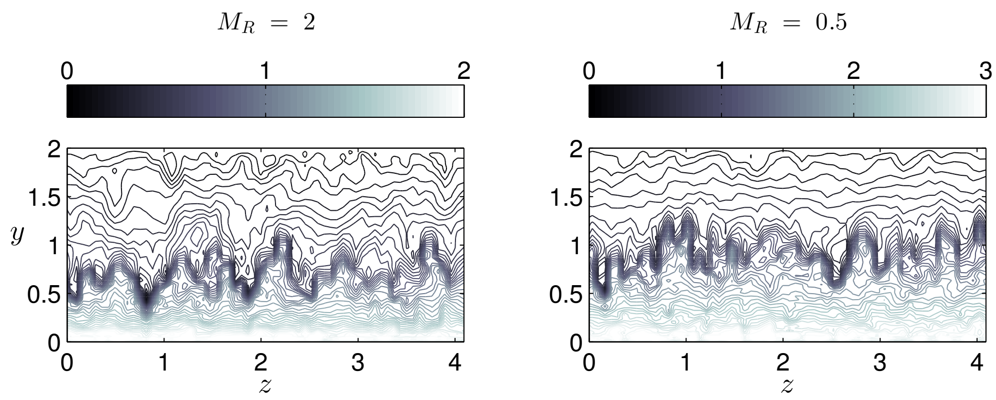

Figure 3.7: Contour plots of the normal velocity component, v, at the $y\,z$-plane at the downstream corner of the entry of the jet ($x = 0$). Left image: $M_R = 2$. Right image: $M_R = 0.5$.

size of the recirculation bubble in this case is larger.

Finally, an interesting feature related to the vorticity field can be evidenced in figure 3.7 which contains contour plots of the normal velocity component v at the yz-plane located right at the downstream corner of the entry of the jet, at $x = 0$. According to this figure, the profiles of v in the shear layer of the upstream corner have the form of finger-like structures. These structures are formed due to the interaction of the incoming jet with the crossflow. Their presence signifies large gradients of the normal velocity component v in the spanwise direction which, in turn, indicate increased streamwise vorticity in this region.

3.3.1 Comparison with experiments

In this section we compare, for validation purposes, the predictions of our numerical results with the experimental results of Hirota et al. [11]. First we examine the streamwise rms velocity component u_{rms}. Contour plots of u_{rms} from our simulations and from the experimental data are juxtaposed in figure 3.8. From this figure, the good agreement between our prediction and the experimental data can readily be deduced. In particular, our simulations predict accurately the spreading rate and bending of the shear layer emanating from the downstream corner of the jet entry, at $x = 0$. Similarly, the size and shape of the large recirculation bubble are accurately predicted by our simulations. Moreover, as can be observed from figure 3.8, our numerical predictions for u_{rms} agree well with the experimental data both in the recirculation bubble and in the mixing zone downstream. Our simulations further predict that the turbulent intensity of the shear layer emanating

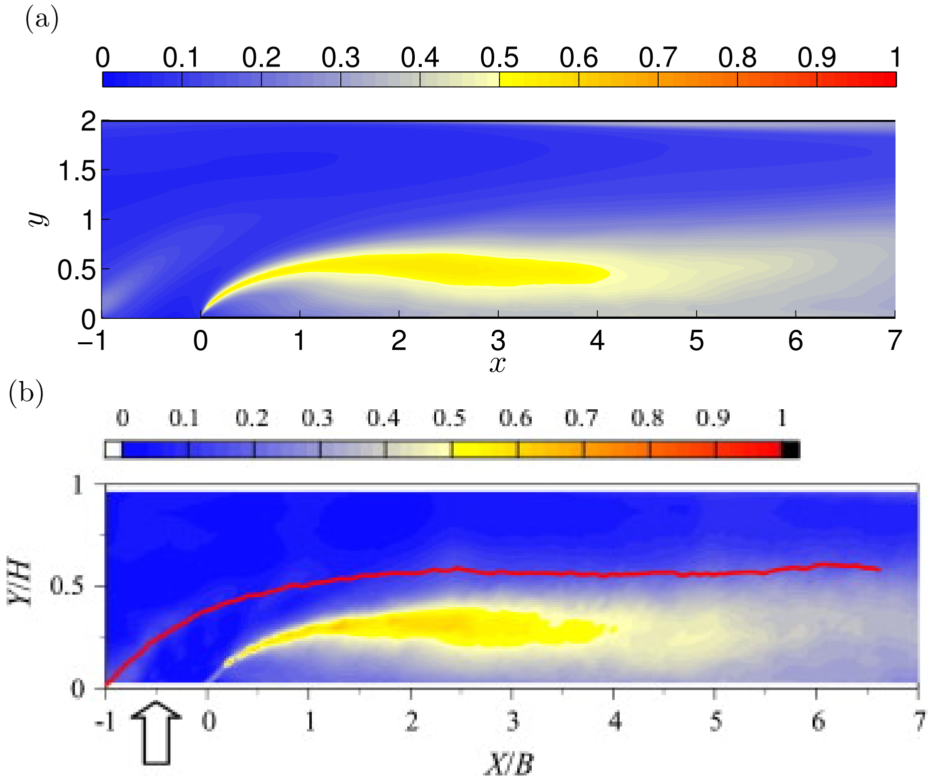

Figure 3.8: Contour plots of the streamwise rms velocity, u_{rms}, for momentum ratio $M_R = 2$. Top image: numerical results from the present study. Bottom image: experimental measurements. The red line superposed to the experimental results shows the centerline of the shear layer emanating from the upstream corner of the entry of the jet. The bottom image is reprinted from [11], with permission from Elsevier.

from the upstream corner of the jet entry is much weaker, in accordance with the measurements of Hirota et al. [11].

Next we compare the results for the rms values of the wall-normal velocity component, v_{rms}, shown in figure 3.9. This figure provides further evidence of the good agreement between our numerical results and the experimental data. It can also be attested that the sizes and locations of the principal structures of the flow (the shear layer emanating from the downstream corner, the recirculation bubble and the mixing zone downstream) are accurately computed in our simulations. Additionally, it can be inferred from figure 3.9, that our simulations predict fairly well the thickness and shape of the (weaker) shear layer that emanates from the upstream corner of the entry of the jet.

A more detailed comparison can be drawn from figures 3.10 and 3.11 which show close-up contour plots of u_{rms} and v_{rms}, respectively, in the vicinity of the jet

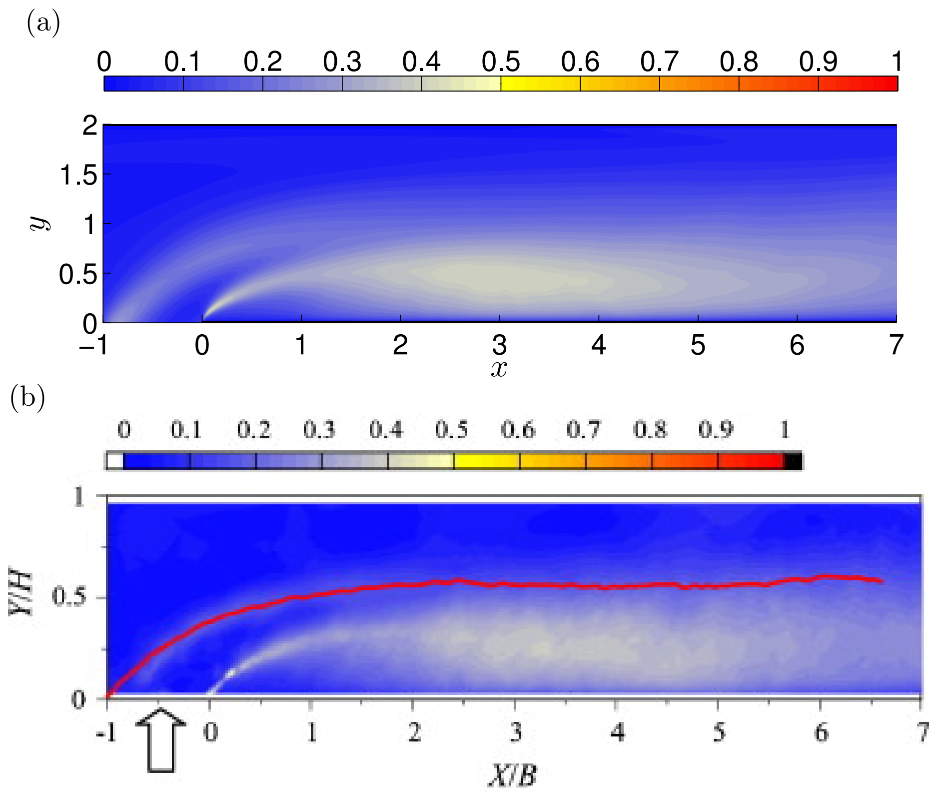

Figure 3.9: Contour plots of the wall-normal rms velocity, v_{rms}. Top image: numerical results from the present study. Bottom image: experimental measurements. The red line superposed to the experimental results shows the centerline of the shear layer emanating from the upstream corner of the entry of the jet. The bottom image is reprinted from [11], with permission from Elsevier.

entry. These figures corroborate the good agreement between the predictions of our simulations and the experimental data of Hirota et al. [11] in this region of the flow field. More specifically, our numerical results for the rms velocity components in the shear layers stemming from the two corners compare favourably with the measurements. Also, our simulations have correctly captured the recirculation zone close to the wall and upstream the entry of the jet. However, as can be inferred from figure 3.10, our simulations slightly overestimate the u_{rms} values in this zone just above the left corner. It should be mentioned that Hirota et al. [11] did not provide data for the flow in the transverse channel (below the entry of the jet) and, therefore, no comparisons are possible for that region. Further, they presented only contour plots instead of specific values of the velocity field at given locations, which does not allow for a more detailed and reliable comparison between our simulations and those experiments. Nevertheless, to the best of our

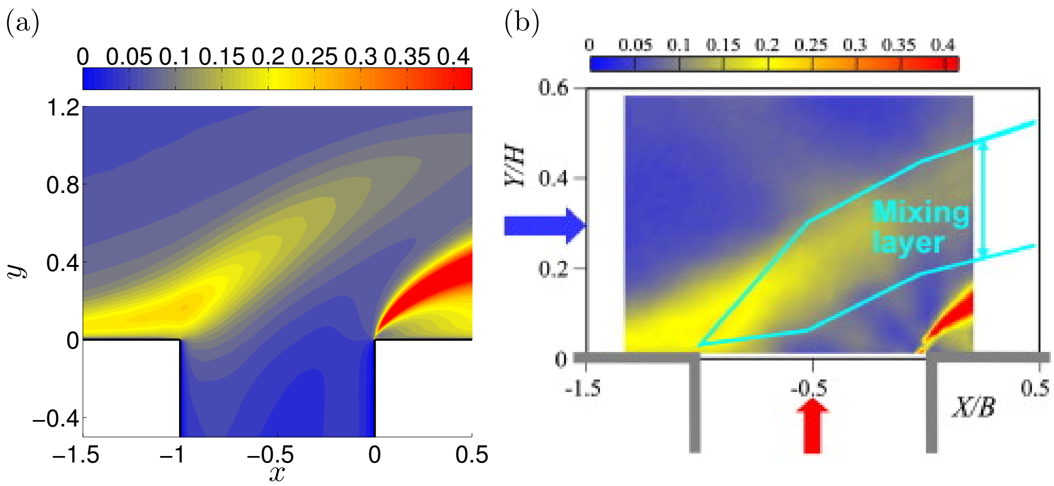

Figure 3.10: Contour plots of the streamwise rms velocity, u_{rms}, in the vicinity of the entry of the jet. Left image: numerical results from the present study. Right image: experimental measurements. The cyan lines superposed to the experimental results show the upper and lower boundaries of the shear layer emanating from the upstream corner of the entry of the jet. The right image is reprinted from [11], with permission from Elsevier.

knowledge, this is the first numerical simulation that compares so favourably with available experimental data in flows in T-junctions.

3.3.2 Flow statistics

In this section we present and analyse the statistical quantities of the flow. In particular, we present first and second-order statistics for both momentum ratios. The results for each momentum ratio M_R are presented separately.

3.3.2.1 Momentum ratio $M_R = 2.0$

Mean streamwise velocity profiles, $< u >$, at different locations of the main channel are shown in figure 3.12. Even though $< u >$ is symmetric at the inlet of the turbulent crossflow at $x = -5$, this symmetry eventually breaks down at a location between the inlet and the entry of the jet. This can be confirmed by figure 3.12.a, according to which the profile of $< u >$ at $x = -2.29$ has already been skewed. This symmetry loss is clearly due to the jet which, as mentioned above, plays the role of an obstacle for the crossflow. In fact, the location where the symmetry loss of $< u >$ occurs coincides with the location where the crossflow starts to bend upwards in order to circumvent the jet.

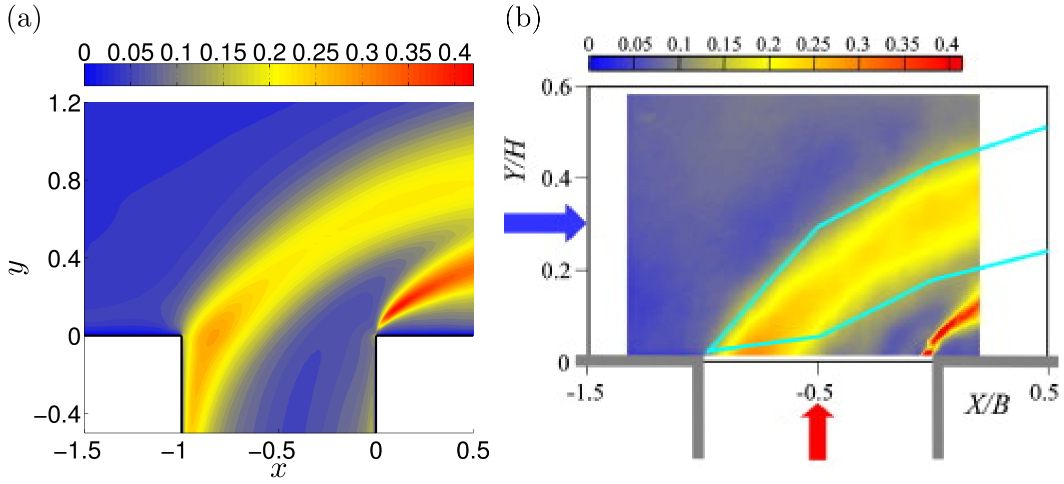

Figure 3.11: Contour plots of the wall-normal rms velocity, v_{rms}, in the vicinity of the entry of the jet. Left image: numerical results from the present study. Right image: experimental measurements. The cyan lines superposed to the experimental results show the upper and lower boundaries of the shear layer emanating from the upstream corner of the entry of the jet. The right image is reprinted from [11], with permission from Elsevier.

Figure 3.12.b shows the profile of $< u >$ at the centre of the incoming jet. The higher values of $< u >$ close to $y = 0$ are caused by the bending of the jet while the increase of the streamwise velocity at the upper half of the channel is due the progressive decrease of the cross section area of the crossflow. This cross section becomes minimal at the vicinity of the large recirculation bubble and, more specifically, at $x = 1.61$. Figure 3.12.c shows the profile of $< u >$ at this location. According to this figure, the further restriction of the cross section area of the crossflow stream results to higher values of $< u >$. This, in turn, causes the decrease of the boundary-layer thickness at the top wall. It is noted that $< u >$ varies very slightly between the centerline of the main channel and the boundary layer of the top wall; this zone corresponds to the cross section of the crossflow. Below that, the zone defined by $y < 1$ is marked by the shear layer emanating from the downstream corner of the entry of the jet and the recirculation bubble. In this zone, $< u >$ reaches its peak and then decreases, eventually becoming negative close to the bottom wall.

Further, figure 3.12.d shows the profile of $< u >$ at the location where the flow reattaches, at the end of the recirculation bubble. Herein the reattachment point is approximated by the first-node point at which $< u >$ changes sign. Finally, figures 3.12.e and 3.12.f show profiles of $< u >$ downstream the recirculation bubble. This

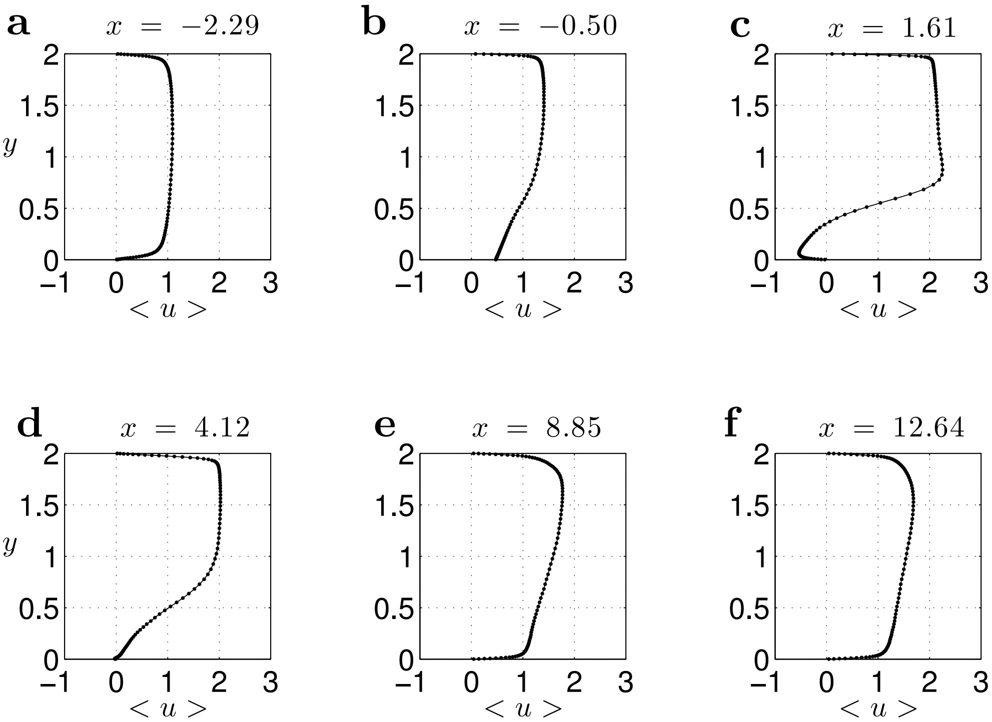

Figure 3.12: Profiles of the mean streamwise velocity, $< u >$, for $M_R = 2$. The above profiles correspond are taken at different representative regions of the flow. (a): upstream the entry of the jet. (b): centre of the incoming jet (c): recirculation bubble. (d): reattachment of the flow. (e) and (f): downstream mixing zone.

is the region where the incoming jet merges with the crossflow. Eventually the merged streams will evolve to a channel flow. Nonetheless, the asymmetry of these profiles implies that the re-establishment of a channel flow does not occur within the computational domain but much further downstream its outflow boundary.

We now proceed to examine in more detail the profiles of $< u >$ in the near-wall regions and compare them to the universal law of the wall. To this end, the distance from the wall and the mean streamwise velocity are expressed in wall coordinates, y^+ and u^+, respectively, with $u^+ = \frac{<u>}{u_\tau}$ and u_τ being computed based on the local velocity gradients. Also, since the velocity profiles are not symmetric, we examine u^+ in the bottom and top walls separately. The law of the wall is given by

$$u^+ = \begin{cases} y^+ \,, & y^+ \leqslant 10 \,, \\ \frac{1}{0.38} \log y^+ + 5 \,, & y^+ > 10 \end{cases} \tag{3.5}$$

where the value $\kappa = 0.38$ at the logarithmic region is chosen so as to achieve the best agreement with the computed velocity profiles.

Figure 3.13 shows profiles of u^+ at the bottom wall and at three different streamwise locations: one location upstream the jet and close to the inlet of the crossflow at $x = -4.3$, and two locations downstream the large separation bubble at $x = 8.66$ and $x = 12.64$. (At the regions of flow separation the law of the wall is not valid anyhow and, therefore, velocity profiles from those regions are not included in the figure). According to the results shown in figure 3.13, the velocity profile at $x = -4.3$ agrees with the law of the wall quite well. This is to be expected because at this location the crossflow remains unaffected by the incoming jet. Moreover, this agreement with the law of the wall provides an additional indication of the good quality of the LES results presented herein.

The profiles at the two locations downstream the separation bubble, at $x = 8.66$ and $x = 12.64$, deviate considerably from the law of the wall. More specifically, even though the profiles collapse to the curve $u^+ = y^+$ in the viscous sublayer, they exhibit an inflection point in the log-law region. This feature is typical of wall-bounded flows with large separation zones and it is due to the adverse pressure gradients that are developed downstream those zones. Another example of occurrence of such inflection points is in the flow over a backwards facing step; see, for example, the discussion of the direct numerical simulations of Le et al. [84]. It is also interesting to observe that the deviation from the law of the wall is smaller in the outmost downstream location, *i.e.* at $x = 12.64$. This further confirms that sufficiently downstream the jet, a channel flow will be re-established.

Profiles of the normalised velocity u^+ at the top wall are presented in figure 3.14. They are shown for three locations: close to the inlet of the crossflow at $x = -4.30$, slightly downstream the jet at $x = 0.21$, and further downstream at $x = 12.43$. As in the case of the bottom wall, at $x = -4.30$ the top-wall profile follows the law of the wall. However, we remark that in the second location, $x = 0.21$, the deviation from the universal law of the wall in the log-law region is significant. Furthermore, as regards the outer region, there is no evidence of a regime where the velocity-defect law applies. Instead, u^+ maintains a logarithmic profile of small growth. This behaviour is attributed to the strong favourable pressure gradient that results from the Venturi effect that was mentioned above, *i.e.*, the decrease in the cross-section area and the ensuing acceleration of the crossflow.

Also, the departure from the universal law of the wall is accompanied by the thinning of the boundary layer, which can be observed upon close inspection of

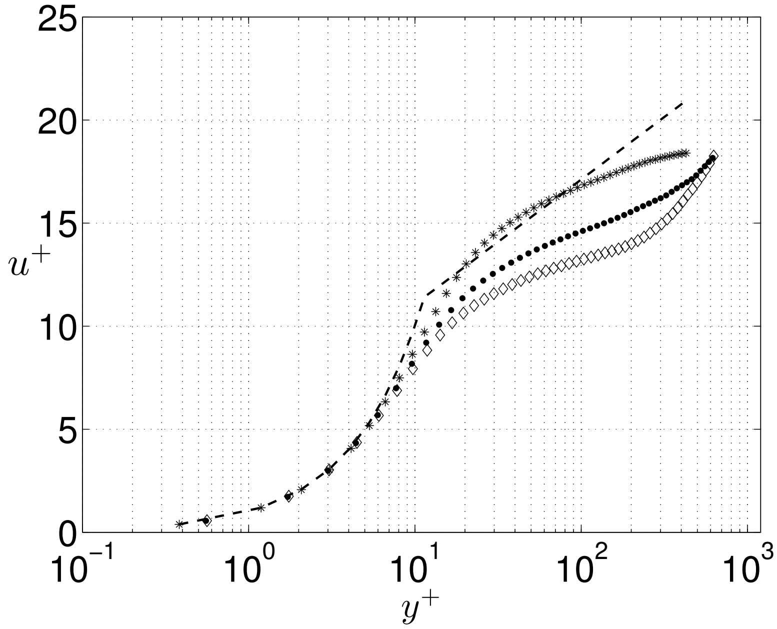

Figure 3.13: Profiles of the wall-normalised streamwise velocity, u^+, at the bottom wall. $--$, law of the wall; $*$, $x = -4.30$; $\diamond$, $x = 8.66$; $\bullet$, $x = 12.64$. The value of $\kappa = 0.38$ for the law of the wall at the logarithmic region is chosen so as to achieve the best agreement with the computed velocity profiles.

the $< u >$ profiles near the top wall in figures 3.12.a and 3.12.b, and by a decrease of the local turbulence intensity, *cf.* figure 3.16 and relevant discussion below. These are typical characteristics of local flow relaminarization (or reverse transition) in accelerated boundary layers [85]. This phenomenon has been the subject of numerous studies; for more information the reader is referred to the recent experimental investigation of Bourassa and Thomas [86] and to references therein. In any case, once the merging of the crossflow and the incoming jet is established, the favourable pressure gradient vanishes and the profile of u^+ starts approaching again the universal law of the wall. This can be clearly ascertained from the profile of u^+ at $x = 12.43$ that is shown in figure 3.14.

As regards the near-wall behaviour of the velocity profiles in the large recirculation bubble, we compare the predictions of our simulations with the empirical equation proposed by Simpson [87],

$$\frac{< u >}{|u_N|} \;=\; A\left(\frac{y}{N} - \log\left(\frac{y}{N}\right) - 1\right) - 1\,. \tag{3.6}$$

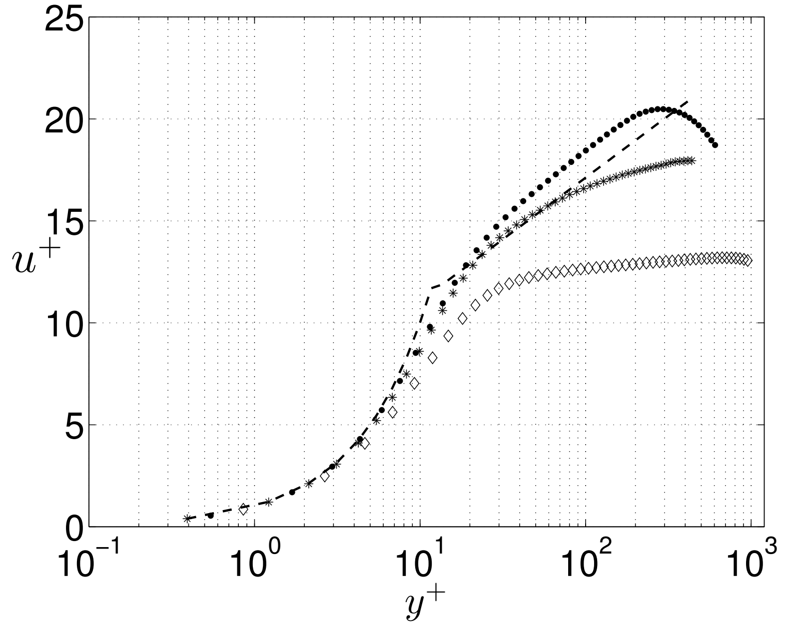

Figure 3.14: Profiles of the wall-normalised streamwise velocity, u^+, at the top wall. $--$, law of the wall; $*$, $x = -4.30$; $\diamond$, $x = 0.21$; $\bullet$, $x = 12.64$. The value of $\kappa = 0.38$ for the law of the wall at the logarithmic region is chosen so as to achieve the best agreement with the computed velocity profiles.

In this relation, u_N is the minimum velocity along the y-axis for a given streamwise location inside the recirculation bubble. Also N is the distance of the point where this minimum value occurs from the wall; in our case N coincides with the y coordinate of this point. Finally, A is a constant whose value, based on the recommendations of Simpson [87], is set to 0.3. According to the author, the above empirical relation is valid for $0.02 < y/N < 1$. In figure 3.15 we compare three numerically computed velocity profiles within the recirculation bubble (at $x = 1.61$, $x = 2.30$, and $x = 3.17$) with the profile obtained by the above empirical relation. We observe that the profiles from our simulations agree reasonably well with the one from the empirical relation within the range of its validity. Nonetheless, some slight discrepancies are observed for $0.02 < y/N < 0.2$.

Next, we proceed to discuss the second-order statistics of the flow. Profiles of the rms values of the streamwise velocity component, u_{rms}, at different locations are shown in figure 3.16. Sufficiently upstream the incoming jet, up to $x \approx -3$, the profiles are symmetric and coincide with those of channel flows, as can be seen in figure 3.16.a. Downstream this location, the profiles start to lose their symmetry due to the presence of the jet, as is the case with the profiles of $< u >$

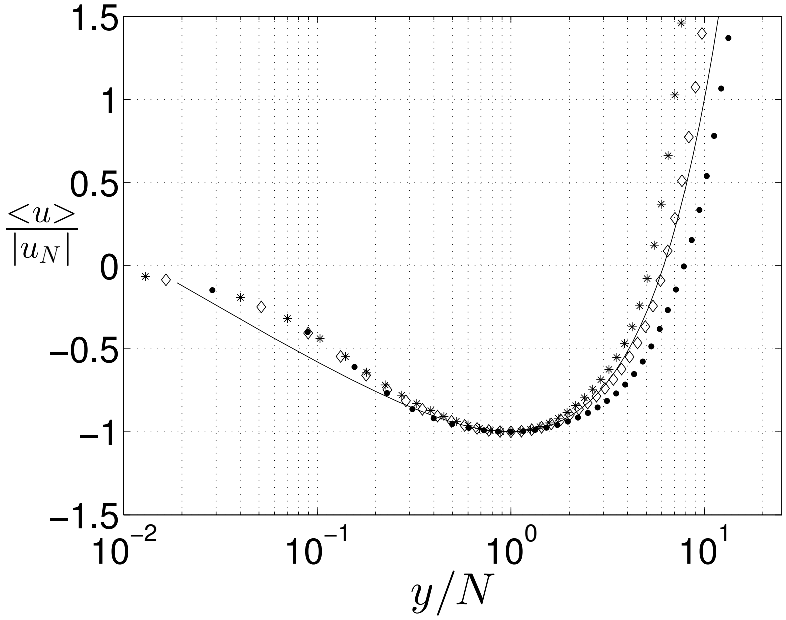

Figure 3.15: Profiles of the mean streamwise velocity, $< u >$, in the recirculation bubble downstream the jet entry. The velocity $< u >$ is normalised with the absolute value of the minimum velocity $|u_N|$ at a given x location. Also, the length y is normalised with the distance N of the point where u_N occurs from the wall. —— , Simpson's formula [1983]; $*$, $x = 1.61$; $\diamond$, $x = 2.30$; $\bullet$, $x = 3.17$.

that were presented above. The plot of figure 3.16.b is taken at the centre of the incoming jet, at $x = -0.5$. The peak u_{rms} that is depicted in this plot coincides with the location of the shear layer emanating from the upstream corner of the entry of the jet. Also, the lower near-wall values of u_{rms} that are observed in this location, with respect to the corresponding rms values upstream, are attributed to the relaminarization of the flow due to the Venturi effect that was mentioned above. Figure 3.16.c shows the u_{rms} profile at $x = 2.4$, which is a streamwise location close to core of the recirculation bubble. In this plot, the peak value of u_{rms} is located at $y \approx 0.5$ and it is due to the mixing induced by the shear layer that emanates from the downstream corner. This peak is also the global maximum of u_{rms}. Figure 3.16.d shows the u_{rms} profile at the location of the reattachment of the flow. It is similar to the one shown in figure 3.16.c but there are also some differences. In particular, the local peaks of u_{rms} close to the walls are considerably amplified, whereas the local peak due to mixing inside the shear layer is smaller. Finally, we remark that further downstream, the turbulent intensity profiles start to regain their symmetry and to approach slowly the ones encountered in channel

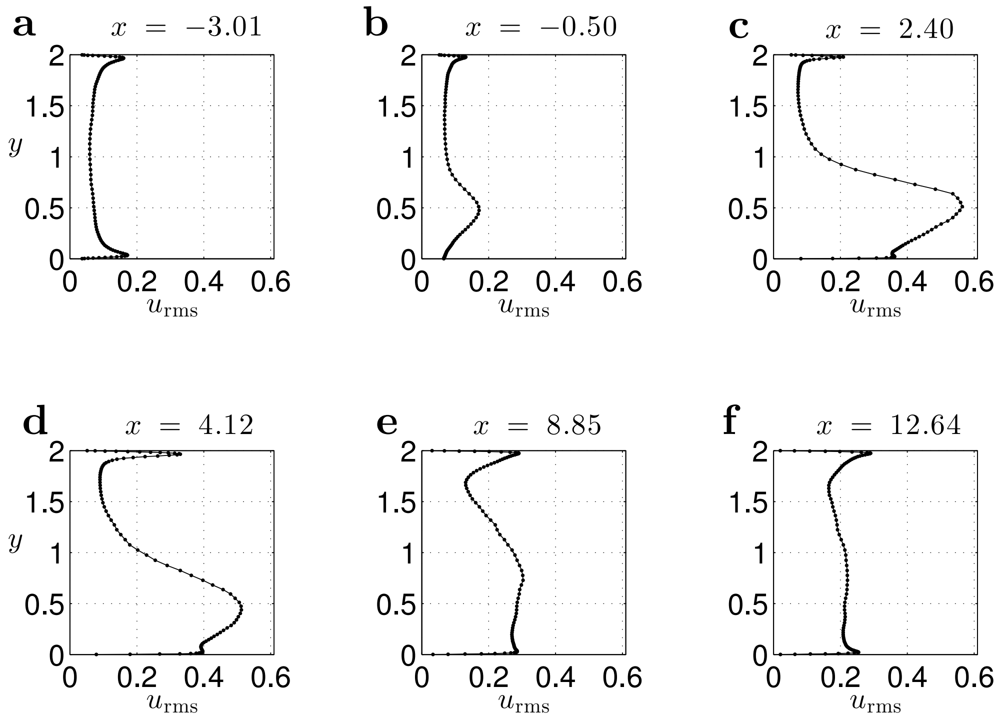

Figure 3.16: Profiles of the rms of the streamwise velocity component, u_{rms}, for $M_R = 2$.

flows, as shown in figures 3.16.e and 3.16.f.

Profiles of the rms values of the normal velocity component, v_{rms}, at different locations are shown in figure 3.17. According to these plots, the evolution of v_{rms} along the streamwise direction has some similarities with the one of u_{rms}, especially as regards the peak values due to the shear layers that emanate from the corners of the jet. Nonetheless, there are some differences too. For example, whereas the profiles of u_{rms} lose their symmetry at $x \approx -3$, the profiles of v_{rms} are less sensitive and start to get skewed further downstream and at $x \approx -1.67$, *c.f.* figure 3.17.a. Another difference is that the maximum of v_{rms} occurs at $x \approx 3.42$ which is downstream the location where the maximum of u_{rms} occurs.

It is also worth mentioning that, according to figures 3.17.e and 3.17.f, the values of v_{rms} downstream the point of reattachment of the flow and away from the walls are of the same order of magnitude as the u_{rms} values. This is a typical feature of mixing layers, see for example Rogers and Moser [88], and not of channel flows. In other words, the flow downstream the recirculation bubble combines features of both shear layers and channel flows. As it progresses though, the features related to shear layers gradually weaken. Eventually these features will disappear and, as

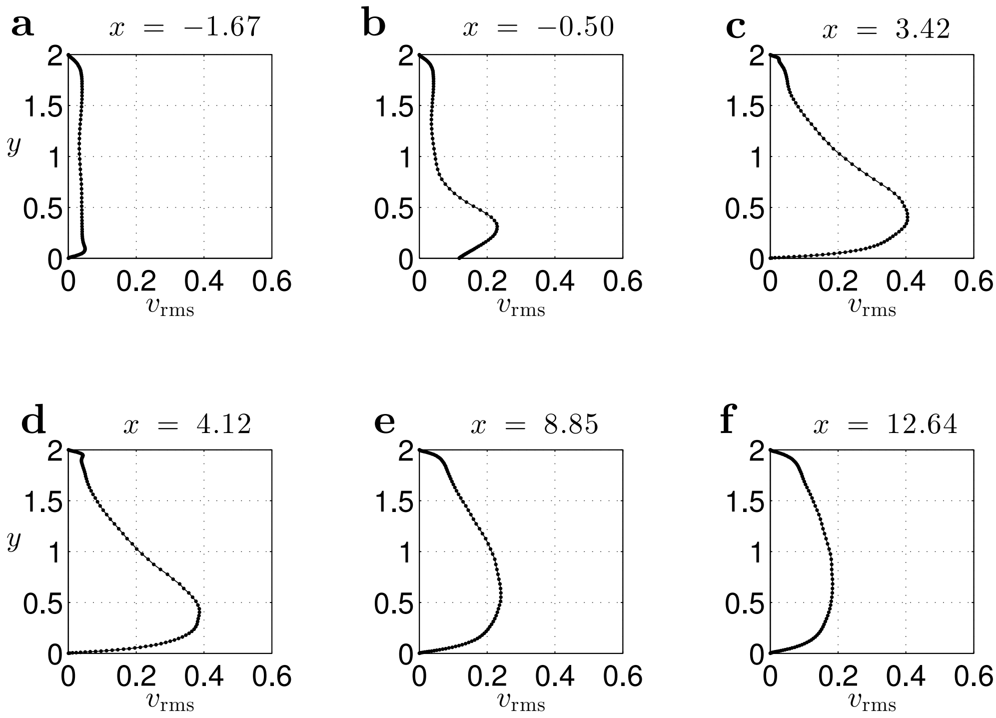

Figure 3.17: Profiles of the rms of the wall-normal velocity component, $v_{\rm rms}$, for $M_R = 2$.

already mentioned, a channel flow will be re-established further downstream at a point outside the computational domain.

Similar trends can be observed in the profiles of $w_{\rm rms}$, shown in figure 3.18. A particularly interesting feature is the high values of $w_{\rm rms}$ close to the bottom wall in the recirculation bubble. More specifically, figure 3.18.c shows the profile at the location where the maximum of $w_{\rm rms}$ occurs, at $x = 3.60$ (which is very close to the location of the maximum of $v_{\rm rms}$). In this plot we can identify two peaks: one inside the shear layer that emanates from the downstream corner of the entry of the jet and one close to the bottom wall. The highest one (and global maximum of $w_{\rm rms}$) is the one close to the wall, which confirms the role of the recirculation bubble as a mechanism for increasing the turbulent intensity near solid boundaries. Furthermore, this peak persists downstream in contrast to the peak inside the shear layer which attenuates, as can be inferred from figures 3.18.d-3.18.f.

Next, we elaborate on the profiles of the Reynolds stresses $< u'v' >$ shown in figure 3.19. These plots confirm that the dominant contribution to $< u'v' >$ comes from the mixing induced by the shear layers. For example, the profile observed in figure 3.19.a is due to the shear layer emanating from the upstream corner.

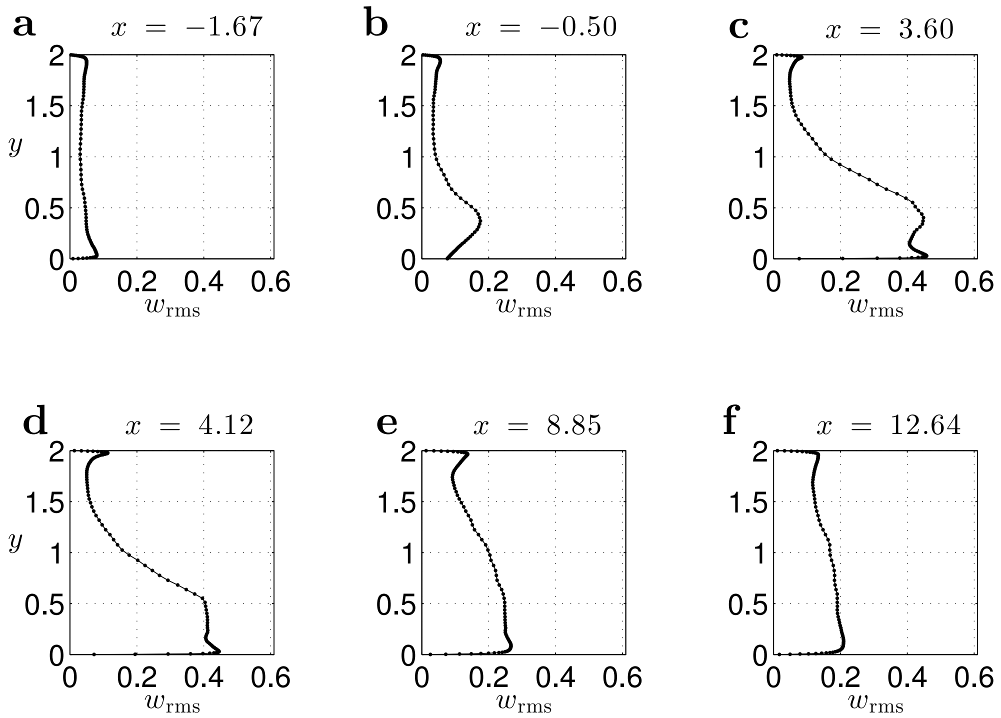

Figure 3.18: Profiles of the rms of the spanwise velocity component, w_{rms}, for $M_R = 2$. In (c) and (d) we remark the high values that w_{rms} attains close to the bottom wall.

Additionally, in figure 3.19.b we can distinguish the contributions of the shear layers to $< u'v' >$ at $x = 0.21$. We also infer that the thickness of the shear layer emanating from the downstream corner is still quite small at this location. Further, the subsequent plots shown in figure 3.19 confirm that, after some distance from the entry of the jet, the two shear layers merge. The combined shear layer diffuses and eventually spans the entire width of the channel, as can be inferred from figure 3.19.f.

Our discussion concludes with an analysis of the turbulent kinetic energy production term, $\mathcal{P}$,

$$\mathcal{P} \;=\; - < u_i' u_j' > \; \frac{\partial < u_i >}{\partial x_j} \,, \tag{3.7}$$

where u_i stands for the velocity components in index notation and summation is implied for repeated indices. In particular, the plots in figures 3.20.a and 3.20.b show the contribution of the shear layers emanating from the corners of the entry of the jet to the production of turbulence. Further, by comparing these plots, we can deduce that the contribution of the shear layer of the downstream corner is at least 30 times higher than the one of the shear layer of the upstream corner.

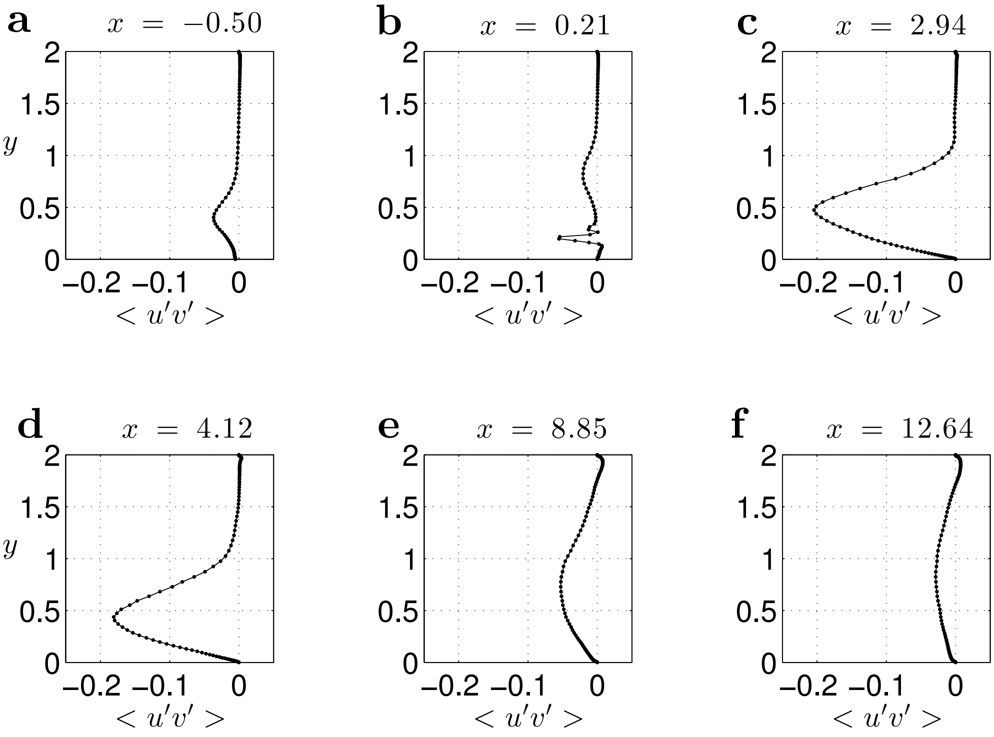

Figure 3.19: Profiles of the Reynolds stress $< u'v' >$ for $M_R = 2$.

More important, in the plots shown in figures 3.20.c and 3.20.d we can observe a small negative production close to the bottom wall in the region of the recirculation bubble. This means that in these locations there is transfer of kinetic energy from the small turbulent scales to the large scales of the flow. In fact, $\mathcal{P}$ becomes negative due to the dominant contribution of the term $-u^2_{\text{rms}} \frac{\partial <u>}{\partial x}$. Indeed, in the region where the flow reattaches, the streamwise gradient of $< u >$ is positive as $< u >$ changes sign (from negative to positive). Also, the rms values of the streamwise velocity in reattachment regions are high, which can be confirmed from figures 3.16.c and 3.16.d. In other words, the negative values of $\mathcal{P}$ could be attributed to the strong recirculation close to the bottom wall and the ensuing reattachment of the flow.

To the best of our knowledge, this phenomenon has not been reported before in studies of flows in T-junctions. This could be explained by the fact that in our study the jet and, therefore, the recirculation bubble span the entire z-direction. As such, this separation zone becomes a prevailing feature of the flow, characterized by strong fluid recirculation. By contrast, in a cylindrical geometry, the curvature of the jet results in a smaller and weaker recirculation bubble; see, for example the numerical work of Howard and Serre [23]. Actually, the occurrence of negative

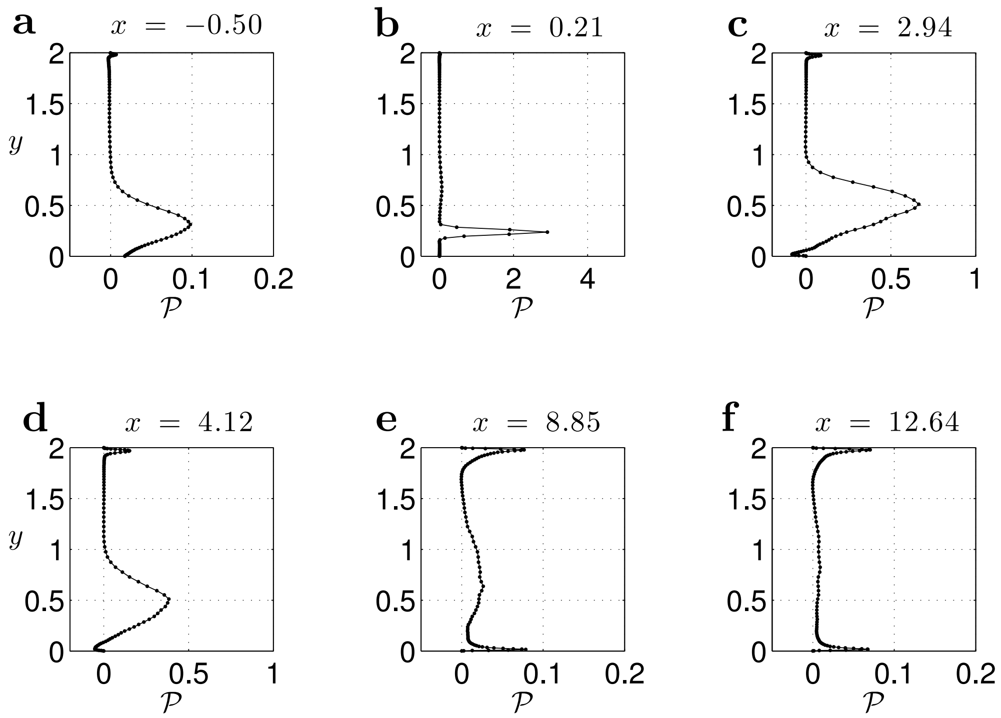

Figure 3.20: Profiles of the turbulent kinetic energy production term $\mathcal{P}$ for $M_R = 2$. For visualisation purposes, the scaling of the $\mathcal{P}$-axis varies from one plot to another. In (c) and (d) we can observe the negative values that $\mathcal{P}$ attains within the recirculation bubble.

turbulent kinetic energy production is rather unusual. Nonetheless, it has already been observed in flows with prevalent recirculation regions; see for example the analysis provided in Hussain [89], as well as the experimental study of Liberzon et al. [90] and the simulations of Gayen and Sarkar [91].

3.3.2.2 Momentum ratio $M_R = 0.5$

In this case, the higher momentum flux of the incoming jet results in higher shear stresses and smaller spreading rates for the shear layers that emanate from the two corners of the entry of the jet. Profiles of the mean streamwise velocity component $< u >$ for this case are shown in figure 3.21. We first remark that due to the higher momentum flux of the jet, the loss of symmetry of the crossflow occurs earlier (closer to the upstream inflow boundary), as can be observed in figure 3.21.a. Further, from figure 3.21.b, which shows the profile at the center of the jet entry, we can deduce that at this specific region $< u >$ is only slightly affected by the higher jet velocity. From figure 3.21.c we can infer that the higher jet velocity produces a larger recirculation bubble downstream the entry of the

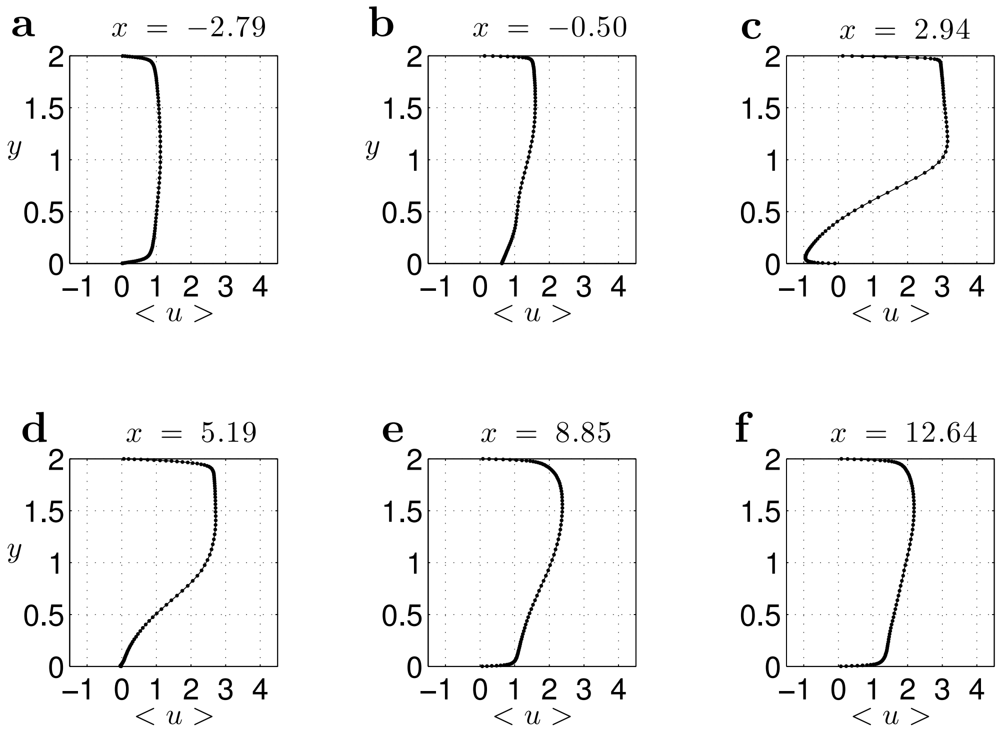

Figure 3.21: Profiles of the mean streamwise velocity, $< u >$, for $M_R = 0.5$.

jet. Also, as a consequence of the larger bubble size, the reattachment of the flow takes place at a larger distance from the entry of the jet, at $x \approx 5.2$, *cf.* figure 3.21.d. Velocity profiles downstream the reattachment point are shown in figures 3.21.e and 3.21.f. According to these plots, the characteristics of the flow in this region are the same as in the previous case. However, the significant variation of $< u >$ along the y-direction indicate that, overall, mixing occurs at a slower rate than in the previous case.

Next, we focus on the differences between the second-order statistics of the two cases. As regards the profiles of u_{rms}, shown in figure 3.22, they are similar to the ones for the previous case, the most notable difference being the higher rms values throughout the domain. Another difference is the profile of u_{rms} above the entry of the jet which appears to be skewed; see figure 3.22.b. This is due to the fact that for $M_R = 0.5$ the incoming jet has increased momentum flux and, therefore, starts to bend farther from the jet entry. The peaks of u_{rms} also occur farther from the bottom wall and closer to the centerline of the main channel, which is a direct consequence of the larger size of the recirculation bubble.

The same observations and remarks can be drawn from the profiles of v_{rms} and w_{rms}, shown in figure 3.23 and figure 3.24, respectively. More specifically, these

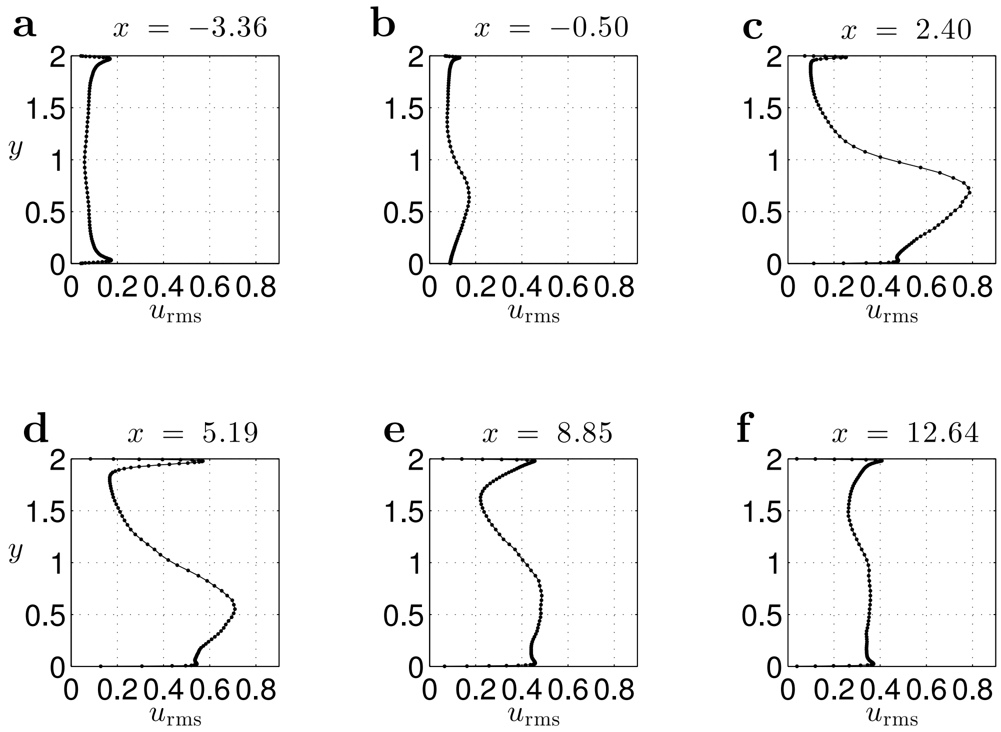

Figure 3.22: Profiles of the rms of the streamwise velocity, u_{rms}, for $M_R = 0.5$. In (b), (c) and (d) we note the gradual increase of the peak of u_{rms} at the top wall.

profiles are also similar to the corresponding ones for $M_R = 2$ but globally they assume higher values. Moreover, their peaks occur closer to the centerline. In other words, as the jet velocity becomes higher, the turbulence intensity increases uniformly in the flow domain downstream the entry of the jet.

Finally, it is worth noting that our simulations predict negative values of the turbulent kinetic energy production term $\mathcal{P}$ for this case as well. As in the previous case, this occurs in the recirculation bubble and close to the wall. We may therefore conclude that this is a persistent feature of the flow under study.

3.4 Conclusions

The turbulent flow in a T-junction of a rectangular cross section has been studied numerically via wall-resolved Large Eddy Simulations. In our study, the bulk Reynolds number of the turbulent crossflow was 15,000 and, furthermore, we considered flows with momentum ratios M_R equal to 2 and 0.5. For validation purposes, we have compared our simulations against existing experimental data.

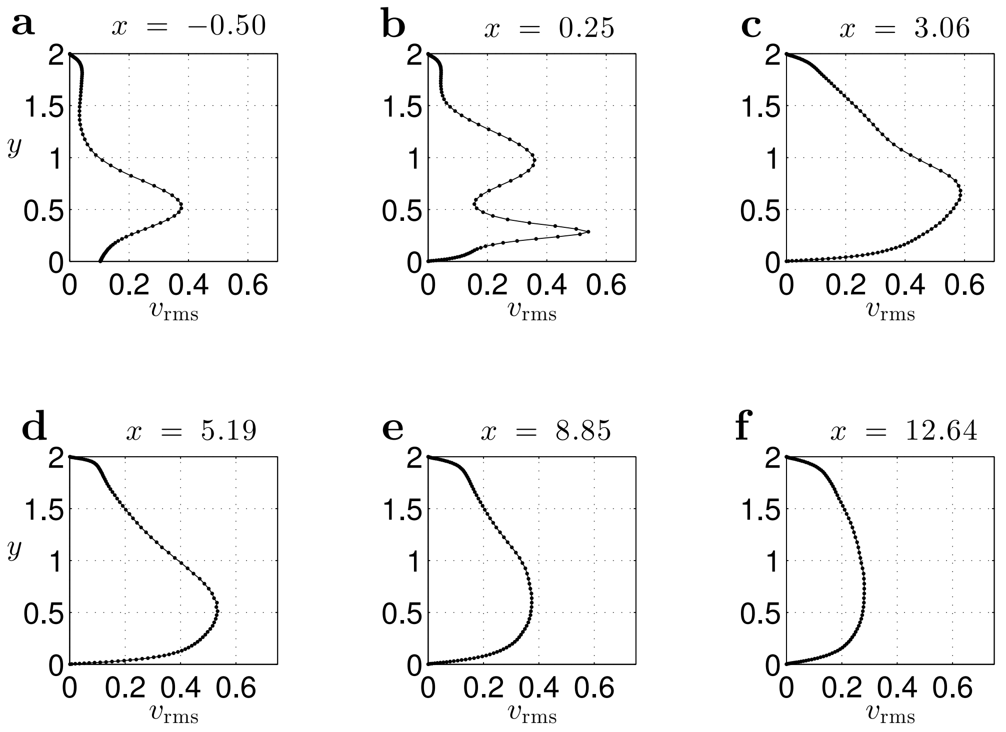

Figure 3.23: Profiles of the rms of the wall-normal velocity, v_{rms}, for $M_R = 0.5$.

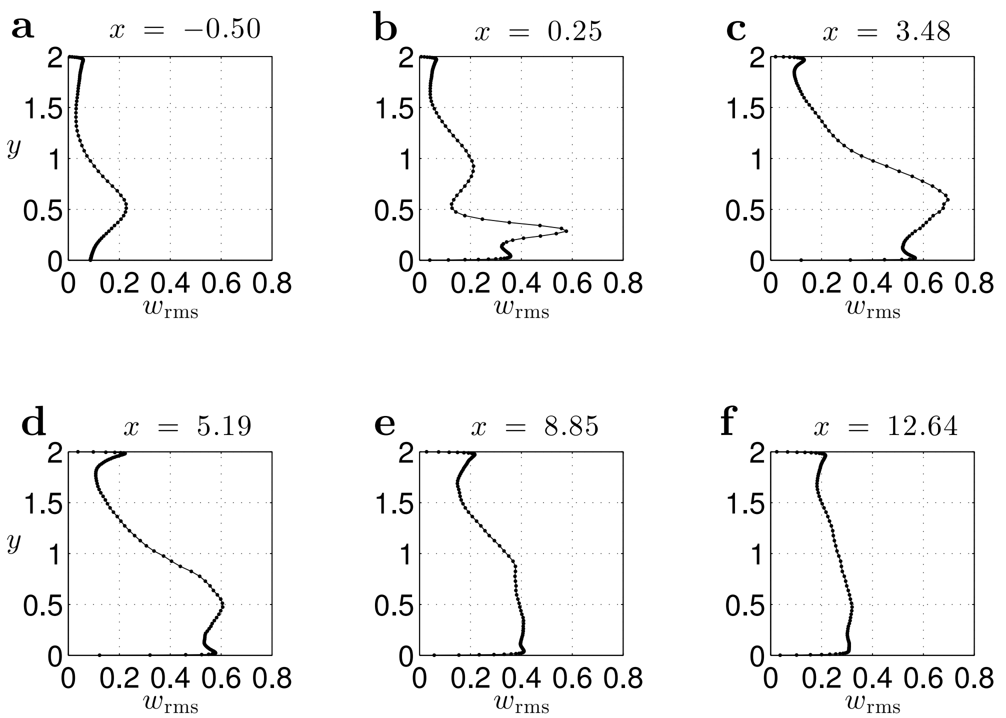

Figure 3.24: Profiles of the rms of the spanwise velocity, w_{rms}, for $M_R = 0.5$.

The comparison shows good agreement between our numerical predictions and the measurements. The flow under study is dominated by the shear layers that emanate from the corners of the entry of the jet and the large recirculation bubble downstream this entry. Our study focused on the properties of these dominant structures, the near-wall behaviour of the flow, and the mixing process downstream the recirculation bubble.

Our simulations reveal two features of the flow that have not been reported before in studies of flows in T-junctions. The first one is a secondary small-scale recirculation region between the entry of the jet and the large recirculation bubble. The second one is the negative turbulent kinetic energy production that occurs in the recirculation bubble, near the wall and close to the reattachment point. At this specific region, we also recorded increased values of the rms velocities, especially as regards thee spanwise component w_{rms}. The analysis of our results also shows that just across the entry of the jet, the boundary layer at the wall experiences a favourable pressure gradient due to the Venturi effect induced by the incoming jet to the crossflow. In turn, this favourable pressure gradient contributes to the local relaminarization of the flow. On the other hand, the boundary layer downstream the recirculation bubble experiences an adverse pressure gradient. In both cases, a significant deviation from the universal law of the wall is confirmed.

Chapter 4

Turbulent heat transfer in gas-gas flows in T-junctions

4.1 Introduction

In this chapter we report on a computational study of turbulent mixing between a cold gas crossflow and a hot gas incoming jet in a T-junction. Currently there is little information about the evolution of the flow field when the temperature is an active scalar. Thus far, most numerical studies dealt with cases where the temperature difference between the two streams was sufficiently small for the temperature to be treated as a passive scalar. A notable exception is the LES of Howard and Serre [24] which, nonetheless, were not wall-resolved but based on wall models. Several numerical studies of turbulent heat transfer in channels [92–94] have shown that the temperature as an active scalar plays a critical role in the evolution of the flow and in the overall mixing process.

The present work aims at filling this gap by focusing on the effects of thermal non-equilibrium on turbulent mixing in T-junctions. To this end, we have performed and present herein wall-resolved LES of the mixing between a cold crossflow and a hot incoming jet in a T-junction. Our numerical predictions compare favourably with existing experimental measurements, as regards both the temperature field and the turbulent heat fluxes. According to our predictions, the

The results of this chapter have been published in: M. Georgiou and M.V. Papalexandris. 2017 Turbulent mixing in T-junctions: the role of the temperature as an active scalar. *Int. J. Heat Mass Transfer.* **115**, 793–809. [33]

temperature gradients increase the turbulent intensity and enhance mixing substantially. Further, the high grid resolution that we employ near solid boundaries has allowed us to study in detail the regions of flow separation and examine how the thermal non-equilibrium between the two streams impacts the structure of these regions.

An additional objective of this work is to gain insight regarding the conditions that lead to the thermal fatigue of the walls in the flows of interest. More specifically, it is well known that high-amplitude temperature fluctuations close to solid boundaries lead to the development of thermal stresses that can result in thermal fatigue cracking [2]. This phenomenon is also referred to as "thermal stripping" and is of particular concern in the design and maintenance of cooling systems of nuclear power reactors; see, for example, the incidents described in [3] and [4]. Herein we present a time-series analysis of the temperature signal at selected locations near the solid boundaries. From this analysis we can identify the dominant frequencies of the temperature fluctuations and estimate the risk of thermal fatigue at the walls.

This chapter is organised as follows. In section 4.2 we outline the mathematical model and the algorithm for its numerical treatment, and describe the setup of our simulations. Section 4.3 is devoted to the presentation and analysis of the numerical results. In this section we briefly explain the main features of the flow and elaborate on the statistics of the temperature, velocity components and turbulent heat fluxes. This section also includes comparisons with experiments and presentation of the time-series analysis of the temperature signal at selected locations of the flow field. Finally, section 4.4 concludes.

4.2 Governing equations and numerical setup

In this section we first outline the mathematical model and the algorithm for its numerical treatment. Subsequently, we describe the setup of our simulations, including flow geometry, computational grid and implementation of boundary conditions. Our setup is chosen so as to match the experimental study [11] of the interaction between a cold turbulent crossflow and a hot incoming jet in a T-junction with a temperature ratio $T_R = 1.17$: this temperature ratio is typical for AC systems in automobiles. In those experiments, the bulk velocities of the two streams were equal, while the bulk Reynolds number of the crossflow was $Re_\mathrm{b} = 15,000$. In our simulations, we kept the same Re_b and studied cases with various temperature ratios while keeping the bulk-velocity ratio equal to unity.

Herein we present results for $T_R = 1.17$ (the same as in the experiments) and for $T_R = 2.0$.

4.2.1 Governing equations and computational algorithm

The governing system of equations for the flows of interest is the filtered version of the low-Mach number approximation for the compressible Navier-Stokes-Fourier equations that are given in (2.40) - (2.42). It is important to mention that, in the cases presented herein, temperature variations are significant and, therefore, inertial effects due to density differences are no longer negligible. For this reason, we do not invoke the Boussinesq approximation.

For non-dimensionalisation purposes, we have chosen the bulk velocity of the crossflow U_c as the reference velocity, and the half-width of the horizontal channel δ as the reference length. Also, the non-dimensionalisation of all thermodynamic variables and transport coefficients has been performed with respect to the thermodynamic state of the fluid at the crossflow stream. Accordingly, the temperature of the crossflow T_c serves as the reference temperature. Let T_jet be the temperature of the incoming jet. Then, the temperature ratio between the two streams is given by $T_R = T_\mathrm{jet}/T_\mathrm{c}$.

In our work the fluid is assumed to be a calorically perfect gas. Therefore, c_p is constant and its non-dimensional value equals unity. Moreover, the temperature and density are related via the perfect-gas equation of state which reads, in non-dimensional form,

$$p^0 \;=\; \bar{\rho}\tilde{T}\,, \tag{4.1}$$

with p^0 being the thermodynamic pressure. In our study we examine flows in open domains, so that p^0 is constant and equal to the ambient pressure. Further, μ and κ stand for the fluid viscosity and thermal conductivity, respectively. They are both assumed to satisfy a Sutherland-type power law which in non-dimensional form reads [42],

$$\mu \;=\; \kappa \;=\; \tilde{T}^{\,0.7}. \tag{4.2}$$

Based on the aforementioned reference quantities, the Reynolds number in our simulations is equal $Re = 7,500$. This value corresponds to a *bulk* Reynolds number of the crossflow $Re_\mathrm{b} = 15,000$, which is the same as in the experiments in [11]. Also, in accordance with those experiments, the Prandtl number is $Pr = 0.71$.

T_R	1.17	2
M_R	2.34	4
ρ_{jet}	0.85	0.50
μ_{jet}	1.11	1.62
U_{jet}	1.0	1.0
Re_{jet}	2781	1157

Table 4.1: Physical parameters for the incoming jet in the two cases considered herein. The Reynolds number, Re_{jet}, is based on the bulk velocity of the jet U_{jet}, the half-width of the vertical channel δ, and the kinematic viscosity at the inflow of the incoming jet μ_{jet}.

Finally, the Richardson number, defined herein as $Ri = g\delta/U_{\text{c}}^2$ with g being the gravitational acceleration, is set to $Ri = 0.023$.

Since the fluid density and transport coefficients are temperature dependent, both the Reynolds number Re_{jet} and the momentum flux of the incoming jet differ in the two cases that we study. Following standard convention, the momentum flux of a stream is defined as $\rho U_{\text{b}}^2 A$ with U_{b} and A being the bulk velocity and cross-section area, respectively. Accordingly, the momentum ratio M_R between the momentum flux of the crossflow and the incoming jet also changes with the temperature ratio T_R. In table 4.1 we present the values of the parameters related to the incoming jet for the two cases considered herein. Based on these data, the incoming jet is turbulent for $T_R = 1.17$, whereas it is laminar for $T_R = 2.0$. Further, we observe that M_R becomes significantly higher when the temperature ratio T_R changes value from 1.17 to 2.0.

For the numerical solution of the governing system of (2.40) - (2.42) we employ the time-accurate algorithm of Lessani and Papalexandris [42] described in chapter 2. In addition, we use a variable time-step with the Courant number being smaller than unity.

4.2.2 Numerical setup

An illustration of the flow domain is shown in figure 4.1. In this chapter we follow the convention adopted in chapter 3 and is described in section 3.2.2. As regards the flow configuration, the cold fluid enters the computational domain from the inflow boundary of the horizontal channel while the hot jet enters from the smaller vertical channel, as depicted in figure 4.1. The two streams interact and start to mix downstream the entry of the jet. The combined stream exits the computational domain from the outflow boundary of the horizontal channel.

Further, the dimensions of the computational domain are kept the same with those described in section 3.2.2.

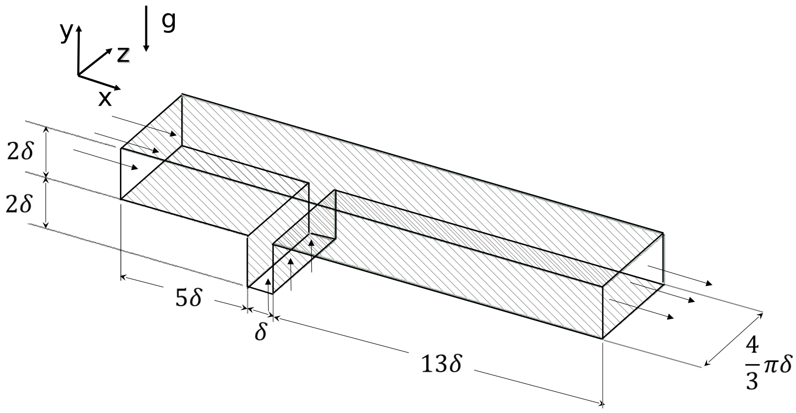

Figure 4.1: Illustration of the computational domain.

With regard to the discretization of the computational domain, initially, we have performed simulations in the grid described in section 3.2.2. However, as it turned out, that grid was not sufficiently fine for flows with thermal gradients because it yielded under-resolved peaks of the rms profiles in certain locations. Accordingly, we started refining the grid until we got sufficiently smooth and well-resolved rms profiles with a grid consisting of approximately 4.5×10^6. In particular, we have increased the number of nodes in the y-direction, from 192 to 300. In addition, we have used 400 nodes in the streamwise direction instead of 340. An overview of the discretization of the computational domain is provided in table 4.2.

Section	1	2	3
Extent	$-6 < x < -1$ $0 < y < 2$	$-1 < x < 0$ $-2 < y < 0$	$-1 < x < 13$ $0 < y < 2$
Number of cells	$60 \times 150 \times 64$	$64 \times 150 \times 64$	$276 \times 150 \times 64$

Table 4.2: Overview of the discretization of the computational domain.

In figure 4.2 we present plots of Δx^+, Δz^+ and $y_{\mathrm{f.n}}$ at the bottom wall of the horizontal channel for the case $T_R = 1.17$, with $y_{\mathrm{f.n}}$ being the wall-normalised distance of the first node in the wall-normal direction. It is important to mention that u_τ varies along the x-direction because μ and ρ are temperature dependent

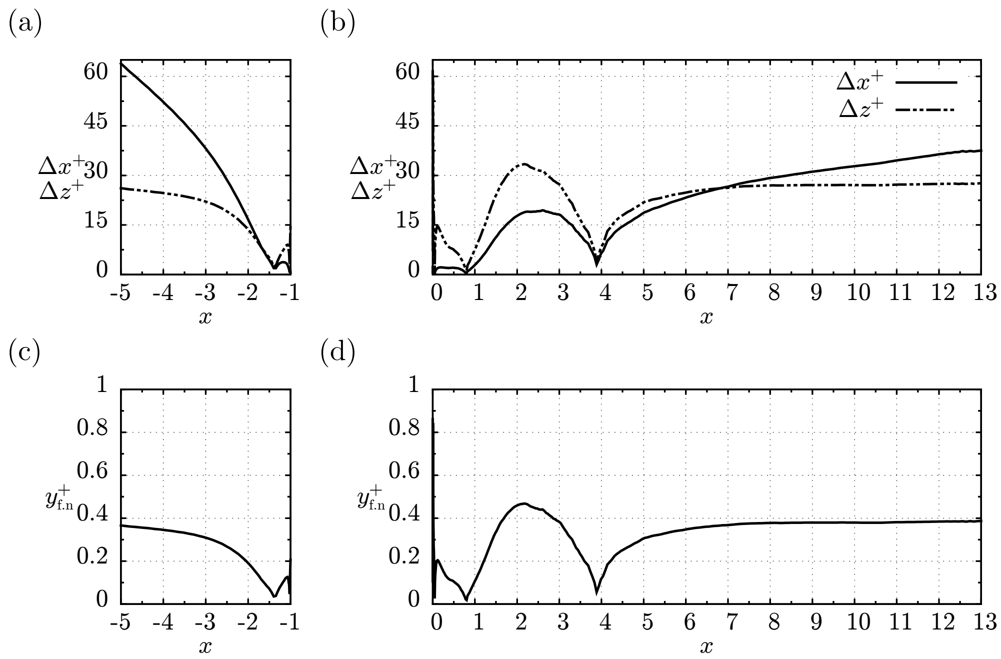

Figure 4.2: Presentation of the grid spacing in wall units at the bottom wall of the horizontal channel, at $y = 0.0$. (a) Δx^+ and Δz^+ upstream the entry of the jet, (b) Δx^+ and Δz^+ downstream the entry of the jet, (c) $y^+_{\mathrm{f.n}}$ upstream the entry of the jet, (d) $y^+_{\mathrm{f.n}}$ downstream the entry of the jet.

and because τ_w also varies with x. As shown in figure 4.2a, the values of both Δx^+ and Δz^+ upstream the entry of the jet are well below the limits recommended in Zang [75]. According to these guidelines, the wall-normalised streamwise spacing Δx^+ should be smaller than 80, $\Delta x^+ < 80$, while the spanwise spacing Δz^+ smaller than 30, $\Delta z^+ < 30$. Similarly, the first node in the wall-normal direction always satisfies the requirement $0 < y^+ < 1$; in fact, its value is always below 0.4.

The values of Δx^+ and Δz^+ at the bottom wall downstream the entry of the jet are shown in figure 4.2b. The streamwise spacing, Δx^+, satisfies the recommendation of Zang throughout the domain. Its maximum value is approximately 38, close to the outflow plane. As for the spanwise spacing, Δz^+, it satisfied the recommendation everywhere, except for a small region defined by $1.7 < x < 2.7$. In this region Δz^+ becomes slightly larger than 30, with a peak of approximately 33 at $x = 2.1$. Nonetheless, according to the guidelines of Piomelli and Chasnov [95] for wall bounded flows, Δz^+ can be as high as 40. Consequently, the grid spacing in the homogeneous direction is deemed adequate for the purposes of our study. As for the first node in the wall-normal direction, $y^+_{\mathrm{f.n}}$ is substantially lower than unity at all points downstream the entry of the jet. More specifically, it is everywhere lower than 0.5, even in the region $0 < x < 4$ where the flow is computationally most demanding.

4.2.3 Implementation of boundary conditions

With regard to the implementation of boundary conditions, we employ two auxiliary simulations for the generation of turbulent inflow data while the convective boundary condition described in equation (2.48) is used for the outflow plane. With respect to the temperature field, uniform temperature profiles are prescribed at the two inflows while the convective boundary condition is employed at the outflow. Further, in order to match the experiments in [11], the walls are considered adiabatic, *i.e.* $\nabla T \cdot \boldsymbol{n} = 0$, with $\boldsymbol{n}$ being the outward normal vector at a surface.

4.3 Discussion of the numerical results

In this section we present and analyse our numerical results for two different temperature ratios between the incoming jet and the crossflow, namely $T_R = 1.17$ and $T_R = 2.0$. In particular, we discuss the main features of the flow and elaborate on the effect of T_R on the emerging patterns of the flow field.

As regards the presentation of our results, we adopt the following standard notation. The mean of a generic quantity ϕ is denoted by $<\phi>$ and refers to averaging both in time and in the homogeneous spanwise direction. The fluctuating component of ϕ is denoted by ϕ'. Also, ϕ_{rms} stands for the root mean square (rms) value of ϕ', *i.e.* $\phi_{\text{rms}} =< \phi'\phi' >^{1/2}$. In the presentation of results, and without loss of clarity, we omit the tilde from the symbols representing Favre-filtered quantities.

The simulations are initialized by injecting hot fluid from the vertical channel to the cold crossflow. To ensure that the flow has reached the statistical steady state we follow the approach described in section 3.3. Once statistical stationarity is confirmed, we collect statistics of the flow quantities for 100 time units.

The main characteristics of the flow can be identified in figure 4.3 which shows streamlines extracted from the mean velocity field superposed by contour plots of the mean temperature $<T>$. According to this figure, due to the presence of the incoming jet, the crossflow tilts upwards and its cross-section area decreases. This results to a Venturi effect, *i.e.* the crossflow accelerates as it passes over the incoming jet. Reciprocally, as soon as the jet enters the horizontal channel, it starts to turn and changes direction until it gets aligned with the direction of the

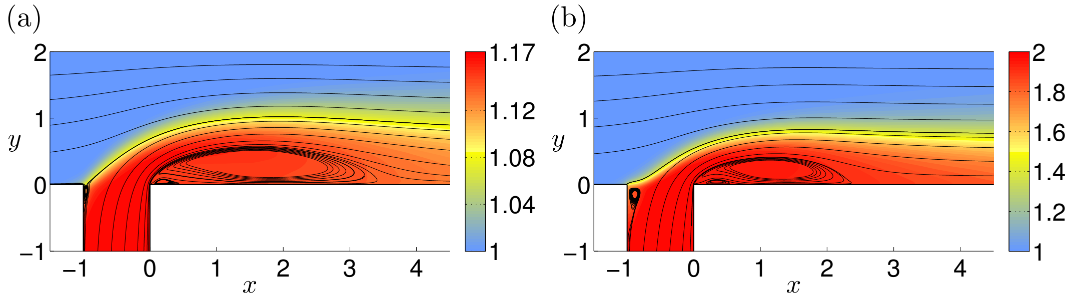

Figure 4.3: Main flow features in the neighbourhood of the entry of the jet. This figure shows streamlines extracted from the mean velocity field superposed by contour plots of the mean temperature field $<T>$. In this figure we show 4 streamlines emerging from the left entry of the horizontal channel. The distance between those is 0.4. In a similar manner, we show 4 streamlines emerging from the bottom entry of the vertical channel with the distance between those being 0.2. We also show streamlines downstream the entry of the jet in order to visualise the large recirculation bubble in this region. Additional streamlines are visualised close to the two corners of the entry of the jet. (a) $T_R = 1.17$, (b) $T_R = 2.0$.

crossflow. The presence of the jet results in the formation of a large recirculation bubble just downstream the entry of the jet. Then, as the jet passes between the recirculation bubble and the crossflow, its cross-section area decreases, resulting in a second Venturi effect in the flow.

Also, figure 4.3 helps to identify two shear layers that emerge in the flow field. The first one is formed between the crossflow and the incoming jet. Its origin lies close to the upstream corner of the entry of the jet. It spans the entire computational domain downstream the entry of the jet and provides the principal mechanism for mixing between the two streams. Henceforth, it will be referred to as the *primary* shear layer. In the region just above the entry of the jet, this layer is subject to a flapping motion which, according to Hirota et al. [11], is induced by the fluctuations of the streamwise velocities of the two interacting streams. The primary shear layer rolls up fairly quickly, and entrains significant amounts of fluid originating from the cold crossflow. The second shear layer is formed between the jet and the recirculation bubble and can reach up to the reattachment point of the flow beyond the recirculation bubble. Henceforth, it will be referred to as the *secondary* shear layer.

In figure 4.3, we can also observe a smaller recirculation zone that is located between the incoming jet and the bubble. This feature was first identified in chapter 3 where we studied isothermal turbulent flows in T-junctions. Further, we note the formation of an additional recirculation region, located in the vicinity of the upstream corner of the entry of the jet.

All of these features are common in both cases, irrespective of the temperature ratio between the two streams. However, the details of these features do depend on T_R. For example, in the case of low temperature ratio, $T_R = 1.17$, the incoming jet goes higher in the y-direction. By contrast, in the case of $T_R = 2.0$ the incoming jet turns rapidly and aligns with the crossflow much faster, which results in a significantly smaller recirculation bubble. These differences are attributed to the fact that an increase of T_R implies a decrease of the momentum flux of the incoming jet; see table 4.1.

Further, upon a close examination of the flow field in the vicinity of the upstream corner of the entry of the jet, shown in figure 4.4, we can observe significant differences between the recirculation regions mentioned above.

In particular, for the case with small temperature ratios $T_R = 1.17$, we can identify the formation of two vortical structures. The first one consists of a thin vortex right before the entry of the jet, very close to the horizontal wall. The second one is a larger roller inside the vertical channel. Based on the streamlines and the contour plots of the pressure field shown in figure 4.4a, we infer that both vortices are formed by fluid coming from the crossflow. As regards the thin vortex close to the horizontal wall, we remark that the incoming jet produces a strong adverse pressure gradient in the vicinity of the upstream corner of the entry of the jet. This causes the separation of the crossflow near the wall which, in turn, results in the formation of this thin structure. This vortex is equivalent to the *horseshoe* vortex that is observed in jets in unconfined crossflows; see, for example, [82] and [79], as well as in chapter 3. It should be noted, however, that in the flows considered herein, a horseshoe vortex cannot be developed because the incoming jet extends over the entire span of the computational domain (in the z-direction).

As regards the second vortex, it results from entrainment of crossflow fluid inside the vertical channel. More specifically, owing to the adverse pressure gradient that is developed in the vertical channel, gas from the crossflow enters this channel and forms the aforementioned vortex. A similar structure was described in [79] in which the authors presented experiments of jets in unconfined crossflows. These authors observed that, for bulk-velocity ratios (jet over crossflow) lower than 2.3, a vortex is formed just outside the vertical channel and called it “hovering vortex”. This observation was subsequently confirmed by both experimental and numerical studies; see, for example, [78] and [96]. In our case the bulk-velocity ratio is unity, which is substantially below the reported threshold of 2.3 and, furthermore, this

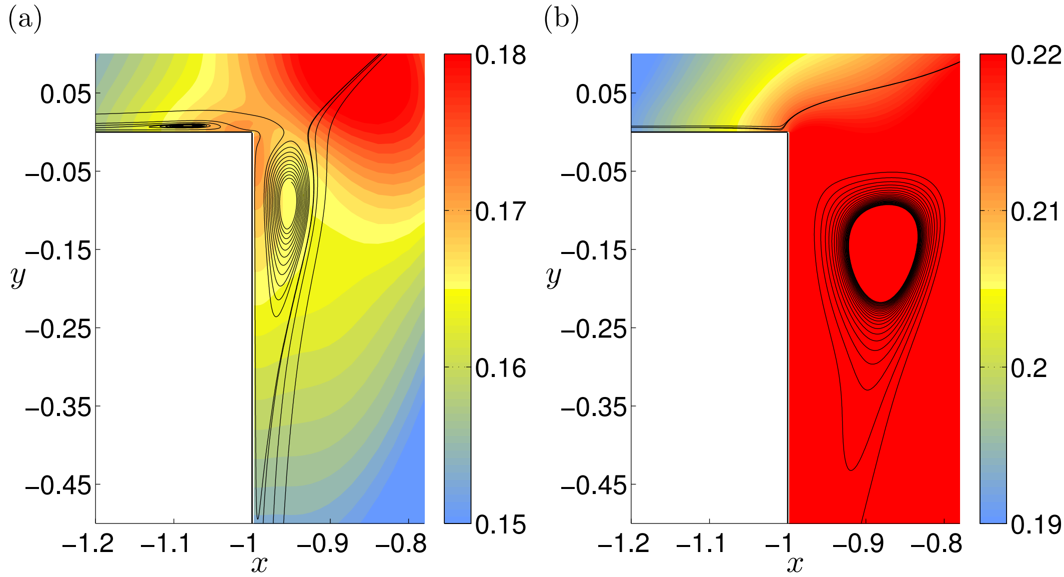

Figure 4.4: Recirculation zones in the the vicinity of the upstream corner of the entry of the jet. The figures show streamlines extracted from the mean velocity field and plots of the mean pressure field $<p>$. (a) $T_R = 1.17$, (b) $T_R = 2.0$.

structure is formed inside the vertical channel, *i.e.* below the entry of the jet. The different location of the hovering vortex in our case may be due to the significantly lower bulk-velocity ratio.

On the other hand, in the case of high temperature ratio $T_R = 2.0$, the flow field in the vicinity of the upstream corner is considerably different. In particular, due to the reduced mass density, the momentum flux of the incoming jet is significantly decreased. As a result, the crossflow changes direction only slightly and does not separate; see figure 4.4b. Further, it does not enter the vertical channel because the adverse pressure gradient due to the incoming jet is not strong enough. Reciprocally, the jet changes direction rapidly upon entrance in the horizontal channel, which results in the formation of the recirculation bubble (roller) shown in figure 4.4b. Moreover, the boundary layer at the vertical wall is laminar and, therefore, much more susceptible to separation than the turbulent boundary layer of the previous case. Consequently, the roller just below the entry of the jet contains fluid from the jet and not from the crossflow as in the previous case. This is due to the combined effect of high momentum ratio and laminarity of the boundary layer at the vertical wall. This structure was also predicted in the LES simulations of jet-in-crossflow reported in [97]. In that study the authors considered a case with turbulent incoming jet and a momentum ratio that was two orders of magnitude

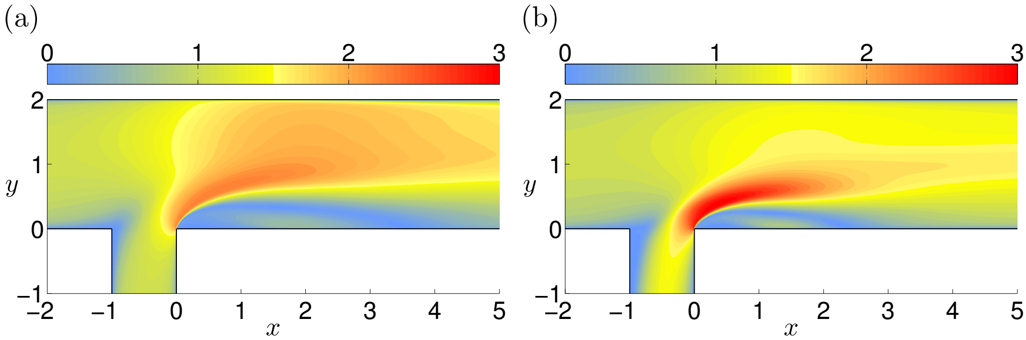

Figure 4.5: Contour plots of the amplitude of the in-plane mean velocity field, $u_a = \sqrt{<u>^2 + <v>^2}$. (a) $T_R = 1.17$, (b) $T_R = 2.0$.

higher than the ones considered herein.

It should be noted that the observations made herein are based on the examination of streamlines extracted from the averaged velocity vector field. However, in order to obtain a more comprehensive picture on the mixing process in this region, additional and more advanced diagnostic tools should be used. For example, one can introduce a passive and artificial tracer, C, that will enable us to quantify the proportions of crossflow and jet fluid in this region. The concentration of the tracing quantity C is defined by an advection-diffusion equation, similar to the one for the temperature given in (2.42) and, therefore, no new equation needs to be solved.

Finally, an additional difference between the two cases concerns the acceleration of the two streams due to the Venturi effect mentioned above. This can be verified upon inspection of figure 4.5 which shows contour plots of the amplitude of the in-plane mean-velocity field $u_a = \sqrt{<u>^2 + <v>^2}$ for both cases under study. To be more specific, we see that the acceleration of the incoming jet increases as the temperature ratio T_R increases. This is also ascribed to the reduced momentum flux of the incoming jet as its temperature increases, but it is further amplified by thermal stratification. On the other hand, the acceleration of the crossflow due to the Venturi effect has the opposite trend, *i.e.* it decreases as T_R increases. The reason for this is the following. As mentioned above, the incoming jet changes direction faster as the temperature ratio increases. This, in turn, implies smaller decrease of the section area of the crossflow and, therefore, smaller acceleration.

4.3.1 Statistics of the temperature field

In this section we present the first and second-order statistics of the temperature field and make comparisons with the experimental data from [11]. The results are presented in terms of the normalised temperature θ, given by

$$\theta = \frac{T - T_\mathrm{c}}{T_\mathrm{jet} - T_\mathrm{c}} \,. \tag{4.3}$$

Figure 4.6 shows profiles of the mean normalised temperature $<\theta>$ for both temperature ratios and at six different streamwise stations of interest. More specifically, figures 4.6a and 4.6b show the profiles of $<\theta>$ at $x = -0.5$ and $x = 0.0$. These stations correspond to the centre and the downstream corner of the entry of the jet, respectively. The main feature of these profiles is the transition zone from the hot to the cold temperature. This transition takes place across the primary shear layer, *i.e.* the one that emanates from the vicinity of the upstream corner of the entry of the jet. Also, based on the thickness of this layer, we can infer that the thermal mixing between the two streams at $x = -0.5$ and $x = 0.0$ is still quite limited. It is also worth mentioning that the profiles for the two different cases are fairly similar. The only noticeable difference is the wall-normal location of the primary shear layer. This difference is due to the different trajectories of this layer in the two cases under study. In particular, for $T_R = 2.0$ it is always positioned lower than the one for $T_R = 1.17$ at all streamwise stations. This is because, as mentioned above, the incoming jet for $T_R = 2.0$ turns faster due to lower momentum flux.

Figures 4.6a and 4.6b also show the experimental data from [11] for the case $T_R = 1.17$. We can readily observe that our numerical predictions agree quite well with the experimental measurements at both streamwise stations. More specifically, our simulations capture accurately the temperature profile, the location and thickness of the primary shear layer and the near-wall temperature gradients.

The plots in figures 4.6c and 4.6d depict the profiles of $<\theta>$ at $x = 0.5$ and $x = 1.0$, respectively. These stations are located at the large recirculation bubble. In both cases, the thickness of the primary shear layer has only moderately increased. Also, according to our predictions, the temperature inside the bubble is almost uniform and slightly lower than the temperature of the incoming jet. Further, we observe another zone of temperature gradients just above the large recirculation bubble, in the interval $0.3 < y < 0.5$. It corresponds to the secondary shear layer, *i.e.* the one that emanates from the downstream corner of the entry of jet.

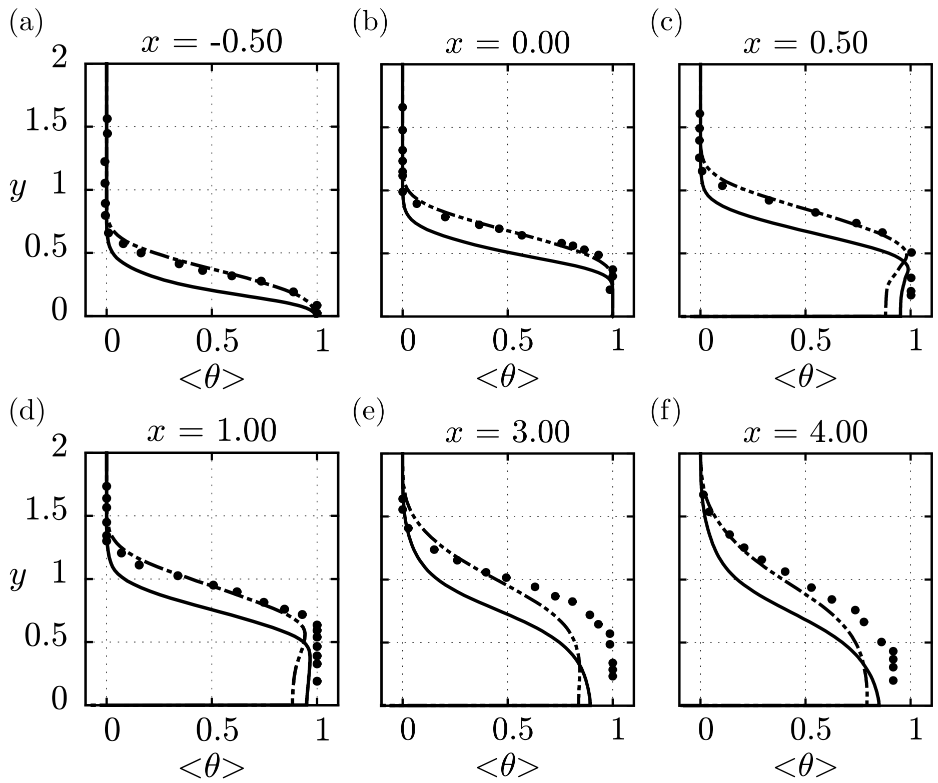

Figure 4.6: Profiles of the mean normalised temperature <θ>. ----, $T_R = 1.17$; —, $T_R = 2.0$; •, experimental data from [11] for $T_R = 1.17$.

According to our simulations, this layer is much thinner than the primary one and the temperature gradients in its interior are smaller. Based on these facts, we conclude that the secondary shear layer does not contribute significantly to the thermal mixing in the flow field.

As regards comparisons with experiments, we infer from figures 4.6c and 4.6d that our numerical predictions at $x = 0.5$ and $x = 1.0$ agree well with the experimental data from [11], especially as regards the location and thickness of the primary shear layer and the temperature distribution across it. On the other hand, the experimental measurements do not capture the temperature variations across the secondary shear layer; instead the temperature of the bubble was measured to be equal to the one of the incoming jet.

Finally, figures 4.6e and 4.6f show profiles of <θ> at the region of the reattachment of the flow and, more specifically, at $x = 3.0$ and $x = 4.0$. The profiles for the two cases are again fairly similar. The primary shear layer has spread considerably and spans more than a unit length, *i.e.* a half-width of the horizontal channel. This implies that the thermal mixing at these stations has become quite significant. Also, according to our simulations, the top-wall temperature remains constant and equal to the one of the crossflow T_c. On the other hand, the bottom-wall temperature is below the one of the incoming jet, T_{jet}, and decreases along the streamwise direction due to thermal mixing. We further note that, as regards the top-wall temperature and the location and thickness of the primary shear layer, our predictions agree well with the experimental data from [11].

However, there is a discrepancy in the bottom-wall region. More specifically, according to those measurements, the temperature decrease at the bottom wall is milder than the one predicted by our simulations. One could attribute it to numerical artefacts or grid resolution effects. However, this discrepancy occurs in a near-wall region where our LES are wall-resolved and use very fine meshing in these regions. Further, if the discrepancy was due to grid resolution only, then we would expect to observe even larger discrepancies in the centerline of the horizontal channel ($y = 1$) because therein our grid is coarser. But this is not the case. For this reason, we think that this discrepancy cannot be attributed solely to grid resolution.

Another factor that contributes to this discrepancy is the difference between the experimental and numerical set-ups. The measurements in [11] are taken at the symmetry plane of a rectangular duct, whereas our computational domain is periodic in the spanwise direction and the computed profiles shown herein have been averaged along this direction. Further, this discrepancy can be attributed, at least partially, to experimental uncertainties. This would not be surprising because the measurements in [11] show that inside the recirculation bubble the temperature field remains constant and equal to the temperature of the hot incoming jet. In other words, according to those measurements, the fluid inside the recirculation bubble originates from the incoming jet only. In view of the intense mixing that takes place between the two streams, we cannot find any physical justification for this; moreover, the authors of [11] did not provide a justification either.

For completion purposes, we provide profiles of $<\theta>$ at stations further downstream, *i.e.* closer to the outflow boundary of the computational domain. In particular, figures 4.7, show the profiles of $<\theta>$ at $x = 5.0$, 8.0, and 11.0. Experimental measurements at these streamwise stations are not available.

Based on these profiles, we infer that the primary shear layer has diffused substantially at these stations. For example, for $T_R = 1.17$ and at $x = 11.0$, the temperature profile across the channel has become almost linear. We also remark that, as a result of the thermal mixing between the crossflow and the incoming jet, the bottom-wall temperature continues to decrease with x. In particular, $<\theta>$ is

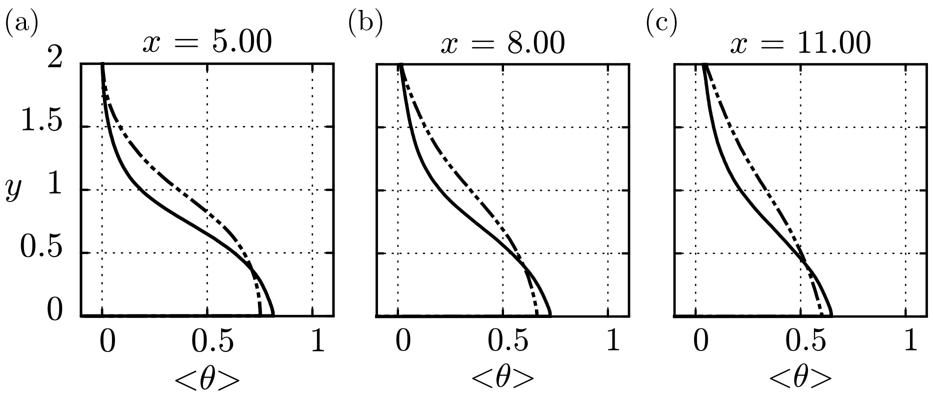

Figure 4.7: Profiles of the mean normalised temperature $<\theta>$ at stations further downstream. ----, $T_R = 1.17$; —, $T_R = 2.0$.

approximately equal to 0.6 for both cases at $x = 11$. We further note that the top-wall temperature is no longer constant but it increases with x, albeit very slowly. More specifically, a slight increase of θ at the top wall can be observed in figure 4.7c for $x = 11.0$. This is because the incoming jet changes direction and turns without ever reaching the top wall. As a result, thermal mixing in the top wall occurs only downstream where the primary shear layer has sufficiently spread.

Next we present results for the second-order statistics of the temperature field. The profiles of θ_{rms} at six different streamwise stations are provided in figure 4.8. According to it, these profiles exhibit the same trends for both cases considered in our study. For example, they both have a strong peak that coincides with the centerline of the primary shear layer. Evidently, the value of this peak progressively decreases as thermal mixing is enhanced along the x-direction. Nevertheless, there are also some differences between the profiles for the two cases. For example, the peak of θ_{rms} for $T_R = 2.0$ is located lower than for $T_R = 1.17$. This is because the momentum flux of the incoming jet at $T_R = 2.0$ is smaller, so that the jet changes direction and turns faster once it enters the horizontal channel. In addition the profiles for $T_R = 2.0$ are skewed in the lower half of the channel. Further, at the top half of the channel, the values of θ_{rms} are higher for $T_R = 1.17$.

4.3.2 Statistics of the velocity field

In this section we present the first and second-order statistics of the velocity field, starting with the properties of the mean streamwise velocity $<u>$. In figure 4.9 we show the profiles of $<u>$ for both cases under study at six streamwise stations downstream the entry of the jet.

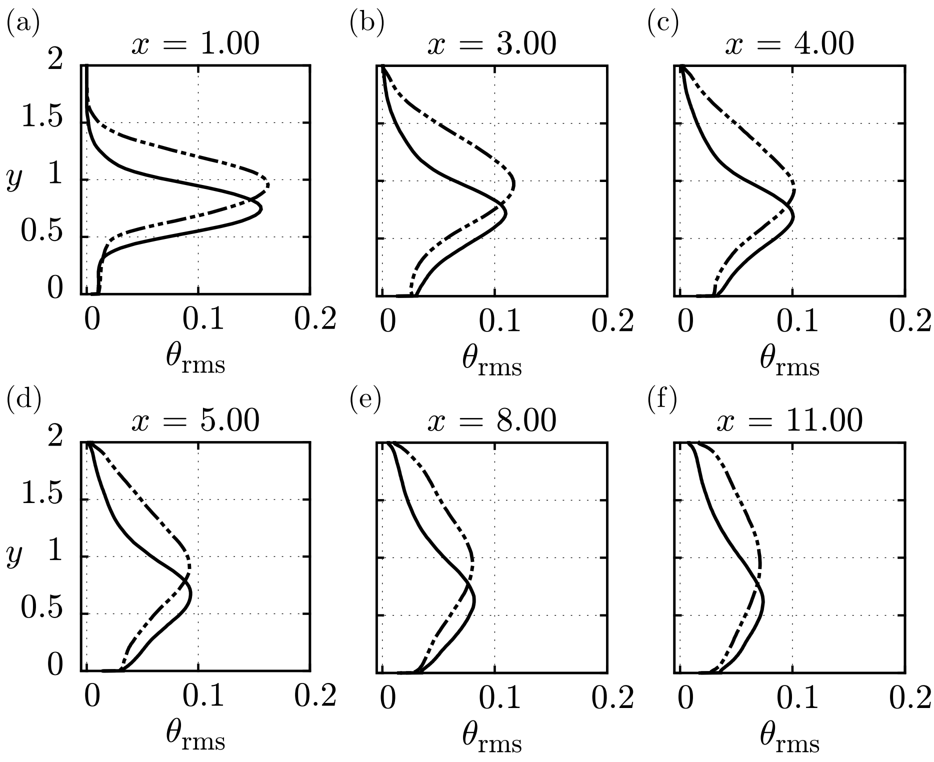

Figure 4.8: Profiles of the rms of the normalised temperature, θ_{rms}. ----, $T_R = 1.17$; —, $T_R = 2.0$.

For $x = 1.0$, the velocity at the upper part of the channel, which is occupied by the crossflow, is almost constant and considerably higher than the inflow velocity. This is a manifestation of the acceleration due to the Venturi effect that is experienced by the crossflow. We also note that $<u>$ is higher for $T_R = 1.17$, in accordance with our earlier remark that the Venturi effect gets stronger as T_R decreases. Below the crossflow, in the region occupied of the jet, $<u>$ is also high due to the Venturi effect on the jet. However, the velocities are higher when $T_R = 2.0$ because, as explained above, the reduction of the cross-section area of the jet becomes more pronounced as T_R increases. We also remark that the wall-normal gradients of $<u>$ in this region are significant due to the presence of the primary and secondary shear layers. Further below, in the region occupied by the large recirculation bubble, the wall-normal gradients are significant too. Eventually, the velocities become negative in the near-wall region.

The profiles of $<u>$ at $x = 3.0$ are plotted in figure 4.9b. In the case of $T_R = 1.17$ the flow has not yet reattached, which can be confirmed by the negative values of $<u>$ near the bottom wall. As a result, the characteristics of the profile for $T_R = 1.17$ are the same as in the previous station. On the other hand, for

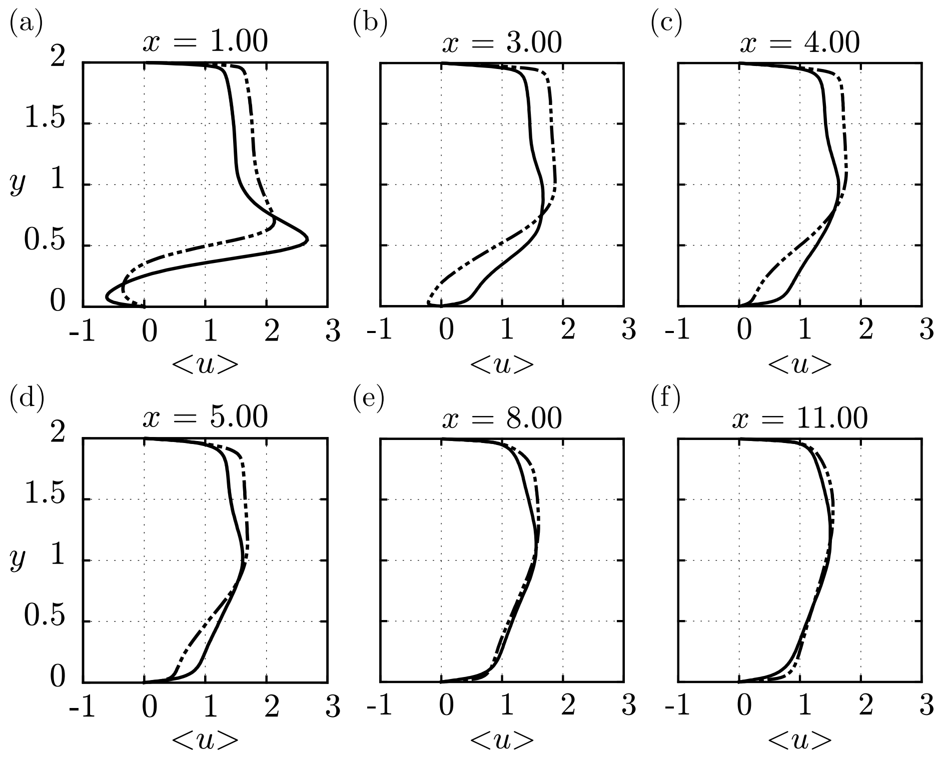

Figure 4.9: Profiles of the mean streamwise velocity $<u>$ at different locations of the horizontal channel. ----, $T_R = 1.17$; —, $T_R = 2$.

$T_R = 2.0$ the flow has already been reattached, the reattachement point being at $x = 2.63$. (In our study the reattachment point is identified as the first-node point where the streamwise velocity changes sign). Downstream this point, the jet expands towards the bottom wall, which leads to lower velocities and milder wall-normal velocity gradients. It is also worth noting that the peak of $<u>$ is shifted upwards and its value is smaller than in the previous station; these features are attributed to the spreading of the primary shear layer.

The station $x = 4.0$ coincides with the reattachment point for the case with $T_R = 1.17$; see figure 4.9c. Besides the fact that the velocities near the bottom wall are no longer negative, the profile of $<u>$ at this station is very similar to the one at the previous station. As regards the profile for $T_R = 2.0$, it is also very similar to the one at the previous station too. The only noticeable difference is the higher location of the peak of $<u>$. Finally, further downstream, the primary shear layer spreads even more and extends over the entire width of the channel. As a result, the profiles of $<u>$ for the two cases become increasingly similar; see, for example the profiles at $x = 11.0$ shown in figure 4.9f.

We proceed to examine in more detail the near-wall profiles of $<u>$ for the two cases under study. For this purpose, it is convenient to express y and $<u>$ in wall units, y^+ and u^+, with $u^+ = \frac{<u>}{u_\tau}$. Since we are concerned with variable-density flows, we apply the Van Driest transformation to the velocity profiles, [98],

$$u^+_{\mathrm{VD}} = \int_0^{u^+} \left(\frac{\rho}{\rho_{\mathrm{w}}}\right)^{0.5} \mathrm{d}u^+, \tag{4.4}$$

with ρ_{w} being the density at the wall. This transformation is quite common in the study of variable-density flows [61, 99] because it enables comparisons of velocity profiles with the universal law of the wall,

$$u^+ = \begin{cases} y^+ \,, & y^+ \leqslant 10 \,, \\ \frac{1}{0.4} \log y^+ + 5 \,, & y^+ > 10 \,. \end{cases} \tag{4.5}$$

In figure 4.10 we present the profiles of u^+_{VD} near the bottom wall at two streamwise stations downstream the recirculation bubble, $x = 8.0$ and $x = 11.0$. The profiles for $T_R = 1.17$ are juxtaposed with the universal law of the wall in figure 4.10a. We readily infer that the values of u^+_{VD} deviate from the law of the wall for $y^+ > 10$ at both stations. Furthermore, they exhibit an inflection point at $y^+ \approx 200$. This is due to the adverse pressure gradient that is developed downstream the reattachment point of the flow [84]. It is also worth mentioning that the profiles of u^+_{VD} shown in this figure are similar to the u^+ profiles for isothermal flows in T-junctions that are provided in chapter 3.

The wall-normalised velocity profiles for $T_R = 2.0$ are presented in figure 4.10b. We observe that they also deviate from the universal law of the wall in the logarithmic region and possess an inflection point therein. However, they have some differences with the profiles for $T_R = 1.17$. For example, they have characteristically higher values in the logarithmic region. Also, the change in the curvature of the profiles at the inflection points is milder, especially at the downstream station $x = 11.0$. This is attributed to the smaller size of the recirculation bubble for $T_R = 2.0$, see figure 4.3. Indeed, a smaller bubble implies a smaller expansion of the jet downstream the reattachment point, hence a weaker adverse pressure gradient.

Profiles of u^+_{VD} near the top wall at two streamwise stations, $x = 1.0$ and $x = 8.0$, are plotted in figure 4.11. We remark that for $T_R = 1.17$ and $x = 1.0$, the growth of u^+_{VD} for $y^+ > 30$ is much smaller than the one predicted by the law of the wall, see figure 4.11a. This deviation arises from the favourable pressure

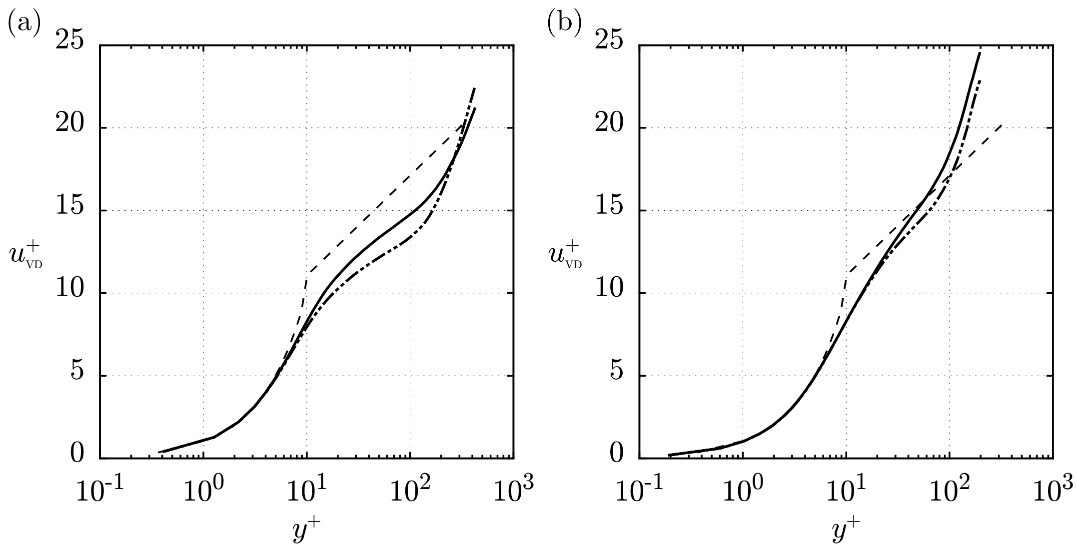

Figure 4.10: Profiles of the wall-normalised velocity u^+_{VD} at the bottom wall. (a) $T_R = 1.17$, (b) $T_R = 2.0$. ----, law of the wall; -··-, $x = 8.0$; —, $x = 11.0$. The value of $\kappa = 0.4$ for the law of the wall at the logarithmic region is chosen so as to achieve the best fit with the velocity profiles.

gradient that is developed due to the Venturi effect on the crossflow; see also the discussion in [86]. On the other hand, sufficiently downstream the reattachment of the flow, $x = 8.0$, the logarithmic profile at the top wall is reestablished.

Interestingly, for $T_R = 2.0$, the profile at $x = 1.0$ is nearly identical to the one for $T_R = 1.17$, and exhibits the same deviation from the law of the wall due to the Venturi effect; see figure 4.11b. Further, for this temperature ratio, the profile of u^+_{VD} at $x = 8.0$ deviates from the law of the wall by almost two wall units in the logarithmic region. According to the authors of [92], who performed simulations of turbulent heat transfer in a channel, this offset is attributed to the effects of density variations which are not fully taken into account by the introduction of the Van Driest transformation.

Next, we examine the properties of the second-order velocity statistics of the flow. Profiles of the rms of the streamwise velocity component, u_{rms}, are plotted in figure 4.12. At $x = 1.0$, the velocity fluctuations at the upper part of the channel are quite small for both temperature ratios. This is a direct consequence of the acceleration of the crossflow due to the Venturi effect. However, at the lower part of the channel, the fluctuations increase substantially because of the primary and secondary shear layers. Actually, at this region, the profiles of u_{rms} exhibit two peaks. The upper peak corresponds to the primary layer and the lower peak corresponds to the secondary layer. We observe that the amplitude of the upper

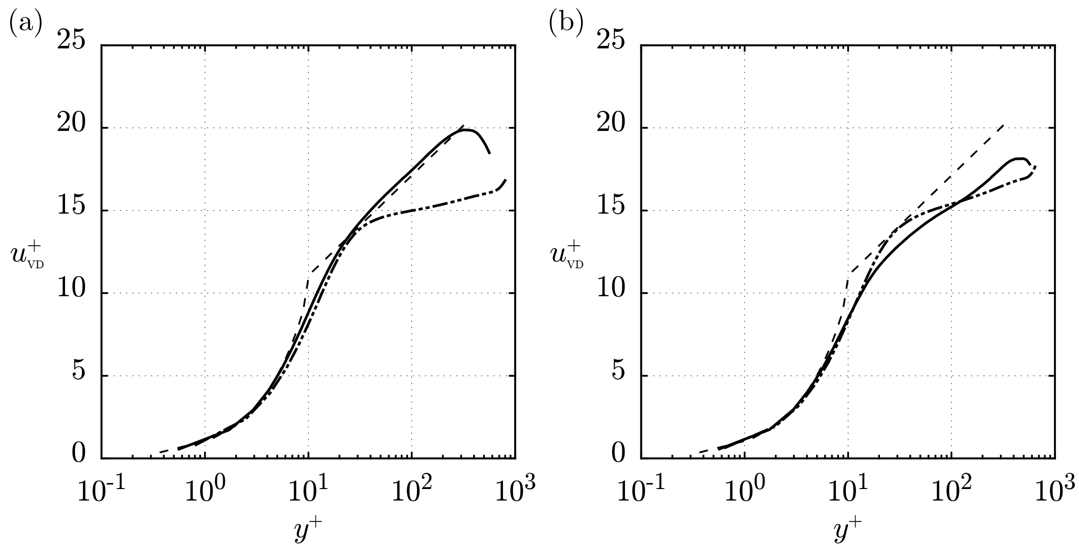

Figure 4.11: Profiles of the wall-normalised velocity u^+_{VD} at the top wall. (a) $T_R = 1.17$, (b) $T_R = 2.0$. ----, law of the wall; ---·-, $x = 1.0$; ——, $x = 8.0$. The value of $\kappa = 0.4$ for the law of the wall at the logarithmic region is chosen so as to achieve the best fit with the velocity profiles.

peak is substantially higher for $T_R = 2.0$; this is due to higher shear rate across the primary layer and stronger stratification effects. We further remark that, based on the u_{rms} profiles at $x = 1.0$, the turbulent intensity is much higher for $T_R = 2.0$.

It is important to mention that this double peak in the profile of the velocity fluctuations has not been observed in chapter 3 where we studied isothermal flows in T-junctions. In other words, this feature is due to the effect of the temperature as an active scalar. Further, this feature implies that the mixing induced by the primary shear layer is enhanced when the crossflow and the incoming jet are not at the same temperature.

The double-peak structure can also be observed at the profiles for $x = 3.0$ shown in figure 4.12b. However, the peak amplitudes have decreased due to the spreading of the shear layers. Also, for $T_R = 2.0$, and based on the u_{rms} profiles at stations downstream, the fluctuations due to the primary shear layer persist at long distances. This is a consequence of the strong stratification effects for this temperature ratio. On the other hand, for $T_R = 1.17$, the peak of u_{rms} due to the secondary shear layer eventually vanishes. In other words, the secondary layer eventually diffuses. At the same time, the velocity fluctuations become more prevalent near the symmetry plane of the channel due to the primary shear layer that spreads substantially downstream the recirculation bubble. Nonetheless, the

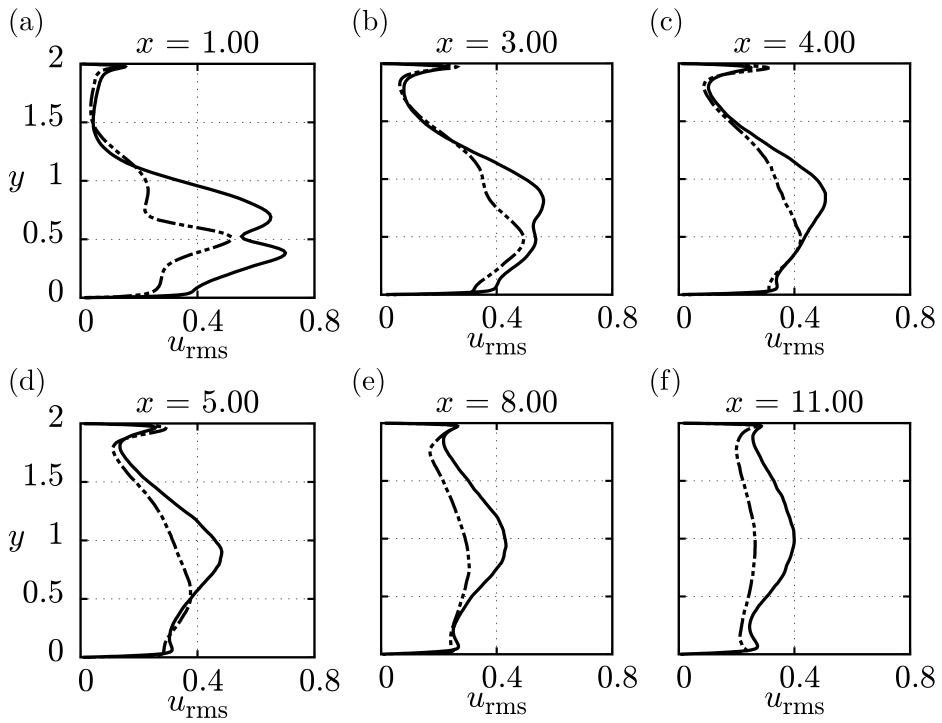

Figure 4.12: Profiles of the rms of the streamwise velocity component u_{rms} at different streamwise stations in the horizontal channel. ----, $T_R = 1.17$; —, $T_R = 2.0$.

amplitude of these fluctuations is smaller than the ones for $T_R = 2.0$ due to weaker stratification.

In figure 4.13 we present the rms profiles of the wall-normal velocity component, v_{rms}, for both cases under study and at the same streamwise stations as before. According to this figure, the profiles of v_{rms} share some common features with the profiles of the streamwise fluctuations. For example, at $x = 1.0$, we can observe the two peaks related to the primary and secondary shear layers for both temperature ratios. Also, for $T_R = 2.0$, the peak related to the primary layer persists and its location is gradually shifted upwards. At the same time, the wall-normal velocity fluctuations become more prevalent in the upper part of the channel. Despite the strong stratification effects, the values of v_{rms} are still smaller than the values of u_{rms}.

Finally, profiles of the rms of the spanwise velocities are presented in figure 4.14. As with the other velocity components, the profiles of w_{rms} also have two peaks at the locations of the primary and secondary shear layers. We also note that in the vicinity of the reattachment point of the flow, w_{rms} takes characteristically high values; see figures 4.14c and 4.14d. Such high values are due to *splatting* of vortices

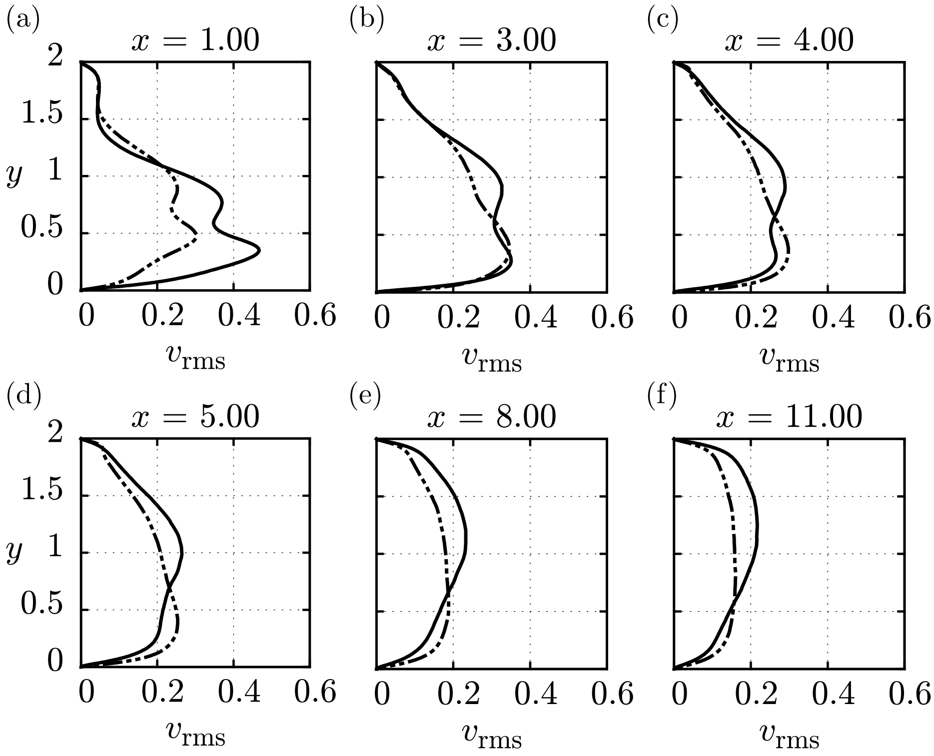

Figure 4.13: Profiles of the rms of the normal velocity component v_{rms} at different streamwise stations of the horizontal channel. -·-·, $T_R = 1.17$; —, $T_R = 2.0$.

that are shed by the shear layers. This phenomenon is frequently encountered near reattachment points of separated flows; see for example the discussion in [77].

4.3.3 Statistics of turbulent heat fluxes

In this section we present and analyse our results for the turbulent heat fluxes $<\theta' u'>$ and $<\theta' v'>$. Comparisons with the experimental data from [11] are also included herein.

First we elaborate on the profiles of the streamwise turbulent heat flux $<\theta' u'>$ for $T_R = 1.17$, shown in figure 4.15. The profile at the streamwise station $x = -0.5$, *i.e.* the centre of the entry of the jet, is given in figure 4.15a. According to it, $<\theta' u'>$ is zero at the upper part of the channel that is occupied by the crossflow, but it assumes a bell-shaped profile with negative values at the lower part, *i.e.* the part occupied by the incoming jet. The negative values imply the heat transfer is directed upstream, which is likely due to the effect of entrainment of packets from one stream to the other. The negative peak coincides with the location of

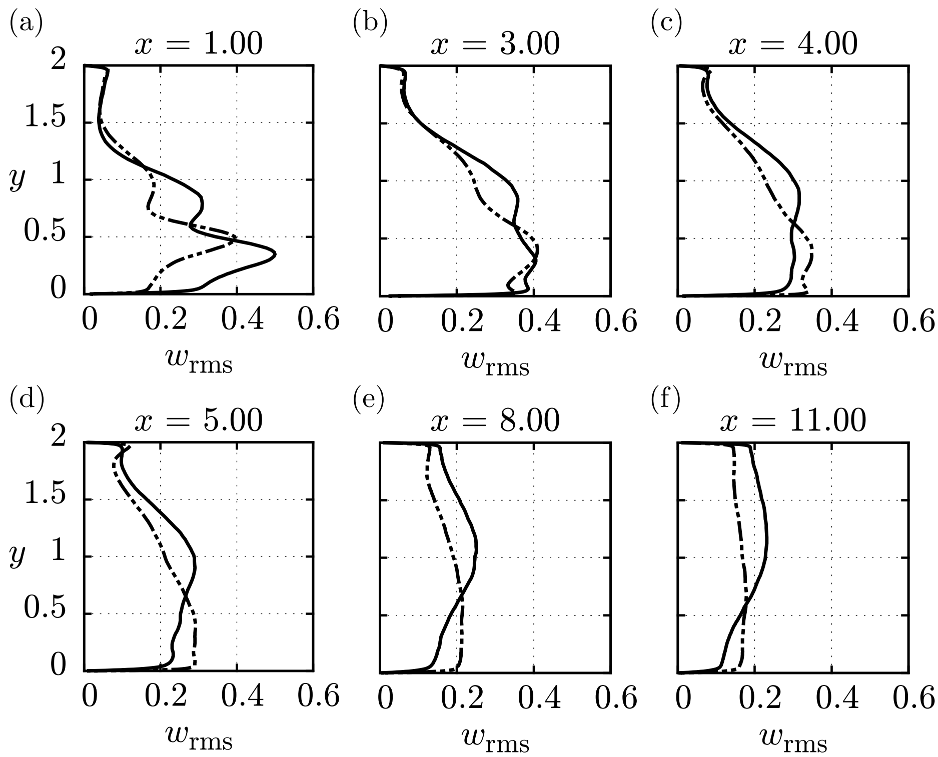

Figure 4.14: Profiles of the rms of the spanwise velocity component w_{rms} at different streamwise stations of the horizontal channel. -··-, $T_R = 1.17$; —, $T_R = 2.0$.

the primary shear layer. Another interesting feature is that the temperature of the incoming jet starts fluctuating as soon as the jet enters the horizontal channel.

The same characteristics can be observed in the profile of $<\theta' u'>$ for $x = 0.0$ shown in figure 4.15b. However, the region of negative values has been shifted upwards; this is due to the trajectory of the incoming jet which turns and changes direction as it moves upwards. Further, the amplitudes of $<\theta' u'>$ have decreased. This occurs because the orientation of the vector of the turbulent heat flux changes with the direction of the incoming jet and the shear layer. In fact, the decrease of the streamwise turbulent heat flux is accompanied by a corresponding increase of the wall-normal one.

The profile of $<\theta' u'>$ at $x = 0.50$ is shown in figure 4.15c. This streamwise station is located at the large recirculation bubble. As the primary shear layer spreads, the streamwise turbulent heat flux inside this layer changes to an S-shaped profile. Also, it has a strong positive peak at $y \approx 0.75$, which is at the side of the hot incoming jet. Further, it takes positive values in the region $0.3 < y < 0.5$, *i.e.* across the secondary shear layer. The same trends can be witnessed in the profile

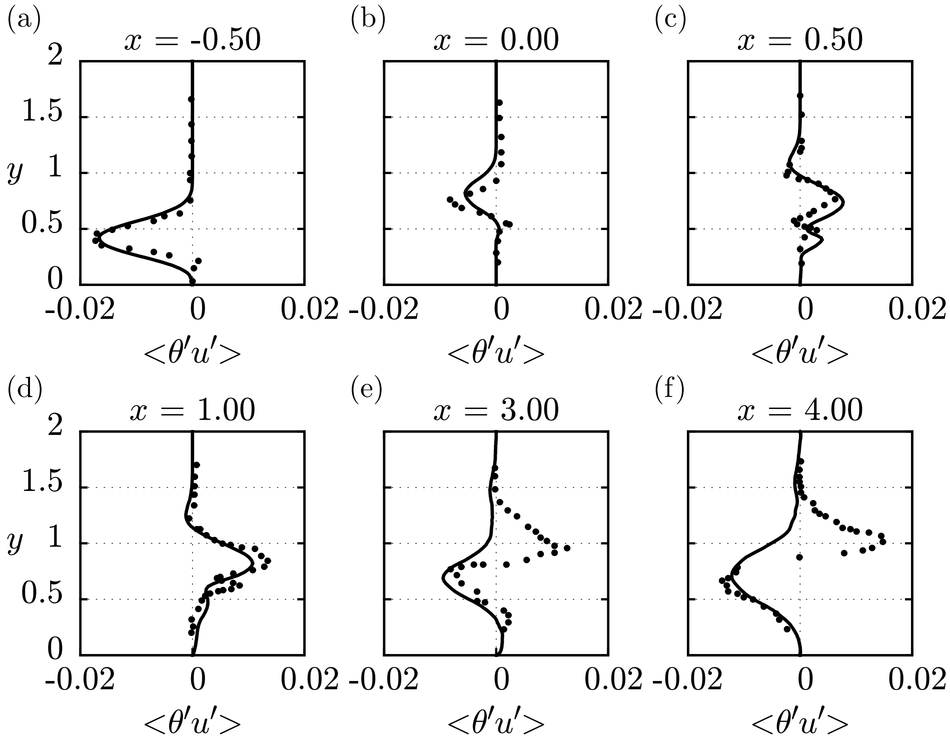

Figure 4.15: Profiles of the streamwise turbulent heat flux $<\theta' u'>$ at the vicinity of the entry of the jet and the recirculation bubble for $T_R = 1.17$. —, our numerical predictions; •, experimental data from [11].

of $<\theta' u'>$ for $x = 1.0$, shown in figure 4.15d. In this case, the value of the positive peak has increased even further due to enhanced thermal mixing between the incoming jet and the crossflow. Finally, in figures 4.15e and 4.15f we provide the profiles of $<\theta' u'>$ at $x = 3.0$ and $x = 4.0$, in the reattachment region of the flow. We observe that as the primary shear layer passes over the recirculation bubble and expands in the channel, $<\theta' u'>$ reverts to a bell-shaped profile of negative values, *i.e.* the heat flux is directed upstream.

Our numerical predictions agree very well with the experimental data from [11] at the stations $x = -0.5$, 0.0, 0.5 and 1.0. On the other hand, at $x = 3.0$ and $x = 4.0$ the measurements show an inverted S profile with negative values at the lower hot side of the expanding primary shear layer and positive values at the upper cold side of it. Our numerical results match well the measurements at the lower side but predict negligible values for $<\theta' u'>$ at the upper part instead of positive ones; see figures 4.15e and 4.15f. The source of this discrepancy is not yet clear to us and the authors of [11] did not provide a physical interpretation for their measurements in this region. It is worth mentioning that the streamwise

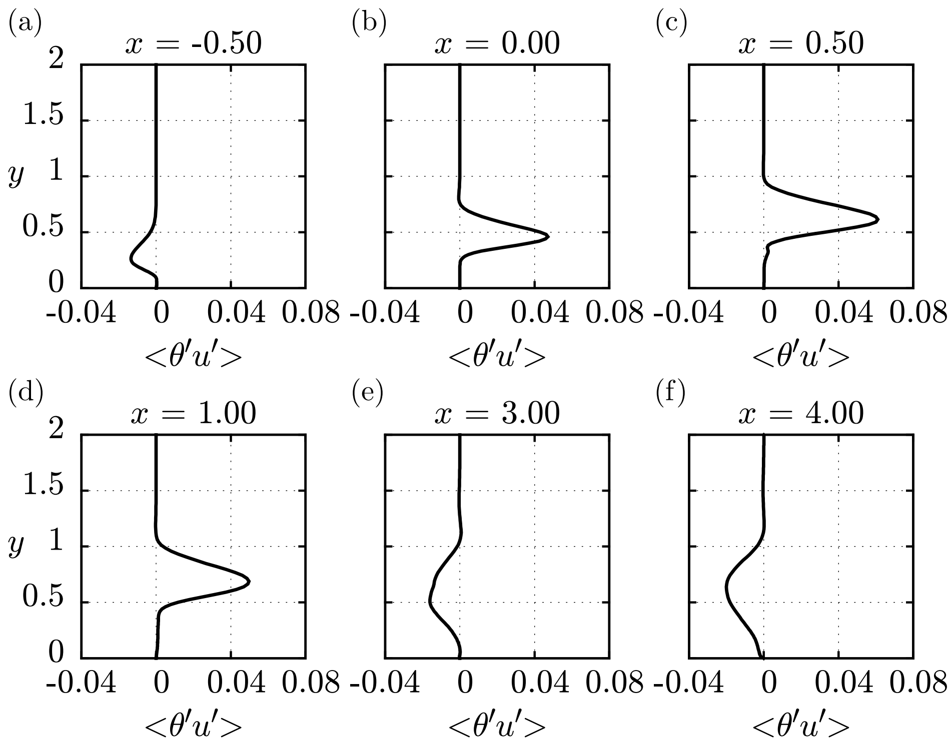

Figure 4.16: Profiles of the streamwise turbulent heat flux $<\theta' u'>$ at the region of the recirculation bubble for $T_R = 2.0$.

gradients of $<T>$ in this region are very small, something that was also noted by the authors of [11]. Therefore, one would expect small values of $<\theta' u'>$ at the cold side of the shear layer, as predicted by our simulations. On the other hand, it should be acknowledged that this discrepancy can be attributed, at least partially, to numerical diffusion errors.

Next we discuss the results of $<\theta' u'>$ for the case of the high temperature ratio, $T_R = 2.0$. The corresponding profiles are shown in figure 4.16. As in the previous case, at $x = 0.5$ the streamwise turbulent heat flux takes negative values across the primary shear layer. However, at $x = 0.0$, $<\theta' u'>$ assume a bell-shaped profile of positive values across this shear layer. This shape is preserved at $x = 0.5$ and $x = 1.0$ contrary to the previous case in which $<\theta' u'>$ had an S-shaped profile. This corroborates our previous conclusion that the secondary shear layer does not contribute significantly to thermal mixing, in the case of $T_R = 2.0$. On the other hand, at $x = 3.0$ and 4.0 the values of $<\theta' u'>$ have become negative and follow a bell-shaped profile, similarly to the case with $T_R = 1.17$.

The results for the vertical turbulent heat fluxes $<\theta' v'>$ are shown in figure

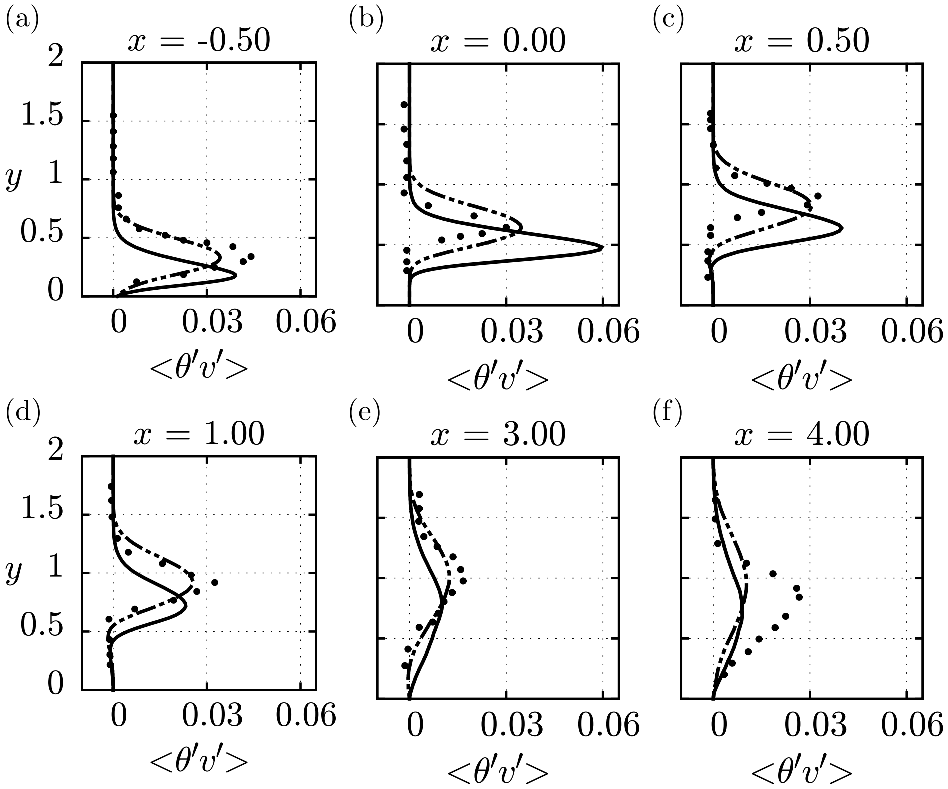

Figure 4.17: Profiles of the vertical heat fluxes $<\theta'v'>$ at the region of the recirculation bubble. -·-·-, $T_R = 1.17$; —, $T_R = 2.0$; •, experimental data from [11] for $T_R = 1.17$.

4.17. According to these plots, the values of $<\theta'v'>$ are positive and have a bell-shaped profile across the primary shear layer but are zero at the upper part of the channel that is occupied by the crossflow. Positive values imply that the heat transfer is directed upwards, *i.e.* from the hot incoming jet to the cold crossflow. Therefore it comes at no surprise that the vertical turbulent remain positive. Further, the profiles of $<\theta'v'>$ spread out as the shear layer passes over the recirculation bubble and expands. Interestingly, the values of the vertical fluxes in the region of the entry of the channel are higher for $T_R = 2.0$. This is attributed to the stronger shear between crossflow and incoming jet for $T_R = 2.0$. However, the peak values become almost equal for both cases as the flow evolves in the streamwise direction.

For comparison purposes, in figure 4.17 we have included the experimental results from [11] for $T_R = 1.17$. Our numerical predictions agree reasonably well with those measurements. The only visible discrepancy is that our simulations under-predict the amplitude of $<\theta' v'>$ at the station $x = 4.0$. We remark, however, that according to the measurements, the values of $<\theta' v'>$ at $x = 3.0$ are considerably lower than the values both at $x = 1.0$ and $x = 4.0$. In other words, the peak of the vertical turbulent heat flux decreases and then increases again, which is rather unexpected for this region of the flow.

4.3.4 Time-series analysis

In this section we present results of the times-series analysis of the temperature. Our motivation is twofold; firstly, to gain additional insight on the dynamics of turbulent heat transfer in T-junctions and, secondly, to assess the risk of thermal fatigue at the walls of the T-junction. To this end, we first compute the spanwise-averaged temperature field $\overline{T(x, y)}$ at selected (x, y) coordinates in the flow field. Subsequently, we compute the power spectral density of the signal S_{TT} that describes the distribution of power into the frequency components comprising the signal. This, in turn, allow us to determine the characteristic frequencies at which the signal of $\bar{T}$ oscillates. The frequencies are then non-dimensionalised with respect to the half-width of the horizontal channel and the bulk velocity of the crossflow in the experiments [11]. This provides the corresponding Strouhal numbers, $St = f\delta/U_c$.

In figure 4.18 we have plotted the signal of $\overline{T(x, y)}$ and the corresponding power spectral density S_{TT} for $T_R = 1.17$ at two different locations, namely, at the primary shear layer above the entry of the jet $(x, y) = (-0.5,\ 0.5)$, and downstream the recirculation bubble at the symmetry plane of the horizontal channel $(x, y) = (8.57,\ 1.0)$. According to our predictions, the temperature at the first location oscillates with a Strouhal number $St = 0.4$, which corresponds to a dominant frequency of $f \approx 43\,\text{Hz}$. This result is very close to the frequency reported in [11], $f = 40\,\text{Hz}$. It is also worth recalling that the primary shear layer is subject to an oscillatory flapping motion. We may therefore infer that the frequency of the temperature oscillation at this location coincides with the frequency of the flapping motion of the primary shear layer.

As regards the second location $(x, y) = (8.57,\ 1.0)$, according to figure 4.18 the power spectral density S_{TT} of the temperature exhibits a strong peak at almost the same Strouhal number as before, $St \approx 0.35$. Therefore, this frequency is related to the flapping motion of the shear layer. We also observe a secondary peak at a lower Strouhal number, $St \approx 0.15$, which can be attributed to spanwise rollers shed by the shear layers.

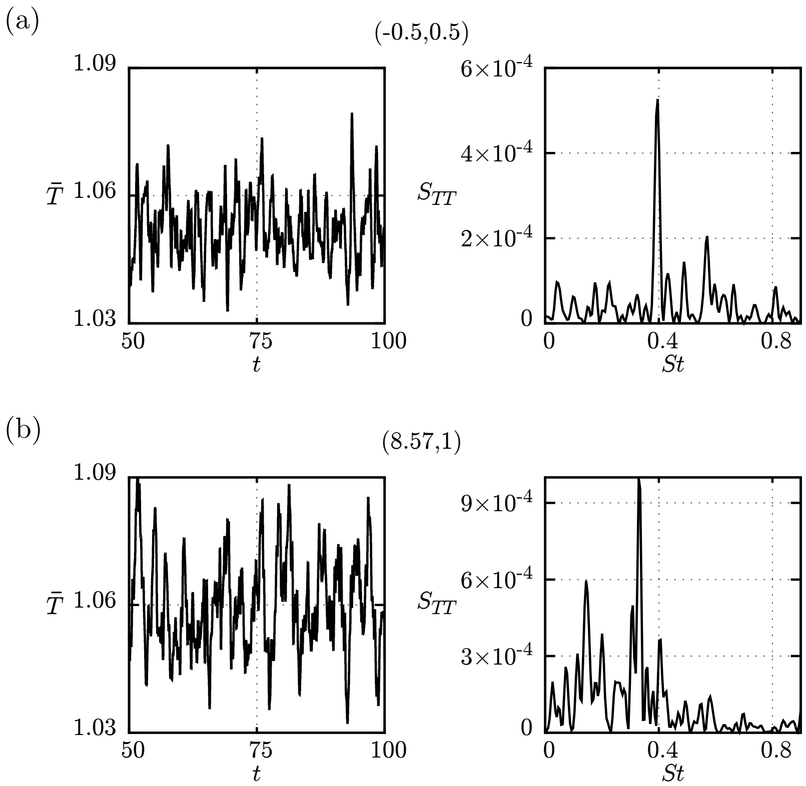

Figure 4.18: Time-series analysis of the spanwise-average temperature, $\overline{T(x,y)}$, for the case with $T_R = 1.17$. (a) $(x,y) = (-0.5,\, 0.5)$. (b) $(x,y) = (8.57,\, 1.0)$. The left images show the temperature signal at these two points over 50 time units while the right images show the power spectral density S_{TT} as a function of the Strouhal number St.

With respect to the issue of thermal fatigue of the walls, we first note that according to the study [100], the critical frequencies are between 0.1 and 10 Hz. In figure 4.19 we present the results of our time-series analysis at two locations at the bottom wall, namely, $(x,y) = (-1.02,\, 0.0)$ and $(x,y) = (4.21,\, 0.0)$. The first location is just before the upstream corner of the entry of the jet. As mentioned in the discussion of the main features of the flow, a thin vortical structure is formed in this region. The power spectral density of the temperature at this location has a dominant peak at $St \approx 0.1$ and a secondary one at $St \approx 0.04$. The corresponding frequencies are 10.75 Hz and 4.3 Hz, respectively. The dominant frequency lies outside but close to the range responsible for thermal fatigue, whereas the second largest frequency is definitely inside. We therefore infer that this region of the bottom wall can be sensitive to thermal fatigue.

On the other hand, our analysis at the location $(x,y) = (4.21,\, 0.0)$, *i.e.* slightly

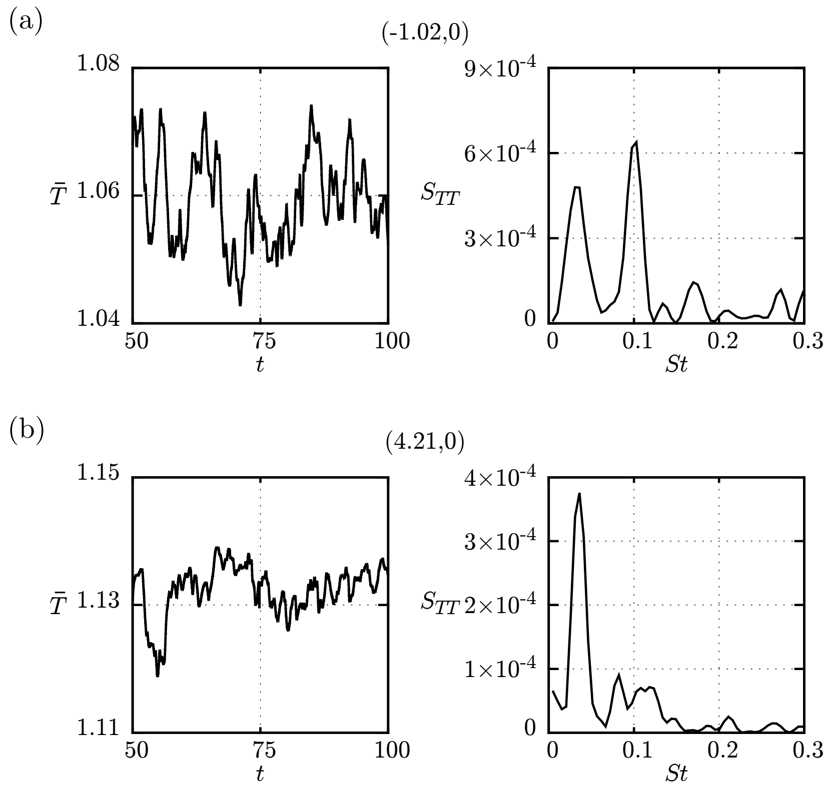

Figure 4.19: Time-series analysis of the spanwise-average temperature, $\overline{T(x,y)}$, for the case with $T_R = 1.17$. (a) $(x, y) = (-1.02, 0.0)$. (b) $(x, y) = (4.21, 0.0)$. The left images show the temperature signal at these two points over 50 time units while the right images show the power spectral density S_{TT} as a function of the Strouhal number St.

downstream the reattachment point of the flow, reveals a dominant peak at $St \approx 0.03$; see figure 4.19. This value corresponds to a frequency of 3.2 Hz, which means that the bottom wall is even more susceptible to thermal fatigue at this location.

We conclude with a discussion on the time-series analysis for the case $T_R = 2.0$. In figure 4.20 we present the plots of the power spectral density at the primary shear layer above the entry of the jet $(x, y) = (-0.5, 0.26)$, and downstream the recirculation bubble at the centerline of the channel $(x, y) = (8.57, 1.0)$. As regards the first location, S_{TT} possesses two strong peaks of similar amplitude at $St \approx 0.2$ and 0.35, as well as a pair of smaller peaks at $St \approx 0.13$ and 0.6; this is considerably different than in the case with $T_R = 1.17$. However, at the second location, the peaks of the temperature signal occur at $St \approx 0.16$ and a secondary one at $St \approx 0.35$. This means that the peaks of S_{TT} at this location occur at the same frequencies for both temperature ratios; compare figure 4.18b and figure

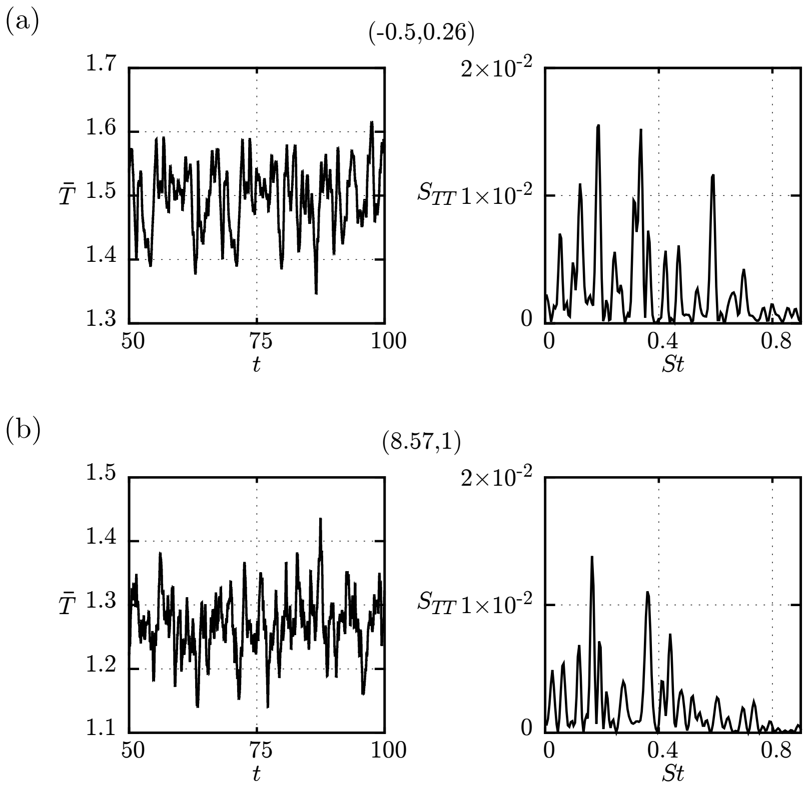

Figure 4.20: Time-series analysis of the spanwise-average temperature, $\overline{T(x,y)}$, for the case with $T_R = 2.0$. (a) $(x,y) = (-0.5,\ 0.26)$. (b) $(x,y) = (8.57,\ 1.0)$. The left images show the temperature signal at these two points over 50 time units while the right images show the power spectral density S_{TT} as a function of the Strouhal number St.

4.20b. As mentioned above, the first frequency corresponds to the flapping motion of the primary shear and the second one to spanwise rollers shed by this layer. In turn, this implies that the flapping frequency of the shear layer is not very sensitive to the temperature ratio.

Finally, as regards the issue of thermal fatigue, the power spectral densities at $(x,y) = (-1.02,\ 0.0)$ and $(x,y) = (2.55,\ 0.0)$ are plotted in figure 4.21. At both locations, the power spectral density peaks at $St \approx 0.05$. The corresponding dominant frequency is 5.35 Hz, which implies that the bottom wall is susceptible to thermal fatigue at both locations.

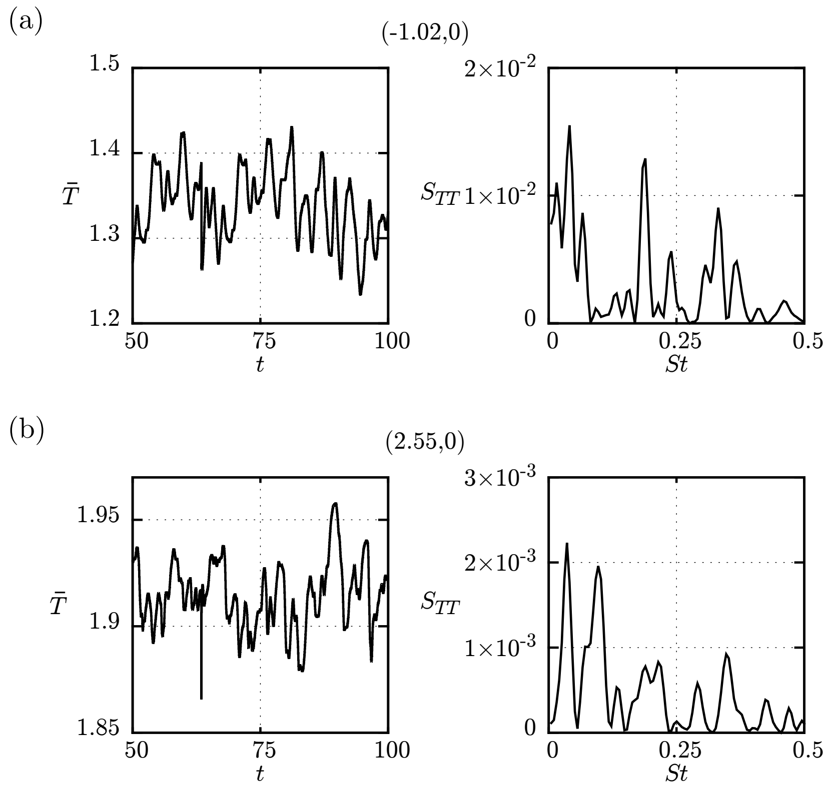

Figure 4.21: Time-series analysis of the spanwise-average temperature, $\overline{T(x, y)}$, for the case with $T_R = 2.0$. (a) $(x, y) = (-1.02, 0.0)$. (b) $(x, y) = (2.55, 0.0)$. The left images show the temperature signal at these two points over 50 time units while the right images show the power spectral density S_{TT} as a function of the Strouhal number St.

4.4 Conclusions

In this chapter we presented a computational study of turbulent mixing between a cold crossflow and a hot incoming jet in a T-junction via wall-resolved LES. In the cases examined herein, inertial effects due to density variations cannot be neglected and for this reason we did not invoke the Boussinesq approximation regarding density variations. Our numerical predictions showed good agreement with previously reported experimental data as regards both the temperature field and the turbulent heat fluxes.

According to our simulations, the shear layer that is formed between the crossflow and the incoming jet provides one of the basic mechanisms for thermal mixing. Fluid entrainment is enhanced by the flapping motion of this shear layer. Also, the rate of shear across this layer increases with the temperature ratio between the two streams, which further enhances thermal mixing. Interestingly though, sufficiently downstream the entry of the incoming jet, the temperature in the core of this shear layer oscillates with the same Strouhal number, irrespective of the temperature ratio.

Our study of the flow field in the near-wall regions has revealed that the velocity profiles close to the bottom wall deviate significantly from the universal law of the wall due to adverse pressure gradients that are developed downstream the large recirculation bubble. On the other hand, the velocity profiles close to the top wall initially deviate from the univeral law due to favourable pressure gradients that is caused by Venturi effects. Nonetheless, sufficiently downstream, the universal law of the wall is reestablished at the top wall. Our simulations further predict that, at low temperature ratios, cold fluid from the crossflow is entrained inside the vertical channel, which leads to the formation of a hovering vortex below the entry of the jet. On the other hand, at high temperature ratios, there is no such entrainment; the flow still separates below the entry of the jet but the vortex that is formed contains hot fluid from the incoming jet. Finally, our time-series of the temperature indicates that the bottom wall is susceptible to thermal fatigue in the vicinity of the reattachment of the flow downstream the recirculation bubble.

Chapter 5

Turbulent heat transfer in liquid-liquid flows in T-junctions

5.1 Introduction

In this chapter we report on a computational study of turbulent heat transfer in liquid-liquid flows in a T-junction, as the one shown in figure 5.1. In the previous chapter we showed that even for moderate temperature ratios, the temperature is an active scalar in gas flows in a T-junction. However, the effect of thermal non-equilibrium in liquid flows differs considerably from the one in gases. Whereas the density of liquids varies only slightly with temperature, their viscosity tends to decrease considerably as the temperature increases.

Currently, it is not well understood how temperature gradients affect the mixing process in liquid-liquid flows in T-junctions. The majority of previous works examined flows in which the temperature differences between the crossflow and the incoming jet were small and the temperature was essentially a passive scalar. Notable exceptions include the experiments of turbulent mixing in horizontal T-junctions, *i.e.* the gravity vector pointing into the spanwise direction, that were performed in the experimental facility described by Kuschewski et al. [101]. These authors performed experiments in closed-loop T-junctions with circular cross-sections at an ambient pressure of 75 bar, thus matching the working conditions of Light Water Reactors (LWR). In addition, several numerical investigations that

The results of this chapter have been included in: M. Georgiou and M.V. Papalexandris. Turbulent heat transfer in liquid-liquid flow in a T-junction. *Under review.* [34].

were based on Large Eddy Simulations (LES) replicated the aforementioned experiments [102–104]. Even though these studies focused on liquid-liquid flows with temperature differences of the order of 100 K, the stratification effects were so strong that dominated the mixing process. Further, Howard and Serre [24] examined liquid-liquid flows with temperature differences of 60 K via LES. However, their simulations were based on wall models which, as mentioned in the previous chapters, have been shown to perform poorly on flows in T-junctions [62, 72].

The objective of this study is to assess the effect of large temperature gradients to the mixing process in liquid-liquid flows in rectangular T-junctions. Currently, there are no available experimental data for such flows. For this reason, we have performed and present herein Direct Numerical Simulations (DNS) of turbulent mixing between a hot liquid crossflow and a cold liquid incoming jet in a rectangular T-junction. To the best of our knowledge, DNS studies of turbulent mixing in T-junctions have not been published before. The fact that all the relevant scales of the flow are fully resolved has allowed us to perform a detailed analysis of the dynamic and structural properties of the flow of interest. Further, in order to assess the capabilities of LES on accurately predicting turbulent flows in T-junctions, we have also performed a wall-resolved LES and compare its results with those of the DNS.

This chapter is organised as follows, In section 5.2 we outline the mathematical model, the numerical algorithm, and describe the computational setup of our simulations. In sections 5.3 we present and analyse the numerical results of our study. In particular, we describe the main features of the flow and examine the structures that are developed in the instantaneous flow field. We also elaborate on the statistics of the temperature, velocity components and turbulent heat fluxes. This part also includes a comparison between the predictions of our DNS and LES. In addition, we examine the budget of the turbulent kinetic energy and analyse the time-signal the temperature. Finally, section 5.4 concludes.

5.2 Computational setup

In this section we outline the governing equations and the algorithm that is used for the numerical treatment of those. We also elaborate on the configuration of our numerical simulations and describe the flow geometry, the computational grid and the implementation of the boundary conditions.

The working medium is liquid water at an ambient pressure of 3 bar. The specific pressure is chosen so as to match the working conditions of AC systems that use liquid water as working medium. The temperature of the crossflow is $\hat{T}_{\mathrm{c}} = 393$ K, , with the superscript $\hat{.}$ denoting dimensional quantities, and the one of the incoming jet is $\hat{T}_{\mathrm{jet}} = 293$ K. Accordingly, the ratio between the temperatures of the two streams is $T_R = 1.34$. The bulk velocities of the crossflow and the incoming jet are equal,

The governing system of equations for the flows of interest is the low-Mach approximation for the compressible Navier-Stokes-Fourier equations given in (2.12) - (2.14). For purposes of non-dimensionalisation we have chosen the bulk velocity of the crossflow, U_{c}, as the reference velocity and the half-height of the horizontal channel, δ, as the reference length. Also, the non-dimensionalisation of the thermodynamic variables and transport coefficients has been performed with respect to the temperature and density of the fluid at the crossflow stream.

The system of governing equations is closed with an equation of state, *i.e.* a relation between density, temperature and thermodynamic (ambient) pressure. For liquid flows at constant ambient pressure, it is common practice to employ a polynomial relation between ρ and T. Herein, we employ a parabolic fit of the tabulated data provided by [31]. This parabolic relation is valid for temperatures between 273 K and 423 K and reads, in non-dimensional form,

$$\rho \;=\; -0.45\,T^2 + 0.55\,T + 0.9\,. \tag{5.1}$$

According to this equation, the ratio between the densities of the crossflow and the incoming jet is equal to 0.945.

For liquids, the variation of the shear viscosity μ with the temperature is typically expressed by an Arrhenius-type relation, [105]. In our study we employ the following (dimensionless) relation, adapted from [106],

$$\mu(T) \;=\; A \times 10^{\frac{B}{T-C}}\,, \tag{5.2}$$

with $A = 0.105$, $B = 0.631$ and $C = 0.356$. It is worth mentioning that, given the aforementioned temperature difference of 100 K, the shear viscosity of the cold stream is 4.38 higher than the one of the crossflow. As for the liquid conductivity κ, we employ a second-order polynomial that matches the data provided in [31]. This expression reads, in non-dimensional form,

$$\kappa \;=\; -1.6\,T^2 + 3.3\,T - 0.7\,. \tag{5.3}$$

In addition, in the range of temperatures that are examined herein, the variations of c_p are smaller than 2%. For this reason c_p is assumed to be constant.

Based on the reference quantities mentioned above, the Reynolds number of the flow is $Re = 3,000$. This value corresponds to a *bulk* Reynolds number, that is based on the height of the horizontal channel 2δ, $Re_{\mathrm{b}} = 6,000$. The Prandtl number, based on the crossflow temperature, is $Pr = 1.44$. Also, the Richardson number is set to $Ri = 0.04$. This value is chosen so as to not allow the mixing process to be dominated by buoyancy effects.

In table 5.1 we provide the values of the flow parameters of the incoming jet, as well as the temperature and momentum ratios, T_R and M_R, respectively. We remark that, due to the considerably higher viscosity and smaller diameter of the incoming jet, its Reynolds number is almost one order of magnitude smaller, $Re_{\mathrm{jet}} = 343$, in comparison with the one of the crossflow, $Re = 3,000$. Also, the momentum ratio M_R is defined as the ratio between the momentum fluxes, $\rho U^2 A$, of the crossflow and the incoming jet, with U and A being the bulk velocity and cross-sectional area, respectively. Since the density and cross-sectional area ratios are equal to 0.945 and 2, respectively, we have that $M_R = 1.89$.

T_R	1.34
M_R	1.89
ρ_{jet}	1.06
μ_{jet}	4.38
U_{jet}	1.0
Re_{jet}	343

Table 5.1: Physical parameters related to the incoming jet for the case considered herein. The Reynolds number, Re_{jet}, is based on the bulk velocity of the jet U_{jet}, the half-width of the vertical channel 0.5δ, and the kinematic viscosity at the inflow of the incoming jet ν_{jet}.

For the numerical solution of the governing system of equations (2.12) - (2.14) we employ the time-accurate algorithm of Lessani and Papalexandris [42], described in chapter 2. In our simulations we use a variable time-step. As mentioned in chapter 2, the Courant number is always kept smaller than unity. Further, in order to fully capture all the turbulent scales [107], we have ensured that the time-step is always kept well below the Kolmogorov time-scale, τ_η. This time-scale is defined by the following expression

$$\tau_\eta = \left(\frac{\nu}{\epsilon_k}\right)^{1/2}, \tag{5.4}$$

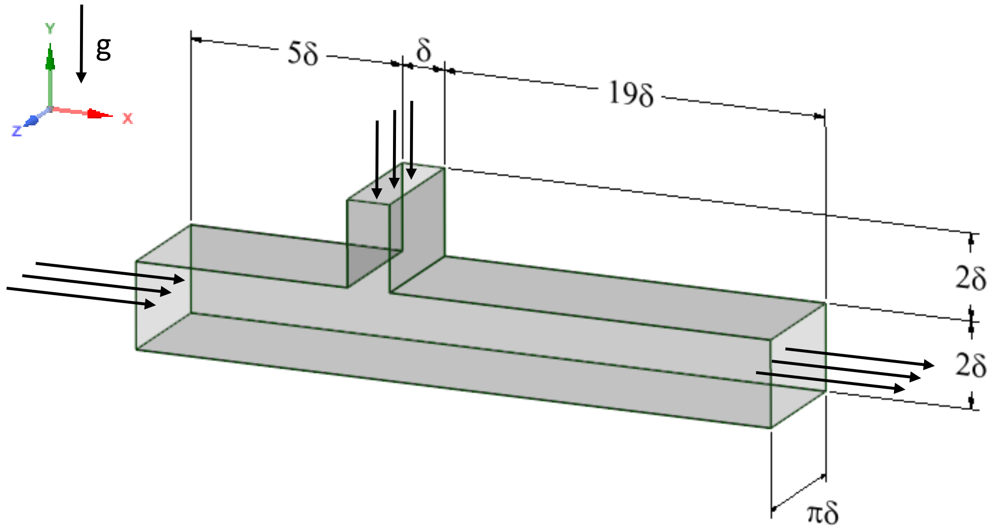

Figure 5.1: Illustration of the computational domain for the T-junction simulation. For purposes of clarity, this image is not to scale.

with ν being the local kinematic viscosity and ϵ_k the local turbulent kinetic energy dissipation. The values of ϵ_k are shown later on.

An illustration of the computational domain is presented in figure 5.1. For the configuration of the flow we have followed the same convention as in chapters 3 and 4. We have also used similar dimensions in the streamwise x-direction and wall-normal y-direction of the computational domain. However, we have increased the distance of the outflow plane from the downstream corner of the entry of the jet, from 13δ to 19δ. The elongation of the domain in this region is motivated by our findings in chapter 4. In particular, in the previous chapter, we observed that the temperature at the wall opposite the entry of the jet changes slightly. For this reason, we decided to increase the distance of the outflow plane from the downstream corner of the entry of the jet so as to check if the temperature close to the bottom wall starts to change downstream 13δ.

In the spanwise z-direction, we assume the flow to be homogeneous and we impose periodic boundary conditions. The spanwise length of the domain should be long enough so as to capture the large structures that are developed in this direction. On the other hand, in order to keep the computational cost of our simulations as low as possible, the length of the domain should not be excessively large. This issue is commonly encountered in numerical simulations of separated flows, such as the one studied herein. For example, Fröhlich et al. [77], who studied flows in channels with periodic hills via LES opted for a length of 3δ. Similarly, in their DNS of external flows over backwards facing steps, Le et al. [84] set the spanwise length equal to $4h$, with h being the height of the step. Schäfer et al. [108] opted for a length equal to $3.77h$ in their DNS of internal flows over backwards facing steps. Therefore, in order to ensure that the turbulent structures are satisfactorily captured and that the grid resolution is sufficiently fine for the purposes of our DNS, we set the spanwise length equal to $\pi\delta$. This length is similar to the ones used in the aforementioned studies.

5.2.1 Configuration of the computational grid

Given these dimensions, the computational grid for the DNS consists of 44.16×10^6 computational nodes. Due to the significant flow inhomogeneities in the streamwise and wall-normal directions, we have employed non-uniform grid spacing along them. On the other hand, a uniform grid spacing is used in the homogeneous z-direction. Henceforth, all lengths will be given in non-dimensional values, that is, normalised by δ. Finally, the origin of the axes is placed at the bottom wall, opposite to the downstream corner of the entry of the jet.

The computational grid can be divided in 3 sections. The first one covers the horizontal channel upstream the entry of the jet, $-6 < x \leq -1$. In this section we have placed 100 computational nodes in the streamwise direction. More specifically, in the zone $-6 < x \leq -2.78$ there are 36 nodes with constant spacing $\Delta x = 0.091$. Then, the grid is progressively refined, with a mild compression ratio of 0.95, up to $\Delta x = 0.004$. The second section is defined by $-1 < x \leq 0$ and includes the vertical channel. Therein we have placed 100 nodes in the streamwise direction with a symmetric distribution with respect to the mid-plane of the vertical channel, $x = -0.50$. For $-1 < x \leq -0.5$ the grid spacing increases smoothly with a stretching factor of 1.03, up to $\Delta x = 0.02$. The third section covers the computational domain downstream the entry of the jet and it is discretized by 900 nodes in the streamwise direction. More specifically, in the interval $0 < x \leq 0.9$ we have placed 85 nodes and the spacing increases with a constant stretching factor of 1.02 up to $\Delta x = 0.022$. Beyond the station $x = 0.9$, the streamwise meshing is uniform.

In the wall-normal direction, we have placed 300 cells across the horizontal channel, 140 nodes above and 160 nodes below the mid-plane. The choice of asymmetric meshing in the (wall-normal) y-direction is motivated by the fact that in some regions of the bottom wall, the thickness of the boundary layer decreases considerably due to flow acceleration; see figure 5.8 and the relevant discussion below. Moreover, the fluid at the top wall is colder than the crossflow and, therefore, has higher shear viscosity. Consequently, the computational requirements at the top wall are not as strict as those at the bottom wall. For these reasons, we opted for higher resolution at the bottom half of the horizontal channel. The centre of the first cell from the bottom wall, $y = 0$, is set at $y_{\mathrm{f.n}} = 8.98 \times 10^{-4}$. In the bottom half of the horizontal channel, the spacing increases smoothly, with a constant stretching factor of 1.013, up to $\Delta y = 0.015$. The remaining 140 nodes are placed at the top half of the channel; therein the grid is refined smoothly as we approach the top wall with a constant stretching factor of 1.012. The first node off the top wall is located at $y_{\mathrm{f.n}} = 1.33 \times 10^{-3}$. Along the vertical channel, $2 < y < 4$, we have placed 150 cells. The grid spacing increases smoothly with y, with a constant stretching factor of 1.018, up to $\Delta y = 0.0195$ at the top inflow boundary.

Finally, in the spanwise direction, the domain is discretized via 128 uniformly distributed nodes, *i.e.* $\Delta z = 0.0245$. An overview of the discretization of the computational domain is provided in table 5.2.

Section	1	2	3
Extent	$-6 < x \leq -1$ $0 < y < 2$	$-1 < x \leq 0$ $0 < y < 4$	$0 < x < 19$ $0 < y < 2$
Number of cells	$100 \times 300 \times 128$	$100 \times 450 \times 128$	$900 \times 300 \times 128$

Table 5.2: Overview of the discretization of the computational domain.

In determining the grid spacing in the near-wall regions we have followed the guidelines of Le et al. [84] according to which at least one node should be placed in the interval $0 < y^+ < 1$, while the grid spacing in the streamwise and spanwise directions should be $\Delta x^+ \approx 10$ and $\Delta z^+ \approx 15$, respectively. In figure 5.2 we show the position of the first node in the vertical direction and the grid spacing (in wall units) at the walls of the horizontal channel. More specifically, from figure 5.2a we can infer that at least two nodes are always placed in the interval $0 < y^+ < 1$. At the bottom boundary, $y^+_{\mathrm{f.n}}$ attains its maximum value of 0.44 at $x \approx 1$ and decreases significantly further downstream. In particular, for $x > 3.0$, $y_{\mathrm{f.n}}$ becomes smaller than 0.3. At the top boundary, $y^+_{\mathrm{f.n}}$ is always smaller than 0.3. Further, according to figure 5.2b, the coarsest grid spacings at the bottom boundary are $\Delta x^+ \approx 10.4$ and $\Delta z^+ \approx 12.0$, and they occur at the station $x = 1$. Further downstream, both grid spacings decrease and are consistently smaller than 8.0. At the top wall, the

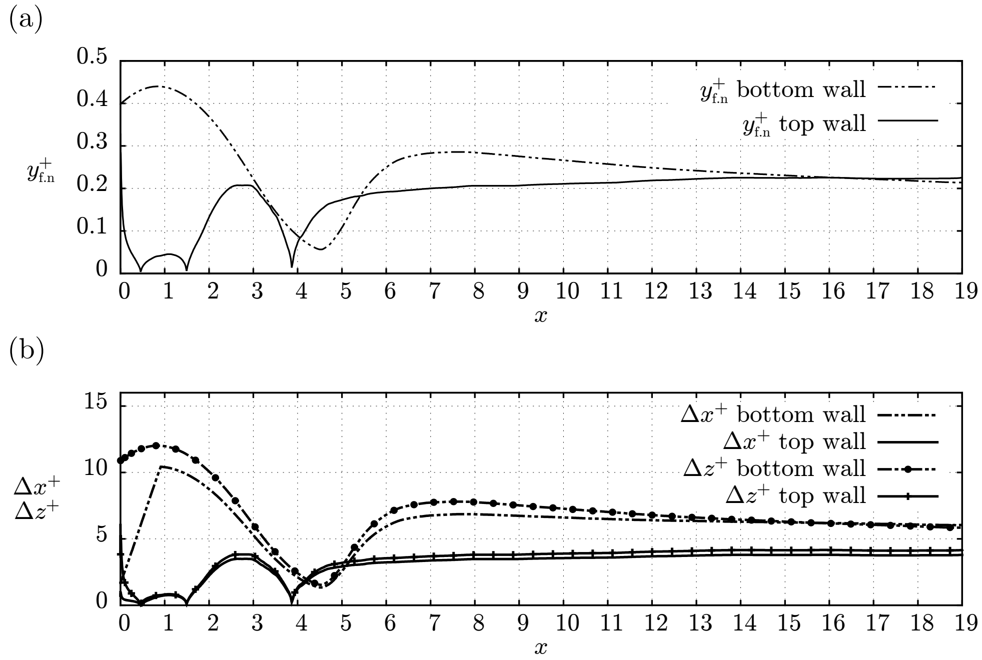

Figure 5.2: Grid spacing at the walls of the horizontal channel expressed in wall units. (a) $y^+_{\mathrm{f.n}}$, (b) Δx^+ and Δz^+. At the top wall and at $x \approx 0.5$, $x \approx 1.4$ and $x \approx 3.9$, the grid spacing drops to zero because the wall shear stress τ_{w} vanishes due to the reattachment of the flow.

values of Δx^+ and Δz^+ are even lower and always smaller than 4.0. We therefore conclude that our computational mesh fulfils the above guidelines of Le et al. [84] for the near-wall regions.

For the assessment of the quality of the grid away from the walls, we compare the local grid spacing, $\Delta = (\Delta x\, \Delta y\, \Delta z)^{1/3}$ with the smallest length-scales of the flow, namely, the Kolmogorov scale

$$\eta = \left(\frac{\nu^3}{\epsilon_k}\right)^{1/4}, \tag{5.5}$$

and the temperature microscale η_θ. For Prandtl numbers significantly higher than unity, η_θ is given by the following relationship [109],

$$\eta_\theta = \eta \left(\frac{1}{Pr}\right)^{1/2}. \tag{5.6}$$

However, in the flow under study, the reference Prandtl number is close to unity; $Pr = 1.44$, which corresponds to $\eta_\theta = 0.83\,\eta$. For this reason, we can examine the quality of the grid on the basis of the Kolmogorov scale η. In figure

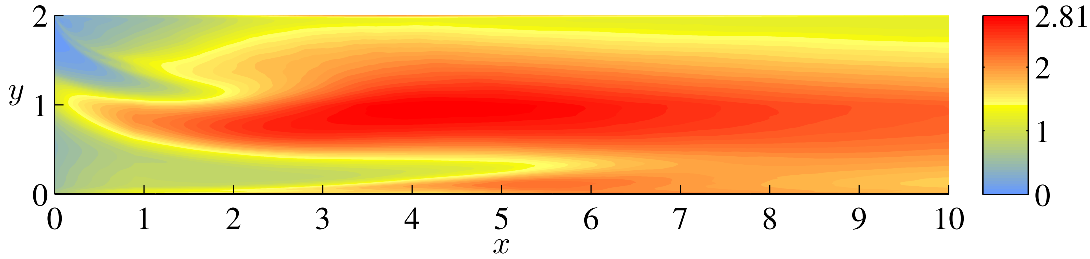

Figure 5.3: Contour plot of the ratio between the local grid spacing and the smallest length-scale of the flow Δ/η.

5.3 we show a contour plot of the ratio between the local grid spacing and the smallest length-scale of the flow, Δ/η, downstream the entry of the jet. The maximum value of this ratio is 2.81. Theoretically, in order for all the scales to be resolved, the computational grid should be able to capture the minimum length-scale. However, according to Pope [110], equation (5.5) tends to underestimate the size of this scale. To show this, Pope devised a carefully designed model spectrum, $D(\kappa) = 2\nu\kappa^2 E(\kappa)$, with $E(\kappa)$ being the energy spectrum, that accurately describes the dissipation range. Based on $D(\kappa)$, he quantified the scales of the dissipative motions.

In figure 5.4 we present a plot of this dissipation spectrum $D(\kappa)$ against the corresponding turbulent structures of size l normalised by η. This plot is a reproduction of [110, figure 6.16]. According to this figure, the peak of the dissipation spectrum is at $l/\eta \approx 24$. In addition, the motions responsible for the bulk (largest percentage) of the dissipation, range between $8 < l/\eta < 60$. Since at least two grid-cells are required to resolve a turbulent structure of size l, when the ratio $\Delta/\eta \approx 4$, the corresponding grid resolves the scales responsible for the bulk of dissipation. Also, at the same figure we fill with grey colour the part of the spectrum that is not resolved by our computational grid. The energy content of this part corresponds to 0.31% of the total energy of the dissipative motions, therefore, we consider that our computational grid is sufficient for the purposes of our DNS study.

On the other hand, the grid that is used for the LES consists of approximately 2×10^6 grid-nodes and fully resolves the wall-regions, as it follows the guidelines proposed in [75]. The maximum stretching factor that is used in the design of this grid is 1.1 in the region upstream the entry of the jet and 1.07 in the region downstream the entry of the jet.

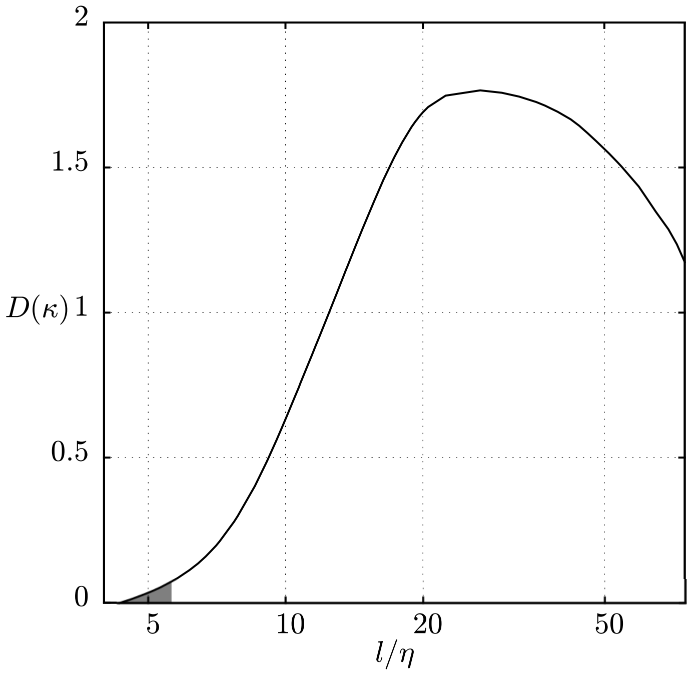

Figure 5.4: Plot of the dissipation spectrum, $D(\kappa)$, against the length of the local structures, l, normalised by η. The area filled with grey colour in this curve illustrates the energy content of the scales of dissipative motion that are not resolved by our computational grid. The energy content of the unresolved scales corresponds to 0.31% of the total energy of the dissipative motions. The curve of $D(\kappa)$ is extracted from [110].

5.2.2 Boundary conditions

As regards the implementation of boundary conditions, we prescribe two inflows conditions, one for the horizontal crossflow and one for the incoming jet. For the horizontal crossflow we provide a turbulent inflow. As mentioned in section 2.6, the inflow data are obtained by auxiliary simulations that run simultaneously with the main simulation. For the DNS, we perform an auxiliary DNS of a channel flow consisting of 5.76×10^6 computational cells. Also, for the LES, we employ an auxiliary wall-resolved channel flow simulation that consists of 4.3×10^5 cells. As for the second inflow, the one for the vertical channel, since the incoming jet is laminar; see table 5.1, we impose a parabolic profile with a bulk velocity equal to unity. For the outflow boundary, we use the convective boundary condition for all velocity components, the expression of which is given in (2.48).

For the temperature field we impose uniform profiles at the two inlets. Further, at the outflow plane, we use the convective boundary condition given in equation

(2.48). Finally, the walls of the T-junction are considered adiabatic. Therefore, a zero Neuman condition is applied at these boundaries.

5.3 Discussion of the numerical results

This section is devoted to the presentation and analysis of our numerical results. The notation adopted herein is standard; the mean of a generic quantity ϕ is denoted by $<\phi>$ and refers to averaging both in time and in the homogeneous spanwise direction. The fluctuating component of ϕ is denoted by ϕ', while ϕ_{rms} stands for the root mean square (rms) value of ϕ', *i.e.* $\phi_{\mathrm{rms}} =< \phi'\phi' >^{1/2}$.

The simulations are initialised by injecting the cold fluid from the vertical channel to the hot crossflow. The accumulation of data for the statistical analysis of the flow field starts once the flow becomes statistically stationary. To ensure that the flow has reached the statistical steady state we follow the approach described in section 3.3. Once statistical stationarity is confirmed we collect statistics of the flow quantities for 55 time units that corresponds to 4.3 flow-through times which is deemed sufficient for the purposes of our analysis. A flow-through time is approximated by the ratio between the length of the domain after the incoming jet and the bulk velocity of the flow just downstream the recirculation bubble, *i.e.* it is approximately equal to 19/1.5=12.67 time units.

In figure 5.5 we present streamlines extracted from the mean velocity field superposed by contour plots of the mean temperature $<T>$, as computed from the DNS. In this figure we remark that the resulting flow field is similar to those described in chapters 3 and 4. More specifically, the crossflow tilts downwards due to the incoming jet. In turn, the jet changes direction steeply and aligns with the one of the crossflow. In addition, due to this steep change of direction of the jet, a large recirculation bubble is formed downstream the entry of the jet. Further, the formation of the recirculation bubble results in the decrease of the cross-section area of both crossflow and incoming jet. Accordingly, the two streams (crossflow and incoming jet) experience a Venturi effect which increases considerably their velocity. Then, the two streams expand as they pass by the recirculation bubble, which results in an adverse pressure gradient in the region defined by $2 < x < 6$. This region includes the reattachment point at the end of the large recirculation bubble, located at $x \approx 3.89$, according to the DNS.

Additionally, figure 5.5 serves to identify the two shear layers that are developed in the flow field. The first one is formed between the crossflow and the incoming jet and originates in the vicinity of the upstream corner of the entry of the jet.

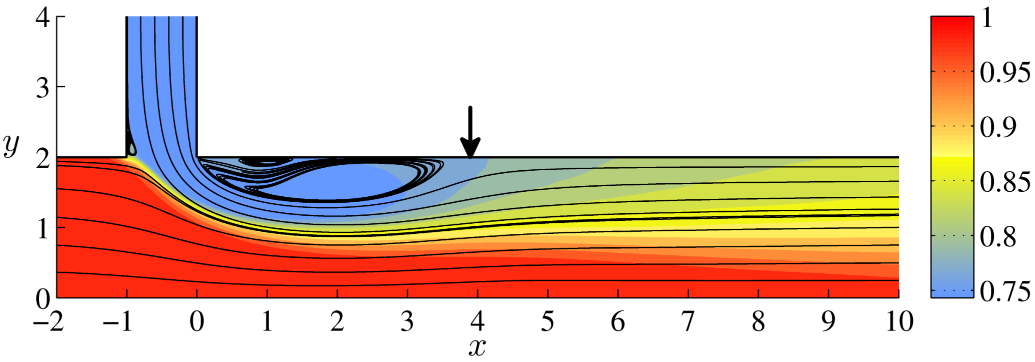

Figure 5.5: Main flow features. This figure shows streamlines extracted from the mean velocity field superposed by contour plots of the mean temperature field $<T>$ as computed from the DNS.
In this figure we show 4 streamlines emerging from the left entry of the horizontal channel. The distance between those is 0.4. In a similar manner, we show 4 streamlines emerging from the top entry of the vertical channel with the distance between those being 0.2. We also show streamlines downstream the entry of the jet in order to visualise the large recirculation bubble in this region. Additional streamlines are visualised close to the two corners of the entry of the jet. With the arrow we show the reattachment point of the flow, as predicted from DNS.

Henceforth, it will be referred to as the *primary* shear layer. The second one is formed between the jet and the recirculation bubble, and it will be referred to as the *secondary* shear layer. These two layers spread rapidly and start to interact, eventually merging to a single shear layer.

In figure 5.5 we also observe two smaller recirculation zones. The first one is located between the downstream corner of the entry of the jet and the large recirculation bubble. Structures similar to this one were identified and described in chapters 3 and 4 as well. As for the second one, it is located close to the upstream corner of the entry of the jet. In figure 5.6 we provide a close-up view of the streamlines in this region superposed by contour plots of the mean temperature $<T>$ and pressure $<p>$, respectively. According to this figure, this roller is located inside the vertical channel and consists of fluid coming exclusively from the incoming jet.

In fact, this recirculation zone bears certain similarities with the one shown in chapter 4 for $T_R = 2.0$; see figure 4.4b. As noted in the previous chapter, this structure is formed because of the combined effect of high momentum ratio and the laminarity of the boundary layer at the vertical wall. However, in the flow studied herein, the momentum ratio is smaller (1.89 instead of 4.0). In other words, the

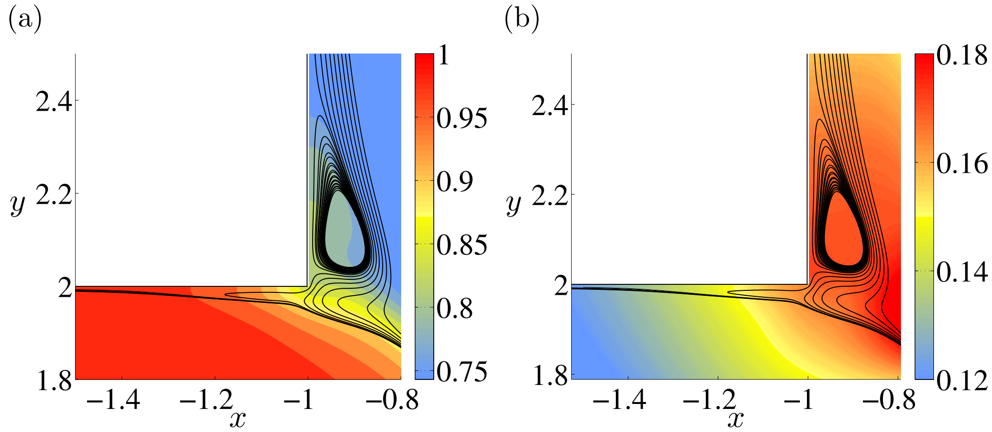

Figure 5.6: Recirculation zones in the vicinity of the upstream corner of the entry of the jet. This figure shows streamlines extracted from the mean velocity field superposed by contour plots of (a) the mean temperature $<T>$ and (b) the mean pressure $<p>$. According to these plots, the jet separates and forms a recirculating zone. This, in turn, decreases the amplitude of the adverse pressure gradient that the crossflow experiences.

momentum flux of the incoming jet is higher in the current case. This results to a feature that has not been observed before in flows in T-junctions. In particular, due to its high momentum flux, the jet reverses in the vicinity of the upstream corner of the entry of the jet and turns upstream.

In order to gain insight of the flow properties at the near-wall regions, we examine the variation of the skin friction and pressure coefficients,

$$C_{\mathrm{f}} = \frac{<\tau_{\mathrm{w}}>}{\frac{1}{2}\rho_{\mathrm{ref}}\, U_{\mathrm{ref}}^2} \quad \text{and} \quad C_p = \frac{<p> - p_{\mathrm{ref}}}{\frac{1}{2}\rho_{\mathrm{ref}}\, U_{\mathrm{ref}}^2}\,, \tag{5.7}$$

respectively, along the walls of the horizontal channel. In the above expression, p_{ref} and ρ_{ref} are the static pressure and density at the inlet of the crossflow. The profiles of C_{f} and C_p at the top wall, as predicted by the DNS and the LES, are plotted in figure 5.7. As the crossflow approaches the entry of the jet, the pressure coefficient C_{p} increases, *i.e.* the pressure increases in the streamwise direction, while C_{f} decreases and becomes negative close to the upstream corner. This is due to the reversal of the jet in the vicinity of the upstream corner that was mentioned above. Also, the large drop in C_p that is observed in the zone $-0.5 < x < 0$ is due to the acceleration of the jet upon its entry in the horizontal channel, *i.e.* it is due to the aforementioned Venturi effect. Downstream the entry of the jet, at the large recirculation bubble, C_{f} decreases considerably and attains large negative values, whereas C_p is kept almost constant. However, as we approach the reattachment

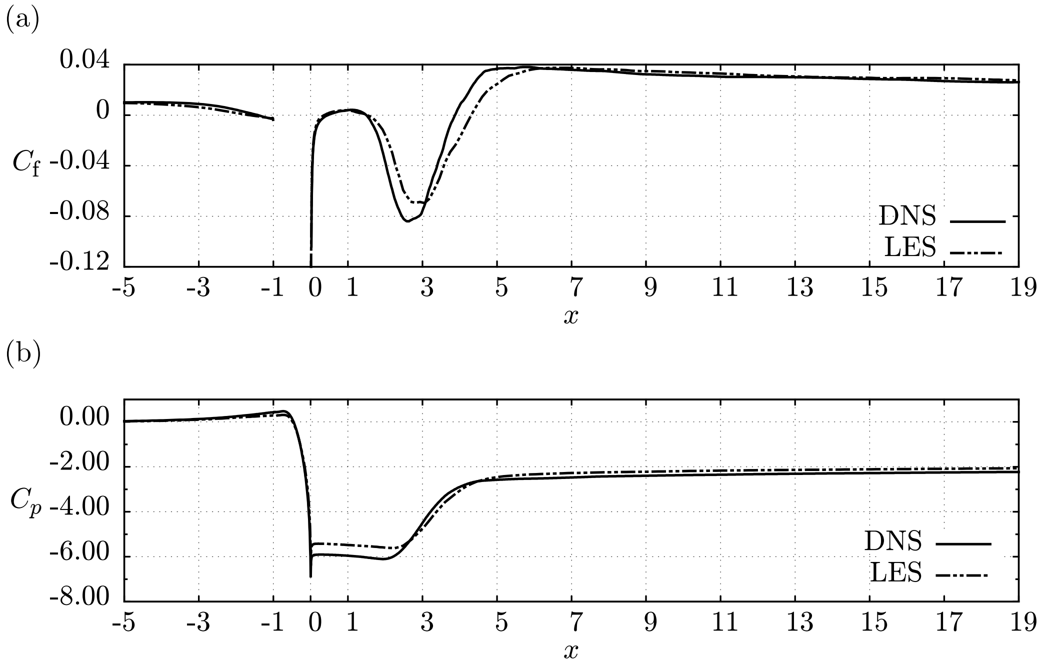

Figure 5.7: Plots of the skin friction and pressure coefficients, C_f and C_p, at the top wall of the horizontal channel. (a) C_f, (b) C_p. There is a small difference between the predictions of LES and DNS on the location of the reattachment point ($x = 4.31$ instead of $x = 3.89$). The interval $-1 < x < 0$ corresponds to the entry of the jet and, therefore, C_f is not defined therein.

point of the flow, both coefficients increase. This is a manifestation of the adverse pressure gradient that is formed due to the expansion of the two streams. Further downstream and up to the outflow boundary, the values of C_f remain higher than at the inlet of the crossflow. This is attributed, primarily, to the thinning of the boundary layer due to the acceleration of the flow (the incoming jet increases the flow rate across the channel by approximately 50%) and, secondarily, to the increased shear viscosity resulting from the lower temperatures near the top wall.

As concerns the comparison between the two simulations, the predictions of the LES agree fairly well with those of DNS for both C_f and C_p. However, we note a small deviation (approximately 10%) in the prediction of the separation and reattachment points, upstream and downstream the entry of the jet, respectively. In addition, it mildly underpredicts the amplitude of C_f in the region of the recirculation bubble and the favourable pressure gradient close to the entry of the jet.

In figure 5.8 we present the plots of C_f and C_p at the bottom wall. In the

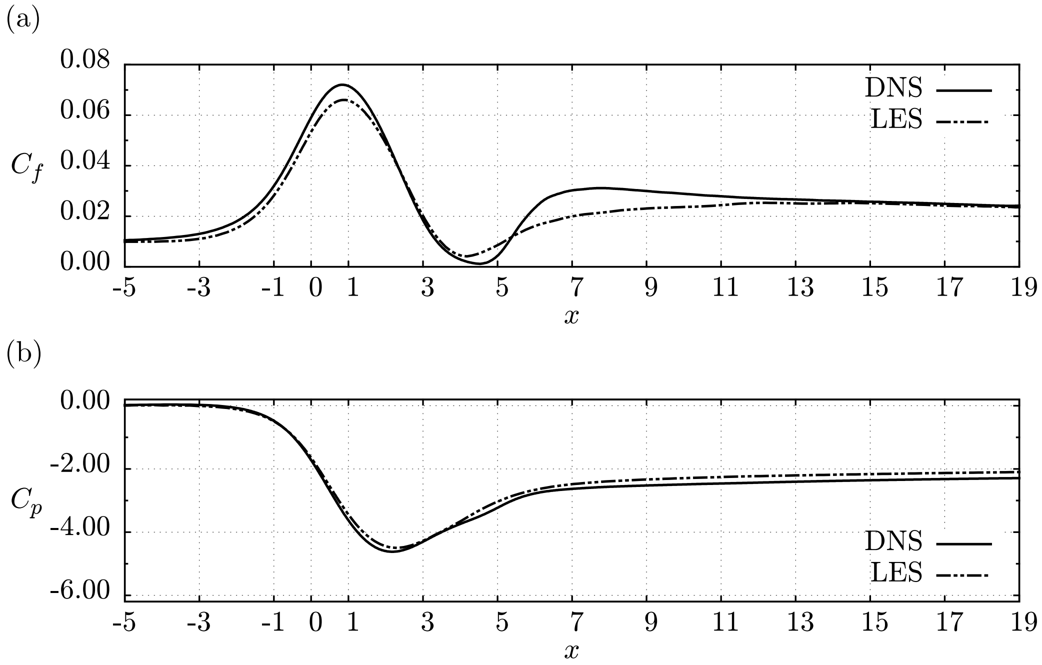

Figure 5.8: Plots of the skin friction and pressure coefficients, C_f and C_p, at the bottom wall of the horizontal channel. (a) C_f, (b) C_p.

interval, $-1.0 < x < 1.0$ they follow opposite trends as the former increases while the latter decreases, which is direct consequence of the Venturi effect that the crossflow experiences in this region. This results to the local relaminarization of the flow which leads to the formation of a favourable pressure gradient and the increase of the wall shear stress τ_w. As described in the previous chapters, the relaminarization of the flow is limited to a small region, see figures 3.13 and 4.10 and the relevant discussion therein. In fact, slightly downstream, the crossflow starts to expand and an adverse pressure gradient is formed. In this region, the flow tends to separate but C_f remains positive across the bottom wall. Regarding the comparison between the two simulations, the predictions of the LES are very close and almost collapse with the ones of DNS for C_p. However, as regards the friction coefficient C_f, the LES profile is somewhat diffused with respect to the DNS predictions. Nevertheless, overall LES compares satisfactorily with DNS.

5.3.1 Instantaneous flow structures

In this section we examine the instantaneous flow structures, as extracted from the DNS data. In our analysis we focus on the primary and secondary shear layers and assess their contribution to the mixing process in the T-junction. We also investigate the effect of the incoming jet on the flow structures near the top and bottom walls. All the figures presented herein show results at the same time instance.

In figure 5.9 we provide contour plots of the amplitude of the instantaneous spanwise vorticity $|\omega_z|$ and normalised temperature θ,

$$\theta = \frac{T - T_{\mathrm{jet}}}{T_{\mathrm{ref}} - T_{\mathrm{jet}}} . \tag{5.8}$$

The results shown in this figure are taken at the xy-plane defined by $z = 1.24$. Both shear layers roll up quickly, leading to the formation and shedding of spanwise rollers such as the one spotted at the secondary layer and at $x \approx 1.8$, see figure 5.9a. These rollers merge with adjacent ones in a pairing process or they are torn apart and their vorticity is absorbed by the surrounding vortical structures. Most of the surviving rollers are convected downstream but some of them interact with the large recirculation bubble and eventually get entrapped therein. Also, as the two shear layers spread, they start to interact and eventually they merge. Downstream the reattachment point of the flow, the merged shear layer continues to spread and eventually extends across the entire channel. In fact, downstream the station $x = 6.0$, many of its rollers interact with the bottom wall. Additionally, we can observe numerous thin and elongated vortical structures close to the bottom wall for $4 < x < 7$. Their formation is attributed to the deceleration of the flow caused by the adverse pressure gradient in this region, see figure 5.8b.

With regard to the instantaneous temperature field, shown in figure 5.9b, we remark that thermal mixing is initiated by the spanwise rollers of the primary shear layer close to the upstream corner of the entry of the jet. The mixing process is significantly enhanced once the two shear layers start to interact with each other. Also, downstream the large recirculation bubble, we can observe the effect of the surviving rollers as they transport hot fluid originating from the crossflow toward the top wall.

In figure 5.10 we show iso-surface plots of the fluctuating pressure at the value $p' = -0.25$. Such plots are frequently used for the identification of large coherent structures. In our case, this particular value, $p' = -0.25$, has been chosen because it provides a clearer visualisation of these structures. The growth of the spanwise rollers from the secondary shear layer can be inferred from the three-dimensional view of figure 5.10a. These rollers are convected downstream and eventually are torn apart into smaller structures in a highly turbulent environment. Also, from figure 5.10b which shows a projection of the iso-surface plot of p' at the xz-plane,

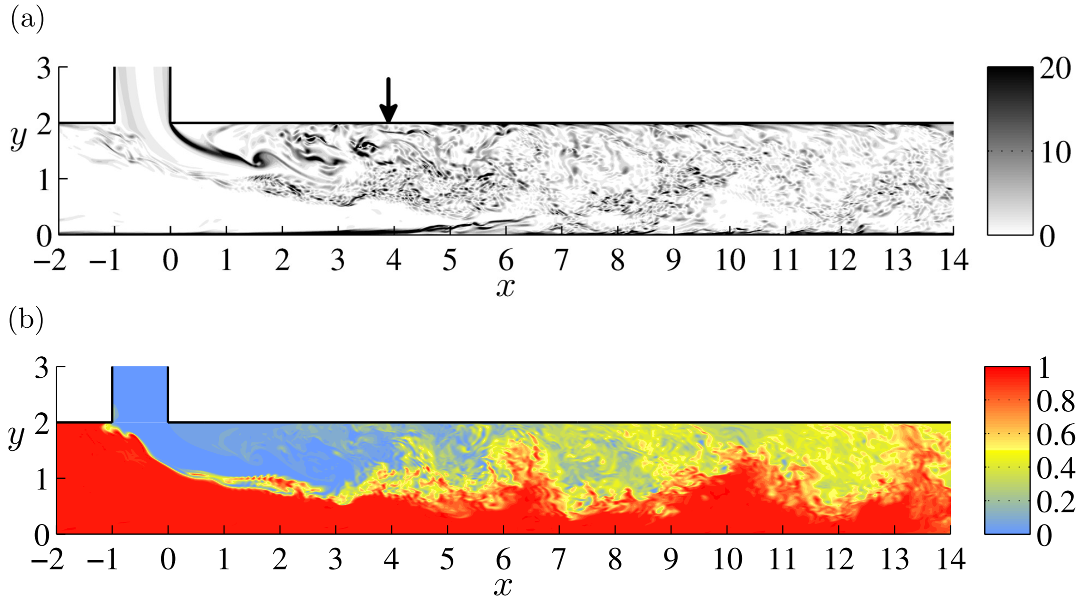

Figure 5.9: Contour plots of the amplitude of the instantaneous spanwise vorticity $|\omega_z|$ and normalised temperature θ at $z = 1.24$. (a) $|\omega_z|$, (b) θ. In figure (a) we observe the formation of a large spanwise roller at the secondary shear layer at $x \approx 1.8$. With the arrow in figure 5.9a we show the reattachment point as predicted from DNS.

we can observe the formation of streamwise vortex tubes, known as "rib" vortices, that connect two adjacent spanwise rollers. On the other hand, the smaller vortex tubes close to the upstream corner of the entry of the jet, $x = 0.0$, are part of the primary shear layer. Examination of the streamwise vorticity field (not shown herein) has revealed that eventually they break up into smaller ones.

In order to elucidate the role of these streamwise vortex tubes to the mixing process, in figure 5.11 we present contour plots of θ at two streamwise stations, namely, at $x = 0.0$ and $x = 3.0$. At the first station, these tubes are located at the primary shear layer and are part of mushroom-like structures that are formed right at the interface of the two streams. A mushroom moving upwards is formed by fluid coming from the crossflow and wraps around itself cold fluid from the incoming jet, thus forming a spiral [111]. Inversely, a mushroom moving downwards is formed by fluid coming from the jet and wraps around itself hot fluid from the crossflow. Such mushroom-like structures are typical of turbulent mixing layers [112–114] and have also been observed experimentally in the shear layers of T-junctions [11]. At the second station, $x = 3.0$, the primary and secondary shear layers have started to interact and these mushroom-like structures have already

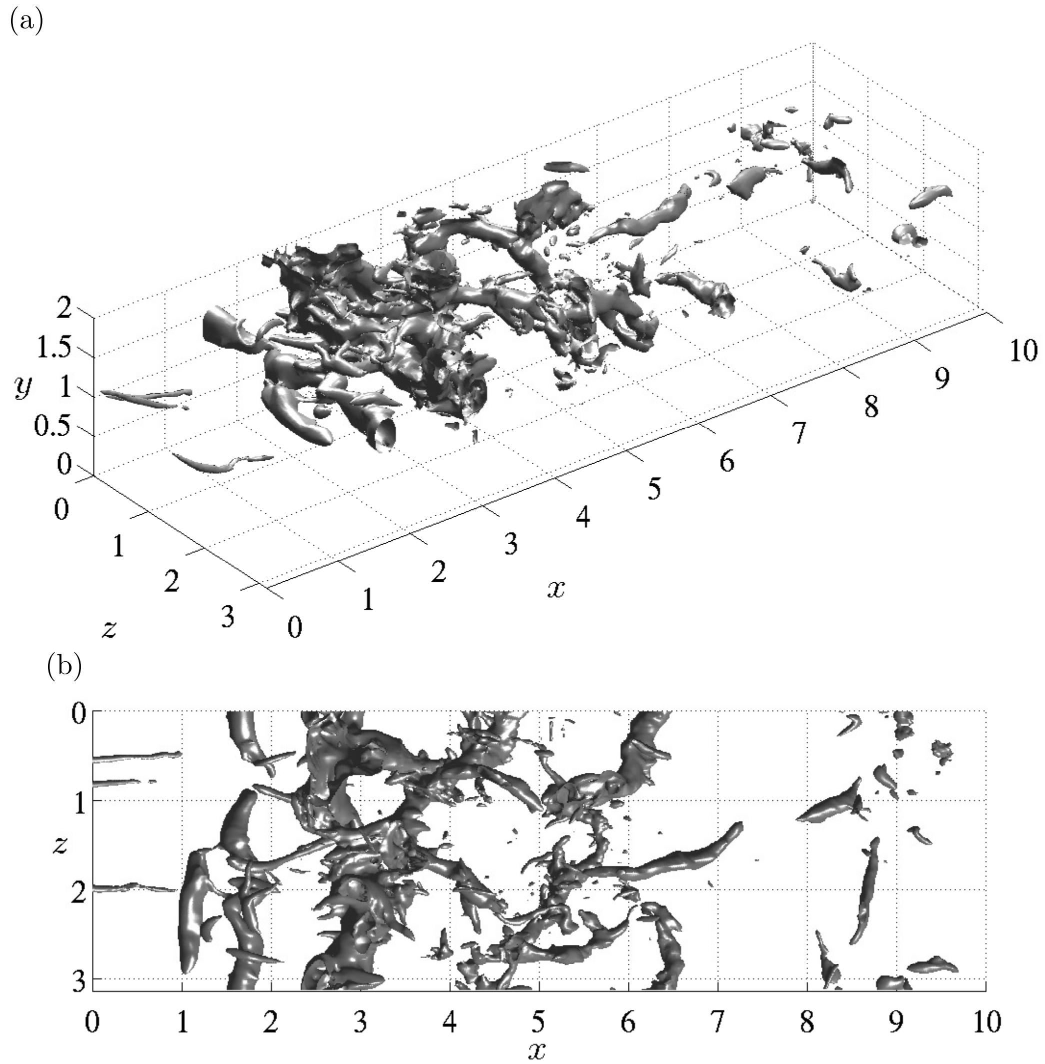

Figure 5.10: Iso-surface plots of the fluctuating pressure at the value $p' = -0.25$. (a) Three-dimensional view, (b) view from above (xz-plane). The large spanwise rollers shown in these plots are shed by the secondary shear layer. Also, the streamwise vortex tubes connecting two consecutive rollers correspond to "rib" vortices.

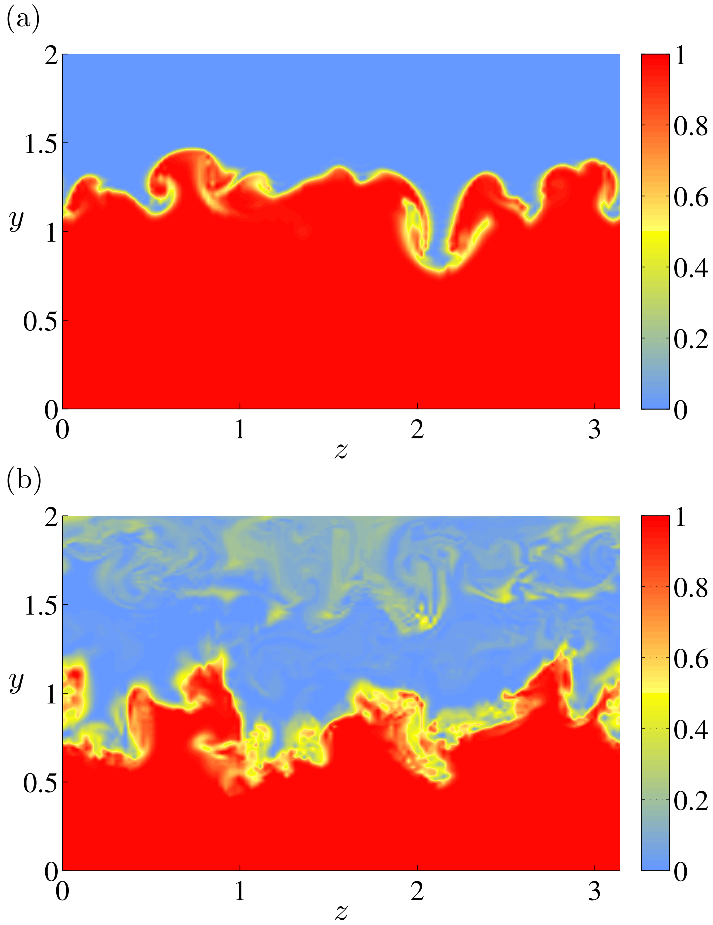

Figure 5.11: Contour plots of the instantaneous normalised temperature θ at two streamwise locations. (a) $x = 0.0$, (b) $x = 3.0$. In figure 5.11a we can observe the formation of mushroom-like structures of streamwise vorticity at the primary shear layer. However at $x = 3.0$, figure 5.11b these strcutures have already been broken up.

broken up. Instead, the vorticity field therein is dominated by the large spanwise rollers of the secondary shear layer.

Our analysis of the instantaneous flow structures concludes with the examination of the near-wall regions. In figure 5.12 we present contour plots of the instantaneous streamwise velocity u close to the walls of the horizontal channel. In the vicinity of the reattachment point of the flow, vortical structures emanating from the shear layers interact with the top wall, leading to the formation of several irregularly shaped streaks. On the other hand, further downstream, the adverse pressure gradient results in the widening and weakening of the velocity streaks. This feature is typical of regions of adverse pressure gradient; see, for example the discussion in [115] and [17]. At the bottom wall and in the region $4 < x < 5$, there

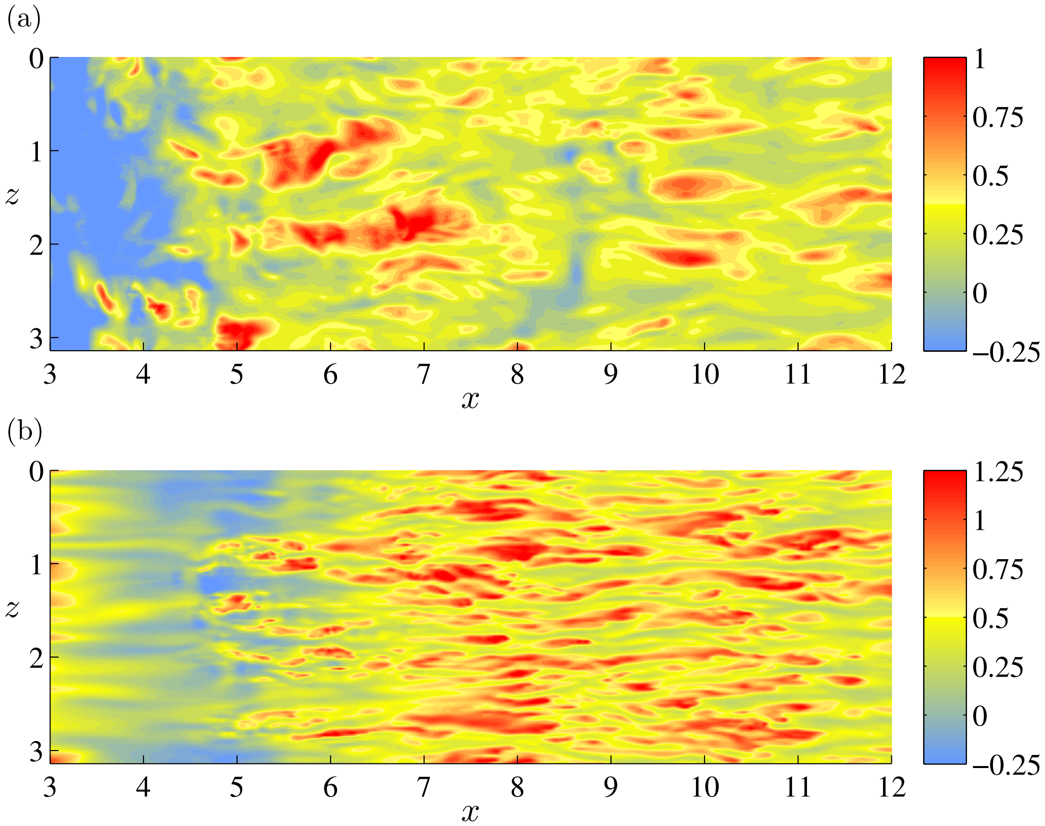

Figure 5.12: Contour plots of the instantaneous streamwise velocity u close to the two walls of the horizontal channel. (a) top wall, $y = 1.98$, (b) bottom wall, $y = 0.02$.

are patches of negative streamwise velocity. This is also due to the adverse pressure gradient which causes the flow to decelerate. It should be noted, however, that this concerns instantaneous values and that the mean streamwise velocities remain positive close to the bottom wall. Also, further downstream, we can identify zones with numerous velocity streaks. These streaks are much longer and thinner than the ones observed near the top wall and are caused by the interaction of vortices from the merged shear layer with the bottom wall.

Finally, in figure 5.13 we show a representation of the instantaneous vorticity field at the walls, based on the quantity Q. This quantity, first introduced by Hunt et al. [83], measures the difference between the amplitudes of the skew-symmetric and symmetric parts of the velocity-gradient tensor, and it aids the visualisation of the vorticity field. In particular, positive values of Q correspond to non-zero vorticity amplitude. Also, the higher the value of Q is, the higher the vorticity amplitude gets. In figure 5.13 we have plotted the iso-surface of the value $Q = 4.0$. At the top wall, we can observe numerous irregularly oriented vortical structures in the region covered by the large recirculation bubble. Downstream the reattachment of the flow, the density of these structures gradually decreases. The dense patches of interwoven vorticity that can be observed in this region coincide with the widened velocity streaks observed in figure 5.12a.

According to figure 5.13b, near the bottom wall there are very few vortical structures for $x < 4$. This is the region where the crossflow accelerates due to the Venturi effect. Downstream this region, we observe a large number of vortical structures. Some of them are formed due to the adverse pressure gradient caused by the expansion of the crossflow, while others are transported by the merged shear layer which spreads and interacts with the bottom wall. We also remark that the density of the vortical structures at the bottom wall is higher than at the top wall, despite the fact that, due to the trajectory of the jets and the unstable stratification, there are more vortices moving upwards that downwards. This difference may be attributed to the lower temperature and, therefore, higher viscosity of the fluid at the top which enhances dissipation of the vortical structures.

5.3.2 Statistics of the temperature field

In this section we present the first and second-order statistics of the temperature field for both DNS and LES. The behaviour of the temperature bears significant similarities with the one described in chapter 4, for $T_R = 1.17$. This can be seen in figure 5.14, where we show the profiles of the averaged normalised temperature field $<\theta>$. The main feature of these profiles is the transition zone from the high temperature at the bottom to the low temperature at the top. Close to the entry of the jet, this transition takes place across the primary shear layer. Also, at the stations $x = 1.0$ and $x = 3.0$, *i.e.* at the large recirculation bubble, the temperature profile is not monotonic but attains a minimum at the core of the secondary shear layer. In other words, the temperature in the recirculation bubble is higher than in the secondary layer. This implies that the bubble does not consist solely of fluid from the incoming jet but it also contains fluid originating from the hot crossflow. Further downstream, the two shear layers merge and a monotonic temperature profile is established due to thermal mixing. As the flow evolves and thermal mixing progresses, the temperature gradients become weaker. Also, the temperature profile becomes almost linear, as can be asserted from figure 5.14f. Since the solid walls are adiabatically isolated, a channel flow of uniform temperature will eventually emerge; however, thermal equilibrium is not established within the limits of our computational domain.

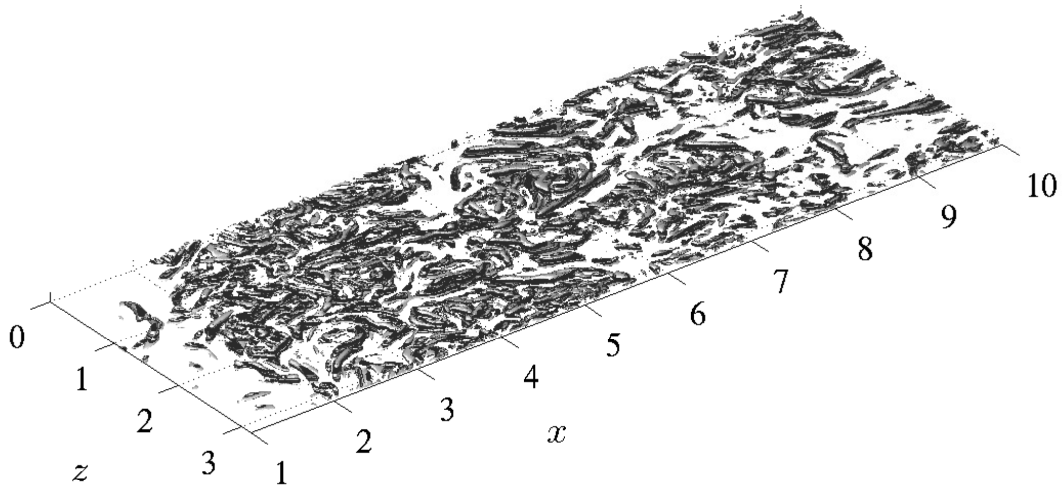

(a)

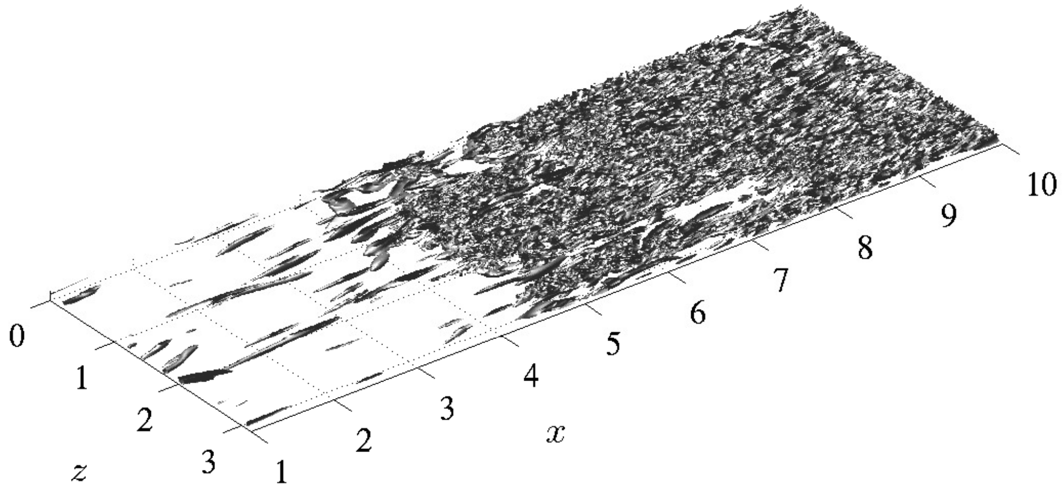

(b)

Figure 5.13: Iso-surface plots of the Q-criterion ($Q = 4.0$) at the wall regions. (a) top wall, (b) bottom wall.

As regards the comparison between the two simulations, the predictions of the LES agree very well with those of DNS. Nonetheless, LES is a little more diffusive. For example, it predicts that the fluid inside the recirculation bubble is at a slightly higher temperature. Further, a larger decrease in $<\theta>$ is noted at the bottom wall, at $x = 12.0$ and $x = 16.0$.

The profiles of the rms normalised temperature θ_{rms} are shown in figure 5.15. Their most characteristic feature is the peak due to the primary shear layer. At $x = 1.0$ this peak is very sharp. However, as the shear layer spreads out, the value of the peak drops and its location moves closer to the bottom wall. This in turn, implies that thermal mixing is most intense in the region between $x = 0.0$ and

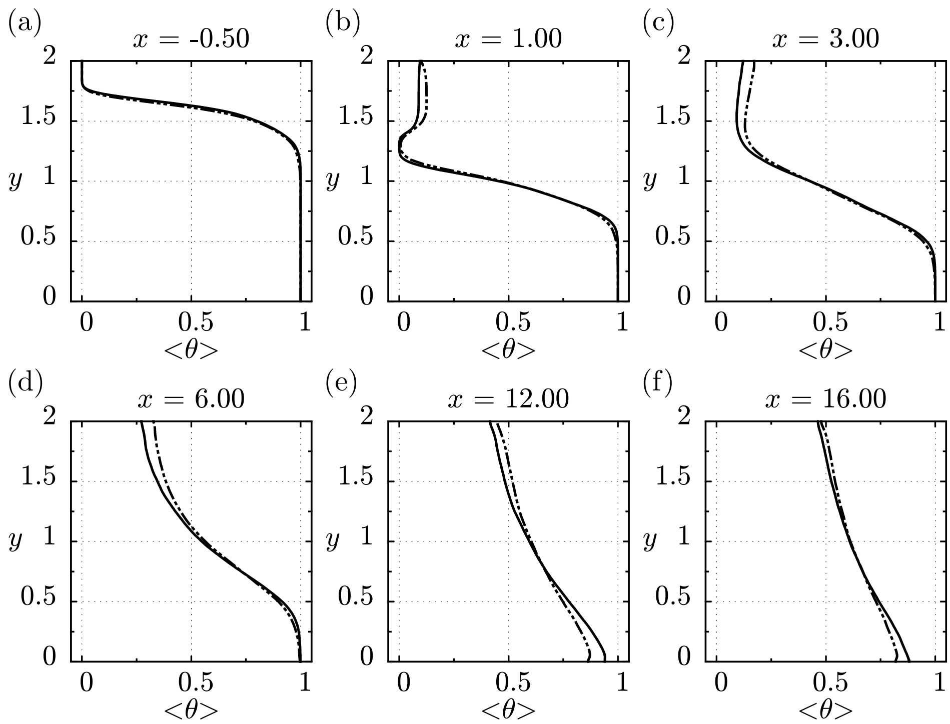

Figure 5.14: Profiles of the mean normalised temperature <θ> at different stations of the horizontal channel. —, DNS; ----, LES.

$x = 4.0$. Finally, it is worth mentioning that the predictions of the LES agree very well with those of the DNS, albeit the LES mildly underpredicts the amplitudes of the peaks of θ_{rms} at $x = 1.0$ and $x = 3.0$.

5.3.3 Statistics of the velocity field

In this section we present the first and second-order statistics of the velocity field. As expected, the predictions for these statistics have certain similarities with the case of gaseous flows in T-junctions, treated in chapter 4 and more specifically the case $T_R = 1.17$. The profiles of the mean streamwise velocity <u> are shown in figure 5.16. The negative values at the top wall for $x = 1.0$ and $x = 3.0$ occur inside the recirculation bubble. Also, the high wall-normal gradients of <u> that can be seen at these streamwise stations correspond to the secondary shear layer. Downstream the reattachment of the flow, the mean velocity approaches a channel-flow profile, albeit at a slow rate as can be attested by the asymmetry of the profiles shown in figures 5.16d - 5.16f. We also remark that the LES predictions of <u> compare quite favourably with the DNS data at all streamwise stations.

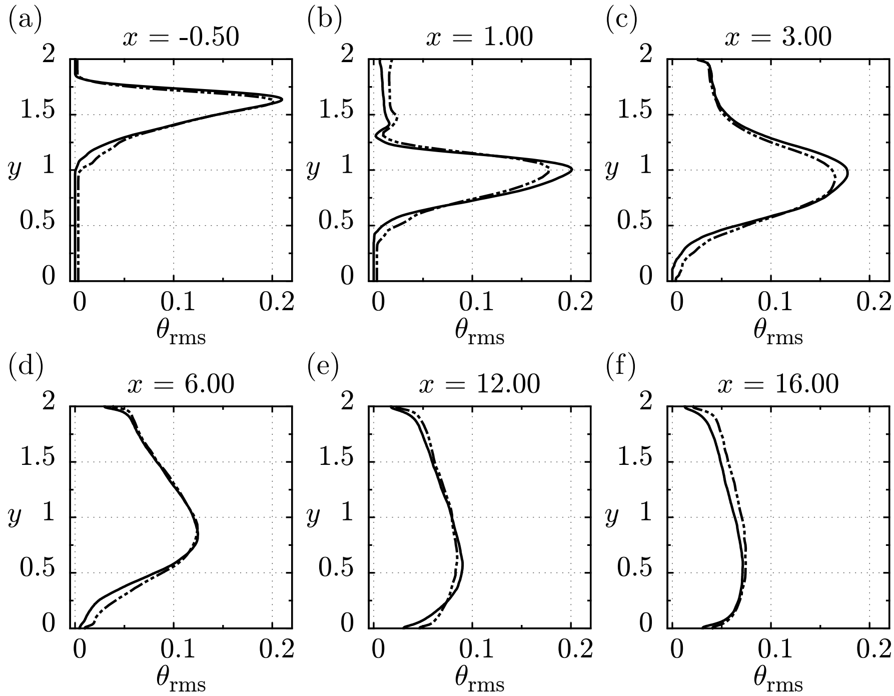

Figure 5.15: Profiles of the rms of the normalised temperature θ_{rms} at different stations of the horizontal channel. —, DNS; -···-, LES.

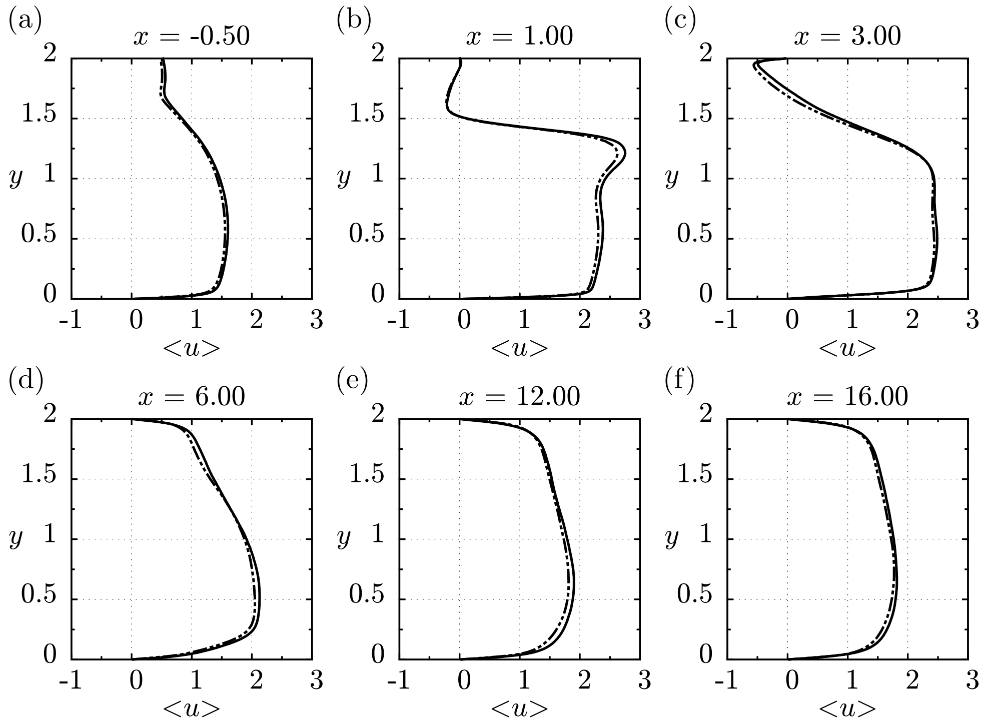

Figure 5.16: Profiles of the mean streamwise velocity $<u>$ at different stations of the horizontal channel. —, DNS; -···-, LES.

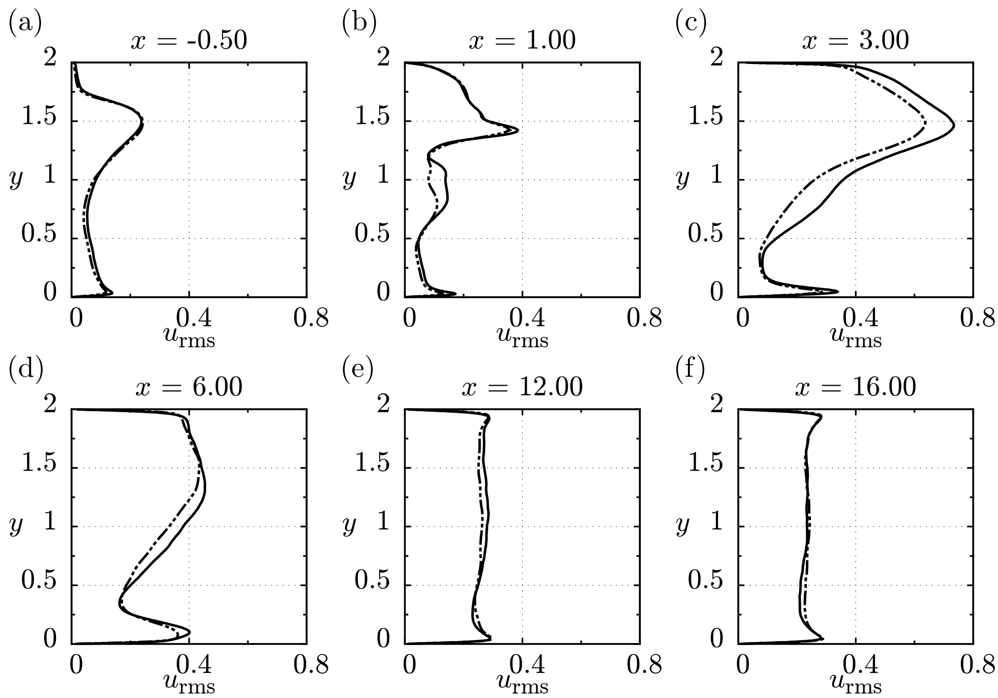

Figure 5.17: Profiles of the rms of the streamwise velocity u_{rms} at different stations of the horizontal channel. —, DNS; -·-·-, LES.

In figure 5.17 we present plots of the rms profile of the streamwise velocity, u_{rms}. The observed peak at $x = -0.50$ corresponds to the primary shear layer. At $x = 1.0$, due to the turning of the two streams, this shear layer is at a lower location. The peak rms inside the shear layer occurs right below the mid-plane of the channel and its value is decreased due to the spreading of the layer. On the other hand, the strong peak at $y \approx 1.5$ is due to the secondary shear layer. We also observe that at $x = 3.0$ the values of u_{rms} below the mid-plane have increased. This is attributed to turbulence generation inside the recirculation bubble and near the bottom wall due to the adverse pressure gradient. Further downstream, u_{rms} becomes almost constant away from the walls and its profile starts to resemble the one in channel flows. By contrast, in the corresponding gas flow, described in chapter 4, the profile of u_{rms} varies considerably across the channel even at large distances from the recirculation bubble. This difference is due to the fact that the flow under study involves liquids and, therefore, buoyancy effects are not as significant as in flows involving gases.

The rms profiles of the wall-normal and spanwise velocities are shown in figures 5.18 and 5.19, respectively. At $x = -0.5$, the observed peak of these profiles corresponds to the primary shear layer. Also, at the streamwise station $x = 1.0$,

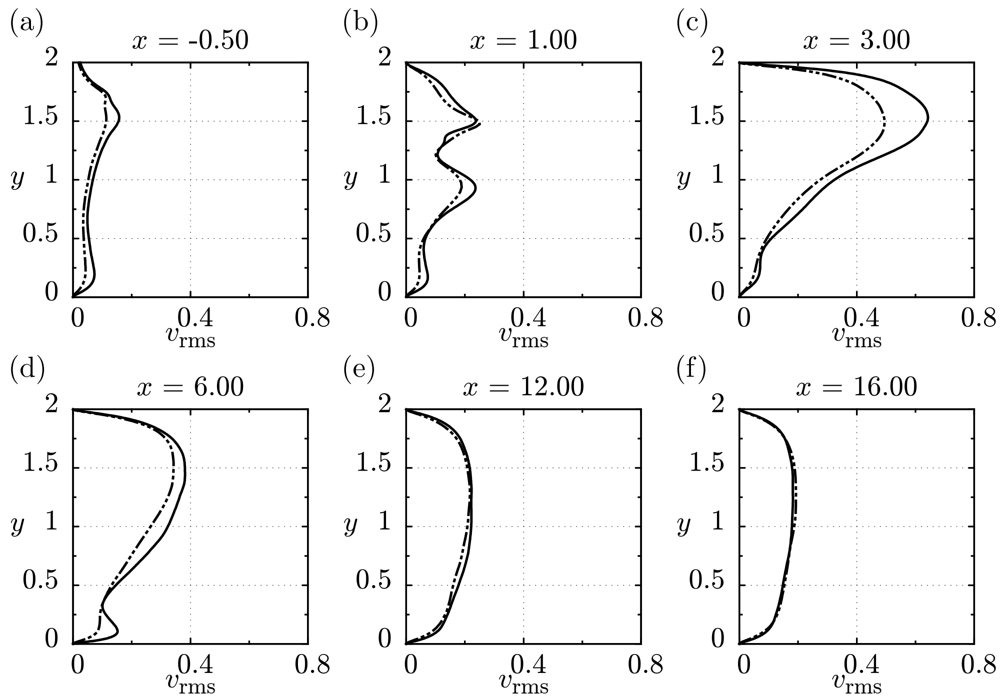

Figure 5.18: Profiles of the rms of the wall-normal velocity v_{rms} at different stations of the horizontal channel. —, DNS; -···-, LES.

the profiles of both v_{rms} and w_{rms} are characterised by a double-peak structure. The upper peak corresponds to the secondary and the lower peak to the primary shear layer. This structure was observed in chapter 4 where we examined gas flow in T-junctions but not in chapter 3 where we studied isothermal flows in T-junctions. We may therefore infer that this double-peak structure is due to the role of the temperature as an active scalar. More specifically, the primary shear layer enhances significantly the mixing between the crossflow and the incoming jet when these two streams are not at the same temperature. On the other hand, the large rms values observed inside the recirculation bubble, figures 5.18c and 5.19c, are a common feature of both isothermal and variable-temperature flows in T-junctions.

As regards the accuracy of the LES, from figures 5.17–5.19 we can infer that it captures fairly well the rms profiles of all velocity components. Nonetheless, there are some discrepancies; most notably, the LES underpredicts the rms values inside the recirculation bubble by up to 25%.

Our discussion on the velocity statistics concludes with the presentation of the Reynolds stresses $<u'v'>$ that are shown in figure 5.20. At the streamwise station $x = 1.0$ they assume an S-shaped profile across the shear layers. Similar profiles

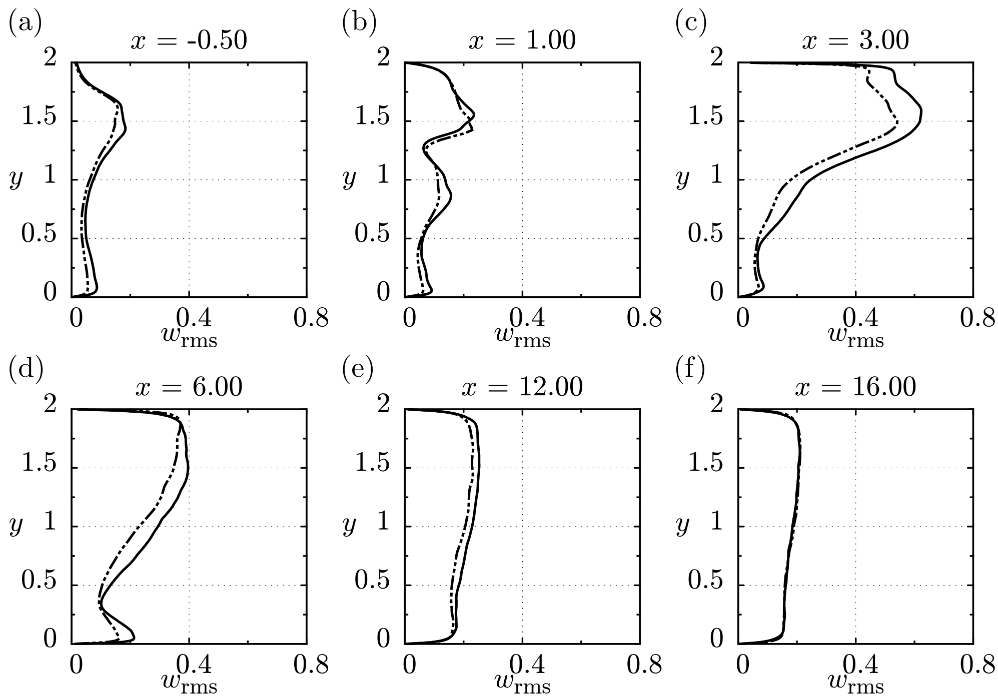

Figure 5.19: Profiles of the rms of the spanwise velocity w_{rms} at different stations of the horizontal channel. —, DNS; -··-, LES.

have been predicted for shear layers at an interface between a pure fluid and a porous medium [116, 117]. In our case, the large negative peak corresponds to the core of the primary shear layer, whereas the large positive peak corresponds at the core of the secondary layer. Further, the secondary peak at $x = 1.0$ close to the top wall ($y \approx 1.75$) is due to the secondary recirculation zone located next to the downstream corner of the entry of the jet, cf. figure 5.5.

5.3.4 Statistics of turbulent heat fluxes

Our discussion of the flow statistics concludes with the results for the turbulent heat fluxes $<\theta' u'>$ and $<\theta' v'>$. Their profiles at different streamwise stations are shown in figures 5.21 and 5.22, respectively. We observe that for $x < 3$, the peaks of these profiles correspond to the core of the primary shear layer. In other words, the primary shear layer provides the main mechanism for thermal mixing. By comparison, the contribution of the secondary shear layer is very small. Further downstream, the amplitudes of both fluxes drop significantly as the merged shear layer spreads out. Another interesting point is that inside the recirculation bubble ($x = 3.0$), both turbulent fluxes are negative, *i.e.* they are directed upstream and downwards, respectively. This implies that, at this station, heat is transferred from

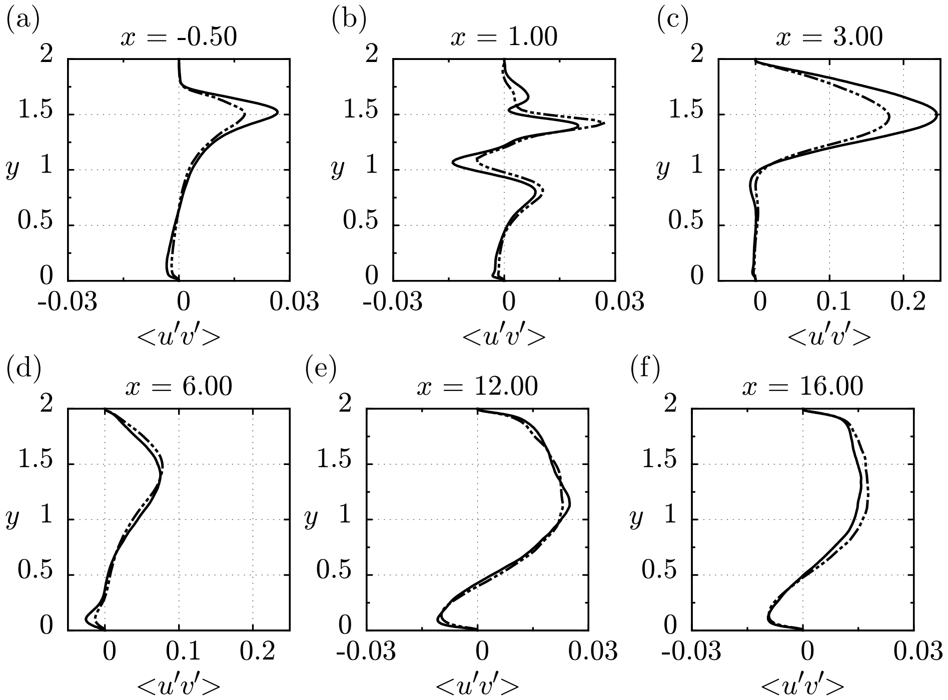

Figure 5.20: Profiles of the Reynolds stress $<u'v'>$ at different stations of the horizontal channel. —, DNS; -··-, LES. For purposes of clarity, the limits of the horizontal axis in figures 5.20c and 5.20d are different than in the other figures.

the outer parts of the bubble toward its core. This is due to vortical structures emanating from the shear layers that get trapped inside the bubble.

Finally, we remark that the LES predictions agree fairly well with the DNS, especially as regards $<\theta'v'>$. The only noticeable disagreement is that the LES overpredicts the values of $<\theta'u'>$ inside the recirculation bubble, and in the bottom half of the channel at $x = 6.0$. Based on the overall comparison of the first- and second-order statistics, we infer that the LES predictions for the flow under study are satisfactorily accurate, even though there are some minor to moderate discrepancies in regions of intense turbulence production.

5.3.5 Budget of the turbulent kinetic energy

In this section we present the budget of the kinetic energy of the velocity fluctuations, $k' = <\boldsymbol{u}' \cdot \boldsymbol{u}'>/2$ based on the DNS results. The equation for the Turbulent Kinetic Energy (TKE) is obtained by subtracting the equation for the mean kinetic energy, $<k> = (<\boldsymbol{u}> \cdot <\boldsymbol{u}>)/2$ from the equation for the total kinetic energy, $k = (\boldsymbol{u} \cdot \boldsymbol{u})/2$, of the flow. However, the derivation of the equation for the TKE in

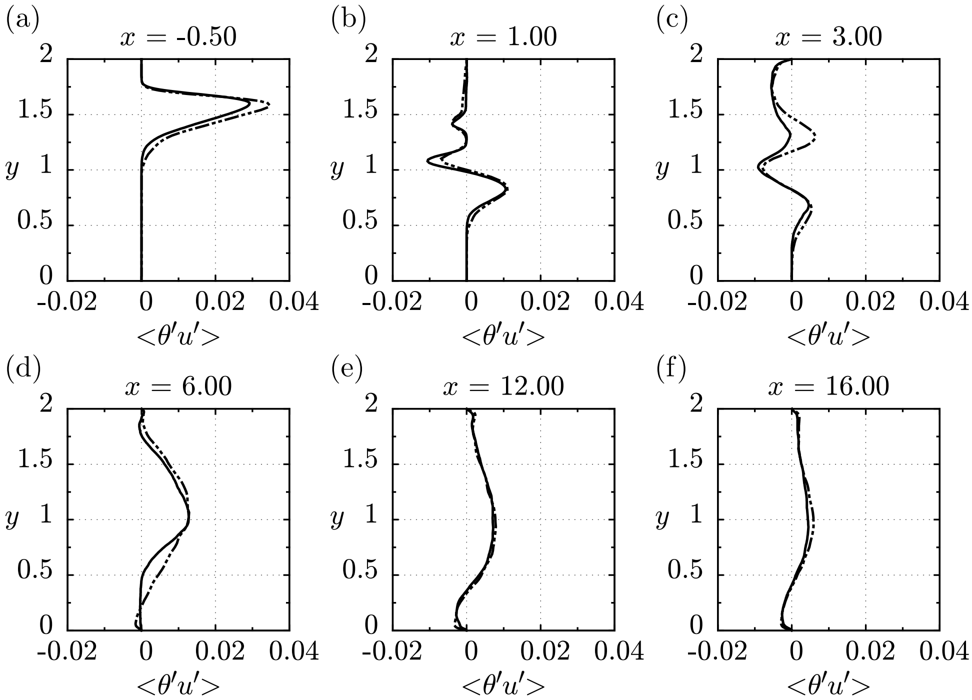

Figure 5.21: Profiles of the streamwise turbulent heat flux $<\theta' u'>$ at different stations of the horizontal channel. —, DNS; -··-, LES.

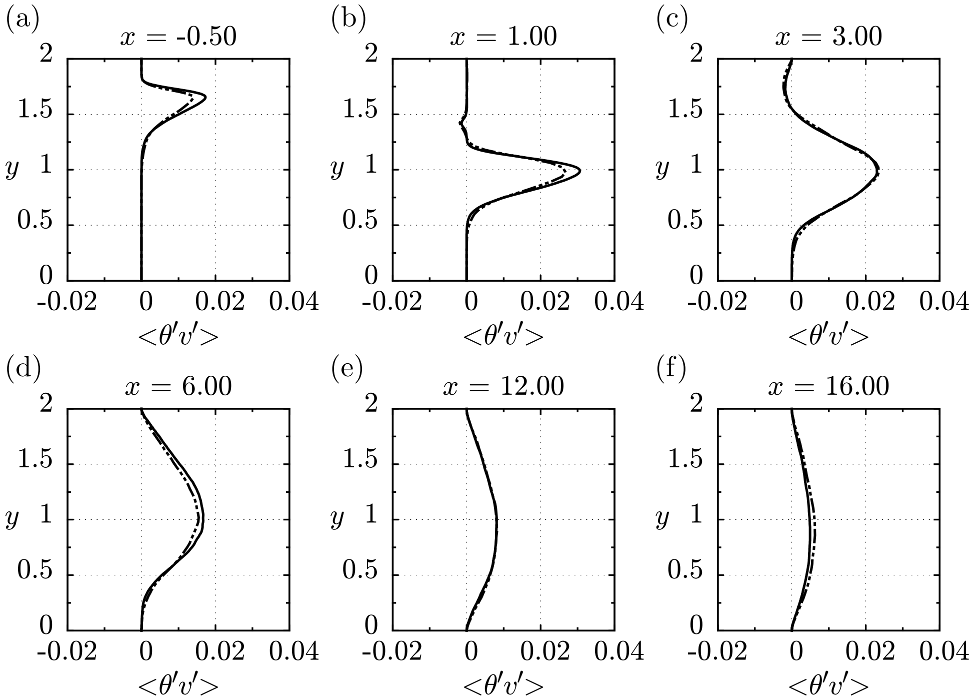

Figure 5.22: Profiles of the wall-normal turbulent heat flux $<\theta' v'>$ at different stations of the horizontal channel. —, DNS; -··-, LES.

variable-density flows is more complicated than for constant-density flows. This is because in variable-density flows the averaging operation, $<\cdot>$, introduces correlations with density fluctuations. For example, when averaging is applied into the non-linear term in the momentum equation, $\rho\boldsymbol{u}\boldsymbol{u}$, one obtains

$$<\rho\boldsymbol{u}\boldsymbol{u}> = <\rho><\boldsymbol{u}><\boldsymbol{u}> + 2<\rho'\boldsymbol{u}'><\boldsymbol{u}> + <\rho><\boldsymbol{u}'\boldsymbol{u}'> + <\rho'\boldsymbol{u}'\boldsymbol{u}'>\,, \quad (5.9)$$

while in constant-density flows one simply gets

$$<\rho\boldsymbol{u}\boldsymbol{u}> = \rho\left(<\boldsymbol{u}><\boldsymbol{u}> + <\boldsymbol{u}'\boldsymbol{u}'>\right)\,. \quad (5.10)$$

In order to simplify the resulting equation for the TKE, one may resort to the density-weighted averaging operation, also known as Favre averaging[1] [51], in terms in which density appears. For a generic quantity ϕ, the Favre decomposition reads $\phi = \{\phi\} + \phi''$ and the Favre-averaged quantity is computed by the following relation

$$\{\phi\} = \frac{<\rho\phi>}{<\rho>}\,. \quad (5.11)$$

An important feature of this decomposition is that the "Favrian" fluctuation is not centred, *i.e.* $<\phi''> \neq 0$. Additional relationships between the standard averaging operation and the Favre-averaging can be found in [118, 119].

The derived equation for the balance of $\{k''\} = \{\boldsymbol{u}''\cdot\boldsymbol{u}''\}/2$, in non-dimensional form read [119]

$$\begin{aligned}\frac{\partial <\rho>\{k''\}}{\partial t} = & -\underbrace{\nabla\cdot(<\rho>\ \{k''\}\{\boldsymbol{u}\})}_{C_k} \underbrace{-<\rho>\{\boldsymbol{u}''\boldsymbol{u}''\}:\nabla\{\boldsymbol{u}\}}_{P_k} \\ & -\underbrace{\nabla\cdot(<\rho>\ \{k''\,\boldsymbol{u}''\})}_{T_k} - \underbrace{\nabla\cdot(<p><\boldsymbol{u}''>)}_{\Phi_k} - \underbrace{\nabla\cdot<p'\boldsymbol{u}''>}_{\phi_k} \\ & + \underbrace{\langle p\,\nabla\cdot<\boldsymbol{u}''>\rangle}_{\Pi_k} + \underbrace{\frac{1}{Re}\nabla\cdot<\boldsymbol{\tau}\cdot\boldsymbol{u}''>}_{D_k} - \underbrace{\frac{1}{Re}<\boldsymbol{\tau}:\nabla\boldsymbol{u}''>}_{\epsilon_k}\,. \end{aligned} \quad (5.12)$$

[1] The Favre filtering has been introduced in chapter 2. Herein we introduce the concept of Favre-decomposition and averaging. The concepts of averaging and filtering are similar but conceptually different.

In the above equation, the term C_k describes convection of TKE, while the terms P_k and T_k represent production and transport of TKE, respectively. The terms Φ_k and ϕ_k describe the work of the mean and fluctuating pressures through fluctuating motions. Also, Π_k represents the pressure correlation with the dilatation fluctuation. Finally, D_k describes the viscous diffusion, which is the work of viscous stresses through fluctuating motions, whereas ϵ_k stands for the viscous dissipation. It should be mentioned that the work of the gravitational force does not enter the above equation.

In statistically stationary flows, the sum of all the terms on the right hand-side of equation (5.12) should be zero. Indeed, according to our DNS data, this sum is always very small and below 5% of the amplitude of the largest term in (5.12), which is an indication of the accuracy of our DNS. Further, since this sum is negligible, it is not included in the presentation of the results.

In figure 5.23 we present the TKE budget across the channel at $x = -0.5$. At this station, the main source of turbulence production is the primary shear layer, which can be confirmed by the high values of P_k therein. Also, T_k takes negative values inside this shear layer, which implies transport of turbulent kinetic energy from the core of the layer toward its edges. On the other hand, the turbulent convection term C_k follows the opposite trend since it is positive at the core and negative at the edges of the primary shear layer. As concerns the turbulent dissipation ϵ_k, it is approximately 3 times smaller than P_k. The high ratio between the production and dissipation terms, $P_k/\epsilon_k \approx 3$, corroborates the fact that, with respect to turbulent kinetic energy, the flow at this region is far from equilibrium.

The TKE budget at $x = -0.5$ and close to the bottom wall is shown in figure 5.23b. Therein, the boundary layer is subject to a favourable pressure gradient due to the aforementioned Venturi effect. The peak of the production term P_k occurs at $y^+ \approx 10$; this is somewhat lower than the location $y^+ \approx 12$ of the corresponding peak in zero-pressure gradient boundary layers [120, 121]. Further, the production term is mostly balanced by the work of the fluctuating viscous forces D_k. Finally, as expected, closer to the wall all terms vanish except for D_k which is balanced by the viscous dissipation.

The profiles of the TKE budget at $x = 1.0$ are plotted in figure 5.24. The basic features of the budget are the high amplitudes of the production and convection terms in the zone occupied by the secondary shear layer. In fact, the peak of the production term is an order of magnitude higher than the one at $x = -0.5$, which confirms that the interaction of the incoming jet with the recirculation bubble is a major source of turbulence generation. Also, the negative values of the convection

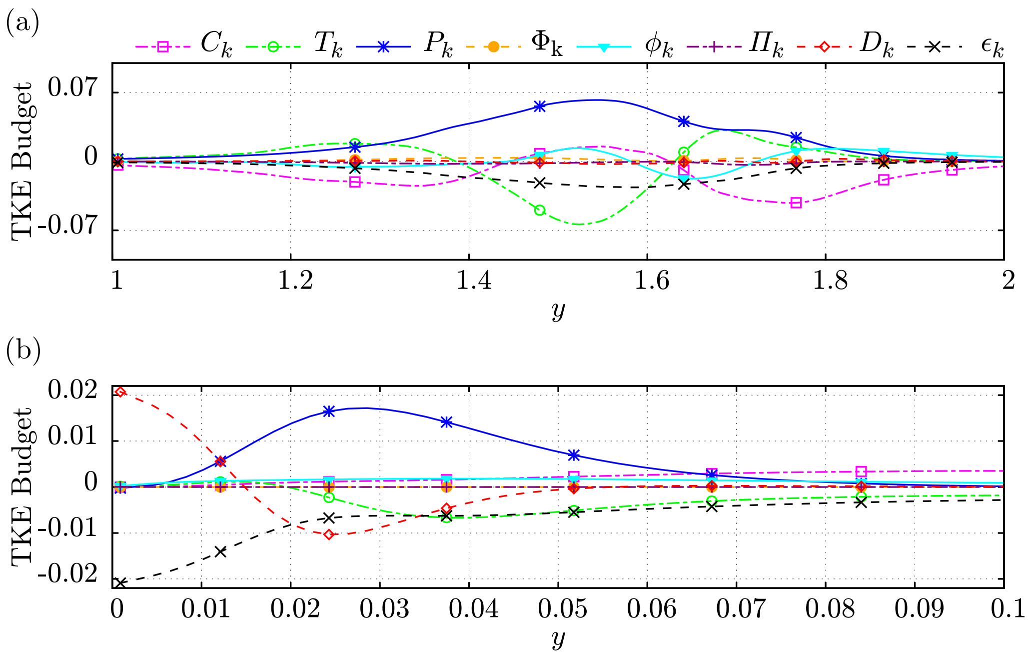

Figure 5.23: Budget of the turbulent kinetic energy at $x = -0.5$. (a) bulk of the channel, (b) close-up look at the bottom wall.

term C_k express the fact that TKE is convected from the core of secondary shear layer toward its edges and the core of the bubble. At the bottom wall, the pressure gradient is still favourable. Therefore, the profiles of the terms of the TKE budget are similar to those at $x = -0.5$.

The TKE budget at $x = 3.0$ is presented in figure 5.25. The spreading of the shear layers and their merging lead to even higher values of turbulence production above the mid-plane. Also, the peak value of P_k is considerably higher; this is in accordance with the high rms velocities at this station that are plotted in figures 5.17 - 5.20. The production term is balanced by turbulence transport, convection, and dissipation. Interestingly, the convection term C_k takes negative values close to the mid-plane. However, inside the recirculation bubble it changes sign and becomes positive, which implies convective transport of turbulent kinetic energy from the reattachment region toward the centre of the bubble. This has also been observed in the simulations of flow in channel with constrictions by [77]. Also, near the bottom wall, the crossflow is subject to the adverse pressure gradient which results to large turbulence generation; see figure 5.25c. In fact, the near-wall peak of P_k, located at $y^+ \approx 12$, is 3 times higher than the corresponding peak at the upstream station $x = 1.0$. Moreover, according to figure 5.25c, the near-wall turbulence production is mostly balanced by C_k, D_k and ϵ_k.

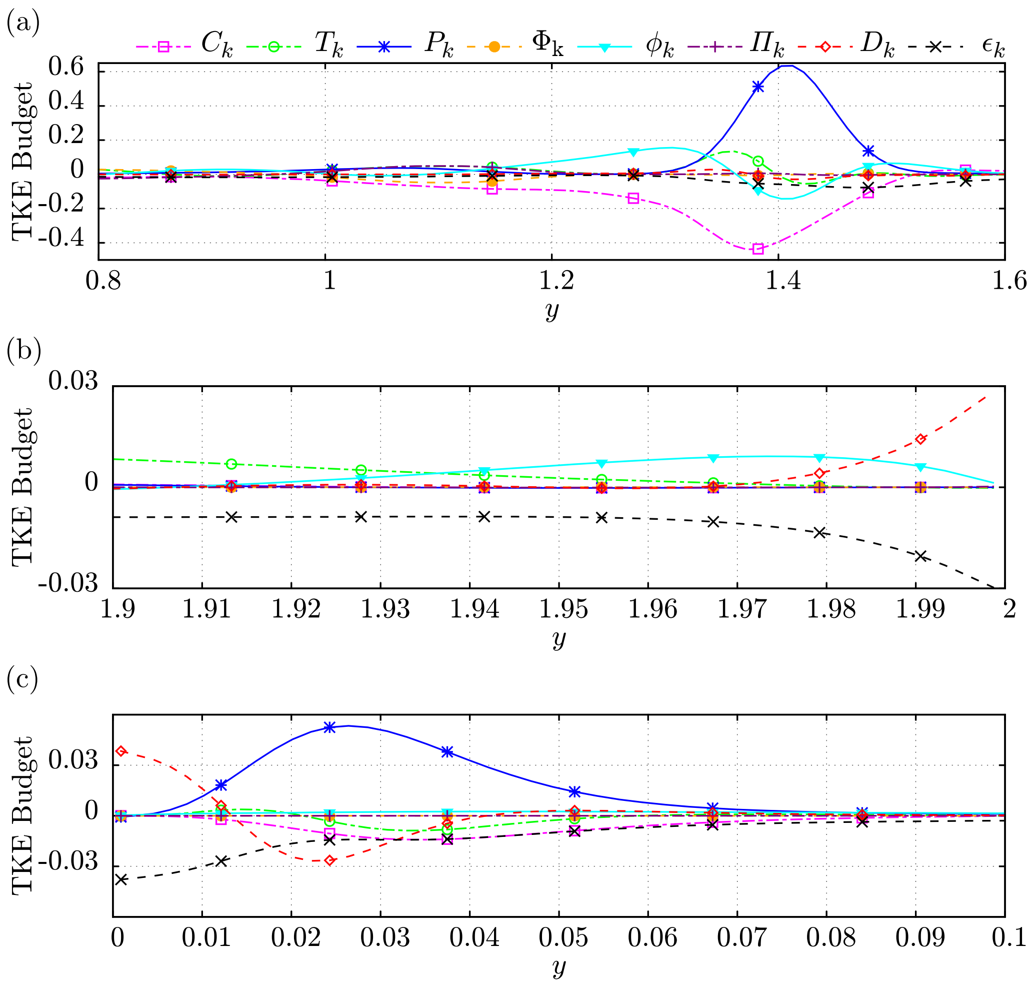

Figure 5.24: Budget of the turbulent kinetic energy at $x = 1.0$. (a) bulk of the channel, (b) close-up look at the top wall, (c) close-up look at the bottom wall.

Downstream the reattachment point of the flow, the amplitudes of all the terms in the TKE equation (5.12) decrease with x. In figure 5.26 we have plotted the TKE budget at $x = 6.0$. We observe that T_k is positive above and negative below the mid-plane, which implies transport of turbulent kinetic energy away from the walls and toward the bulk of the channel. Also, the amplitudes of the convective, production, and viscous dissipation terms are significantly higher at the top half of the horizontal channel, which is due to the spreading of the merged shear layer downstream the recirculation bubble. Additionally, the ratio P_k/ϵ_k is close to unity, which implies that TKE approaches equilibrium.

At the top wall, the amplitudes of the peaks of D_k and ϵ_k are significantly decreased while ϕ_k is still high at the viscous sublayer. At the bottom wall, the

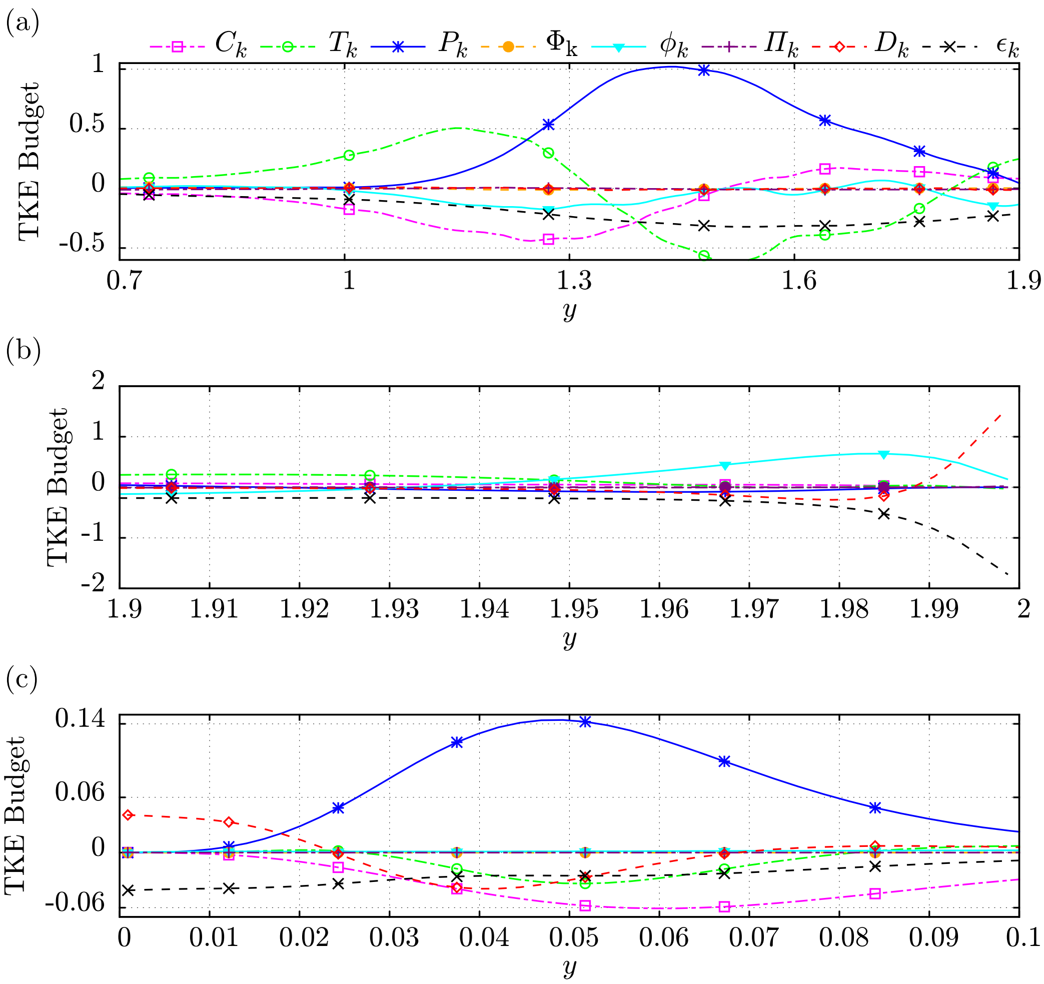

Figure 5.25: Budget of the turbulent kinetic energy at $x = 3.0$. (a) bulk of the channel, (b) close-up look at the top wall, (c) close-up look at the bottom wall.

adverse pressure gradient has vanished and the positive of P_k is balanced by T_k and the viscous dissipation, ϵ_k.

Finally, in figure 5.27 we provide the TKE budget far downstream, at the station $x = 12.0$. We can readily observe that as the flow evolves, the amplitudes of the various terms in the TKE budget decrease even further. Moreover, the profiles at the near-wall regions start to resemble those of zero pressure-gradient boundary layers; see, for example, [120] and [121].

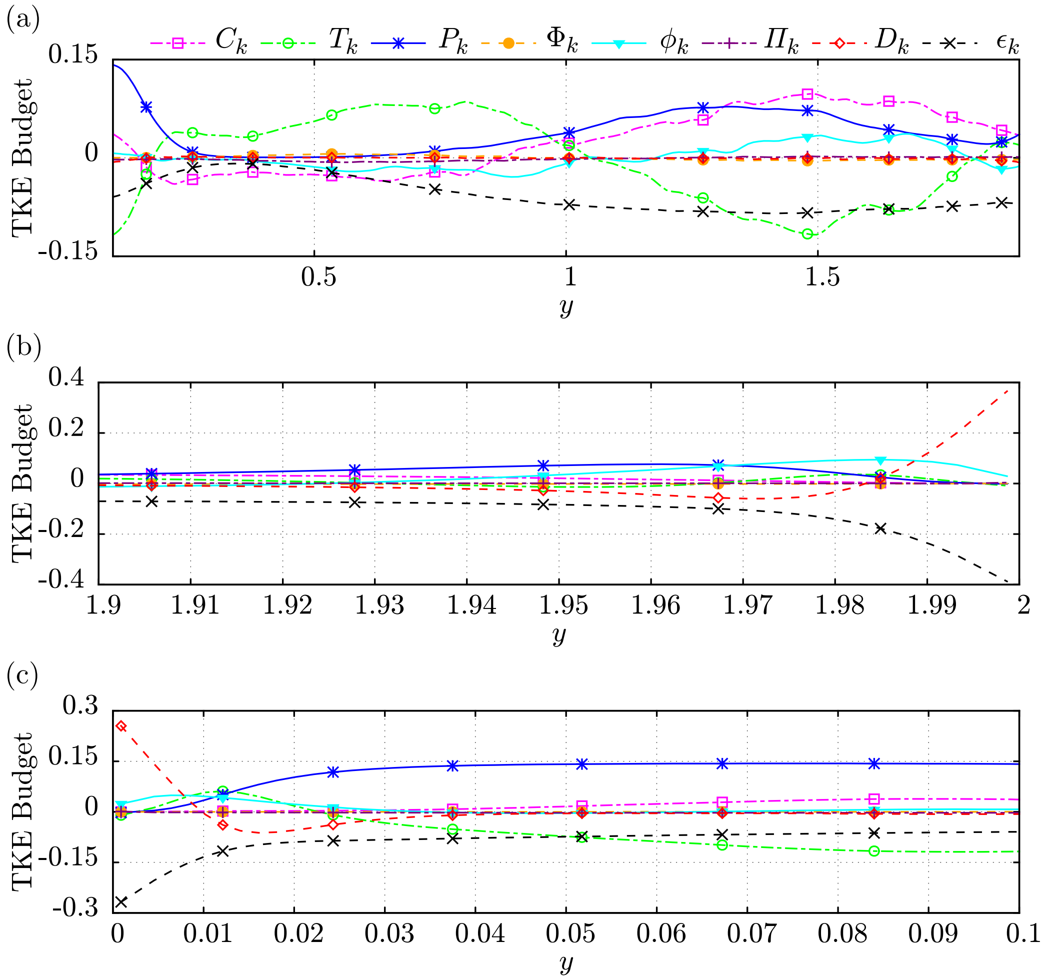

Figure 5.26: Budget of the turbulent kinetic energy at $x = 6.0$. (a) bulk of the channel, (b) close-up look at the top wall, (c) close-up look at the bottom wall.

5.3.6 Spectral analysis of the velocity and temperature signals

We conclude this chapter with an analysis of the time-series of the velocity vector and temperature signal. More specifically, for the DNS study, we record the spanwise averaged velocities $\overline{\boldsymbol{u}}(x, y)$ and temperature $\overline{T(x, y)}$ at selected (x, y) coordinates in the flow field.

As in chapter 4, we then compute the power spectral densities, $S_{uu}(f)$, $S_{vv}(f)$ and $S_{TT}(f)$, of these signals so as to estimate the characteristic frequencies f with which they oscillate. The frequency is then normalised with respect to the half-width of the horizontal channel and the bulk velocity of the crossflow, which

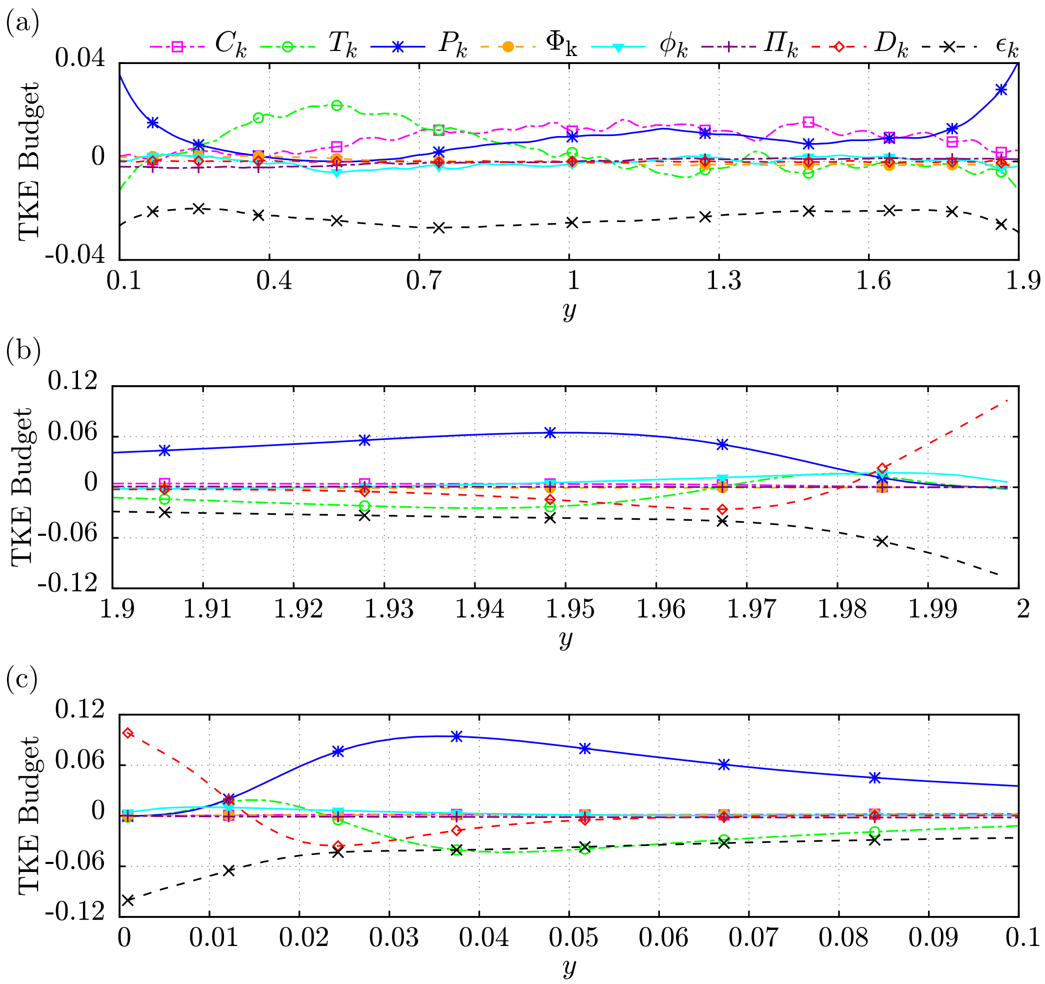

Figure 5.27: Budget of the turbulent kinetic energy at $x = 12.0$. (a) bulk of the channel; (b) close-up look at the top wall; (c) close-up look at the bottom wall.

provides the corresponding Strouhal number $St = f\delta/U_c$. The signals has been recorded for 39 non-dimensional time units that corresponds to approximately 3.1 flow-through times. To support our interpretations we examined animation sequences of the flow in planes that the time-signal is taken at. Herein, we should note that a small uncertainty may be introduced in our conclusions that are based on animations of the flow.

Figure 5.28 shows the power spectral densities at two locations of the horizontal channel. At the first one, $(x, y) = (-0.5, 1.6)$, they all exhibit three low-St peaks, at $St = 0.035, 0.09, 0.15$. Further, the peaks of S_{uu} and S_{vv} occur at the same frequencies. These peaks are thus attributed to the oscillatory motion of the primary shear layer and to its shedding of vortices. Also, the three low-St peaks of S_{TT} occur at slightly different Strouhal numbers than those of S_{uu} and S_{vv}; this is due to the fact that thermal mixing at this location is still at an early stage and, therefore, the fluctuations of the temperature are not yet synchronised with those of the velocity. We further observe that the profile of S_{TT} has a strong peak at a higher Strouhal number, $St \approx 0.5$, in contrast to the profiles of S_{uu} and S_{vv}. Based on the video animations of the DNS, we may attribute this peak to the wrapping of fluid of different temperature by the mushroom-like structures at the interface of the two streams such as the ones depicted in figure 5.11a.

On the other hand, at the second location $(x, y) = (12.00, 1.0)$, the peaks of the power spectral densities occur at the same frequencies. In other words, the dominant frequencies of the oscillatory motion of u, v and T coincide. The synchronisation of the power spectral densities is due to the extent of thermal mixing that has taken place. It also implies that once the two streams have been aligned sufficiently downstream the recirculation bubble and turbulence reaches equilibrium, the convective motions of spanwise vortices provide the main mechanism for thermal mixing.

Our analysis concludes with a discussion on the power spectral densities of the temperature at the walls of the T-junction. In particular, in figure 5.29 we show S_{TT} at the top wall, in the vicinity of the upstream corner of the jet $(x, y) = (-1.1, 2.0)$ and in the vicinity of the reattachment point of the flow $(x, y) = (4.0, 2.0)$. Close to the upstream corner of the jet, S_{TT} has two dominant frequencies at $St = 0.04$ and 0.09. These Strouhal numbers, based on the Re and Ri of the flow, correspond to frequencies of 17 Hz and 39 Hz respectively. According to the study of Chapuliot et al. [100], the critical frequencies for thermal fatigue are between 0.1 and 10 Hz. Therefore, the walls of the T-junction are not susceptible to thermal fatigue in this vicinity. Finally, close to the reattachment point of the flow the dominant frequencies of the fluctuations of the temperature are at 34 Hz and 12 Hz. These frequencies lie outside the interval 0.1 Hz $< f <$ 10 Hz, thus, the walls of the T-junction are not susceptible to thermal fatigue.

As the above analysis have shown, in the flow studied in this chapter the walls of the T-junction are not susceptible to thermal fatigue. This result is in contrast to the one for the flows studied in chapter 4 where the walls of the T-junction were prone to thermal fatigue for both temperature ratios studied therein. This is because the reference length in the flow studied in this chapter is much smaller than in the previous one (1.3 mm instead of 30 mm). Thus, since $St \sim 1/\delta$, St correspond to higher frequencies f for the flow studied in this chapter.

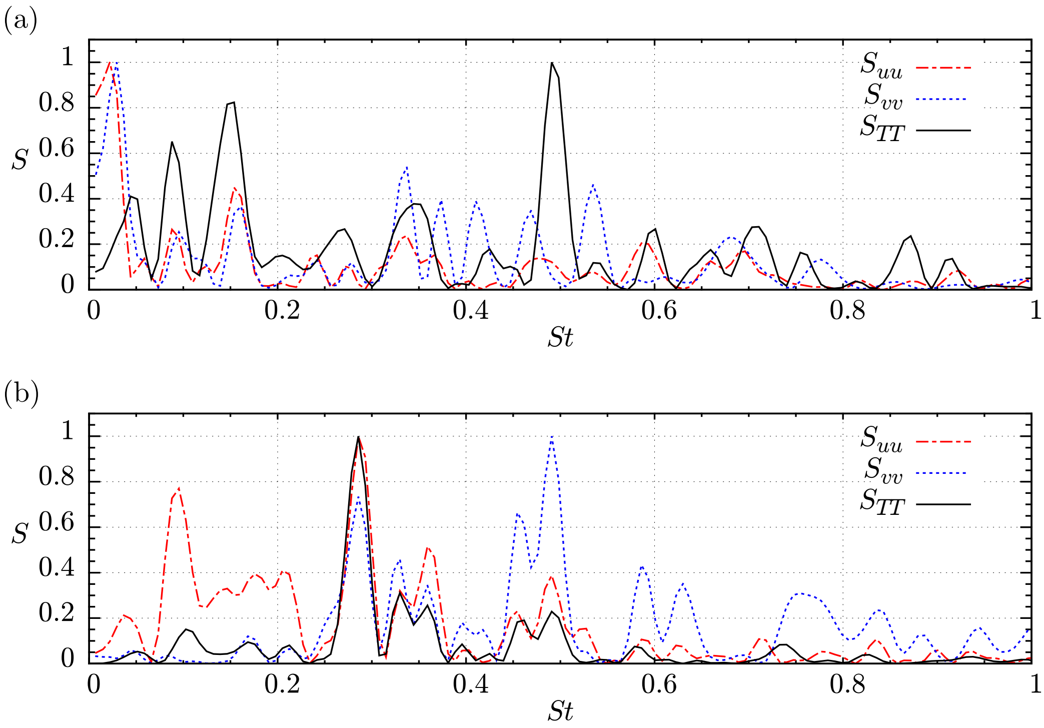

Figure 5.28: Power spectral density of the spanwise-averaged signals $\overline{u}$, $\overline{v}$, and $\overline{T}$, at two locations in the horizontal channel. Each profile has been normalised with respect to its maximum value. (a) $(x,\, y) = (-0.5,\, 1.6)$, (b) $(x,\, y) = (12.0,\, 1.0)$

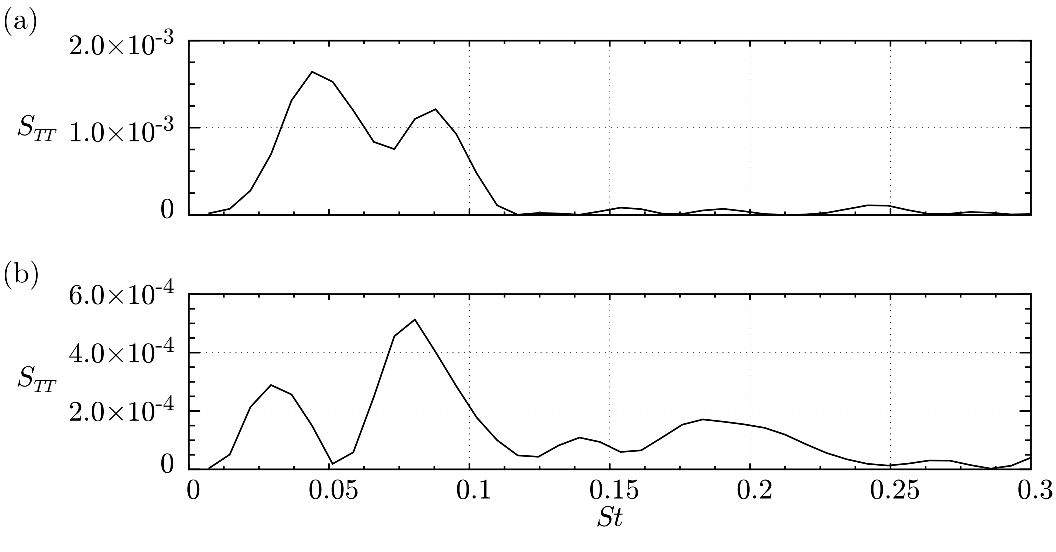

Figure 5.29: Time-series analysis of the spanwise-averaged temperature, $\overline{T(x,y)}$ at two near-wall locations. (a) $(x, y) = (-1.1, 2.0)$, (b) $(x, y) = (4.0, 2.0)$

5.4 Conclusions

In this chapter we presented an analysis of turbulent heat transfer in liquid-liquid flows in a T-junction under non-Boussinesq conditions. The temperature difference between the two streams is $\Delta\hat{T} = 100$K that results to a cold incoming jet with 4.38 times higher viscosity. Despite the different effect that thermal non-equilibrium has in liquid flows, in comparison to gas flows in T-junctions, the general features of the flow do not change significantly in the case presented in this chapter.

Our study was based on DNS of the interaction and thermal mixing between a hot incoming crossflow and a cold vertical jet coming from above, supplemented with wall-resolved LES of the same flow. According to our simulations, both thermal mixing and turbulence production are driven by the two shear layers that originate from the corners of the entry of the jet, *i.e.* the primary shear layer formed by the two streams and the secondary shear layer formed by the incoming jet and the large recirculation bubble. These two layers roll up rapidly, thereby shedding numerous spanwise and streamwise vortical structures. Most of them break up in small vortices that are convected downstream in a highly turbulent environment, whereas others are trapped in the recirculation bubble. As the two shear layers spread, they start to interact and eventually merge, which further enhances mixing and heat diffusion. Our analysis of the turbulent kinetic energy budget further corroborates the dominant role of these shear layers in turbulence production and transport. Most of the turbulent kinetic energy is dissipated at the walls of the horizontal channel with particularly high values recorded close to the reattachment point of the flow. Nonetheless, further downstream, the turbulence reaches equilibrium as the production and dissipation of turbulent kinetic energy become equal.

Another important feature of the flow is that the recirculation bubble leads to a Venturi effect that produces a favourable pressure gradient and accelerates both crossflow and incoming jet. Subsequently though, as the flow expands, an adverse pressure gradient is formed which contributes considerably to turbulence generation, especially in the bottom half of the horizontal channel. Our simulations further reveal that the flow at the vertical branch detaches before it enters the horizontal channel, which leads to the formation a secondary recirculation zone inside the vertical channel. Also, due to its high momentum flux, part of the incoming jet turns upstream upon entry in the horizontal channel, which produces a thin and elongated separation zone close to the top wall.

Comparison between our different simulations revealed that the wall-resolved LES provides satisfactory predictions the first and second order statistics of the flow quantities. The most noticeable discrepancy is that the LES produced mildly diffused profiles for the second-order statistics in the regions of intense turbulence production such as the large recirculation bubble. Even so, these discrepancies are not deemed detrimental, given the significant computational savings that LES offers.

Chapter 6

Concluding remarks and perspectives

The objective of this PhD thesis was to advance our knowledge of turbulent heat transfer in T-junctions. We first examined constant-density flows. Our analysis was based on wall-resolved and experimentally validated LES. To the best of our knowledge this is the first wall-resolved simulation with such a good agreement with available experimental data for the flows of interest. The analysis we performed allowed us to reveal two features of the flow field that have not been reported before. The first one is a small-scale recirculating region between the entry of the jet and the large recirculation bubble. The second one is a region with negative turbulent-kinetic-energy production located in the vicinity of the reattachment point of the flow past the large bubble.

Subsequently, we conducted the first wall-resolved LES of turbulent heat transfer in T-junctions without invoking the Boussinesq approximation. In this part of the thesis we examined cases of gas-gas flows with high and low temperature ratios between the two streams. Our studies confirmed the important role of the temperature as an active scalar, which enhances turbulence production and mixing between the two streams. Also, the examination of the flow statistics showed that mixing is mainly driven by the shear layer that is formed between the crossflow and the incoming jet. Further, we performed spectral analysis of the temperature signal at certain locations in the flow field. Our analysis revealed that, for the flow conditions considered herein, the walls of the T-junctions are susceptible to thermal fatigue. The results presented in this part are related to air-conditioning systems of automobiles and they can be used in order to optimise their performance.

We also investigated turbulent heat transfer in liquid-liquid flows via both DNS and LES. This was the first DNS study of turbulent flows in T-junctions. Our analysis was based on an extensive examination of the instantaneous flow field which allowed us to identify features that contribute to the mixing process, such as the mushroom-like structures of streamwise vorticity right below the entry of the jet, and the large spanwise rollers shed by the shear layers that emanate from the corners of the jet entry. In addition, we computed the budget of turbulent kinetic energy so as to delineate the regions of strong turbulence production and the mechanisms for its transport. For example, large amounts of turbulence are produced at the cores of the shear layers and are tranported towards the walls where they eventually they dissipate. Finally, we assessed the predicitve capacity of LES for the flows of interest. Overall, the LES results compare favourably with our DNS data, which shows that wall-resolved LES can be a viable alternative to DNS, thereby offering tremendous computational savings.

Future work and perspectives

The present work can be extended in many ways. For instance, one can apply more sophisticated and accurate methods for the quantification of mixing in flows in T-junctions. For example, as described in section 4.3, a passive and artificial tracer may be used. Such analysis will provide additional insight on the flow behaviour in the near-wall regions close to the entry of the jet.

Another extension of this PhD dissertation is to examine flows in which the incoming jet does not extend through the entire spanwise direction, *i.e.* flows with a jet of circular shape. In these cases the dynamics of the flow change considerably in comparison with those studied in the context of this thesis. For example, in flows in T-junctions with circular jets, the interaction of the crossflow with the incoming jet results in the formation of a horseshoe vortex. This structure is expected to affect significantly the mixing process. Thus, an examination of these flows can provide additional insight regarding turbulent heat transfer in T-junctions. In order to achieve this, the immersed boundary method [122] can be implemented to the existing software. This methodology allows the use of this computational tool for the analysis of the interaction of a crossflow with a circular incoming jet with minor modifications.

Further, our study can be extended to flows at higher Reynolds numbers. In particular, we can examined flows with Reynolds numbers at the order of 10^5 via wall-resolved simulations. In this case a grid of size of some hundreds million grid nodes must be used. These simulations provide information that are more relevant to nuclear applications while their computational cost is not prohibitively high.

It is also interesting to examine flows in Y-junctions because they are also encountered in industrial applications. In these cases, the recirculation bubble downstream the incoming jet is of smaller size. This, is expected to substantially modify the dynamics of the mixing process, as well as the flow field in the near-wall regions, the later having implications to the thermal-fatigue issue of the walls of the junction. These flows can be studied with the numerical tools that we developed in this thesis. For that, it suffices to perform a coordinate transformation to the governing equations.

Finally, another valuable future direction is to study turbulent heat-transfer in T-junctions with phase change (evaporation or condensation). Such flows are of primarily interest in both the nuclear-reactor and the heating and air-conditioning industries. The study of phase-change phenomena with homogeneous models can be realised with mild modifications of the existing software. On the other hand, the introduction of heterogeneous models (such as, for example, individual tracking of bubbles) would require a significant upgrade of the software that we developed in the context of this thesis.

Bibliography

[1] M. Hirota, M. Kuroki, H. Nakayama, H. Asano, and S. Hirayama. Promotion of turbulent thermal mixing of hot and cold airflows in T-junction. *Flow Turbul. Combust.*, 81(1-2):321–336, 2008.

[2] Y. Lejeail and N. Kasahara. Thermal fatigue evaluation of cylinders and plates subjected to fluid temperature fluctuations. *Int. J. Fatigue*, 27(7): 768–772, 2005.

[3] C. Faidy, T. Courtois, E. Fraguier, J. Leduff, A. Lefrancois, and J. Dechelotte. Thermal fatigue in French RHR system. In *Int. Conf. on Fatigue of Reactor Components, Napa, CA.*, 2000.

[4] O. Gelineau, C. Escaravage, J.P. Simoneau, and C. Faidy. High cycle thermal fatigue: experience and state of the art in French LMFRs. In *Trans. of 16th Int. Conference on Structural Mechanics in Reactor Technology (SMiRT-16), Washington DC, Paper*, volume 1311, pages 1–7, 2001.

[5] B.L. Smith, J.H. Mahaffy, and K. Angele. A CFD benchmarking exercise based on flow mixing in a T-junction. *Nucl. Eng. Des.*, 264:80–88, 2013.

[6] M.S. Loginov, E.M.J. Komen, and T. Höhne. Application of large-eddy simulation to pressurized thermal shock: Assessment of the accuracy. *Nucl. Eng. Des.*, 241(8):3097–3110, 2011.

[7] H. Kamide, M. Igarashi, S. Kawashima, N. Kimura, and K. Hayashi. Study on mixing behavior in a tee piping and numerical analyses for evaluation of thermal striping. *Nucl. Eng. Des.*, 239(1):58–67, 2009.

[8] C. Walker, M. Simiano, R. Zboray, and H.-M. Prasser. Investigations on mixing phenomena in single-phase flow in a T-junction geometry. *Nucl. Eng. Des.*, 239(1):116–126, 2009.

[9] A. de Tilly and J.M.M. Sousa. An experimental study of heat transfer in a two-dimensional T-junction operating at a low momentum flux ratio. *Int. J. Heat Mass Transfer*, 51(3):941–947, 2008.

[10] M. Hirota, H. Asano, H. Nakayama, T. Asano, and S. Hirayama. Three-dimensional structure of turbulent flow in mixing T-junction. *JSME Int. J., Ser. B*, 49(4):1070–1077, 2006.

[11] M. Hirota, E. Mohri, H. Asano, and H. Goto. Experimental study on turbulent mixing process in cross-flow type T-junction. *Int. J. Heat Fluid Flow*, 31(5):776–784, 2010.

[12] J. Westin, M. Henriksson, F. Alavyoon, L. Andersson, P. Veber, and C. Andersson. Experiments and unsteady CFD-calculations of thermal mixing in a T-junction. 2006.

[13] J. Westin, P. Veber, L. Andersson, C.T. Mannetje, U. Andersson, J. Eriksson, M.E. Henriksson, F. Alavyoon, and C. Andersson. High-cycle thermal fatigue in mixing tees. large-eddy simulations compared to a new validation experiment. *ICONE16, Orlando*, 2008.

[14] V.S. Naik-Nimbalkar, A.W. Patwardhan, I. Banerjee, G. Padmakumar, and G. Vaidyanathan. Thermal mixing in T-junctions. *Chem. Eng. Sci.*, 65(22): 5901–5911, 2010.

[15] C.H. Lin, M.S. Chen, and Y.M. Ferng. Investigating thermal mixing and reverse flow characteristics in a T-junction by way of experiments. *Appl. Therm. Eng.*, 99:1171–1182, 2016.

[16] L.-W. Hu and M.S. Kazimi. LES benchmark study of high cycle temperature fluctuations caused by thermal striping in a mixing tee. *Int. J. Heat Fluid Flow*, 27(1):54–64, 2006.

[17] J.I. Lee, L.-W. Hu, P. Saha, and M.S. Kazimi. Numerical analysis of thermal striping induced high cycle thermal fatigue in a mixing tee. *Nucl. Eng. Des.*, 239(5):833–839, 2009.

[18] T. Lu, P.X. Jiang, Z.J. Guo, Y.W. Zhang, and H. Li. Large-eddy simulations (LES) of temperature fluctuations in a mixing tee with/without a porous medium. *Int. J. Heat Mass Transfer*, 53(21-22):4458–4466, 2010.

[19] S. Kuhn, O. Braillard, B. Ničeno, and H.-M. Prasser. Computational study of conjugate heat transfer in T-junctions. *Nucl. Eng. Des.*, 240(6):1548–1557, 2010.

[20] A.K. Kuczaj, E.M.J. Komen, and M.S. Loginov. Large-Eddy Simulation study of turbulent mixing in a T-junction. *Nucl. Eng. Des.*, 240(9):2116–2122, 2010.

[21] A. Sakowitz, M. Mihaescu, and L. Fuchs. Effects of velocity ratio and inflow pulsations on the flow in a T-junction by Large Eddy Simulation. *Comput. Fluids*, 88:374–385, 2013.

[22] A. Sakowitz, M. Mihaescu, and L. Fuchs. Turbulent flow mechanisms in mixing T-junctions by Large Eddy Simulations. *Int. J. Heat Fluid Flow*, 45: 135–146, 2014.

[23] R.J.A. Howard and E. Serre. Large-eddy simulation in a mixing tee junction: High-order turbulent statistics analysis. *Int. J. Heat Fluid Flow*, 51:65–77, 2015.

[24] R.J.A. Howard and E. Serre. Large eddy simulation in Code_Saturne of thermal mixing in a T-junction with brass walls. *Int. J. Heat Fluid Flow*, 63:119–127, 2017.

[25] R. Tunstall, D. Laurence, R. Prosser, and A. Skillen. Large eddy simulation of a T-junction with upstream elbow: The role of dean vortices in thermal fatigue. *Appl. Therm. Eng.*, 107:672–680, 2016.

[26] W.R. Dean. Xvi. Note on the motion of fluid in a curved pipe. *Phil. Mag.*, 4(20):208–223, 1927.

[27] W.R. Dean. Lxxii. The stream-line motion of fluid in a curved pipe (second paper). *Phil. Mag.*, 5(30):673–695, 1928.

[28] Z. Wu, D. Laurence, H. Iacovides, and I. Afgan. Direct simulation of conjugate heat transfer of jet in channel crossflow. *Int. J. Heat Mass Transfer*, 110:193–208, 2017.

[29] Z. Wu, D. Laurence, and I. Afgan. Direct numerical simulation of a low momentum round jet in channel crossflow. *Nucl. Eng. Des.*, 313:273–284, 2017.

[30] J.-M. Ndombo and R.J.A. Howard. Large Eddy Simulation and the effect of the turbulent inlet conditions in the mixing Tee. *Nucl. Eng. Des.*, 241(6): 2172–2183, 2011.

[31] W. Wagner and H.-J. Kretzschmar. *International Steam Tables - Properties of Water and Steam based on the Industrial Formulation IAPWS-IF97*. Springer, 2008.

[32] M. Georgiou and M.V. Papalexandris. Numerical study of turbulent flow in a rectangular T-junction. *Phys. Fluids*, 29(6):065106, 2017.

[33] M. Georgiou and M.V. Papalexandris. Turbulent mixing in T-junctions: the role of the temperature as an active scalar. *Int. J. Heat Mass Transfer*, 115 (B):793–809, 2017.

[34] M. Georgiou and M.V. Papalexandris. Turbulent heat transfer in liquid-liquid flow in a T-junction. *Under review*.

[35] G. Gallavotti. *Foundations of fluid dynamics*. Springer, 2013.

[36] A.J. Chorin. A numerical method for solving incompressible viscous flow problems. *J. Comput. Phys.*, 2:12, 1967.

[37] A.W. Cook and J.J. Riley. Direct numerical simulation of a turbulent reactive plume on a parallel computer. *J. Comput. Phys.*, 129:263, 1996.

[38] J. de Charentenay, D. Thévenin, and B. Zamuner. Comparison of direct numerical simulations of turbulent flames using compressible or low Mach number formulations. *Int. J. Num. Meth. Fluids*, 39:497, 2002.

[39] C.D. Pierce and P. Moin. Progress-variable approach for large-eddy simulation of non-premixed turbulent combustion. *J. Fluid Mech.*, 504:73–97, 2004.

[40] F. Nicoud. Conservative high-order finite-difference schemes for low Mach number flows. *J. Comput. Phys.*, 158:71, 2000.

[41] R. Knikker. A comparative study of high-order variable-property segregated algorithms for unsteady low Mach number flows. *Int. J. Numer. Meth. Fluids*, 66(4):403–427, 2011.

[42] B. Lessani and M.V. Papalexandris. Time-accurate calculation of variable density flows with strong temperature gradients and combustion. *J. Comput. Phys.*, 212(1):218–246, 2006.

[43] C.M. Rhie and W.L Chow. Numerical study of the turbulent flow past an airfoil with trailing edge separation. *AIAA J.*, 21(11):1525–1532, 1983.

[44] A. Majda and J. Sethian. The derivation and numerical solution of the equations for zero Mach number combustion. *Combust. Sci. Technol.*, 42: 185, 1985.

[45] J.M. Beckers. Analytical linear numerical stability conditions for an anisotropic three-dimensional advection-diffusion equation. *SIAM J. Numer. Anal.*, 29(3):701–713, 1992.

[46] W.-L. Hong and D.T. Walker. Reynolds-averaged equations for free-surface flows with application to high-froude-number jet spreading. *J. Fluid Mech.*, 417:183–209, 2000.

[47] B. Lessani and M.V. Papalexandris. Numerical study of turbulent channel flow with strong temperature gradients. *Int. J. Numer. Method. H*, 18(3/4): 545–556, 2008.

[48] S. Muppidi and K. Mahesh. Direct numerical simulation of passive scalar transport in transverse jets. *J. Fluid Mech.*, 598:335–360, 2008.

[49] R.W. Johnson and R.J. MacKinnon. Equivalent versions of the quick scheme for finite-difference and finite-volume numerical methods. *Int. J. Numer. Meth. Bio.*, 8(12):841–847, 1992.

[50] J. Thuburn. TVD schemes, positive schemes, and the universal limiter. *Mon. Weather Rev.*, 125(8):1990–1993, 1990.

[51] A. Favre. Turbulence: Space-time statistical properties and behavior in supersonic flows. *Phys. Fluids*, 26(10):2851–2863, 1983.

[52] J. Boussinesq. *Essai sur la théorie des eaux courantes.* Imprimerie nationale, 1877.

[53] J. Smagorinsky. General circulation experiments with the primitive equations: I. The basic experiment. *Mon. Weather Rev.*, 91(3):99–164, 1963.

[54] P. Sagaut. *Large eddy simulation for incompressible flows: an introduction*. Springer, 2006.

[55] J.P. Boris, F.F. Grinstein, E.S Oran, and R.L Kolbe. New insights into large eddy simulation. *Fluid dynamics research*, 10(4-6):199–228, 1992.

[56] P. Moin, K. Squires, W.H. Cabot, and S. Lee. A dynamic subgrid-scale model for compressible turbulence and scalar transport. *Phys. Fluids A*, 3 (11):2746–2757, 1991.

[57] M. Germano, U. Piomelli, P. Moin, and W.H. Cabot. A dynamic subgrid-scale eddy viscosity model. *Phys. Fluids A*, 3(7):1760–1765, 1991.

[58] D.K. Lilly. A proposed modification of the Germano subgrid-scale closure method. *Phys. Fluids A*, 4(3):633–635, 1992.

[59] U. Piomelli and J. Liu. Large-eddy simulation of rotating channel flows using a localized dynamic model. *Phys. Fluids*, 7(4):839–848, 1995.

[60] T.M. Eidson. Numerical simulation of the turbulent Rayleigh–Bénard problem using subgrid modelling. *J. Fluid Mech.*, 158:245–268, 1985.

[61] A. Zainali and B. Lessani. Large-eddy simulation of unstably stratified turbulent channel flow with high temperature differences. *Int. J. Heat Mass Transfer*, 53(21):4865–4875, 2010.

[62] S.T Jayaraju, E.M.J. Komen, and E. Baglietto. Suitability of wall-functions in Large Eddy Simulation for thermal fatigue in a T-junction. *Nucl. Eng. Des.*, 240(10):2544–2554, 2010.

[63] A. Smirnov, S. Shi, and I. Celik. Random flow generation technique for large eddy simulations and particle-dynamics modeling. *J. Fluids Eng.*, 123(2): 359–371, 2001.

[64] M. Klein, A. Sadiki, and J. Janicka. A digital filter based generation of inflow data for spatially developing direct numerical or large eddy simulations. *J. Comput. Phys.*, 186(2):652–665, 2003.

[65] N. Jarrin, S. Benhamadouche, D. Laurence, and R. Prosser. A synthetic-eddy-method for generating inflow conditions for large-eddy simulations. *Int. J. Heat Fluid Flow*, 27(4):585–593, 2006.

[66] C.D. Pierce. Progress-variable approach for large-eddy simulation of turbulent combustion. *Ph.D. Thesis, Stanford Univ.*, 2001.

[67] L. Dagum and R. Menon. OpenMP: an industry standard API for shared-memory programming. *IEEE Comput Sci Eng*, 5(1):46–55, 1998.

[68] H.A. Van der Vorst. Bi-CGSTAB: A fast and smoothly converging variant of Bi-CG for the solution of nonsymmetric linear systems. *SIAM J. Sci. and Stat. Comput.*, 13(2):631–644, 1992.

[69] G. Guennebaud, B. Jacob, et al. Eigen v3. http://eigen.tuxfamily.org, 2010.

[70] O. Schenk and K. Gärtner. Solving unsymmetric sparse systems of linear equations with PARDISO. *Future. Gener. Comp. Sy.*, 20(3):475–487, 2004.

[71] M. Frigo and S.G. Johnson. The design and implementation of FFTW3. *Proceedings of the IEEE*, 93(2):216–231, 2005. Special issue on "Program Generation, Optimization, and Platform Adaptation".

[72] R. Tunstall, D. Laurence, R. Prosser, and A. Skillen. Benchmarking LES with wall-functions and RANS for fatigue problems in thermal–hydraulics systems. *Nucl. Eng. Des.*, 308:170–181, 2016.

[73] S. Muppidi and K. Mahesh. Direct numerical simulation of round turbulent jets in crossflow. *J. Fluid Mech.*, 574:59–84, 2007.

[74] W.P. Jones and M. Wille. Large-eddy simulation of a plane jet in a crossflow. *Int. J. Heat Fluid Flow*, 17(3):296–306, 1996.

[75] T.A. Zang. Numerical simulation of the dynamics of turbulent boundary layers: perspectives of a transition simulator. *Philos. Trans. R. Soc. London, A*, 336(1641):95–102, 1991.

[76] N.J. Georgiadis, D.P. Rizzetta, and C. Fureby. Large-Eddy Simulation: current capabilities, recommended practices, and future research. *AIAA J.*, 48 (8):1772–1784, 2010.

[77] J. Fröhlich, C.P. Mellen, W. Rodi, L. Temmerman, and M.A. Leschziner. Highly resolved large-eddy simulation of separated flow in a channel with streamwise periodic constrictions. *J. Fluid Mech.*, 526:19–66, 2005.

[78] S. Muppidi and K. Mahesh. Study of trajectories of jets in crossflow using direct numerical simulations. *J. Fluid Mech.*, 530:81–100, 2005.

[79] R.M. Kelso, T.T. Lim, and A.E. Perry. An experimental study of round jets in cross-flow. *J. Fluid Mech.*, 306:111–144, 1996.

[80] N. Fukushima, K. Fukagata, N. Kasagi, H. Noguchi, and K. Tanimoto. Numerical and experimental study on turbulent thermal mixing in a T-junction flow. In *The 6th ASME-JSME Thermal Engineering Joint Conference*, pages 16–20, 2003.

[81] C. Schaupp, R. Friedrich, and H. Foysi. Transverse injection of a plane-reacting jet into compressible turbulent channel flow. *J. Turbul.*, 13:N24, 2012.

[82] J. Andreopoulos and W. Rodi. Experimental investigation of jets in a cross-flow. *J. Fluid Mech.*, 138:93–127, 1984.

[83] J.C.R. Hunt, A.A. Wray, and P. Moin. Eddies, stream, and convergence zones in turbulent flows. *Center For Turbulence Research, Report CTR-S88*, 1988.

[84] H. Le, P. Moin, and J. Kim. Direct numerical simulation of turbulent flow over a backward-facing step. *J. Fluid Mech.*, 330(1):349–374, 1997.

[85] K.R. Sreenivasan. Laminarescent, relaminarizing and retransitional flows. *Acta Mech.*, 44:1–48, 1982.

[86] C. Bourassa and F.O. Thomas. An experimental investigation of a highly accelerated turbulent boundary layer. *J. Fluid Mech.*, 634:359–404, 2009.

[87] R.L. Simpson. A model for the backflow mean velocity profile. *AIAA J.*, 21 (1):142–143, 1983.

[88] M.M. Rogers and R.D. Moser. Direct simulation of a self-similar turbulent mixing layer. *Phys. Fluids*, 6 (2):903–923, 1994.

[89] A.K.M.F. Hussain. Coherent structures and turbulence. *J. Fluid Mech.*, 173: 303–356, 1986.

[90] A. Liberzon, B. Lüthi, M. Guala, W. Kinzelbach, and A. Tsinober. Experimental study of the structure of flow regions with negative turbulent kinetic energy production in confined three-dimensional shear flows with and without buoyancy. *Phys. Fluids*, 17(9):095110, 2005.

[91] B. Gayen and S. Sarkar. Negative turbulent production during flow reversal in a stratified oscillating boundary layer on a sloping bottom. *Phys. Fluids*, 23(10):101703, 2011.

[92] W.-P. Wang and R.H. Pletcher. On the large eddy simulation of a turbulent channel flow with significant heat transfer. *Phys. Fluids*, 8(12):3354–3366, 1996.

[93] B. Lessani and A. Zainali. Numerical investigation of stably stratified turbulent channel flow under non-Boussinesq conditions. *J. Turbul.*, 10:1–25, 2009.

[94] F. Zonta, M. Onorato, and A. Soldati. Turbulence and internal waves in stably-stratified channel flow with temperature-dependent fluid properties. *J. Fluid Mech.*, 697:175–203, 2012.

[95] U. Piomelli and J.R. Chasnov. Large-eddy simulations: theory and applications. In *Turbulence and transition modelling*, pages 269–336. Springer Netherlands, 1996.

[96] S. Megerian, J. Davitian, L.S. de B. Alves, and A.R. Karagozian. Transverse-jet shear-layer instabilities. Part 1. Experimental studies. *J. Fluid Mech.*, 593:93–129, 2007.

[97] X. Guo, W. Schröder, and M. Meinke. Large-eddy simulations of film cooling flows. *Comput. Fluids*, 35(6):587–606, 2006.

[98] E.R. Van Driest. Turbulent boundary layer in compressible fluids. *J. Aeronaut. Sci.*, 18(3):145–160, 1951.

[99] P.G. Huang and G.N. Coleman. Van Driest transformation and compressible wall-bounded flows. *AIAA J.*, 32(10):2110–2113, 1994.

[100] S. Chapuliot, C. Gourdin, T. Payen, J.P. Magnaud, and A. Monavon. Hydro-thermal-mechanical analysis of thermal fatigue in a mixing tee. *Nucl. Eng. Des.*, 235(5):575–596, 2005.

[101] M. Kuschewski, R. Kulenovic, and E. Laurien. Experimental setup for the investigation of fluid–structure interactions in a t-junction. *Nucl. Eng. Des.*, 264:223–230, 2013.

[102] P.K. Selvam, R. Kulenovic, and E. Laurien. Large eddy simulation on thermal mixing of fluids in a T-junction with conjugate heat transfer. *Nucl. Eng. Des.*, 284:238–246, 2015.

[103] P. Gauder, P.K. Selvam, R. Kulenovic, and E. Laurien. Large eddy simulation studies on the influence of turbulent inlet conditions on the flow behavior in a mixing tee. *Nucl. Eng. Des.*, 298:51–63, 2016.

[104] J. Kickhofel, H.-M. Prasser, P.K. Selvam, E. Laurien, and R. Kulenovic. T-junction cross-flow mixing with thermally driven density stratification. *Nucl. Eng. Des.*, 309:23–39, 2016.

[105] C.O. Popiel and J. Wojtkowiak. Simple formulas for thermophysical properties of liquid water for heat transfer calculations (from 0 ^{o}C to 150 ^{o}C). *Heat Transfer Eng.*, 19(3):87–101, 1998.

[106] F. Zonta, C. Marchioli, and A. Soldati. Modulation of turbulence in forced convection by temperature-dependent viscosity. *J. Fluid Mech.*, 697:150–174, 2012.

[107] H. Choi and P. Moin. Effects of the computational time step on numerical solutions of turbulent flow. *J. Comput. Phys.*, 113(1):1–4, 1994.

[108] F. Schäfer, M. Breuer, and F. Durst. The dynamics of the transitional flow over a backward-facing step. *J. Fluid Mech.*, 623:85–119, 2009.

[109] H. Tennekes and J.L. Lumley. *A first course in turbulence*. MIT press, 1972.

[110] S.B. Pope. *Turbulent flows*. Cambridge Univ. Press, 2001.

[111] S.J. Lin and G.M. Corcos. The mixing layer: deterministic models of a turbulent flow. Part 3. The effect of plane strain on the dynamics of streamwise vortices. *J. Fluid Mech.*, 141:139–178, 1984.

[112] G.M. Corcos and S.J. Lin. The mixing layer: deterministic models of a turbulent flow. Part 2. The origin of the three-dimensional motion. *J. Fluid Mech.*, 139:67–95, 1984.

[113] L.P. Bernal and A. Roshko. Streamwise vortex structure in plane mixing layers. *J. Fluid Mech.*, 170:499–525, 1986.

[114] M.M. Rogers and R.D. Moser. The three-dimensional evolution of a plane mixing layer: the Kelvin-Helmholtz rollup. *J. Fluid Mech.*, 243:183–226, 1992.

[115] M. Skote and D.S. Henningson. Direct numerical simulation of a separated turbulent boundary layer. *J. Fluid Mech.*, 471:107–136, 2002.

[116] P.D. Antoniadis and M.V. Papalexandris. Dynamics of shear layers at the interface of a highly porous medium and a pure fluid. *Phys. Fluids*, 27: 014104, 2015.

[117] P.D. Antoniadis and M.V. Papalexandris. Numerical study of unsteady, thermally-stratified shear flows in superposed porous and pure-fluid domains. *Int. J. Heat Mass Transfer*, 96(C):643 – 659, 2016.

[118] P.G. Huang, G.N. Coleman, and P. Bradshaw. Compressible turbulent channel flows: DNS results and modelling. *J. Fluid Mech.*, 305:185–218, 1995.

[119] P. Chassaing, R.A. Antonia, F. Anselmet, L. Joly, and S. Sarkar. *Variable Density Fluid Turbulence*. Kluwer, 2002.

[120] J. Kim, P. Moin, and R. Moser. Turbulence statistics in fully developed channel flow at low Reynolds number. *J. Fluid Mech.*, 177:133–166, 1987.

[121] P.R. Spalart. Direct simulation of a turbulent boundary layer up to R_θ= 1410. *J. Fluid Mech.*, 187:61–98, 1988.

[122] C.S. Peskin. The immersed boundary method. *Acta Numer.*, 11:479 – 517, 2002.